

Copyright  
by  
Prabhat Bhattarai  
2016

The Dissertation Committee for Prabhat Bhattarai  
certifies that this is the approved version of the following dissertation:

**Two-particle Correlations of Identified Particles in  
Heavy Ion Collisions at STAR**

Committee:

---

Christina Markert, Supervisor

---

Robert Ray, Co-Supervisor

---

Arno Bohm

---

Stephen Walker

---

Peter Onyisi

**Two-particle Correlations of Identified Particles in  
Heavy Ion Collisions at STAR**

by

**Prabhat Bhattarai, M.S., M.S., M.S. Stat.**

**DISSERTATION**

Presented to the Faculty of the Graduate School of  
The University of Texas at Austin  
in Partial Fulfillment  
of the Requirements  
for the Degree of

**DOCTOR OF PHILOSOPHY**

The University of Texas at Austin

August 2016

*To my mother Sita Devi and father Dharmananda Bhattarai*

## Acknowledgments

I would like to deeply acknowledge my supervisor G.W. Hoffmann. He provided me such a great opportunity to work in the field of Heavy-Ion Nuclear Physics. It was very sad moment that he passed away in 18<sup>th</sup> March 2016, just two months before my final PhD defense. He will always be remembered. I am very thankful to Christina Markert who accepted me as her student and supervised me during my last three months of my PhD. Even in a short time interval she taught me a lot on how to present my analysis. My deepest appreciation goes to my co-supervisor Robert Lanny Ray. He guided me in every steps of physics analysis. Thank you Lanny for your teaching and guidance.

I am grateful to PhD committee members Stephen G Walker, Peter Onyisi and Arno Bohm for the wonderful comments suggestions.

I am lucky to have worked with great colleagues such as Alexander Jentsch, Jo Schambach, Deepa Thomas, Justin Blair and Erin Gauger.

I would like to thank my mother, Sita Devi Bhattarai, and father, Dharmananda Bhattarai for support and encouragement to accomplish this project. I would also like to thank my mother-in-law Narayani Subedi for her support. I am especially thankful to my wife, Sharmila, and daughter Arya. Thank you very much for your support in every step. I am very grateful to have brothers and every member of family who encouraged me to pursue my

goals.

Furthermore, I would like to extend my sincere thanks to Naresh Neupane, Kumar Mainali, Madan Siwakoti, Naween Dahal, Gene Van Buren, Jerome Lauret and Saskia Mioduszeewski.

Prabhat Bhattarai

# Two-particle Correlations of Identified Particles in Heavy Ion Collisions at STAR

Prabhat Bhattarai, Ph.D.  
The University of Texas at Austin, 2016

Supervisor: Christina Markert  
Co-Supervisor: Robert Ray

The study of quarks and their interactions through gluons has been an active area of research since their discovery. For two decades the Relativistic Heavy Ion Collider (RHIC) at Brookhaven National Laboratory has been dedicated to studying the interactions between quarks by producing nuclear matter in an extremely dense and hot environment. It has been hypothesized that colliding beams of atomic nuclei near the speed of light creates the hot and dense environment in which all quarks in the nuclei de-confine to form a short-lived state of matter called a Quark Gluon Plasma (QGP). Because of the short lifetime of QGP, it is impossible to observe it directly and, the only way to study such matter is through the final state particles. Two-particle correlation, which is defined using Pearson's normalized covariance, is one of the techniques to study the early interactions via the final state particles. A broad survey has been made to study the two-particle correlations of identified-charged hadrons ( $\pi^\pm$ ,  $K^\pm$  and  $p^\pm$ ) in various ranges of momentum

for the hadrons produced in  $\sqrt{s_{NN}} = 200$  GeV Au+Au collisions at the STAR experiment at RHIC. A total of 2123 two-dimensional independent structures made by correlation coefficients in relative angular space in  $(\eta, \phi)$  for different combinations of identified hadrons have been studied. Correlations between any two identified particles contrasts to all-particle correlations giving an opportunity to study the contribution of each particle species in the hadronization processes. As a new feature, same-side anti-correlations are observed in both like-sign and unlike-sign pairs in certain  $y_T$  bins and in certain identified particles. A significant feature of the final state distribution of particles is an azimuthal anisotropy which is defined as the second Fourier component; the amplitude is proportional to parameter  $v_2$ . We report the measure of azimuthal anisotropy of identified hadrons for the first time and test for the factorization used in conventional analysis. The data presented here constitute a comprehensive measurement of the light-flavor, di-hadron density as function of collision centrality, transverse momentum and 2D relative angles in longitudinal (beam direction) and azimuthal directions.

# Table of Contents

<b>Acknowledgments</b>	<b>v</b>
<b>Abstract</b>	<b>vii</b>
<b>Contents</b>	<b>ix</b>
<b>List of Tables</b>	<b>xii</b>
<b>List of Figures</b>	<b>xiv</b>
<b>Chapter 1. Introduction</b>	<b>1</b>
1.1 QCD . . . . .	1
1.2 QGP . . . . .	3
1.3 Heavy-Ion Collisions . . . . .	6
1.3.1 Hydrodynamics . . . . .	7
1.3.2 Angular Correlations . . . . .	11
1.4 Outline . . . . .	16
<b>Chapter 2. Experimental Facility</b>	<b>17</b>
2.1 Introduction . . . . .	17
2.2 RHIC . . . . .	17
2.3 Overview of STAR . . . . .	20
2.4 Trigger . . . . .	23
2.5 Time Projection Chamber . . . . .	24
2.6 Time of Flight . . . . .	28

<b>Chapter 3. Data Analysis</b>	<b>32</b>
3.1 Introduction . . . . .	32
3.2 Coordinate System . . . . .	33
3.3 Event Selection . . . . .	35
3.3.1 Trigger . . . . .	35
3.3.2 Pileup . . . . .	36
3.4 Track Selection . . . . .	36
3.4.1 Particle Pair Selection . . . . .	37
3.4.2 Pair Weighting . . . . .	42
3.5 Centrality . . . . .	42
3.5.1 Definition . . . . .	43
3.5.2 Centrality in Runs 2010 and 2011 . . . . .	44
3.6 Particle Identification . . . . .	56
3.7 Momentum Ranges . . . . .	56
3.8 Two-Particle Correlation . . . . .	61
3.8.1 Charge Dependence of Correlations . . . . .	65
3.9 Normalization . . . . .	66
3.10 Statistical Uncertainties . . . . .	77
3.11 Systematic Uncertainties . . . . .	78
<b>Chapter 4. Pileup</b>	<b>80</b>
4.1 Introduction . . . . .	80
4.2 Pileup . . . . .	81
4.3 Pileup Signatures in STAR Run 2010 . . . . .	82
4.3.1 Pileup Removal . . . . .	84
4.4 Pileup Signatures in STAR Run 2011 . . . . .	95
4.4.1 Pileup Removal . . . . .	98
4.5 Conclusion . . . . .	99

<b>Chapter 5. Particle Identification</b>	<b>100</b>
5.1 Introduction . . . . .	100
5.2 PID using $dE/dx$ . . . . .	101
5.3 PID using $\beta^{-1}$ . . . . .	103
5.4 PID using $dE/dx$ and $\beta^{-1}$ . . . . .	105
5.5 Probability cut . . . . .	108
5.6 Efficiency and Purity . . . . .	109
<b>Chapter 6. Identified Particle Correlation</b>	<b>114</b>
6.1 Introduction . . . . .	114
6.2 Unidentified Particle Correlations . . . . .	115
6.2.1 Run 2010 . . . . .	118
6.2.2 Run 2011 . . . . .	122
6.3 $\pi - \pi$ Correlations . . . . .	128
6.4 $K - K$ Correlations . . . . .	137
6.5 $p - p$ Correlations . . . . .	149
6.6 $\pi - K$ Correlations . . . . .	158
6.7 $\pi - p$ Correlations . . . . .	165
6.8 $K - p$ Correlations . . . . .	173
6.9 $v_2[2D]$ and measured $v_2[EP]$ . . . . .	180
6.10 Systematic error in $v_2^2$ and $v_2$ . . . . .	183
6.11 Factorization . . . . .	187
6.12 Discussion . . . . .	195
6.13 Future Work . . . . .	202
<b>Chapter 7. Conclusion</b>	<b>204</b>
<b>Chapter 8. Appendix</b>	<b>207</b>
8.0.1 Approximation . . . . .	207
8.0.2 Fit Parameters . . . . .	208
<b>Bibliography</b>	<b>209</b>
<b>Vita</b>	<b>220</b>

## List of Tables

3.1	A complete list of track quality cut. . . . .	37
3.2	A complete list of conditions to accept track pairs. The charge of the track pairs are listed in the first column. If all conditions are met on one or more rows for a given charge pair, then the pair is accepted. Note: these are not pair cut conditions but are acceptance criteria. . . . .	40
3.3	Mapping of multiplicity classes to centrality classes and centrality numbers [1]. The raw multiplicity cuts are defined to achieve the same centrality fractions in each centrality. . . . .	44
3.4	Efficiency correction parameters, $\alpha_{corr}$ and $\beta_{corr}$ in Expressions 3.12 and 3.13. . . . .	52
3.5	Mapping of Mult(multiplicity) classes to Cent(centrality) classes for run 2004, 2010 and 2011. There are 22 multiplicity classes and 11 centrality classes. For example, for Run 2011, multiplicity 3 has $67 \leq N_{ch} < 115$ . Different multiplicity sub-classes having $\Delta N_{ch} \sim 50$ are combined make a centrality class e.g. multiplicity classes 18, 19, 20, and 21 are combined together to make a centrality class 10. . . . .	53
3.6	Lower and upper values of $p_T$ and $y_T$ for different particle type. Because of the mass dependance of $y_T$ , the $y_T$ ranges vary. . .	57
3.7	Ranges of $y_T$ sub-bins for different particle types. There are 5 sub-bins in $\pi^+$ and $\pi^-$ , 4 sub-bins in $K^+$ and $K^-$ and 3 sub-bins in $p$ and $\bar{p}$ . . . . .	58
3.8	Choice of cut bin IDs for $(y_{T1}, y_{T2})$ pairs. There are 25 unique IDs for a charge combination (e.g ++, +-, -+ or --) of $\pi\pi$ pairs. . . . .	58
3.9	Choice of cut bin IDs for $(y_{T1}, y_{T2})$ pairs. There are 20 unique IDs for a charge combination (e.g ++, +-, -+ or --) of $\pi K$ pairs. . . . .	59
3.10	Choice of cut bin IDs for $(y_{T1}, y_{T2})$ pairs. There are 15 unique IDs for a charge combination (e.g ++, +-, -+ or --) of $\pi p$ pairs. . . . .	59
3.11	Choice of cut bin IDs for $(y_{T1}, y_{T2})$ pairs. There are 16 unique IDs for a charge combination (e.g ++, +-, -+ or --) of $KK$ pairs. . . . .	59

3.12	Choice of cut bin IDs for $(y_{T1}, y_{T2})$ pairs. There are 12 unique IDs for a charge combination (e.g ++, +-, -+ or --) of $\bar{K}p$ pairs. . . . .	60
3.13	Choice of cut bin IDs for $(y_{T1}, y_{T2})$ pairs. There are 9 unique IDs for a charge combination (e.g ++, +-, -+ or --) of $pp$ pairs. . . . .	60
3.14	STAR to PHENIX scale factors for $\pi^\pm, K^\pm, \bar{p}$ and $p$ . . . . .	70
3.15	Centrality evolution of integrals in $y_T$ bins for $\pi^-$ . . . . .	74
3.16	Centrality evolution of integrals in $y_T$ bins for $\pi^+$ . . . . .	74
3.17	Centrality evolution of integrals in $y_T$ bins for $K^-$ . . . . .	75
3.18	Centrality evolution of integrals in $y_T$ bins for $K^+$ . . . . .	75
3.19	Centrality evolution of integrals in $y_T$ bins for $\bar{p}$ . . . . .	76
3.20	Centrality evolution of integrals in $y_T$ bins for $p$ . . . . .	76
6.1	The opening angle $\theta$ for different combination of $y_{T1}$ and $y_{T2}$ . . . . .	142
6.2	Observed particle probability. . . . .	185
6.4	Particle identification errors and fractional errors in $v_2$ and $v_2^2$ . . . . .	186
6.3	. . . . .	186
6.5	Fractional errors in $v_2$ for non-identified particles. . . . .	187
8.1	Pre-factor for $\pi^-\pi^+$ for centrality - 0 - 5% . . . . .	208

# List of Figures

1.1	A hypothesized illustration of the phase diagram of QCD matter [2]. The white line shows the phase boundary. Orange star on top left indicates Au+Au collisions at 200 GeV. The relativistic heavy-ion collisions provide a unique environment to explore the phases of QCD matter at high temperature and low baryon chemical potential. . . . .	5
1.2	An illustration of formation of almond-shaped interaction volume after mid-central collision of two nuclei. Spatial anisotropy in the interaction volume with respect to reaction-plane ( $x$ - $z$ plane) causes anisotropy in momentum of produced particles [3].	8
1.3	Measured $v_2$ of identified particles for Au+Au at 200 GeV. The results are compared with a hydrodynamic model [4]. . . . .	10
1.4	Centrality evolution of angular correlations, $\frac{\Delta\rho}{\sqrt{\rho_{ref}}}$ , in $(\eta_\Delta, \phi_\Delta)$ for Au+Au collisions at $\sqrt{s_{NN}} = 200$ GeV (top row) and $\sqrt{s_{NN}} = 62$ GeV (bottom row). The collision centrality increases left to right from the most peripheral to the most central [5]. . . . .	13
1.5	Centrality evolution of fit parameters for $(\eta_\Delta, \phi_\Delta)$ correlations data from Au+Au collisions at $\sqrt{s_{NN}} = 200$ GeV (solid symbol) and $\sqrt{s_{NN}} = 62$ GeV (open symbol). The centrality measure, $\nu$ , was computed at fixed energy of 200 GeV. The same-side 2D Gaussian amplitudes are shown on the top row. The amplitude of the dipole and quadrupole are shown in the bottom left and middle panel respectively. In the bottom right panel, the ratio of widths of the same-side 2D Gaussian are shown. The dashed line indicates the estimation from Glauber linear superposition. The systematic uncertainties are shown in the hatched region. Four of 11 centralities of this evolution are shown in Figure 1.4. This figure was taken from Reference [5]. . . . .	14
2.1	An overview of the RHIC facility. The STAR experiment is at 6 o'clock position of the RHIC ring. Source [6]. . . . .	19
2.2	An overview of upgraded STAR detector as of 2016. . . . .	20

2.3	A schematic diagram of STAR detector. The TOF detector (not shown in diagram) is just outside of TPC. The yellow (counter-clock-wise) and blue (clock-wise) beams along the $z$ -axis cross at the center of TPC. Source: [7] . . . . .	22
2.4	The STAR TPC which surrounds a beam-beam interaction region at RHIC. The beam-beam collisions take place near the center of the TPC . . . . .	24
2.5	One full sector of the anode pad plane. The inner sub-sector is on the right (1 through 13 pads) and the outer sub-sector is on the left (1 through 144) [8]. . . . .	25
2.6	Schematics diagram of the TOF system: 120 TOF trays and upVPDs on east and west side of beam pipe. . . . .	29
2.7	Side views of MRPC structure (not in scale) : top and bottom show length and width view of the tray respectively [9]. . . . .	31
3.1	Angular correlation for Au+Au at $\sqrt{s_{NN}} = 200$ GeV. In the left panel, correlations of all particles in centrality 9 in $y_{T1}(2.0, 2.5) - y_{T2}(1.0, 1.5)$ ( $y_T$ is transverse rapidity, see Section 3.7) range for Run4 data are shown. Similarly, in the right panel correlations of all particles in same centrality and similar $y_T$ range for Run11 data is shown. The gash like structure near $(\eta_{\Delta}, \phi_{\Delta}) \rightarrow 0$ is sharper and deeper in the Run11 data. . . . .	39
3.2	Track crossing cartoons showing transverse views of tracks in the TPC in full magnetic field. The panels show the distinction between track crossing for negative charges (top), positive charge (middle), and for opposite signed charges (bottom). . . . .	41
3.3	An illustration of a heavy-ion collision with an impact parameter of $b$ . On the left, two heavy-ions are approaching to collide. On the right, just after the collision, spectator nucleons are shown to be unaffected from the participant nucleons [10]. . . . .	43
3.4	Multiplicity frequency distribution of run 2004, 2010 and 2011 data. The differences in the distributions are significant at low and high multiplicity ( $N_{ch}$ ). . . . .	45
3.5	Unit normal frequency distributions of Run 2004 and 2010 data and MCG on $N_{ch,corrected}^{1/4}$ . The bold and slightly slanted horizontal line represents the extrapolation of the Run4 data. Similarly, the bold and slightly slanted vertical line is drawn parallel to the lower edge of the MCG model. The rectangular dot on the extrapolated slanted line in left of the graph corresponds to the lower half-max point (source: L. Ray private communication). . . . .	48

3.6	Multiplicity distributions of Run4, 10 and 11 data. . . . .	54
3.7	Multiplicity distributions of Run4, 10 and 11 data. . . . .	55
3.8	Centrality dependence of the $p_T$ distribution for $\pi^+$ (left) and $\pi^-$ (right) in Au+Au collisions at $\sqrt{s_{NN}}=200$ GeV. The different symbols are chosen for different centrality bins. The error bars are statistical only. For visual clarity, data points are scaled vertically as quoted in the figure [11]. . . . .	69
3.9	Particle yield for $\pi^-$ as a function of $(N_{part})^{1/3}$ . STAR and PHENIX spectra are in dashed blue and bold black lines respectively. The dotted red line is obtained by scaling the PHENIX spectrum to STAR. . . . .	71
3.10	Particle yield per unit $\eta$ as a function of $(N_{part})^{1/3}$ . The dashed line represents the sum of particle yields for all PID (obtained from the scaled PHENIX spectrum) while the solid line represents the all-particle yield (obtained from [12]). . . . .	72
4.1	Au-Au 62 GeV Run 2004. Left: Uncorrected angular correlations from 62 GeV 37-46% central Au-Au collisions showing pileup distortions, especially evident as the W-shaped non-uniformity of the away-side ridge on $\eta_\Delta$ . Right: The same data with pileup correction applied [5]. . . . .	83
4.2	Au-Au 200 GeV Run 2010 charge independent angular correlations showing significant distortion of the angular correlations for different approximate centralities. No vertex ranking cut has been applied. . . . .	84
4.3	Au-Au 200 GeV Run 2011 charge independent angular correlations for different approximate centralities. Vertex Ranking $> -2.5$ . . . . .	85
4.4	Au-Au 200 GeV Run 2010 charge independent angular correlations. Duncan's pileup filter $\left[ \frac{\Delta\rho}{\sqrt{\rho_{ref}}} (Cut) \right]$ (-20,20)cm has been implemented. Vertex ranking cut is not included. . . . .	86
4.5	Au-Au 200 GeV Run 2010 charge independent angular correlations. Duncan's pileup corrected $\left[ \frac{\Delta\rho}{\sqrt{\rho_{ref}}} (NoPileup) \right]$ for efficiency 75%. Vertex ranking cut is not included. . . . .	87
4.6	Au-Au 200 GeV Run 2010 charge independent angular analysis. Duncan's pileup $\left[ \frac{\Delta\rho}{\sqrt{\rho}} (Pileup) \right]$ for efficiency 75%. . . . .	88

4.7	Au-Au 200 GeV Run 2010 charge independent angular correlations. Duncan's pileup filter $\left[\frac{\Delta\rho}{\sqrt{\rho_{ref}}}(Cut)\right]$ as well as vertex ranking cut ( $> -2.5$ ) are included. . . . .	89
4.8	Au-Au 200 GeV Run 2010 charge independent angular correlations. Duncans pileup corrected $\left[\frac{\Delta\rho}{\sqrt{\rho_{ref}}}(NoPileup)\right]$ for efficiency 75% along with vertex ranking cut. . . . .	89
4.9	Au-Au 200 GeV Run 2010 charge independent angular correlations for tracks having both TPC and TOF hits. Vertex ranking cut is not included (compare this figure with Figure 4.2). The lower TOF acceptance than TPC acceptance is reflected in lower value of $ \eta_{\Delta} $ . . . . .	90
4.10	Au-Au 200 GeV Run 2010 charge independent angular correlations. Global DCA cut 0-1 cm. Vertex ranking cut is included. . . . .	91
4.11	Run 2010 multiplicity distribution. Left: Multiplicity distribution for global DCA 0-1 cm and 0 – 3 cm. Right: Power law based transformation of the distribution in the left panel. . . . .	92
4.12	Au-Au 200 GeV Run 2010 momentum versus global DCA distributions for a centrality 30-40%. There is a significant density of low momentum particles between $1 < DCA < 3$ cm . . . . .	92
4.13	Global versus primary tracks distribution. . . . .	93
4.14	Au-Au 200 GeV Run 2011 charge independent angular correlations. A $4\sigma$ band cut is applied. The correlations do not show signatures of pileup explicitly. . . . .	94
4.15	Au-Au 200 GeV Run 2011 charge independent angular correlations of $4\sigma$ band rejected events. The pileup contributes significantly to the correlations. . . . .	94
4.16	Au-Au 200 GeV Run 2011 (half protected trigger IDs 350003 and 350013) Charge Independent Angular Correlations. Vertex ranking cut is not included. . . . .	96
4.17	Au-Au 200 GeV Run 2011 (half protected trigger IDs 350023, 350003 and 350013) Charge Independent Angular Correlations. Vertex ranking cut is included. . . . .	96
4.18	Au-Au 200 GeV Run 2011 (fully protected trigger IDs 350023, 350033 and 350043) Charge Independent Angular Correlations. Vertex ranking cut is not included. . . . .	97
4.19	Au-Au 200 GeV Run 2011 (fully protected trigger IDs 350023, 350033 and 350043) Charge Independent Angular Correlations. Vertex ranking cut is included. . . . .	97

4.20	Au-Au 200 GeV Run 2011 (fully protected trigger IDs 350023, 350033 and 350043) charge independent angular correlations. Vertex ranking cut is included. Duncan's pileup filter $\left[\frac{\Delta\rho}{\sqrt{\rho_{ref}}}(Cut)\right]$ is applied. . . . .	98
4.21	Au-Au 200 GeV Run 2011 (fully protected trigger IDs 350023, 350033 and 350043) Duncan's pileup corrected $\left[\frac{\Delta\rho}{\sqrt{\rho_{ref}}}(NoPileup)\right]$ for efficiency 75%. Vertex ranking cut is included. . . . .	99
5.1	Energy loss by charged particles per unit distance in TPC for the particles of different momenta. . . . .	101
5.2	Inverse velocity distribution of the charged particles as a function of momentum. . . . .	104
5.3	2-dimensional distribution charged particles in $\Delta\beta_k^{-1}/\beta^{-1}$ and $n\sigma_{dE/dx}^k$ . The distribution is fit for <i>kaons</i> using both Gaussian ( <i>y</i> -axis) and Student's T( <i>x</i> -axis) distributions. The pull-distribution is the ratio of difference of data and fitting function to error in each bin. . . . .	106
5.4	2-Dimensional distribution charged particles in $\Delta\beta_k^{-1}/\beta^{-1}$ and $n\sigma_{dE/dx}^k$ . The distribution is fit for <i>kaons</i> using both Gaussian ( <i>y</i> -axis) and Student's T( <i>x</i> -axis) distributions. The pull-distribution is the ratio of difference of data and fitting function to error in each bin. . . . .	107
5.5	Efficiency and Purity of $\pi$ as a function of $p$ and $\eta$ . Together with the probability cut of 0.6, $2D n\sigma$ cut, $a = b = 3$ , was applied. . . . .	111
5.6	Efficiency and Purity of $K$ as a function of $p$ and $\eta$ . Together with the probability cut of 0.6, $2D n\sigma$ cut, $a = b = 3$ , was applied.	112
5.7	Efficiency and Purity of $\pi$ as a function of $p$ and $\eta$ . Together with the probability cut of 0.6, $2D n\sigma$ cut, $a = b = 3$ , was applied.	113
6.1	Like-Sign correlations, $\frac{\Delta\rho}{\rho_{ref}}$ , of all particles for 200 GeV $p_T$ -integrated data from Run 2010. Correlations are in approximately 10% fractional centrality from centrality IDs 0 through 8 and in 5% fractional centrality in centrality IDs 9 and 10. No pre-factor has been applied. . . . .	120

6.2	Unlike-Sign correlations, $\frac{\Delta\rho}{\rho_{ref}}$ , of all particles for 200 GeV $p_T$ -integrated data from Run 2010. Correlations are in approximately 10% fractional centrality from centrality IDs 0 through 8 and in 5% fractional centrality in centrality IDs 9 and 10. No pre-factor has been applied. . . . .	121
6.3	Like-Sign correlations, $\frac{\Delta\rho}{\rho_{ref}}$ , of all particles for 200 GeV $p_T$ -integrated data from Run 2011. Correlations are in approximately 10% fractional centrality from centrality IDs 0 through 8 and in 5% fractional centrality in centrality IDs 9 and 10. No pre-factor has been applied. . . . .	123
6.4	Unlike-Sign correlations, $\frac{\Delta\rho}{\rho_{ref}}$ , of all particles for 200 GeV $p_T$ -integrated data from Run 2011. Correlations are in approximately 10% fractional centrality from centrality IDs 0 through 8 and in 5% fractional centrality in centrality IDs 9 and 10. No pre-factor has been applied. . . . .	124
6.5	Fit decomposition of the 55-64% centrality Unlike-Sign correlations, $\frac{\Delta\rho}{\rho_{ref}}$ , of all particles for 200 GeV $p_T$ -integrated data from Run 2011. The top panels show from left to right the correlations from data, model fit and residuals. The middle panels show the dipole, quadrupole and same-side 2D Gaussian. The bottom panels similarly show the 1D Gaussian on $\eta_\Delta$ and the 2D exponential. For visual clarity the middle and bottom rows are zoomed in by a factor of 2. . . . .	125
6.6	Fits to Unlike-Sign correlations, $\frac{\Delta\rho}{\rho_{ref}}$ , in Figure 6.4. . . . .	126
6.7	Residuals from fits to Unlike-Sign correlations, $\frac{\Delta\rho}{\rho_{ref}}$ , in Figure 6.4.	127
6.8	Like-Sign correlations, $\frac{\Delta\rho}{\rho_{ref}}$ , of <i>pions</i> for 200 GeV $p_T$ -integrated data from Run 2011. The correlations are in centrality IDs 0, 4 and 8 (i.e., centrality percentages 84 – 93%, 50 – 60% and 10 – 20% respectively). No pre-factor has been applied. . . . .	128
6.9	Unlike-Sign correlations, $\frac{\Delta\rho}{\rho_{ref}}$ , of <i>pions</i> for 200 GeV $p_T$ -integrated data from Run 2011. The correlations are in centrality IDs 0, 4 and 8 (i.e., centrality percentages 84 – 93%, 50 – 60% and 10 – 20% respectively). No pre-factor has been applied. . . . .	129

6.10	Like-Sign correlations, $\frac{\Delta\rho}{\rho_{ref}}$ , of <i>pions</i> for 200 GeV in different $y_T$ sub-bins for a centrality 38 – 46%. The $y_T$ spectrum is subdivided into 5 sub-bins that creates $5 \times 5 = 25$ cut bins for the correlations. The binning scheme is discussed in Chapter 3. Correlations in $(y_{T1}, y_{T2})$ are statistically equal to those in symmetric bin $(y_{T2}, y_{T1})$ . . . . .	132
6.11	Unlike-Sign correlations, $\frac{\Delta\rho}{\rho_{ref}}$ , of <i>pions</i> for 200 GeV in different $y_T$ sub-bins for a centrality 38 – 46%. The $y_T$ spectrum is sub-divided into 5 sub-bins that creates $5 \times 5 = 25$ cut bins for correlations. The binning scheme is discussed in Chapter 3. Correlations in $(y_{T1}, y_{T2})$ are statistically equal to those in symmetric bin $(y_{T2}, y_{T1})$ . . . . .	133
6.12	<i>pion-pion</i> $v_2^2[2D]$ as a function of centrality measure $\nu$ (most peripheral in left to most central in right). LS: bold line with filled circle. US: dotted line with open circle. The 25 cut bins are according to binning scheme for $\pi - \pi$ correlations as discussed in Chapter 3. . . . .	136
6.13	Like-Sign correlations, $\frac{\Delta\rho}{\rho_{ref}}$ , of <i>kaons-kaons</i> for 200 GeV $p_T$ -integrated data from Run 2011. The correlations are in centrality IDs 0, 4 and 8 (i.e., centrality percentages 84–93%, 50–60% and 10 – 20% respectively). No pre-factor has been applied. . . . .	137
6.14	Unlike-Sign correlations, $\frac{\Delta\rho}{\rho_{ref}}$ , of <i>kaons-kaons</i> for 200 GeV $p_T$ -integrated data from Run 2011. The correlations are in centrality IDs 0, 4 and 8 (i.e., centrality percentages 84–93%, 50–60% and 10 – 20% respectively). No pre-factor has been applied. . . . .	138
6.15	Like-Sign correlations, $\frac{\Delta\rho}{\rho_{ref}}$ , of <i>kaons</i> for 200 GeV in different $y_T$ sub-bins for a centrality 38 – 46%. The $y_T$ spectrum is subdivided into 4 sub-bins that creates $4 \times 4 = 16$ cut bins for correlations. The binning scheme is discussed in Chapter 3. . . . .	139
6.16	Unlike-Sign correlations, $\frac{\Delta\rho}{\rho_{ref}}$ , of <i>kaons</i> for 200 GeV in different $y_T$ sub-bins for a centrality 38 – 46%. The $y_T$ spectrum is subdivided into 4 sub-bins that creates $4 \times 4 = 16$ cut bins for correlations. The binning scheme is discussed in Chapter 3. . . . .	140
6.17	Top row: LS correlations, $\frac{\Delta\rho}{\rho_{ref}}$ , of <i>kaons</i> in cut bin 5 for centralities 38 – 46%, 28 – 38% and 18 – 28%. Middle row: model fit of the correlations on the top row. Bottom row: residual (data from top row - model fit from middle row) showing that the model describes all the statistically significant structures . . . . .	145

6.18	Top row: US correlations, $\frac{\Delta\rho}{\rho_{ref}}$ , of <i>kaons</i> in cut bin 5 for centralities 38-46%, 28-38% and 18-28%. Middle row: model fit of the correlations. Bottom row: residual (data - model fit). The volcano like region was excluded before fitting the correlations.	146
6.19	<i>kaon-kaon</i> $v_2^2[2D]$ as a function of centrality measure $\nu$ for $(y_T, y_T)$ cut bin 5. The error bars are fitting errors only. Because of low statistics in the most peripheral centrality bin, the correlation was not fitted there. . . . .	147
6.20	<i>kaon-kaon</i> $v_2^2[2D]$ as a function of centrality measure $\nu$ (most peripheral in left to most central in right). LS: bold line with filled circle. US: dotted line with open circle. The 16 cut bins are according to binning scheme for $K - K$ correlations as discussed in Chapter 3. Due to low statistics the fitting parameters for the most peripheral centrality bin were not obtained and were set to 0. . . . .	148
6.21	Like-Sign correlations, $\frac{\Delta\rho}{\rho_{ref}}$ , of <i>protons</i> for 200 GeV $p_T$ -integrated data from Run 2011. The correlations are in centrality IDs 0, 4 and 8 (i.e., centrality percentages 84 - 93%, 50 - 60% and 10 - 20% respectively). No pre-factor has been applied. . . . .	150
6.22	Unlike-Sign correlations, $\frac{\Delta\rho}{\rho_{ref}}$ , of <i>protons</i> for 200 GeV $p_T$ -integrated data from Run 2011. The correlations are in centrality IDs 0, 4 and 8 (i.e., centrality percentages 84 - 93%, 50 - 60% and 10 - 20% respectively). No pre-factor has been applied. . . . .	150
6.23	Like-Sign correlations, $\frac{\Delta\rho}{\rho_{ref}}$ , of <i>protons</i> for 200 GeV in different $y_T$ sub-bins for a centrality 38-46%. The $y_T$ spectrum is subdivided into 3 sub-bins that creates $3 \times 3 = 9$ cut bins for correlations. The binning scheme is discussed in Chapter 3. . . . .	151
6.24	Unlike-Sign correlations, $\frac{\Delta\rho}{\rho_{ref}}$ , of <i>protons</i> for 200 GeV in different $y_T$ sub-bins for a centrality 38-46%. The $y_T$ spectrum is subdivided into 3 sub-bins that creates $3 \times 3 = 9$ cut bins for correlations. The binning scheme is discussed in Chapter 3. . . . .	152
6.25	Top row: LS correlations, $\frac{\Delta\rho}{\rho_{ref}}$ , of <i>protons</i> in cut bin 5 for centralities 38 - 46%, 28 - 38% and 18 - 28%. Middle row: model fit of the correlations on top row. Bottom row: residual (data from top row - model fit from middle row). . . . .	154
6.26	Top row: US correlations, $\frac{\Delta\rho}{\rho_{ref}}$ , of <i>protons</i> in cut bin 4 for centralities 38-46%, 28-38% and 18-28%. Middle row: model fit of the correlations. Bottom row: residual (data - model fit). . . . .	155

6.27	<i>proton-proton</i> $v_2^2[2D]$ as a function of centrality measure $\nu$ for $(y_T, y_T)$ cut bin 4. The error bars are fitting errors only. Because of low statistics in the most peripheral centrality bin, the correlation was not fitted there. . . . .	156
6.28	<i>proton-proton</i> $v_2^2[2D]$ as a function of centrality measure $\nu$ (most peripheral in left to most central in right). LS: bold line with filled circle. US: dotted line with open circle. The 9 cut bins are according to binning scheme for $p - p$ correlations as discussed in Chapter 3. Due to low statistics the fitting parameter for the most peripheral centrality bin, the correlations were not fitted. The results for this bin are plotted at 0. . . . .	157
6.29	Like-Sign correlations, $\frac{\Delta\rho}{\rho_{ref}}$ , of <i>pion-kaon</i> for 200 GeV $p_T$ -integrated data from Run 2011. The correlations are in centrality IDs 0, 4 and 8 (i.e., centrality percentages 84 – 93%, 50 – 60% and 10 – 20% respectively). No pre-factor has been applied. . . . .	158
6.30	Unlike-Sign correlations, $\frac{\Delta\rho}{\rho_{ref}}$ , of <i>pion-kaon</i> for 200 GeV $p_T$ -integrated data from Run 2011. The correlations are in centrality IDs 0, 4 and 8 (i.e., centrality percentages 84–93%, 50–60% and 10 – 20% respectively). No pre-factor has been applied. . . . .	159
6.31	Like-Sign correlations, $\frac{\Delta\rho}{\rho_{ref}}$ , of <i>pion-kaon</i> for 200 GeV in different $y_T$ sub-bins for a centrality 38-46%. The $y_T$ spectrum for <i>pion</i> is sub-divided into 5 sub-bins and <i>kaon</i> is sub-divided into 4 sub-bins that creates $5 \times 4 = 20$ cut bins for correlations. The binning scheme is discussed in Chapter 3. . . . .	160
6.32	Unlike-Sign correlations, $\frac{\Delta\rho}{\rho_{ref}}$ , of <i>pion-kaon</i> for 200 GeV in different $y_T$ sub-bins for a centrality 38-46%. The $y_T$ spectrum for <i>pion</i> is sub-divided into 5 sub-bins and <i>kaon</i> is sub-divided into 4 sub-bins that creates $5 \times 4 = 20$ cut bins for correlations. The binning scheme is discussed in Chapter 3. . . . .	161
6.33	Top row: LS correlations, $\frac{\Delta\rho}{\rho_{ref}}$ , of <i>pion-kaon</i> in cut bin 7 for centralities 38 – 46%, 28 – 38% and 18 – 28%. Middle row: model fit of the correlations on top row. Bottom row: residual (data from top row - model fit from middle row). . . . .	162
6.34	Top row: US correlations, $\frac{\Delta\rho}{\rho_{ref}}$ , of <i>pion-kaon</i> in cut bin 7 for centralities 38 – 46%, 28 – 38% and 18 – 28%. Middle row: model fit of the correlations on top row. Bottom row: residual (data from top row - model fit from middle row). . . . .	163

6.35	<i>pion-kaon</i> $v_2^2[2D]$ as a function of centrality measure $\nu$ for $(y_T, y_T)$ cut bin 7. The error bars are fitting errors only. Because of low statistics in the most peripheral centrality bin, the correlation was not fitted there. . . . .	164
6.36	Like-Sign correlations, $\frac{\Delta\rho}{\rho_{ref}}$ , of <i>pion-proton</i> for 200 GeV $p_T$ -integrated data from Run 2011. The correlations are in centrality IDs 0, 4 and 8 (i.e., centrality percentages 84–93%, 50–60% and 10 – 20% respectively). No pre-factor has been applied. .	165
6.37	Unlike-Sign correlations, $\frac{\Delta\rho}{\rho_{ref}}$ , of <i>pion-proton</i> for 200 GeV $p_T$ -integrated data from Run 2011. The correlations are in centrality IDs 0, 4 and 8 (i.e., centrality percentages 84–93%, 50–60% and 10 – 20% respectively). No pre-factor has been applied. .	166
6.38	Like-Sign correlations, $\frac{\Delta\rho}{\rho_{ref}}$ , of <i>pion-proton</i> for 200 GeV in different $y_T$ sub-bins for a centrality 38-46%. The $y_T$ spectrum for <i>pion</i> is sub-divided into 5 sub-bins and <i>proton</i> is sub-divided into 3 sub-bins that creates $5 \times 3 = 15$ cut bins for correlations. The binning scheme is discussed in Chapter 3. . . . .	168
6.39	Unlike-Sign correlations, $\frac{\Delta\rho}{\rho_{ref}}$ , of <i>pion-proton</i> for 200 GeV in different $y_T$ sub-bins for a centrality 38-46%. The $y_T$ spectrum for <i>pion</i> is sub-divided into 5 sub-bins and <i>proton</i> is sub-divided into 3 sub-bins that creates $5 \times 3 = 15$ cut bins for correlations. The binning scheme is discussed in Chapter 3. . . . .	169
6.40	Top row: LS correlations, $\frac{\Delta\rho}{\rho_{ref}}$ , of <i>pion-proton</i> in cut bin 7 for centralities 38-46%, 28-38% and 18-28%. Middle row: model fit of the correlations. Bottom row: residual (data - model fit). .	170
6.41	Top row: US correlations, $\frac{\Delta\rho}{\rho_{ref}}$ , of <i>pion-proton</i> in cut bin 7 for centralities 38-46%, 28-38% and 18-28%. Middle row: model fit of the correlations. Bottom row: residual (data - model fit). .	171
6.42	<i>pion-proton</i> $v_2^2[2D]$ as a function of centrality measure $\nu$ for $(y_T, y_T)$ cut bin 7. The error bars are fitting errors only. Because of low statistics in the most peripheral centrality bin, the correlation was not fitted there. . . . .	172
6.43	Like-Sign correlations, $\frac{\Delta\rho}{\rho_{ref}}$ , of <i>kaon-proton</i> for 200 GeV $p_T$ -integrated data from Run 2011. The correlations are in centrality IDs 0, 4 and 8 (i.e., centrality percentages 84–93%, 50–60% and 10 – 20% respectively). No pre-factor has been applied. .	173

6.44	Unlike-Sign correlations, $\frac{\Delta\rho}{\rho_{ref}}$ , of <i>kaon-proton</i> for 200 GeV $p_T$ -integrated data from Run 2011. The correlations are in centrality IDs 0, 4 and 8 (i.e., centrality percentages 84–93%, 50–60% and 10–20% respectively). No pre-factor has been applied. . . . .	174
6.45	Like-Sign correlations, $\frac{\Delta\rho}{\rho_{ref}}$ , of <i>kaon-proton</i> for 200 GeV in different $y_T$ sub-bins for a centrality 38-46%. The $y_T$ spectrum for <i>kaon</i> is sub-divided into 4 sub-bins and <i>proton</i> is sub-divided into 3 sub-bins that creates $4 \times 3 = 12$ cut bins for correlations. The binning scheme is discussed in Chapter 3. . . . .	175
6.46	Unlike-Sign correlations, $\frac{\Delta\rho}{\rho_{ref}}$ , of <i>kaon-proton</i> for 200 GeV in different $y_T$ sub-bins for a centrality 38-46%. The $y_T$ spectrum for <i>kaon</i> is sub-divided into 4 sub-bins and <i>proton</i> is sub-divided into 3 sub-bins that creates $4 \times 3 = 12$ cut bins for correlations. The binning scheme is discussed in Chapter 3. . . . .	176
6.47	Top row: LS correlations, $\frac{\Delta\rho}{\rho_{ref}}$ , of <i>kaon-proton</i> in cut bin 5 for centralities 38-46%, 28-38% and 18-28%. Middle row: model fit of the correlations. Bottom row: residual (data - model fit). . . . .	177
6.48	Top row: US correlations, $\frac{\Delta\rho}{\rho_{ref}}$ , of <i>kaon-proton</i> in cut bin 5 for centralities 38-46%, 28-38% and 18-28%. Middle row: model fit of the correlations. Bottom row: residual (data - model fit). . . . .	178
6.49	<i>kaon-proton</i> $v_2^2[2D]$ as a function of centrality measure $\nu$ for $(y_T, y_T)$ cut bin 5. The error bars are fitting errors only. Because of low statistics in the most peripheral centrality bin, the correlation was not fitted there. . . . .	179
6.50	Measurement of azimuthal anisotropy $v_2[2D]$ of $\pi$ , $K$ and $p$ as a function of $p_T$ in Au+Au at 200 GeV. PHENIX results for centrality 40-60% (filled points) have been taken from Reference [13]. Open points are results from current thesis for centrality 46-55%. Error bars in STAR data are systematic errors. . . . .	182
6.51	Peak values of $v_2[2D]$ near mid-central for identified particles as a function $p_T$ for centrality 46-55%. . . . .	183
6.52	Factorization test. $x$ -axis in each plot is the centrality measure in previous figures, e.g., Figure 6.49. LS $v_2^2$ for $\pi$ - $\pi$ is shown with filled red circle connected by solid red lines and results from factorization for each centrality are shown in green triangles connected with dashed green lines. Results for the lowest $y_T$ cut bins are excluded due to possible fitting instabilities in cut bin 0. The match between filled lines and dashed line in diagonal bins is by construction. . . . .	190

6.53	Factorization test. $x$ -axis in each plot is the centrality measure in previous figures, e.g., Figure 6.49. LS $v_2^2$ for $K\text{-}K$ is shown with filled red circle connected by solid red lines and results from factorization for each centrality are shown in green triangles connected with dashed green lines. Results for the lowest $y_T$ cut bins are excluded due to possible fitting instabilities in cut bin 0. The match between filled lines and dashed line in diagonal bins is by construction. . . . .	191
6.54	Factorization test. $x$ -axis in each plot is the centrality measure in previous figures, e.g., Figure 6.49. LS $v_2^2$ for $p\text{-}p$ is shown with filled red circle connected by solid red lines and results from factorization for each centrality are shown in green triangles connected with dashed green lines. The match between filled lines and dashed line in diagonal bins is by construction. . . . .	192
6.55	Factorization test. $x$ -axis in the figure is the centrality measure. LS $v_2^2$ for $\pi\text{-}K$ for cut bin 7 is shown with filled red circles connected by solid red lines and result from factorization for each centrality are shown in green triangles connected with a dashed green line. . . . .	193
6.56	Factorization test. $x$ -axis in the figure is the centrality measure. LS $v_2^2$ for $\pi\text{-}p$ for cut bin 7 is shown with filled red circle connected by solid red lines and result from factorization for each centrality are shown in green triangles connected with a dashed green line. . . . .	194
6.57	Factorization test. $x$ -axis in the figure is the centrality measure. LS $v_2^2$ for $K\text{-}p$ for cut bin 5 is shown with filled red circle connected by solid red line and result from factorization for each centrality are shown in green triangles connected with a dashed green line. . . . .	195

# Chapter 1

## Introduction

### 1.1 QCD

The quest for understanding the nature of the nuclear force has been one of the central problems in physics. The strong force is one of the four fundamental forces in nature and it is responsible for binding quarks and gluons together to form particles like neutrons and protons, which form the matter around us. Quantum chromodynamics (QCD) is the modern theory of the strong interaction. In the strong interaction, *gluons* are the force carriers that mediate the interaction between quarks. QCD can be taken as an extension of quantum electrodynamics (QED) theory, which explains how the force between electric charges is mediated by *photons*. However, QCD becomes complicated because of the larger number of degrees of freedom involved in it. In QED, there is only one kind of charge (called *electric charge*), whereas QCD has three charges (called *color-charges*), commonly labelled as *red*, *blue* and *green*, and their corresponding *anti-colors*. Also, unlike the QED mediator photon, which is electrically neutral, the gluons can also carry the color charges and therefore couple to each other producing non-linearities in the theory.

In QCD, there are 6 flavors of quarks called up( $u$ ), down( $d$ ), strange( $s$ ), charm( $c$ ), bottom( $b$ ) and top( $t$ ), with  $u$  being the lightest and  $t$  being the heaviest. The two light quarks,  $u$  and  $d$ , play an important role in the formation of matter because the other heavier quarks are unstable and quickly decay into lighter quarks. In addition to electric charge, a quark of any of the six types can carry any of the three colors. The quarks are allowed to have fractional electric-charges ( $u, c$  and  $t$  carry  $+\frac{2}{3}e$ , and  $d, s$  and  $b$  carry  $-\frac{1}{3}e$ ). The combination of two or more quarks forms a *hadron*. The stability of a particle, however, depends on if the particle thus formed is color neutral and in a color singlet state. The particle made of two quarks is color neutral if the color of one quark is the anti-color of another. In the case of a particle with three quarks, each of the quarks should contain each of the three colors making the particle colorless overall. The particles with 2 and 3 quarks are called *mesons* and *baryons* respectively.

QCD is a conceptually simple theory but it is typically very complicated to solve [14]. There are different approaches to solve it. Lattice QCD is a computational approach to solving QCD. Improved computing facilities have made it possible to get some key predictions of QCD. However, solving the QCD Lagrangian is not easy. The second approach to solve the QCD Lagrangian is to attempt to make simpler physical models which are easier to solve and that approximately mimic nature. Such an approach has added to some understanding in QCD. For example, PYTHIA [15] and HIJING [16] models have been successful in jet studies and the associated particle produc-

tion in high energy nuclear collisions. However, the modelistic approaches are successful in describing only certain subsets of data; they fail to represent the whole spectrum of nature. The results from the models have to confront with the physical reality. The third approach is to conduct physical experiments and measure important parameters. Experimental facilities such as STAR at BNL are devoted to such experiments by colliding ions at relativistic speeds.

## 1.2 QGP

The behavior of QCD at high temperature is interesting because asymptotic freedom plays an important role in making the interaction coupling weaker and making quarks and gluons approximately free [17]. Such a state of matter in which quark and gluon degrees of freedom are mostly liberated is called the Quark Gluon Plasma (QGP) [4]. The QGP can be well-described using statistical mechanics as a free relativistic parton gas and the QCD Lagrangian of such a system can be solved using a perturbative approach called perturbative QCD (pQCD). Present theoretical ideas provide a picture of the QGP in which quarks and gluons are no longer confined within the dimensions of the nucleon, but free to move around over a volume in which a high enough energy density exists. It was hoped that such high energy density could be achieved in nuclear collisions at relativistic energies. RHIC allows us to collide ion beams at relativistic speeds in search for such a deconfined state of quarks and gluons.

In heavy-ion collisions, if the energy is high, there will be an inelastic

interaction between the participating nuclei. At these energies, it is hypothesized that the quarks and gluons are dissociated and a thermalized dense medium (QGP) is formed. This medium will quickly expand and cool due to a high pressure gradient between the medium and the external vacuum. As the system cools down, the quarks and gluons recombine to form color-neutral hadrons. This process is called *hadronization*. Therefore, if the QGP is created, its state would have only a very transient existence [18]. Whether or not the QGP is formed in the early stage of a collision, the collision system eventually turns into hadrons that we observe in the detectors. Because of a very short life time ( $\sim 10 \text{ fm}/c$ ), it is not possible to directly observe such a short-lived phase; at best only indirect evidence can be obtained. Many advanced analysis techniques are needed to study the interactions and the medium in this early stage via the final state particles.

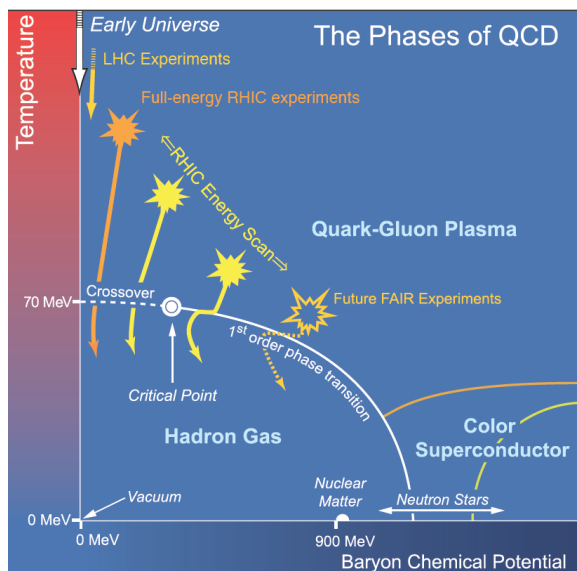


**Figure 1.1** A hypothesized illustration of the phase diagram of QCD matter [2]. The white line shows the phase boundary. Orange star on top left indicates Au+Au collisions at 200 GeV. The relativistic heavy-ion collisions provide a unique environment to explore the phases of QCD matter at high temperature and low baryon chemical potential.

The mission of the relativistic heavy-ion program is centered on searching for the QGP, studying matter at extreme temperature and pressure, studying QCD in these conditions, and perhaps getting some insight into the QCD phase diagram (see Figure 1.1.) [19][20]. To achieve these goals, we study the nuclear initial-state in previously unexplored regions of momentum transfer ( $Q^2$ ) and momentum fraction of parton ( $x$ ) where gluon densities are large and effects of gluon saturation are possible, and we study the final state where many body partonic interactions and collective modes are possible.

### 1.3 Heavy-Ion Collisions

High energy heavy-ion collision have been studied since 1954 when the BEVALAC experiment utilized the 6 GeV Bevatron accelerator at the Lawrence Berkeley National Laboratory and the SuperHILAC linear accelerator facilities to collide various ions in fixed-target mode. Although the energy of the projectile ions in the BEVALAC were not large enough to study the QGP, observations from the BEVALAC were consistent with hydrodynamic models of nucleon collective motion[21]. The Alternating Gradient Synchrotron (AGS) was the next major experimental facility for studying heavy-ion collisions [22]. It was built at the Brookhaven National Laboratory in 1960 and started operating at an energy of 28 GeV. The AGS has been continuously operating since then. Before the RHIC program the highest-energy heavy-ion fixed-target was the Super Proton Synchrotron (SPS) at CERN [23]. SPS started operating in 1976 and continues operating today as the booster for the Large Hadron Collider. The BEVALAC, AGS and SPS accelerators all drove fixed-target high energy collision experiments but collision energy was not sufficient to study the behavior of nuclear matter at very high energy.

The Relativistic Heavy Ion Collider (RHIC) has been operating since the summer of 2000 with the primary objective being to recreate and study the ultra-hot and dense matter similar to that which may have existed right after the Big Bang [24]. The RHIC has provided an opportunity to address a wide range of questions related to the formation and evolution of this ultra-hot matter. By studying of collision data at different energies, the Solenoidal Tracker

at RHIC (STAR) experiment has observed many of the proposed signatures of formation of the QGP in heavy-ion collisions, but unambiguous interpretation of the data is lacking. Nevertheless, data from the STAR experiment provides valuable information for extending our understanding of QCD in hot dense nuclear matter. RHIC has provided data from Au+Au collisions at center of mass energies ranging from 7.7 to 200 GeV per nucleon-nucleon collision pair. Other ion species including protons, He, Cu, U have also been collided.

### 1.3.1 Hydrodynamics

Conventionally, the QGP is described in terms of hydrodynamics but has also been described as a stochastic many-body transport system [25][26]. In a hydrodynamic description of heavy-ion collisions, a large pressure is assumed to arise early in the initial state of QGP and drives collective expansion (flow). The system expands based on the pressure gradient; the pressure gradient of the expanding system is based on the geometry of the system. The collective motion of the particles in the system is determined by the geometry of the collision. An illustration of formation of spatially-asymmetric interaction volume after mid-central collision of two nuclei is shown in Figure 1.2. If the overlap of the nuclei during the collision is asymmetric (in a non-central collision the initial-state overlap is anisotropic), so will be the pressure gradient resulting in the asymmetric final-state particle momentum distribution. The anisotropy in the azimuthal distribution of the particles is described as *azimuthal anisotropy* or *elliptic flow*. Because the initial-state anisotropy

quickly decreases, the anisotropic flow is expected to probe the very early state of the medium [27][3]. So the anisotropic flow is taken as an attractive experimental observable throughout the heavy-ion community.

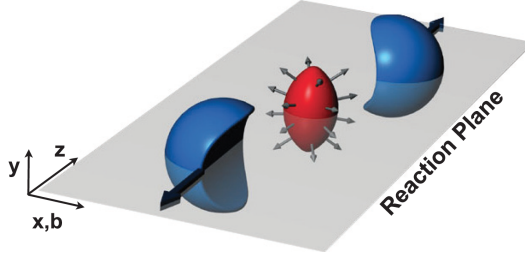


**Figure 1.2** An illustration of formation of almond-shaped interaction volume after mid-central collision of two nuclei. Spatial anisotropy in the interaction volume with respect to reaction-plane ( $x$ - $z$  plane) causes anisotropy in momentum of produced particles [3].

To characterize the various patterns of anisotropic flow, a Fourier expansion of the invariant triple differential distribution is used.

$$E \frac{d^3 N}{d^3 \vec{p}} = \frac{1}{2\pi} \frac{d^2 N}{p_T dp_T dy} \left[ 1 + 2 \sum_{n=1}^{\infty} v_n \cos[n(\phi - \Psi)] \right], \quad (1.1)$$

where  $E$  is the energy of the particle,  $p$  is the momentum,  $p_T$  is the transverse momentum,  $\phi$  is the azimuthal angle,  $y$  is the rapidity,  $\Psi$  is the reaction plane angle [3] and  $v_n$  are Fourier coefficients. The reaction plane angle ( $\Psi$ ) is the azimuthal angle of the impact parameter vector. In the context of azimuthal correlations, which we will measure in this thesis, Equation 1.1 can be written in terms of a pair density [28][29][30][31].

$$\frac{dN_{pair}}{d\phi_{\Delta}} \propto \left[ 1 + 2 \sum_{n=1}^{\infty} v_n^2(p_{Ti}, p_{Tj}) \cos[n(\phi_{\Delta})] \right], \quad (1.2)$$

where  $N_{pair}$  is the number of particle-pairs and,  $(p_{Ti}, p_{Tj})$  are momenta and  $\phi_{\Delta} = \phi_i - \phi_j$  is relative azimuthal angle between arbitrary pairs of particles  $i$  and  $j$  where  $i \neq j$  in general. Such pair construction will be discussed in Chapter 3.

The Fourier components, which are functions of  $p_T$  and  $y$  are given as follows.

$$v_n^2(p_{Ti}, p_{Tj}) = \langle \cos [n(\phi_{\Delta})] \rangle, \quad (1.3)$$

where the angular brackets denote an average over the particles, summed over all events, within the range of  $p_T$  and  $y$ . For diagonal momentum bins (i.e., when  $p_{Ti} = p_{Tj}$ ), the  $v_n$  can be obtained for a given  $p_T$  by [30]

$$v_n(p_T) = \sqrt{v_n^2(p_T, p_T)}, \quad (1.4)$$

where  $n = 1, 2, 3, \dots$  is index for different Fourier components.

In the heavy-ion community, the first three Fourier components,  $v_1$ ,  $v_2$  and  $v_3$  are frequently discussed;  $v_2$  and  $v_3$  are conventionally referred as *elliptic flow* and *triangular flow*, respectively.

Alternatively, the azimuthal anisotropy can be described as a manifestation of gluonic multipole radiation [32]. The QCD based approach has successfully described  $v_2^2$  results for p+p and p+Pb collisions but has not successfully accounted for  $v_2^2$  results in A+A collisions. Although, the physical

interpretation of the azimuthal anisotropy varies among scholars, the Fourier coefficients have been measured with good precision [32][27]. Among the coefficients, the second coefficient of the Fourier expansion,  $v_2$ , has the largest measured magnitude and is a subject of interest in this thesis.

Figure 1.3 shows the measured  $v_2$  of identified particles from STAR and PHENIX experiments [4]. In this thesis, we will measure  $v_2^2$  for different combinations of identified particles in different ranges of momenta using a 2-dimensional fitting model of the 2D angular correlations. Therefore, we will symbolize it as  $v_2^2[2D]$  using the notation of Reference [5].

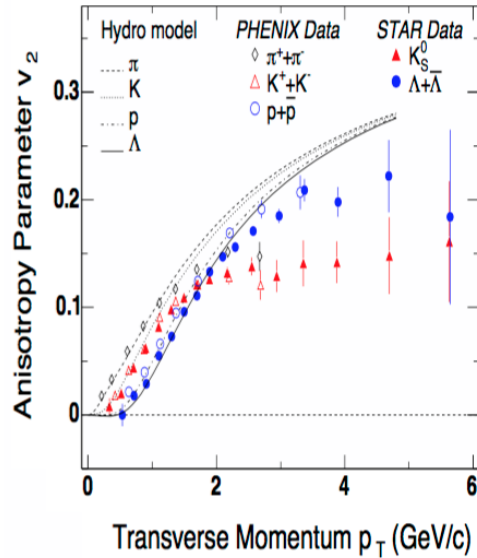


**Figure 1.3** Measured  $v_2$  of identified particles for Au+Au at 200 GeV. The results are compared with a hydrodynamic model [4].

### 1.3.2 Angular Correlations

From the analysis of a wide range of data in different ranges of momenta, it has been claimed that the QGP has been found [4]. Some of the main evidences for the discovery of the QGP are the observation of jet suppression, a very large amount of azimuthal anisotropy, and the very high temperature inferred for the medium produced by the collisions. Comparison of anisotropy data and hydrodynamic models have lead many in the high energy community to claim that the new state of matter acts as a perfect fluid. However, some dispute these claims [5] in favor of a more conventional QCD understanding based on fragmentation, gluon radiation and interference. One of the most common ways to study the initial-state of the medium is to use correlations of final-state particles. Correlation measurements in angular and momentum space are common.

Ideally, it would be useful to measure the many-body final-state density. However, it is challenging to analyze data to obtain accurate results for more than two-particle correlations. Although the single particle distribution provides essential information, it gives limited information about the initial and final states. Correlations, for example, provide valuable information about how conservation of momentum, flavor and baryon number affects the final state. Similarly, correlation structure can differentiate between a thermal distribution and fragmenting final state distributions. For example, correlation structure due to thermal distribution produces *quadrupole* structure on relative azimuth but final state distribution due to fragmenting soft gluons pro-

duces *Gaussian* structure in relative pseudorapidity. Different components of correlation structures are discussed in Chapter 6. The evolution of correlations from the most-peripheral to the most-central collisions provides an essential tool for understanding the dense gluonic initial state and the partonic medium formed in heavy ion collisions.

Correlations are used to measure azimuthal anisotropy. The azimuthal anisotropy seen in heavy-ion collisions is proposed as a signature of collective process such as pressure driven hydrodynamic flow of the hot and dense nuclear medium. However, similar correlations have been predicted in multi-gluon interference models [33][34][35]. Further study is needed to differentiate these contradictory interpretations of the correlations. The systematic measurements of flavor dependent di-hadron correlations as a function of the collision energy, collision centrality, colliding species (p+p, p+A, A+A) in the ranges of momentum of final state particles provide essential information to enhance understanding of the nuclear medium.

The UT Austin heavy-ion group in collaboration with other members of STAR has been involved in correlation analysis since the first RHIC data in 2000. 2D angular correlations in relative azimuth and relative pseudorapidity, developed and implemented by the UT group, has been instrumental in the study of heavy-ion collision physics. In 2004, Aya Ishihara observed strong medium modification of jet fragmentation (mini-jets) in central heavy-ion collisions [36]. Michael Daugherty used charge independent correlations to study the evolution of correlation structures with collision centrality in  $p_T$ -integral

data [1]. Many important discoveries such as the sudden increase in amplitude and  $\eta$ -width correlation mini-jets were made. In 2013, Elizabeth Oldag studied non-identified particle correlations in various ranges of momentum [37]. It was observed that back-to-back dijets fragment in the  $p_T$  range 0.5-4.0 GeV/c with no suppression. David Kettler [38] from the University of Washington applied similar techniques of angular correlations to study quadrupole and jet-like structures [38]. The results from the analysis have constrained theoretical models based on hydrodynamics, pQCD jets and multi-gluon interference processes.

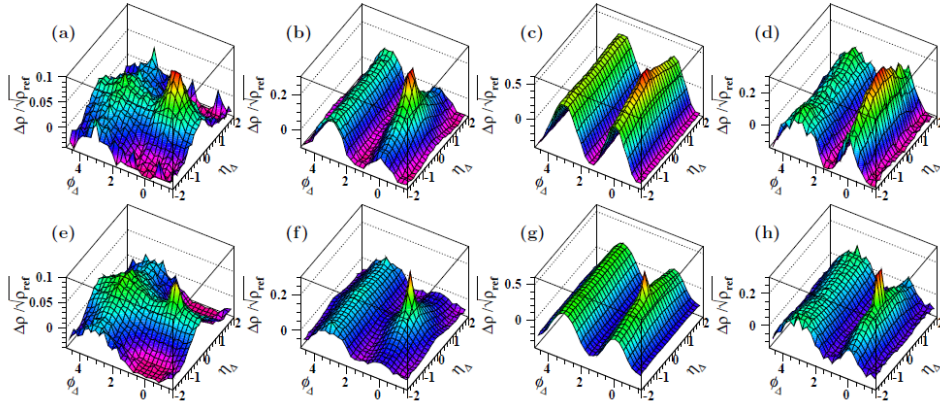


**Figure 1.4** Centrality evolution of angular correlations,  $\frac{\Delta\rho}{\sqrt{\rho_{ref}}}$ , in  $(\eta_\Delta, \phi_\Delta)$  for Au+Au collisions at  $\sqrt{s_{NN}} = 200$  GeV (top row) and  $\sqrt{s_{NN}} = 62$  GeV (bottom row). The collision centrality increases left to right from the most peripheral to the most central [5].

Figure 1.4 shows that there is a strong evolution of the correlation structure as the centrality changes. The correlations were fitted with a 2-dimensional 6-component (11-parameter) model. The details of the fitting

parameters are also discussed in Chapter 3. In Figure 1.5, the evolution of different fit parameters with centrality is given.

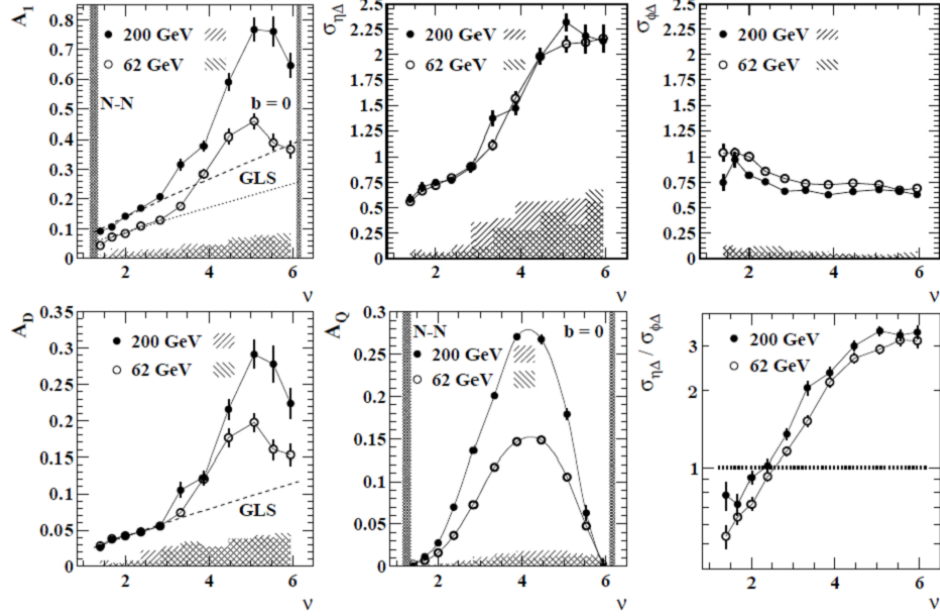


**Figure 1.5** Centrality evolution of fit parameters for  $(\eta_\Delta, \phi_\Delta)$  correlations data from Au+Au collisions at  $\sqrt{s_{NN}} = 200$  GeV (solid symbol) and  $\sqrt{s_{NN}} = 62$  GeV (open symbol). The centrality measure,  $\nu$ , was computed at fixed energy of 200 GeV. The same-side 2D Gaussian amplitudes are shown on the top row. The amplitude of the dipole and quadrupole are shown in the bottom left and middle panel respectively. In the bottom right panel, the ratio of widths of the same-side 2D Gaussian are shown. The dashed line indicates the estimation from Glauber linear superposition. The systematic uncertainties are shown in the hatched region. Four of 11 centralities of this evolution are shown in Figure 1.4. This figure was taken from Reference [5].

The detailed interpretation of the features in correlations are discussed in References [1] and [37]. The structures in correlations were studied for unidentified particles. The sharp transitions in the trends of parameter  $A_1, \sigma_{\eta\Delta}$

and  $A_D$  are especially noteworthy, where these parameters characterize the amplitude and  $\eta$ -width of jet and di-jet related structures.

Many observed features in the correlation structures of non-identified particles are dominated by the features of the most abundant particles: *pions*. Measurement of the 2D angular correlations as a function of momentum with identified particles, (*pion*, *kaon* and *proton*) allow access to possible medium effects on correlations induced by flavor and baryon number conservation. Improved particle identification methods using both TPC and TOF information allows correlation measurements for like-sign and unlike-sign combinations of  $(\pi, \pi)$ ,  $(K, K)$ ,  $(p, p)$ ,  $(\pi, K)$ ,  $(\pi, p)$  and  $(K, p)$  in various ranges of momentum.

In this thesis, I will investigate the features of correlations of identified particles in different ranges of momenta. I will investigate both the evolution of correlations with centrality and with momentum. Such analysis gives us an opportunity to study the soft and semi-hard physics contributed by each identified particle, the flavor dependence, and meson-vs-baryon dependence of the correlation structures. I will focus on investigating the evolution of one of the components of correlations called the *quadrupole* ( $\cos(2\phi_\Delta)$ ) which is proportional to  $v_2^2$  in the measurement of anisotropic “flow” (discussed in the previous section). In Figure 1.5, the collision centrality evolution of the quadrupole amplitude,  $A_Q$  for unidentified particles is shown. The study of the quadrupole is important because it has been predicted to be either a manifestation of gluonic multipole radiation [32][5][39] or a manifestation of hydrodynamic flow of the medium [27][4].

The  $v_2$  scaling with the number of constituent quarks ( $n_q$ ) is one of the often cited signals for the strongly interacting QGP and collective flow in heavy-ion collisions. Those results are based on two-particle distributions of  $(\pi, K, p)$  on azimuth where non-identified particles are used for event-plane determination. The two particle correlation of identified particles enables measurement of  $v_2$  and possible  $n_q$  scaling without using an event-plane. These new correlation data therefore enable independent tests of hydrodynamic model predictions of azimuthal harmonics. Obtaining such information is one of the primary goals of this thesis.

## 1.4 Outline

I will divide this thesis into seven chapters. In Chapter 2, the experimental setup is discussed. Then I will describe the correlation formalism in Chapter 3. In two short Chapters 4 and 5, pileup and particle identification are discussed. Finally, two-particle correlations of identified particles in different momentum ranges are presented in Chapter 6. Also, in this chapter I discuss important features in correlations including the evolution of quadrupole amplitude with centrality in different ranges of momentum and provide tests of the factorization assumption in analysis of  $v_2$ . Finally, conclusions and interpretations of some of the measurements are given in Chapter 7.

# Chapter 2

## Experimental Facility

### 2.1 Introduction

The pioneering research in nuclear physics laboratories has been possible by the combined support of the government funding agencies of the United States and the international scientific community. Brookhaven National Laboratory is one of 17 national laboratories dedicated to facilitating research in science and technology. In this chapter we present information on the basics of the facility and the detectors that are needed to collect heavy-ion collision data that are used in this analysis.

### 2.2 RHIC

The Relativistic Heavy Ion Collider (RHIC) is a nuclear physics facility situated at Brookhaven National Laboratory in Upton, New York (Long Island). RHIC has been successfully operating since 2000. In the last 16 years, different types of collisions such as *proton + proton*, *proton + gold*, *copper + copper*, *gold + gold* etc. have been investigated at various center of mass energy ranging from 9-500 GeV per colliding nucleon pair in search of the quark gluon plasma (QGP) and its characteristics. Utilizing a unique

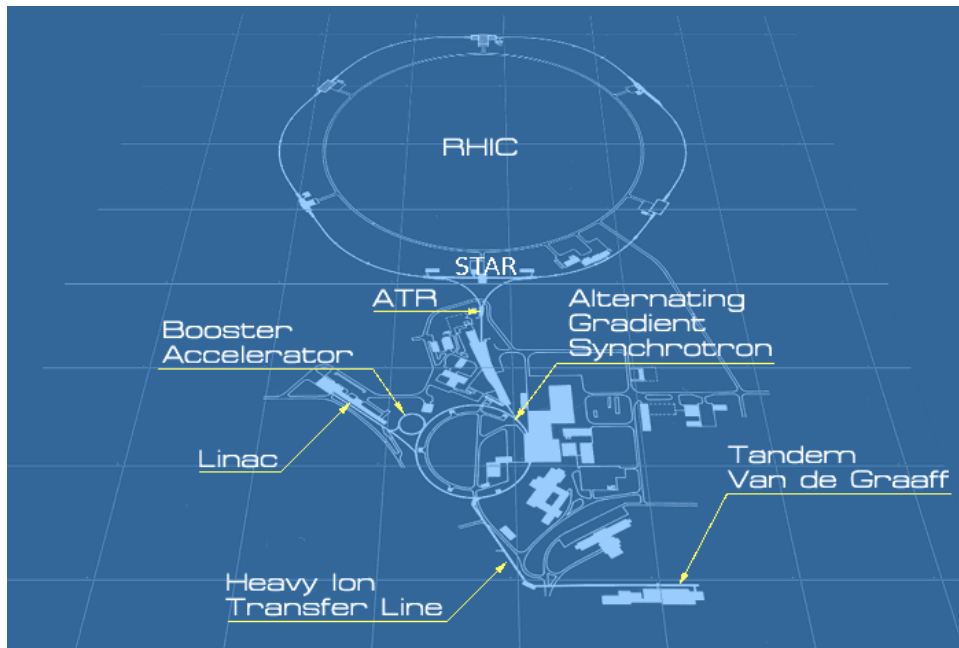
feature of polarized proton beams, RHIC has been successfully able to collide polarized protons in the range of center of mass energy,  $\sqrt{s} = 62.4 - 500 \text{ GeV}$ <sup>1</sup>, to address additional aspects of Quantum Chromodynamics (QCD), such as the gluon contribution to proton spin, as well as providing a crucial baseline for heavy-ion measurements.

Figure 2.1 shows the layout of RHIC. RHIC is capable of storing and accelerating both protons and heavy-ions. A brief description of key steps of the operations for heavy-ion collisions is as follows [40][41][42]. The heavy-ions are stepwise ionized as they are accelerated to RHIC injection energy, at which point they are fully ionized. The Tandem Van de Graaff accelerates negatively charged ions, for example  $Au^{-1}$ , from a sputter source to about 1 MeV/nucleon. About half of the electrons are stripped off of the atom in this step. The beam is then injected into the Booster. Here ions are further stripped of electrons and accelerated further. In the case of gold-ions, the acceleration reaches 100 MeV/nucleon and the beam is ionized to  $Au^{+77}$ . The beam is then transferred to the Alternating Gradient Synchrotron (AGS), where the beam is accelerated to the RHIC injection kinetic energy of 8.6 GeV/nucleon. The final ionization of the ions occurs before the beam reaches RHIC. The beam is then transferred to RHIC via the AGS-to-RHIC Beam Transfer Line (ATR).

---

<sup>1</sup> $s = (p_1 + p_2)^2$ , where  $s$  is called Mandelstam variable and  $p_1$  and  $p_2$  are four momenta of incoming colliding particle pair. In relativistic limit,  $\sqrt{s}$  represents center of mass energy of colliding particle pair.  $\sqrt{s_{NN}}$  represents center of mass energy per nucleon pair ( $N-N$ ).

In RHIC, two counter rotating beams, one (Blue Ring) for clockwise and the other (Yellow Ring) for counter-clockwise, accelerated, steered and focused using RF (Radio Frequency) klystron and super-conducting magnets. The circumference of RHIC is 3.8km. The ion beams are accelerated to 100GeV/nucleon ( $\sqrt{s_{NN}} = 200\text{GeV}$ ). Each beam consists of 60 to 120 bunches. A beam luminosity of  $2 \times 10^{26} \text{cm}^{-2} \text{s}^{-1}$  was achieved in 2000. There are six interaction points, and focusing of the bunches is done via quadrupole electromagnetic fields at these points [40]. Of the six interaction points, two of them house the STAR and PHENIX experiments at the 6:00 and 8:00 o'clock positions of the quasi-circular ring, respectively.



**Figure 2.1** An overview of the RHIC facility. The STAR experiment is at 6 o'clock position of the RHIC ring. Source [6].

## 2.3 Overview of STAR

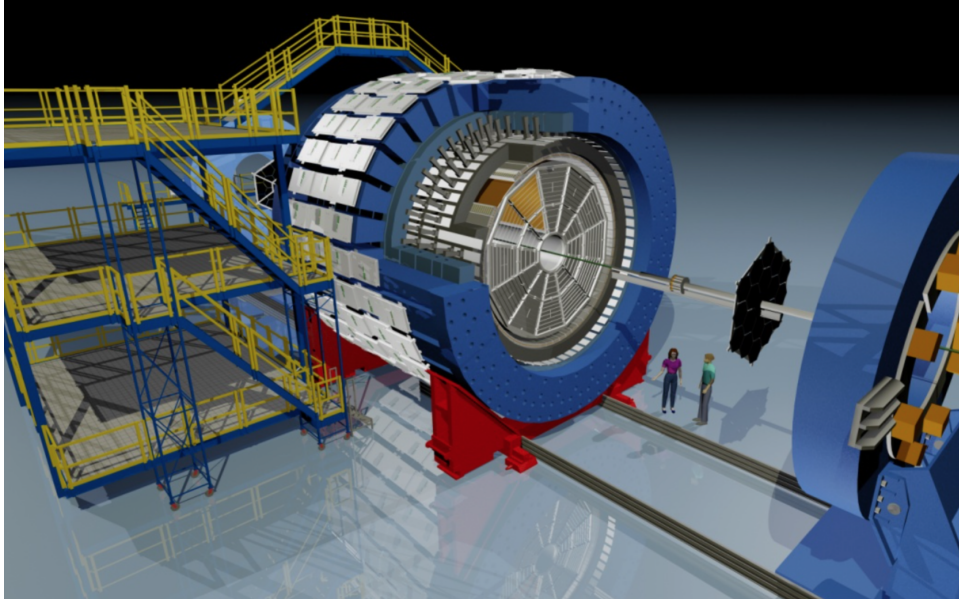


**Figure 2.2** An overview of upgraded STAR detector as of 2016.

Figure 2.2 shows a schematic diagram of STAR (Solenoidal Tracker at RHIC). It is a cylindrical detector system of length and diameter about 8m each. It is placed in such a way that ion-beams pass through its  $z$ -axis and cross at the center of the detector. The vertical axis is  $y$  and the axis perpendicular to  $yz$  plane is  $x$  in the STAR coordinate system. Like many other high energy detectors [43][44], it is a detector system made up of many specialized components shown in Figure 2.2. The main detector sub-systems are the Time Projection Chamber (TPC), Time Of Flight (TOF) and the Electromagnetic Calorimeter (EMC) together with a key part of triggering detectors called Zero Degree Calorimeter (ZDC). The solenoid magnet wraps around the detector

creating a magnetic field along the  $z$ -direction. The magnetic field along the  $z$ -direction bends the trajectories of charged particles moving through the TPC in the  $xy$ -plane. The curvature of the particle trajectories in the magnetic field enables the measurement of a particle's momentum. The field strength of the magnet can be set from 0.25T to 0.5T and reversible direction along  $z$ . The ZDC together with some parts of TOF trigger the collision event. The TPC is the main tracking detector. It is capable of measuring the momentum of charged particles,  $p_T \geq 0.1$  GeV/c within pseudo-rapidity<sup>2</sup>,  $|\eta| \leq 1.8$ , with complete coverage in azimuth<sup>3</sup>,  $0 \leq \phi \leq 2\pi$ .

Identification of particles is possible via a measurement of the rate of energy loss of the particles,  $\frac{dE}{dx}$ , through the TPC detector. The energy loss mechanism is described in Section 2.5. Starting time of the particle track at the pseudo vertex is measured using upgraded pseudo Vertex Position Detector (upVPD). Together with the VPD, the TOF detector measures the time of flight from the VPD to the TOF detector itself. Using the particle momentum information from the TPC and the distance between the VPD and TOF detectors together with the time of flight, the mass of the particle can be obtained. Thus, the TOF detector offers another approach of particle identification via determination of the mass of the particles. The particle identification method can be improved to achieve higher efficiency and purity using both  $\frac{dE}{dx}$  information from the TPC and  $\beta^{-1}$  (as a function of time)<sup>4</sup> from TOF detector.

---

<sup>2</sup>The pseudo-rapidity,  $\eta$ , is defined and discussed in Chapter 3 in detail.

<sup>3</sup>The  $\eta$  acceptance is quoted with respect to center of cylinder,  $(x, y, z)=(0,0,0)$ .

<sup>4</sup>The  $\beta^{-1}$  is defined in Chapter 5.

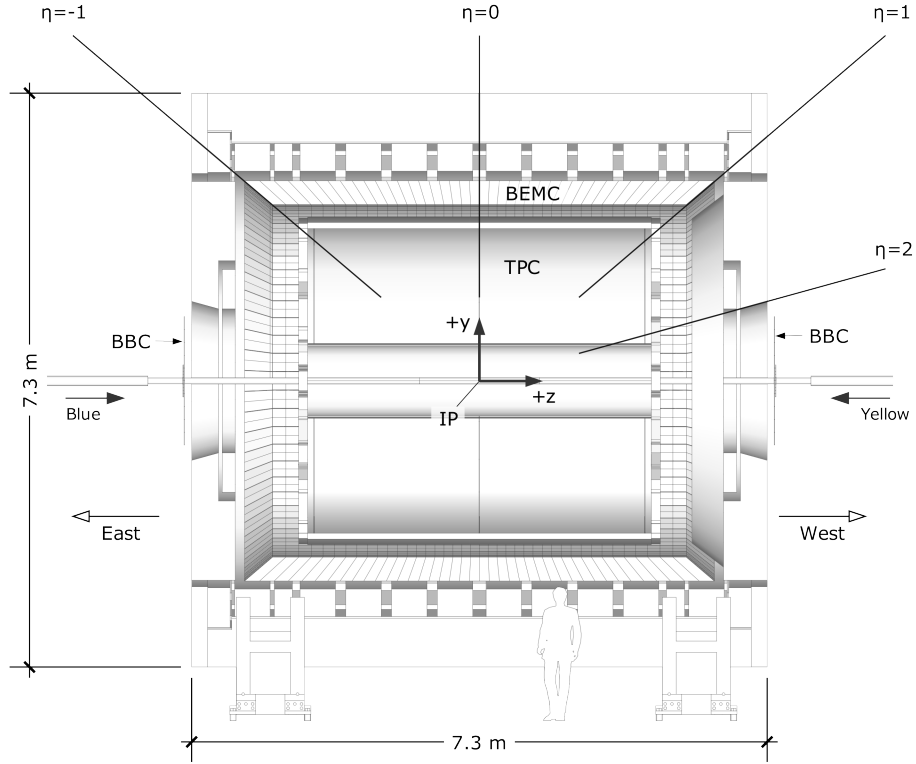


**Figure 2.3** A schematic diagram of STAR detector. The TOF detector (not shown in diagram) is just outside of TPC. The yellow (counter-clock-wise) and blue (clock-wise) beams along the  $z$ -axis cross at the center of TPC. Source: [7]

This thesis adopts the improved method for particle identification using both TPC and TOF. We have identified particles up to  $p_T \leq 3.2\text{GeV}$  with efficiency and purity of more than 80% for both. The particle identification method is described in Chapter 5. Another important detector, the Electromagnetic Calorimeter (EMC), allows fast detection of high energy photons and electrons. The EMC is divided into two components; the Barrel EMC (BEMC)

which has an acceptance of  $|\eta| < 1$ , and the Endcap EMC (EEMC) which covers  $1 < \eta < 2$ .

## 2.4 Trigger

The collision rate at RHIC is thousands of times more than the rate at which the Data Acquisition system (DAQ) can process and store information from the collision events. For example, the beam-beam interaction rate in 2004 was 10 MHz, while slow detectors such as the TPC could only process information at rates of 100 Hz. Even after upgrades (eg, decommissioning of one of the trigger detectors, the Central Trigger Barrel (CTB), and installing TOF), STAR can currently record events at a rate of just about 500 Hz [45][46]. Therefore, certain criteria are needed to select the events that have the potential for meaningful physics. A trigger is a set of criteria used to accept or reject an event during data collection. The triggers are categorized into levels (L0 through L3) based primarily on the speed of execution. Trigger L0 receives information from the ZDCs and the EMC for every bunch crossing. The ZDC sum and the  $z$ -position as well as EMC information on high energy hits are available on this level. If the interaction passes the event selection criteria, a trigger is issued to the slow detectors (L1 trigger). L1 and L2 will then carry out further processing, and work with the larger time constraints of  $100\mu s$  and  $5ms$  respectively. For a minimum bias trigger, both L1 and L2 levels are not required. However, L1 and L2 are important for other triggers such as the  $\gamma$ -trigger. Beyond L2, the DAQ system is responsible for the collection of data

from all detectors. Before this information is transferred to a hard disk and/or data tape, L3 can be used for further event selection with information from all the STAR detectors available.

## 2.5 Time Projection Chamber

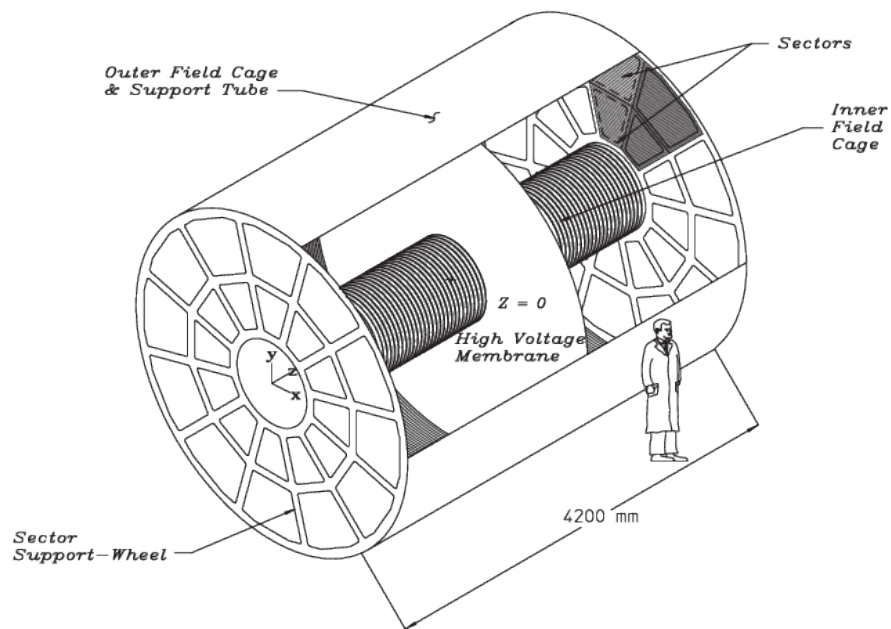


**Figure 2.4** The STAR TPC which surrounds a beam-beam interaction region at RHIC. The beam-beam collisions take place near the center of the TPC

Figure 2.4 shows the STAR TPC: one of the most important detector subsystems in STAR. The details of the STAR TPC subsystem are presented in [8]. It consists of an 4.2 m long cylindrical volume with the cross section

of an annulus with an inner radius of 50 cm and an outer radius of 200 cm. It is filled with P10 gas (10% methane, 90% argon). The central membrane is held at about 28 kV and separates the chamber into two halves, east and west, with uniform, opposite electric fields toward the anodes at the endcaps. Because of the potential, the electrons drift to the opposite ends in an electric field of 135 V/cm. When the chamber is held at 2 mbar above atmospheric pressure, P10 sustains a high, stable drift velocity of  $5.45 \text{ cm}/\mu\text{s}$  for electrons. Common electron absorbers that can exist in the TPC volume are water and oxygen, which is kept at less than 10 ppm and 100 ppm, respectively.

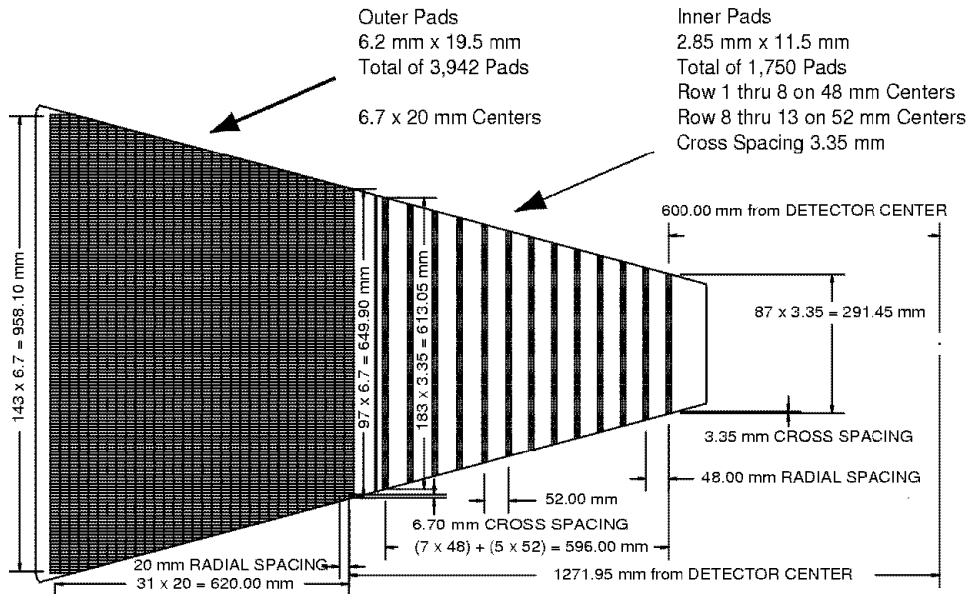


**Figure 2.5** One full sector of the anode pad plane. The inner sub-sector is on the right (1 through 13 pads) and the outer sub-sector is on the left (1 through 144) [8].

Drifting electrons are measured in the endcap readout using Multi-Wire

Proportional Chambers (MWPC) with readout pads. There are 136,608 such pads in the detector. A diagram of a single TPC sector is given in Figure 2.5. Drifting electrons induce an avalanche when they approach the thin anode wires. The number of avalanche electrons is proportional to the number of drift electrons, where the ratio is referred to as the gain, and for the inner and outer sectors this gain is approximately 3770 and 1230, respectively. Image charge is spread over several adjacent pads, allowing for accurate reconstruction of the original track position to within a small fraction of a pad width. The reconstruction is described as follows. The positive ions created in this process induce an image charge on the cathode pads. The charge is digitized to give an ADC value for every pad. Each endcap is arranged into 12 sectors with each sector containing 45 rows of pads, which indicate the  $xy$ -position of the elements of a track. The pad dimensions are chosen so that a drifting charge cloud will typically deposit charge over 3 pads in a row, and this configuration leads to optimal position resolution. If a Gaussian is used to determine the centroid of cluster, the uncertainty represented by the Gaussian width is typically 20% narrower than the pad width. The  $xy$ -position of the cluster is thus determined by the radial distance of the pad row and the centroid from the Gaussian fit. The arrival time of the drifting element is used to deduce the  $z$ -position, as the drift velocity and the time of the collision are recorded. As the signal from a drifting element of charge will often cover several time intervals due to diffusion, a weighted average is taken (weights will depend on signal strength in the time interval), and the extracted mean is used to

determine the  $z$  position of the element. The recorded  $xyz$ -position is thus known as a “hit”. In total, around 70 million pixels are available in order to take a 3D picture of the charged particles emerging from an event.

The anode field wires are supported by a ground grid plane in order to terminate the field in the avalanche region and provide additional shielding for the pads. This ground grid is located 2 mm from the inner sub-sector and 4 mm from the outer sub-sector. There is also a gating grid, 6 mm from the ground grid, which acts as a shutter to control the entry of electrons from the TPC drift volume to the anode planes. It can be made transparent to electrons while events are being recorded and block them otherwise. The solenoidal magnet coils around STAR carry up to 4500 A of current and consume 3.5 MW of power to produce a maximum field strength of 0.5 T in both forward and reverse directions. The tracks of the drifting charged particles in the electric field curve because of the static magnetic field. The particle track curvature is measured using reconstructed track information. Using the curvature, the momentum of the particle, one of the most important variables, is determined using equation 2.1.

$$p_T = 0.3BRq(GeV/c), \tag{2.1}$$

where  $B$  is the magnitude of the magnetic field (in  $T$ ),  $R$  the radius of curvature (in  $m$ ), and  $q$  is the charge of the particle (in electron charge unit).

The other important information that is extracted from the TPC is ionization energy loss per unit length ( $dE/dx$ ) of charged particles. As a charged particle ionizes the TPC gas, it will lose energy, which is then transferred to

the liberated electrons that drift toward the anode pads. The intensity of the readout signal is related to the energy loss of the passing particle. For a given cluster, the energy loss per unit length ( $dE/dx$ ) is measured by associating the sum of the drift electrons with the energy loss, and dividing this by the track path-length across the sensitive pad length. Using the Bichsel function, an extension of the Bethe-Bloch formula, which shows expected  $dE/dx$  as a function of velocity, the velocity of the particle is calculated. Finally, the mass of the particle is obtained from the velocity and the momentum. Therefore,  $dE/dx$  serves as a variable to identify particles (see Chapter 5).

## 2.6 Time of Flight

The TOF detector was an upgrade STAR fully installed in 2010. As its name suggests, TOF measures the time of flight of a charged particle starting from the collision vertex as it traverses the TPC and hits the TOF detector itself. The main objective of the detector was to improve the particle identification (PID) capability of STAR by increasing timing resolution to 100 ps and by providing another measurement to identify particles. The main component of the detector is based on recently developed Multi-gap Resistive Plate Chamber (MRPC) technology.

The TOF system consists of two sub-systems: the upgraded pseudo Vertex Position Detector (upVPD) and the TOF detector itself. The upVPD detector is designed to measure the collision time of an event with a resolution of 10-20 ps. The upVPDs are placed around the beam pipe and are located

at  $z = \pm 5.7$  m away from the center covering  $4.24 < |\eta| < 5.1$  of STAR. It is schematically shown in Figure 2.6. The upVPD has 19 photomultiplier (PMT) detectors in both the east and west side. In the collisions, large numbers of very forward, very high energy, photons are produced which travel away from the collision vertex and effectively serve as a signal for the PMTs [47]. In the TOF system, the upVPD measures the start time ( $t_{start}$ ) of the charged particle as it moves out toward other detectors. The TOF detector measures the end time ( $t_{end}$ ) enabling us to measure the time of flight ( $t_{end} - t_{start}$ ).

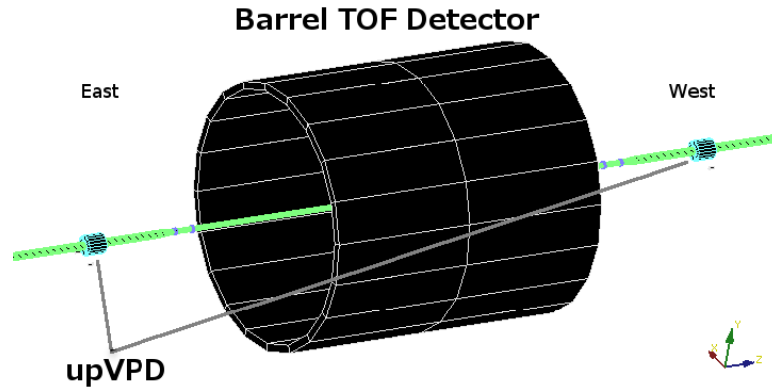


**Figure 2.6** Schematics diagram of the TOF system: 120 TOF trays and upVPDs on east and west side of beam pipe.

Figure 2.6 shows a schematic view of TOF detector system. The TOF detector is a barrel detector made of 120 trays surrounding the TPC covering  $|n| \leq 0.9$  and  $2\pi$  in *azimuth*. Each tray measures 241.3 cm in length  $\times$  21.3 cm in width  $\times$  8.5 cm in height. A single tray is made of 32 Multigap Resistive Plate Chamber (MRPC) modules with dimensions 9.4 cm  $\times$  21 cm.

Side views of a MRPC module are shown in Figure 2.7. Five layers of 0.54 mm thick glass plates are surrounded by two outer 1.1 mm thick glass layers, a graphite electrode, six copper pads, a PC board and structural honeycomb material. A high voltage of 7000V is applied to the electrodes which generate an electric field at each gap between the plates. The trays are completely shielded and are filled with 90% tetra-fluoro-ethane ( $C_2H_2F_4$ ), 5% iso-Butane and 5% SF6 gas. When a charged particle passes through a given MRPC, it ionizes the gas and the strong electric field generates avalanches in each glass-glass gap. The signal induced in the pads is the sum of the signals from each avalanche [9].

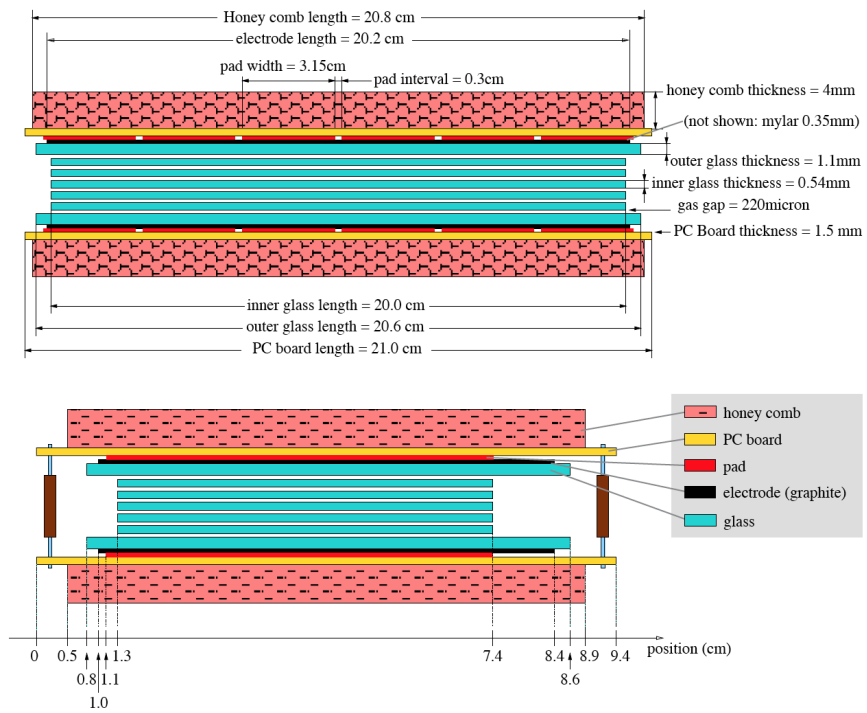


**Figure 2.7** Side views of MRPC structure (not in scale) : top and bottom show length and width view of the tray respectively [9].

# Chapter 3

## Data Analysis

### 3.1 Introduction

This thesis is based on the Minimum Bias Au+Au collision data for center of mass energy 200 GeV per nucleon pair collected by the STAR experiment during RHIC runs in 2010 and 2011<sup>1</sup>. The results from the 2001 and 2004 Au+Au data at the same center of mass energy are frequently considered as a benchmark for comparison with data from later runs of the results because of lower pileup and less detector material near the collision vertex. The data include some artificial effects due to limits in hardware and reconstruction algorithms. In this chapter, event-wise, track-wise and pair-wise data selection processes with the objective of reducing the experimental and detector artifacts in the current study are discussed. The data selection cuts are applied before constructing two-particle correlations. In this chapter different parameters required to define the correlation measure are discussed.

---

<sup>1</sup> RHIC runs in 2001, 2004, 2010 and 2011 are also called Run2, Run4, Run10 and Run11 respectively. Note: The second RHIC run was in 2001.

## 3.2 Coordinate System

A cylindrical coordinate system is favorable for the geometry of the STAR detector [8]. Collisions between the ion beams take place near the center of the longitudinal axis ( $z$ -axis) of STAR. The particles produced after a collision are scattered in all possible directions. The detectors in STAR are configured such that particle trajectories pass through multiple subsystems. The detectors provide data used to measure properties of the particles such as momentum, energy, charge and speed of the particles. The direction of the colliding beams defines the  $z$ -axis, the vertical upward direction defines the  $y$ -axis and the axis perpendicular to the  $yz$ -plane is the  $x$ -axis. Azimuthal ( $\phi$ ) and inclination ( $\theta$ ) angles are defined using components of momentum in Cartesian coordinates,  $p_x, p_y$  and  $p_z$ .

$$\begin{aligned}\phi &= \tan^{-1} \left( \frac{p_y}{p_x} \right) \\ \theta &= \tan^{-1} \left( \frac{p_T}{p_z} \right),\end{aligned}\tag{3.1}$$

where  $\phi$  covers entire azimuth from 0 to  $2\pi$  and  $\theta$  extends from 0 to  $\pi$  and transverse momentum ( $p_T$ ) is the component of momentum in the  $xy$ -plane.

$$p_T = \sqrt{p_x^2 + p_y^2}\tag{3.2}$$

*Rapidity* and *pseudorapidity* are frequently used variables in high-energy physics. The longitudinal rapidity of a particle is a function of energy ( $E$ ) and the  $z$ -component of momentum ( $p_z$ ) of the particle.

$$y_z = y = \frac{1}{2} \ln \left[ \frac{E + p_z}{E - p_z} \right] \quad (3.3)$$

In the ultra-relativistic limit, the energy of the particle is much larger than its rest mass (i.e.,  $E \gg m$ ) and hence the mass can be neglected. In such a limit, the rapidity is approximately equal to *pseudorapidity* ( $\eta$ ), given by

$$\begin{aligned} \eta = y|_{E \gg m} &= \frac{1}{2} \ln \left[ \frac{\sqrt{p^2 + m^2} + p_z}{\sqrt{p^2 + m^2} - p_z} \right] \\ &= \frac{1}{2} \ln \left[ \frac{p + p_z}{p - p_z} \right] \\ &= \frac{1}{2} \ln \left[ \frac{1 + \cos(\theta)}{1 - \cos(\theta)} \right] \\ &= -\ln \left[ \tan \left( \frac{\theta}{2} \right) \right], \end{aligned} \quad (3.4)$$

where  $p_z = p \cos(\theta)$  and  $p$  is the momentum magnitude. The magnitude of  $\eta$  changes from 0 to  $\pm\infty$  as  $\theta$  changes from  $\pi/2$  to 0 or  $\pi$ .

Throughout this thesis correlations are measured in angular difference coordinates defined as:

$$\begin{aligned} \phi_\Delta &\equiv \phi_1 - \phi_2 \\ \eta_\Delta &\equiv \eta_1 - \eta_2, \end{aligned} \quad (3.5)$$

where subscripts 1 and 2 are particle labels. The commonly used difference symbols such as  $\Delta\eta, \Delta\phi$  are reserved for a different type of pair difference or sometimes for the detector acceptance.

## 3.3 Event Selection

### 3.3.1 Trigger

A minimum-bias (MB) trigger is a least-constrained trigger for which a nuclear interaction occurs. The minimum-bias trigger requires a coincidence between the two ZDC detectors on the East and West side of STAR [48]. The photo-multiplier tubes (PMTs) attached to the detectors measure the intensity of neutral particles (i.e. neutrons and photons) moving in the  $z$ -direction. One of the required conditions for the minimum-bias trigger is that the sum of signals from the East and West detectors should exceed the signal from a single neutron peak [48]. The other condition based on the timing difference, is that the collision should take place near the center of the detector. In the present analysis, the collision vertex position requirement is fixed to be  $|V_z| < 25\text{cm}$  relative to the geometrical center of the STAR TPC<sup>2</sup>.

Throughout the run period the detailed trigger conditions are changed. The trigger IDs are provided for different conditions. In this thesis, the triggers 260001, 260011, 260021 and 260031 for Run10 and 350023, 350033 and 350043 for Run11 are included.

About 50M events collected using both forward and reverse full magnetic field of 0.5T in Run11 are used to produce identified particle correlations for different momentum ranges presented in Chapter 6.

---

<sup>2</sup>The distribution of collision vertex position is approximately Gaussian centered at  $\sim 0$  with RMS value of  $\sim 13\text{cm}$ .

### 3.3.2 Pileup

Pileup refers to a contamination of the tracks from untriggered event(s) with those from the triggered event. Pileup can produce false correlation results. In correlations, event pileup contributes to enhanced angular correlations in large relative pseudorapidity  $\eta_\Delta$  regions. As a result, a characteristic  $W$  shape is produced in the correlation structure [5]. In Chapter 4, the pileup in the Run10 and Run11 data and the correction procedure used is discussed in detail.

## 3.4 Track Selection

In a minimum-bias trigger, we tend to apply the lowest possible schemes of data reduction. However, because of kinetic acceptance restrictions, we must reject certain tracks. For example, for a given full magnetic field of 0.5T, a track having  $p_T < 0.15$  GeV/c curls before generating a sufficient number of hit points for the reconstruction algorithm to obtain a good fit to the track. Similarly, a track having  $|\eta| > 1$  doesn't generate enough points in the TPC. A minimal set of track selection cuts are listed in Table 3.1.

Variable	Range	Remarks
$p_T$	(0.15, 50) GeV/c	Only a small fraction of tracks are rejected
$\eta$	(-1,1)	Covers largest acceptance of TPC
$\phi$	(0,2 $\pi$ )	The range covers entire azimuth
Charge	-1 and 1	Only positive and negative tracks
NFitPoints	(15,50)	Fewer number of fit points doesn't give good track fit
GlobalDCA	(0,3.0) cm	Distance of closest approach of global tracks to vertex
$\chi^2$ per degree of freedom	(0,3.0)	Error in fitting tracks
NSigmaElectron	(-1.5,1.5)	Remove electron using the range of energy loss $dE/dx$

**Table 3.1** A complete list of track quality cut.

### 3.4.1 Particle Pair Selection

In the correlation studies, improper selection of track pairs causes either enhancement or reduction in the correlations. Therefore, besides requiring certain quality in single tracks, we also require quality in pairs of tracks. Track merging/splitting or crossing are the main issues involved in track pair quality cuts.

## Merging

When two tracks are too close to each other within the TPC, the track reconstruction algorithm could potentially fit them as a single track. Such a situation is called track merging and results in a suppression in the number of track pairs at small  $\eta_\Delta$  and  $\phi_\Delta$ .

## Crossing

The trajectories of oppositely charged particles are curved in a magnetic field in opposite directions. When two tracks cross each other at close separation distance in the TPC, the reconstruction algorithm may reconstruct them into up to four tracks. That is, two tracks are split into four tracks. However, because the split tracks are short, the track quality cut rejects them. This could further suppress the overall number of track pairs.

Merging and crossing issues were observed and addressed in analysis of Run2/4 data [1][37]. The implemented solution for the merging was to reject pairs of tracks that are closer than a certain minimum longitudinal distance. Similarly, the solution for the crossing issue was to reject pairs of tracks that are curved in opposite directions and are likely to cross before they reach the outer field cage of the TPC. Pairs of tracks having longitudinal (drift direction in TPC gas) separation  $< 5$  cm were rejected in the Run4 data. However, the Run4 set of cuts were not sufficient for identified particles in Run10/11. Because of the pair loss in sibling events due to merging and crossing, the correlation at small  $(\eta_\Delta, \phi_\Delta)$  falls sharply, making a gash-like

structure. Furthermore, artifacts introduced by track merging and crossing for different momentum ranges were different. An example of the artifact for one range of momentum in Run4 and Run11 is shown in Figure 3.1. The cuts for Run11 were extended to 10 cm to remove the artifact in correlations introduced, particularly, by crossing of tracks. Besides extending longitudinal separation cuts, the tracks were required to have TOF hits. The tracks hitting the TOF are less likely to cross in the TPC. However, this requirement was not sufficient to remove the gash-like structure completely.

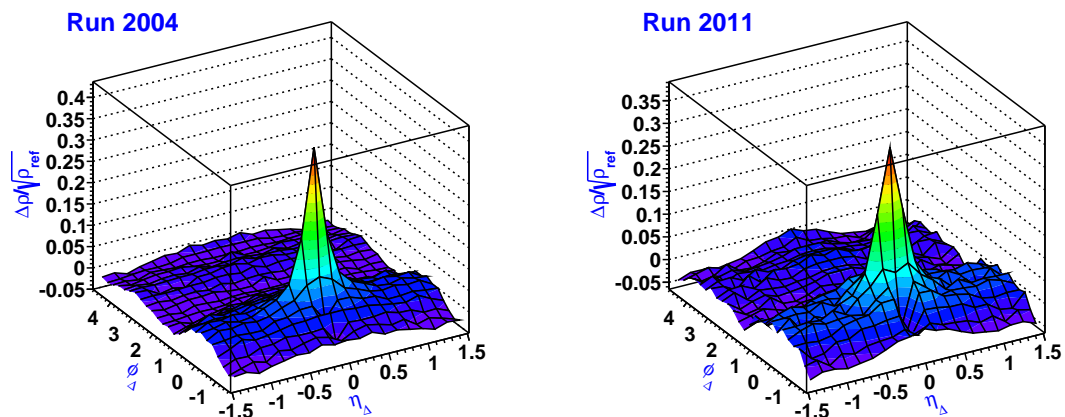


**Figure 3.1** Angular correlation for Au+Au at  $\sqrt{s_{NN}} = 200$  GeV. In the left panel, correlations of all particles in centrality 9 in  $y_{T1}(2.0, 2.5) - y_{T2}(1.0, 1.5)$  ( $y_T$  is transverse rapidity, see Section 3.7) range for Run4 data are shown. Similarly, in the right panel correlations of all particles in same centrality and similar  $y_T$  range for Run11 data is shown. The gash like structure near  $(\eta_\Delta, \phi_\Delta) \rightarrow 0$  is sharper and deeper in the Run11 data.

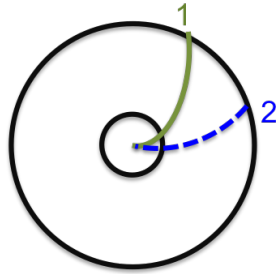
Track crossing is a function of charge, opening angle (angle at the col-

lision vertex) and momentum ( $p_T$ ) of the two tracks. The smaller the opening angle, the greater the chance that the tracks will cross. Similarly, tracks having smaller momentum bend more in the magnetic field making it more likely to cross to other tracks. Three examples of track crossing are shown in Figure 3.2(b), (d) and (f). On the top and middle rows, crossing of the negative and positive charged tracks are shown, respectively. In the bottom row of Figure 3.2, crossing of oppositely charged tracks is shown.

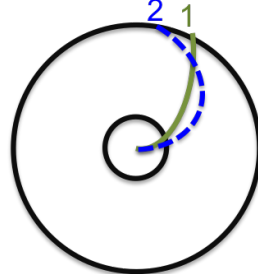
Charge pair (1, 2)	Opening Angle ( $\phi_1 - \phi_2$ )	Transvers Rapidity ( $y_{T1} - y_{T2}$ )
- , +	$\phi_1 - \phi_2 > 0$ $\phi_1 - \phi_2 < -\pi/2$	
+ , -	$\phi_1 - \phi_2 < 0$ $\phi_1 - \phi_2 > \pi/2$	
+ , +	$\phi_1 - \phi_2 < 0$ $\phi_1 - \phi_2 > 0$ $\phi_1 - \phi_2 < -\pi/4$ $\phi_1 - \phi_2 > \pi/4$	$y_{T1} - y_{T2} < 0$ $y_{T1} - y_{T2} > 0$
- , -	$\phi_1 - \phi_2 > 0$ $\phi_1 - \phi_2 < 0$ $\phi_1 - \phi_2 < -\pi/4$ $\phi_1 - \phi_2 > \pi/4$	$y_{T1} - y_{T2} < 0$ $y_{T1} - y_{T2} > 0$

**Table 3.2** A complete list of conditions to accept track pairs. The charge of the track pairs are listed in the first column. If all conditions are met on one or more rows for a given charge pair, then the pair is accepted. Note: these are not pair cut conditions but are acceptance criteria.

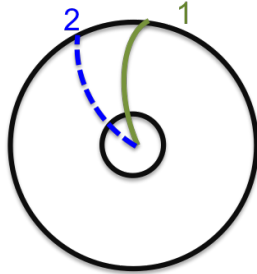
In the analysis of Run11, the conditions for the acceptance of a track pair are presented in Table 3.2. If the charged track pair meets the condition in either of the rows, the pair is accepted. In addition to the conditions in



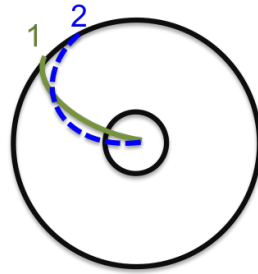
(a)  $(-, -)$ ,  $p_{T2} > p_{T1}$ ,  $\phi_1 - \phi_2 > 0$



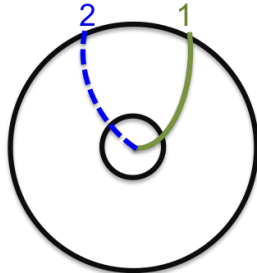
(b)  $(-, -)$ ,  $p_{T2} < p_{T1}$ ,  $\phi_1 - \phi_2 > 0$



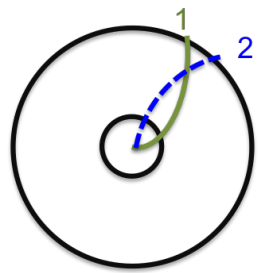
(c)  $(+, +)$ ,  $p_{T2} > p_{T1}$ ,  $\phi_1 - \phi_2 < 0$



(d)  $(+, +)$ ,  $p_{T2} < p_{T1}$ ,  $\phi_1 - \phi_2 < 0$



(e) Opposite charges,  $|\phi_1 - \phi_2| > \pi/2$



(f) Opposite charges,  $|\phi_1 - \phi_2| < \pi/2$

**Figure 3.2** Track crossing cartoons showing transverse views of tracks in the TPC in full magnetic field. The panels show the distinction between track crossing for negative charges (top), positive charge (middle), and for opposite signed charges (bottom).

Table 3.2, longitudinal separation of  $> 10$  *cm* between track pairs is required.

### 3.4.2 Pair Weighting

The distribution of particle pair density on  $\eta_\Delta$  is not uniform. It monotonically falls from a maximum value at  $\eta_\Delta = 0$  to minimum value at  $\eta_\Delta = \pm 2$ . That is,  $\eta_\Delta$  has a triangular shape. Therefore, the number of track pairs having differences in  $\eta_\Delta \rightarrow 0$  is higher than the pairs having differences  $\eta_\Delta \rightarrow \pm 2$ . A weight factor is chosen to correct the pair acceptance. Pair weighting is described in detail in [1].

The weight is defined as in Equation 3.6.

$$weight = \frac{1}{1 - \frac{|\eta_\Delta|}{\eta_{\Delta,max}}}, \quad (3.6)$$

where  $\eta_{\Delta,max} = 2$  is set for correlations in this thesis. The ‘triangular acceptance’ cancels in the angular correlation. Therefore, the weight factor is not applied in the angular correlation measure. However, the weight factor is applied to each pair binned in momentum space while calculating  $(y_T, y_T)$  correlations.

## 3.5 Centrality

All heavy-ion collisions are not head-on. The centrality of a collision event refers to the degree of overlap between the nuclei during a collision. A head-on collision with an impact parameter ( $b$ ) of 0 has the highest degree

of overlap and is called the *most central* event. Similarly, a collision with largest impact parameter is called a *peripheral* event. In Figure 3.3 a cartoon of the collision geometry for a *mid-central* collision is shown. In the analysis of Au+Au collisions at  $\sqrt{s_{NN}} = 200$  GeV, we have divided centrality into 11 classes, centrality 10 being the most central and 0 being the most peripheral.

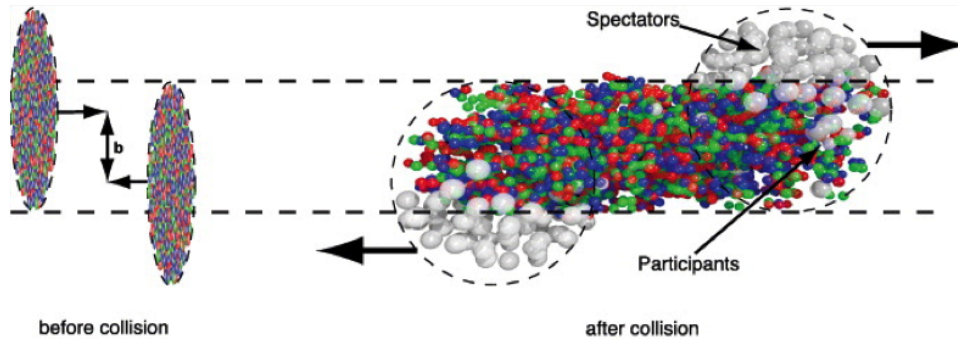


**Figure 3.3** An illustration of a heavy-ion collision with an impact parameter of  $b$ . On the left, two heavy-ions are approaching to collide. On the right, just after the collision, spectator nucleons are shown to be unaffected from the participant nucleons [10].

### 3.5.1 Definition

Since the impact parameter of a nuclear collision cannot be directly measured, the centrality is inferred from the particle multiplicity measured after the collision. The *multiplicity* is the number of reconstructed particle tracks in a collision where the track quality cuts in Table 3.1 are imposed before making the multiplicity measure. This multiplicity measure includes detector inefficiencies. The efficiency-corrected centrality classes were defined for Au+Au collisions at  $\sqrt{s_{NN}} = 200$  GeV [1]. Table 3.3 shows the centrality

Centrality Number	Raw Centrality(%)	Corrected Centrality (%)	Multiplicity Ranges
0	90-100	84-93	2-15
1	80-90	74-84	15-35
2	70-80	64-74	35-68
3	60-70	55-64	68-117
4	50-60	46-55	117-187
5	40-50	38-46	187-281
6	30-40	28-38	281-401
7	20-30	18-28	401-551
8	10-20	9-18	551-739
9	5-10	5-9	739-852
10	0-5	0-5	739-2000

**Table 3.3** Mapping of multiplicity classes to centrality classes and centrality numbers [1]. The raw multiplicity cuts are defined to achieve the same centrality fractions in each centrality.

classes used for Au+Au collisions in the Run4 data at  $\sqrt{s_{NN}} = 200$  GeV.

### 3.5.2 Centrality in Runs 2010 and 2011

Figure 3.4 shows the multiplicity frequency distributions for the Run4, Run10 and Run11 data. The distributions at low and high multiplicities are significantly different. Although the collision energies in Run10 and Run11 are sane as in Run4, the trigger, vertex finding and tracking inefficiencies in the various runs are different. Therefore, the centrality classes are different in different runs. However, a similar efficiency correcting method and centrality finding procedure are expected to apply for all runs of the same energy: Run4, Run10 and Run11.

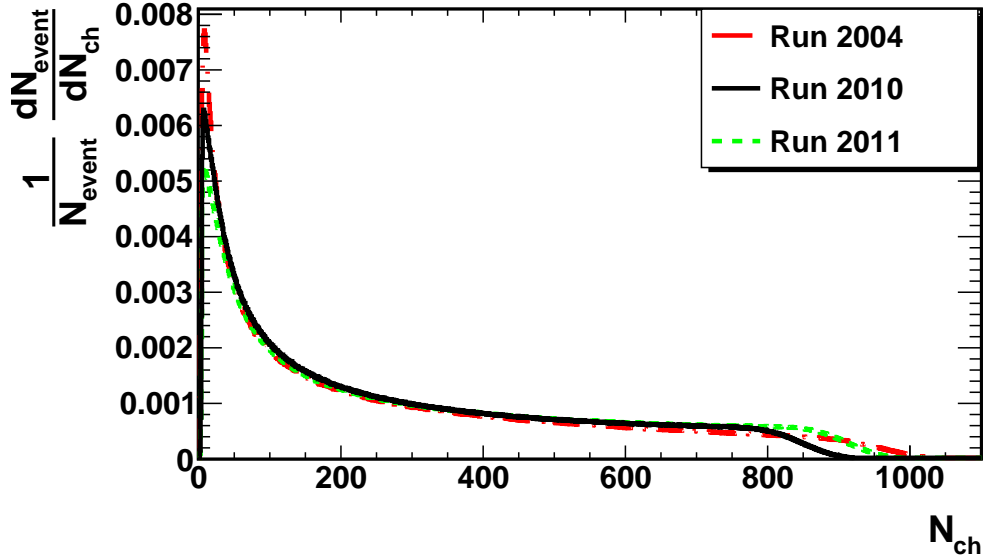


**Figure 3.4** Multiplicity frequency distribution of run 2004, 2010 and 2011 data. The differences in the distributions are significant at low and high multiplicity ( $N_{ch}$ ).

The centrality percentages in Run10 and Run11 are determined using the efficiency-corrected multiplicity distributions for Run4. In summary, Run4 real data is matched to simulated data. Using efficiency corrected multiplicities in the STAR spectra paper, multiplicities for centralities in Run4 were estimated. Then Run10 and 11 multiplicity distributions are matched to Run4, and the multiplicity bins for all centralities in each run were estimated based on Run4 multiplicities. A general method of determining centrality involves an iterative process as described in the steps below:

1. Plot the raw multiplicity distribution of both real data and simulated

data obtained using Monte Carlo Glauber (MCG) method on  $N_{ch,raw}^{1/4}$ . The distribution is approximately a flat distribution with sharp falling edges at the ends [5]. In Figure 3.5 the multiplicity from the MCG model and from the Run4 and Run10 data are shown.

2. Next, extrapolate the data trend in the approximately flat region to lower multiplicity. Find the intersection point between the extrapolated trend and a line parallel to MCG at the lower edge. Use the intersection point as a lower maximum point and decide the lower half-max ( $N_{ch,raw,LHM}^{1/4}$ ) point. This provides the first iterative estimate of the lower end-point corrected for trigger and vertex inefficiency. In Figure 3.5, bold and slightly slanted horizontal line represents the extrapolation of the Run4 data. Similarly, in the same figure, the bold and slightly slanted vertical line is drawn parallel to the lower edge of the MCG model.
3. The STAR spectra paper [49] provides efficiency corrected multiplicities,  $\frac{dN_{ch,corrected}}{d\eta}$ , in centrality ranges 0-5%, 5-10%, 10-20%, ..., 70-80%. Next, subdivide the extrapolated data distribution into those centrality ranges and calculate the mean multiplicity  $\langle N_{ch,raw} \rangle$  in each range from 0-5% to 70-80%. Then, using the corrected multiplicities provided in the spectra paper [49], fit the corrected centrality dependence with the above raw  $\frac{dN_{ch,raw}}{d\eta}$  using the multiplicity dependent tracking efficiency equation, Equation 3.7, determined from previous studies of efficiency

versus centrality [50] and determine the trial parameters  $\alpha$  and  $\beta$ .

$$N_{ch,corrected} = \frac{1 + \alpha N_{ch,raw}}{\beta} N_{ch,raw}, \quad (3.7)$$

4. Use the raw multiplicity,  $N_{ch,raw}$ , derived from Equation 3.7, and Equation 3.8 to calculate the frequency distribution,  $\frac{dN_{event}}{dN_{ch,corrected}}$  on  $N_{ch,corrected}^{1/4}$ . Extrapolate the corrected distribution to obtain the lower half-max ( $N_{ch,corrected,LHM}^{1/4}$ ) point following the same procedure as in step 2.

$$\begin{aligned} \frac{dN_{event}}{dN_{ch,corrected}^{1/4}} &= \frac{dN_{ch,raw}^{1/4}}{dN_{ch,corrected}^{1/4}} \frac{dN_{event}}{dN_{ch,raw}^{1/4}} \\ &= \frac{1}{4} N_{ch,raw}^{-3/4} \frac{dN_{ch,raw}}{dN_{ch,corrected}^{1/4}} \frac{dN_{event}}{dN_{ch,raw}^{1/4}} \\ &= \frac{1}{4} \frac{4\beta N_{ch,corrected}^{3/4}}{\sqrt{1 + 4\alpha\beta N_{ch,corrected}}} \frac{dN_{event}}{dN_{ch,raw}^{1/4}} \end{aligned} \quad (3.8)$$

5. Repeat the procedures in steps 2 through 4 by adjusting the estimated lower half-max end-point until the corrected lower half-max end-point  $N_{ch,corrected,LHM}$  obtained in step 4 equals the true value.

The true half-max point is obtained by convoluting the non-singly diffractive minimum-bias p+p event frequency distribution with the A+A nucleon participant distribution obtained from MCG simulation. The tracking efficiency correction parameters, for Run 2004, are estimated as  $\alpha = 0.000203$  and  $\beta = 0.819$  for  $\eta$ -acceptance  $(\Delta\eta) = 2$  (source: L. Ray private communication).

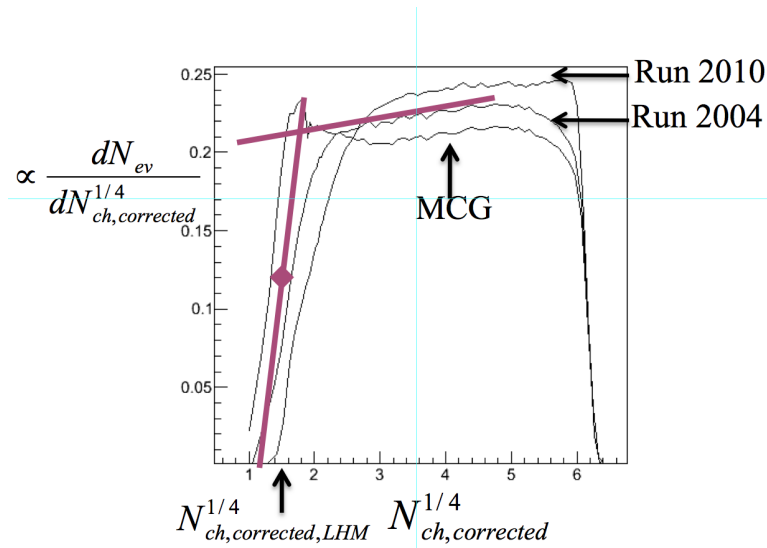


**Figure 3.5** Unit normal frequency distributions of Run 2004 and 2010 data and MCG on  $N_{ch,corrected}^{1/4}$ . The bold and slightly slanted horizontal line represents the extrapolation of the Run4 data. Similarly, the bold and slightly slanted vertical line is drawn parallel to the lower edge of the MCG model. The rectangular dot on the extrapolated slanted line in left of the graph corresponds to the lower half-max point (source: L. Ray private communication).

6. Next, fit the corrected frequency distribution using MCG. The adjustable parameter is the hard scattering parameter  $x$  in the Kharzeev-Nardi two component multiplicity model [51].
7. Finally, estimate the final centrality bins to the corrected data.

This general procedure which was applied to Run4, was applied to the Run10 and 11 data. Before applying the steps to calculate the centrality bins a minimum number of cuts are applied to produce the raw centrality distribution. Specifically, the track cuts listed in Table 3.1 were applied. To calculate the efficiency-corrected centrality bins in Run10 and Run11 data, the following procedure was used:

1. As a first step, apply tracking efficiency correction to Run 2010 raw multiplicity to be consistent with the Run 2004 multiplicities.

$$\begin{aligned}
 N_{ch,raw,2004,new} &= \frac{1 + \alpha N_{ch,raw,2010}}{\beta} N_{ch,raw,2010} \\
 N_{ch,raw,2010} &= \frac{\sqrt{1 + 4\alpha\beta N_{ch,raw,2004,new}} - 1}{2\alpha},
 \end{aligned} \tag{3.9}$$

where the parameters  $\alpha$  and  $\beta$  correct the Run 2010 raw data to a ‘new’ set of data that matches to Run4 raw data. Also,  $N_{ch,raw,2004,new} \approx N_{ch,raw,2004}$ .

2. Express the Run10 distribution of centrality on  $dN_{ch,raw,2004,new}^{1/4}$ .

$$\begin{aligned}
\frac{dN_{event,2010}}{dN_{ch,raw,2004,new}^{1/4}} &= \frac{dN_{ch,raw,2010}^{1/4}}{dN_{ch,raw,2004,new}^{1/4}} \frac{dN_{event,2010}}{dN_{ch,raw,2010}^{1/4}} \\
&= \frac{1}{4} N_{ch,raw,2010}^{-3/4} \frac{dN_{ch,raw,2010}}{dN_{ch,raw,2004,new}^{1/4}} \frac{dN_{event,2010}}{dN_{ch,raw,2010}^{1/4}} \\
&= \frac{1}{4} N_{ch,raw,2010}^{-3/4} \frac{4\beta N_{ch,raw,2004,new}^{3/4}}{\sqrt{1 + 4\alpha\beta N_{ch,raw,2004,new}}} \frac{dN_{event,2010}}{dN_{ch,raw,2010}^{1/4}}
\end{aligned} \tag{3.10}$$

3. Use the Run4 efficiency correction to convert the Run10 raw distribution to the corrected multiplicity.

$$\begin{aligned}
N_{ch,corrected,2010} &= \frac{1 + \alpha_{corrected} N_{ch,raw,2004,new}}{\beta_{corrected}} N_{ch,raw,2004,new} \\
N_{ch,corrected,2004} &= \frac{1 + \alpha_{corrected} N_{ch,raw,2004}}{\beta_{corrected}} N_{ch,raw,2004},
\end{aligned} \tag{3.11}$$

where  $\alpha_{corrected} = 0.000203$  and  $\beta_{corrected} = 0.819$ , as discussed in the general efficiency correction procedure step 5.

Further,

$$\begin{aligned}
\frac{dN_{event,2010}}{dN_{ch,corrected,2010}^{1/4}} &= \frac{dN_{ch,raw,2004,new}^{1/4}}{dN_{ch,corrected,2010}^{1/4}} \frac{dN_{event,2010}}{dN_{ch,raw,2004,new}^{1/4}} \\
&= \frac{1}{4} N_{ch,raw,2004,new}^{-3/4} \frac{dN_{ch,raw,2004,new}}{dN_{ch,corrected,2010}^{1/4}} \frac{dN_{event,2010}}{dN_{ch,raw,2004,new}^{1/4}} \\
&= \frac{1}{4} N_{ch,raw,2004,new}^{-3/4} \frac{4\beta_{corr} N_{ch,corr,2010}^{3/4}}{\sqrt{1 + 4\alpha_{corr}\beta_{corr} N_{ch,corr,2010}}} \frac{dN_{event,2010}}{dN_{ch,raw,2004,new}^{1/4}},
\end{aligned} \tag{3.12}$$

and

$$\begin{aligned}
\frac{dN_{event,2004}}{dN_{ch,corr,2004}^{1/4}} &= \frac{dN_{ch,raw,2004}^{1/4}}{dN_{ch,corr,2004}^{1/4}} \frac{dN_{event,2004}}{dN_{ch,raw,2004}^{1/4}} \\
&= \frac{1}{4} N_{ch,raw,2004}^{-3/4} \frac{dN_{ch,raw,2004}}{dN_{ch,corr,2004}^{1/4}} \frac{dN_{event,2004}}{dN_{ch,raw,2004}^{1/4}} \\
&= \frac{1}{4} N_{ch,raw,2004}^{-3/4} \frac{4\beta_{corr} N_{ch,corr,2004}^{3/4}}{\sqrt{1 + 4\alpha_{corr}\beta_{corr} N_{ch,corr,2004}}} \frac{dN_{event,2004}}{dN_{ch,raw,2004}^{1/4}},
\end{aligned} \tag{3.13}$$

where the subscript ‘corr’ means corrected.

4. Next, adjust  $\alpha$  and  $\beta$  such that the upper half-max points for  $\frac{dN_{event,2004}}{dN_{ch,corr,2004}^{1/4}}$  and  $\frac{dN_{event,2010}}{dN_{ch,corr,2010}^{1/4}}$  match and, the slopes of  $\frac{dN_{event,2004}}{dN_{ch,corr,2004}^{1/4}}$  and  $\frac{dN_{event,2010}}{dN_{ch,corr,2010}^{1/4}}$  match near mid-centrality.
5. Finally, using the cuts in multiplicities and sub-multiplicity bins from M. Daugherty’s thesis [1] (also shown in Table 3.5) find the cuts for Run 2010 centrality using Equation 3.9 and round off to the nearest integer.

6. Apply the same procedure to the Run11 data.

Figures 3.6 and 3.7, show how the distributions were matched. In Table 3.4 the value of parameters  $\alpha_{corr}$  and  $\beta_{corr}$  for both Run10 and 11 are listed. In Table 3.5 all the multiplicity and sub-multiplicity cuts for all centralities for Run4, 10 and 11 are listed.

Run	$\alpha_{corr}$	$\beta_{corr}$
2010	0.000015	0.91
2011	0.000009	0.98

**Table 3.4** Efficiency correction parameters,  $\alpha_{corr}$  and  $\beta_{corr}$  in Expressions 3.12 and 3.13.

Mult Number	Cent Number	Raw Cent (%)	Corrected Cent (%)	Mult (Run 2004)	Mult (Run 2010)	Mult (Run 2011)
21	10	0-5	0-5	>1002	>900	>973
20				952-1002	855-900	925-973
19				902-952	811-855	877-925
18				852-902	767-811	829-877
17	9	5-10	5-9	796-852	717-767	775-829
16				739-796	666-717	720-775
15	8	10-20	9-18	676-739	610-666	659-720
14				614-676	554-610	598-659
13				551-614	498-554	537-598
12	7	20-30	18-28	501-551	453-498	489-537
11				451-501	408-453	440-489
10				401-451	363-408	392-440
9				341-401	309-363	333-392
8	6	30-40	28-38	281-341	255-309	275-333
7				234-281	212-255	229-275
6	5	40-50	38-46	187-234	170-212	183-229
5				152-187	138-170	149-183
4				117-152	106-138	115-149
3	3	60-70	55-64	68-117	62-106	67-115
2	2	70-80	64-74	35-68	32-62	34-67
1	1	80-90	74-84	15-35	14-32	15-34
0	0	90-100	84-93	2-15	2-14	2-15

**Table 3.5** Mapping of Mult(multiplicity) classes to Cent(centrality) classes for run 2004, 2010 and 2011. There are 22 multiplicity classes and 11 centrality classes. For example, for Run 2011, multiplicity 3 has  $67 \leq N_{ch} < 115$ . Different multiplicity sub-classes having  $\Delta N_{ch} \sim 50$  are combined make a centrality class e.g. multiplicity classes 18, 19, 20, and 21 are combined together to make a centrality class 10.

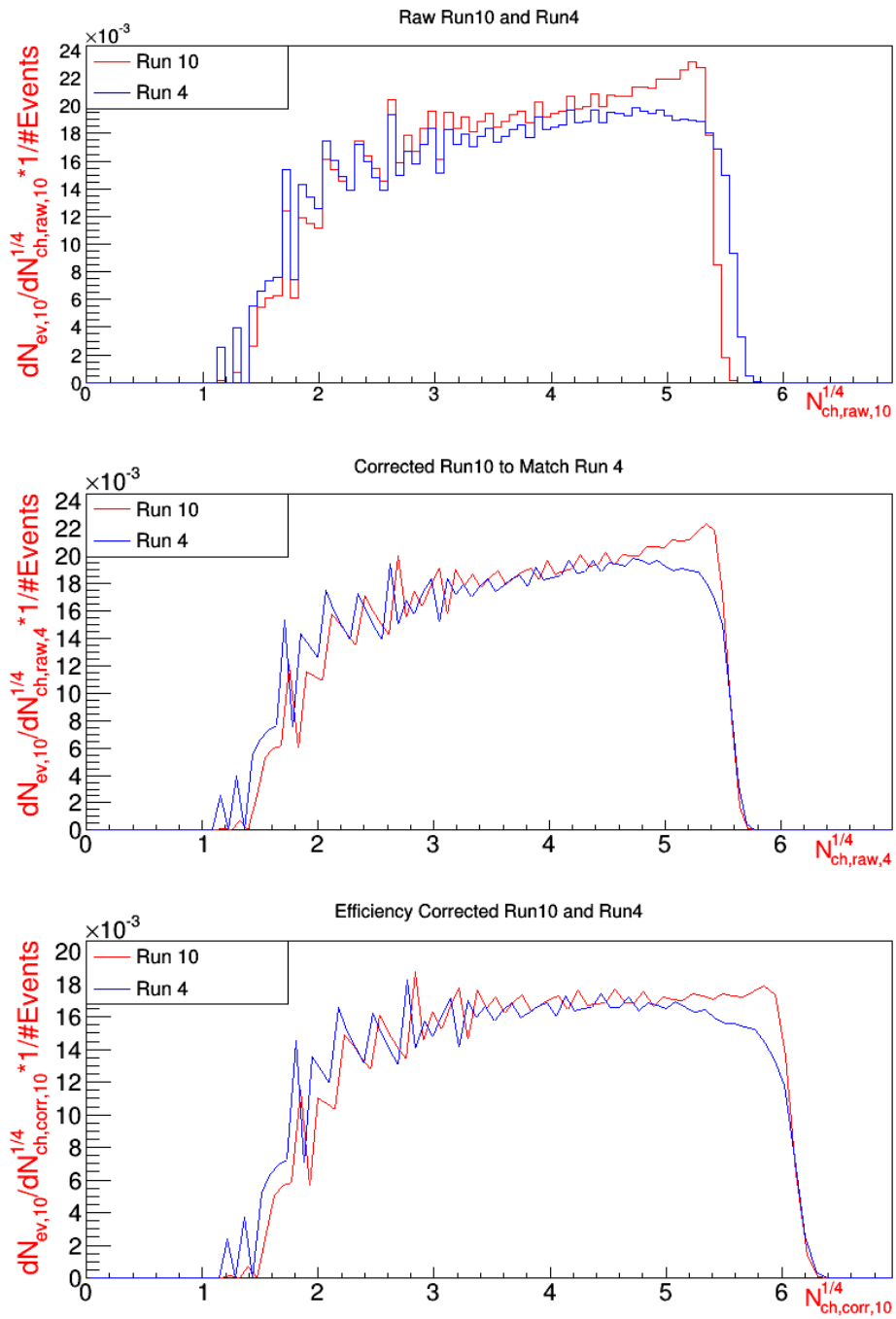


Figure 3.6 Multiplicity distributions of Run4, 10 and 11 data.

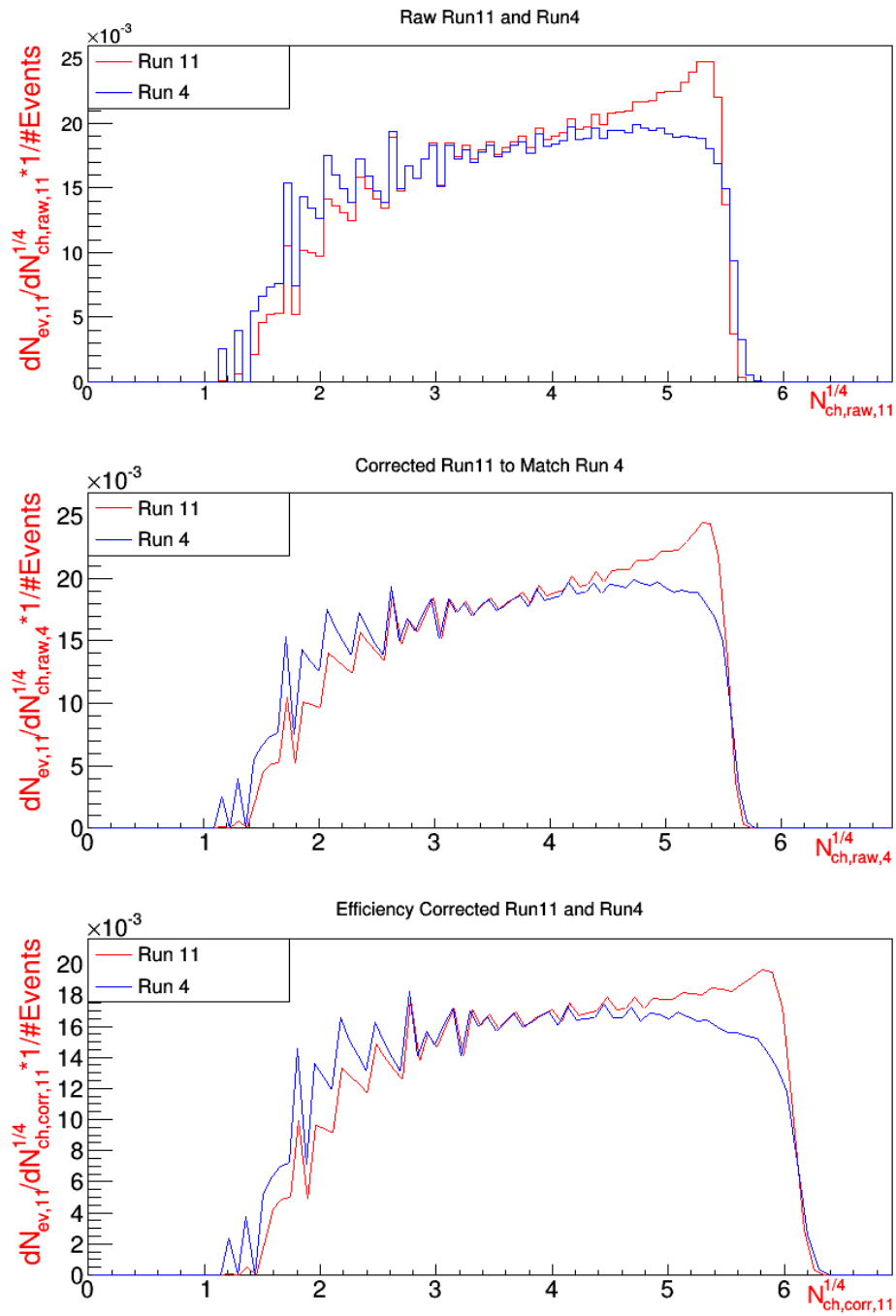


Figure 3.7 Multiplicity distributions of Run4, 10 and 11 data.

### 3.6 Particle Identification

The main objective of this thesis is to measure the angular correlations for pairs of identified particles. Therefore, particle identification was one of the important steps in this analysis. The charge particle tracks were identified as  $\pi^-$ ,  $\pi^+$ ,  $K^-$ ,  $K^+$ ,  $\bar{p}$  and  $p$  in the transverse momentum range of  $0.15 < p_T < 3.2$  GeV/c. Particle identification is achieved using a 2-dimensional distribution of measures obtained from both TOF and TPC. The details of particle identification are given in Chapter 5.

### 3.7 Momentum Ranges

The angular correlations in different ranges of momentum are significantly different. Therefore, ranges of momentum are constructed and the correlations of identified particles in each range of momentum was measured. The momentum distribution of particles ( $\frac{dN_{ch}}{dp_T}$ ) is such that the distribution peaks around 1 GeV/c and falls off quickly with an exponentially decreasing tail. A construction of momentum ranges of uniform width was not optimum in terms of statistics. Therefore, we transform the transverse momentum ( $p_T$ ) to a quantity called transverse rapidity ( $y_T$ ) which is a logarithmic measure of  $p_T$ .  $y_T$  is an optimum coordinate for studying fragmentation distributions transverse to the beam direction as in jet analysis [52]. It also gives a better visual access to the correlation structure at both low and high momentum. For a hadron rest mass  $m_0$ ,  $y_T$  is defined as in Equation 3.14

$$\begin{aligned}
y_T &= \frac{1}{2} \ln \left[ \frac{E + |p_T|}{E - |p_T|} \right] \\
y_T &\xrightarrow{\eta=0} \ln \left[ \frac{p_T + m_T}{m_0} \right], \quad m_T = \sqrt{m_0^2 + p_T^2}
\end{aligned}
\tag{3.14}$$

$y_T$  is a mass dependent measure. Therefore, different particles have different ranges of  $y_T$ . Table 3.6 summarizes the lower and upper values of  $y_T$  for corresponding  $p_T$  values.

Hadrons	Lower $p_T(GeV/c)$	Lower $y_T$	Upper $p_T(GeV/c)$	Upper $y_T$
$\pi^+, \pi^-$	0.15	0.93	3.15	3.81
$K^+, K^-$	0.15	0.29	3.15	2.55
$p, \bar{p}$	0.15	0.16	3.15	1.92

**Table 3.6** Lower and upper values of  $p_T$  and  $y_T$  for different particle type. Because of the mass dependance of  $y_T$ , the  $y_T$  ranges vary.

To make an extensive survey of the momentum dependence of angular correlations of identified particles, the momentum space for each identified particle was divided into sub-spaces called “*cut bins*” as shown in Table 3.7. The size of the cut bin was chosen such that there were enough particle-pair statistics in each cut bin and that the correlations in each cut bin could be compared with previous studies for unidentified particles [37]. Because of different lower and upper bounds of  $y_T$  for different particles, a slightly different sub-binning for different particles was selected.

Then, for each particle-pair, a unique *cut bin* was chosen according to the values of  $y_T$  in the ordered pair  $(y_{T1}, y_{T2})$ . The pair correlation in each cut

Hadrons	Bin 0	Bin 1	Bin 2	Bin 3	Bin 4
$\pi^+, \pi^-$	1.0-1.5	1.5-2.0	2.0-2.5	2.5-3.0	3.0-3.8
$K^+, K^-$	0.0-1.0	1.0-1.5	1.5-2.0	2.0-2.5	
$p, \bar{p}$	0.0-1.0	1.0-1.5	1.5-2.0		

**Table 3.7** Ranges of  $y_T$  sub-bins for different particle types. There are 5 sub-bins in  $\pi^+$  and  $\pi^-$ , 4 sub-bins in  $K^+$  and  $K^-$  and 3 sub-bins in  $p$  and  $\bar{p}$ .

$\pi\pi$

(3.0, 3.8)	20	21	22	23	24
(2.5, 3.0)	15	16	17	18	19
(2.0, 2.5)	10	11	12	13	14
(1.5, 2.0)	5	6	7	8	9
(1.0, 1.5)	0	1	2	3	4
$\uparrow y_{T2} \quad y_{T1} \rightarrow$	(1.0, 1.5)	(1.5, 2.0)	(2.0, 2.5)	(2.5, 3.0)	(3.0, 3.8)

**Table 3.8** Choice of cut bin IDs for  $(y_{T1}, y_{T2})$  pairs. There are 25 unique IDs for a charge combination (e.g  $++$ ,  $+-$ ,  $-+$  or  $--$ ) of  $\pi\pi$  pairs.

bin were constructed. For 3 identified particle types ( $\pi$ ,  $K$ , and  $p$ ), 4 kinds of charged-particle pairs ( $++$ ,  $+-$ ,  $-+$  and  $--$ ) were constructed for each pair of particle types. For example, for a  $\pi K$  particle pair, 4 pairs of  $\pi^+ K^+$ ,  $\pi^+ K^-$ ,  $\pi^- K^+$  and  $\pi^- K^-$  were constructed. All together 24 different correlations were measured in each cut bin for each particle pair in each centrality. The cut bin IDs for different particle pairs is shown in Table 3.8-3.13.

$\pi K$ 

(2.0, 2.5)	15	16	17	18	19
(1.5, 2.0)	10	11	12	13	14
(1.0, 1.5)	5	6	7	8	9
(0.0, 1.0)	0	1	2	3	4
$\uparrow y_{T2} \quad y_{T1} \rightarrow$	(1.0, 1.5)	(1.5, 2.0)	(2.0, 2.5)	(2.5, 3.0)	(3.0, 3.8)

**Table 3.9** Choice of cut bin IDs for  $(y_{T1}, y_{T2})$  pairs. There are 20 unique IDs for a charge combination (e.g ++, +-, -+ or --) of  $\pi K$  pairs.

 $\pi p$ 

(1.5, 2.0)	10	11	12	13	14
(1.0, 1.5)	5	6	7	8	9
(0.0, 1.0)	0	1	2	3	4
$\uparrow y_{T2} \quad y_{T1} \rightarrow$	(1.0, 1.5)	(1.5, 2.0)	(2.0, 2.5)	(2.5, 3.0)	(3.0, 3.8)

**Table 3.10** Choice of cut bin IDs for  $(y_{T1}, y_{T2})$  pairs. There are 15 unique IDs for a charge combination (e.g ++, +-, -+ or --) of  $\pi p$  pairs.

 $KK$ 

(2.0, 2.5)	12	13	14	15
(1.5, 2.0)	8	9	10	11
(1.0, 1.5)	4	5	6	7
(0.0, 1.0)	0	1	2	3
$\uparrow y_{T2} \quad y_{T1} \rightarrow$	(0.0, 1.0)	(1.0, 1.5)	(1.5, 2.0)	(2.0, 2.5)

**Table 3.11** Choice of cut bin IDs for  $(y_{T1}, y_{T2})$  pairs. There are 16 unique IDs for a charge combination (e.g ++, +-, -+ or --) of  $KK$  pairs.

$Kp$

(1.5, 2.0)	8	9	10	11
(1.0, 1.5)	4	5	6	7
(0.0, 1.0)	0	1	2	3
$\uparrow y_{T2} \quad y_{T1} \rightarrow$	(0.0, 1.0)	(1.0, 1.5)	(1.5, 2.0)	(2.0, 2.5)

**Table 3.12** Choice of cut bin IDs for  $(y_{T1}, y_{T2})$  pairs. There are 12 unique IDs for a charge combination (e.g ++, +-, -+ or --) of  $Kp$  pairs.

$pp$

(1.5, 2.0)	6	7	8
(1.0, 1.5)	3	4	5
(0.0, 1.0)	0	1	2
$\uparrow y_{T2} \quad y_{T1} \rightarrow$	(0.0, 1.0)	(1.0, 1.5)	(1.5, 2.0)

**Table 3.13** Choice of cut bin IDs for  $(y_{T1}, y_{T2})$  pairs. There are 9 unique IDs for a charge combination (e.g ++, +-, -+ or --) of  $pp$  pairs.

### 3.8 Two-Particle Correlation

In general, the number of particles produced in heavy-ion collisions is large enough that physics signals of interest are overwhelmed by the large combinatorial background. It is challenging to extract the signals, if any, from such a vast background of particles. However, using correlations, the physics signals can be amplified to see otherwise obscured structures produced in the aftermath of a collision. The two-particle correlation measure is established using a standard definition; i.e., Pearson's normalized covariance [53]. The variables in the correlation are derived from the kinematic variables such as azimuthal angle ( $\phi$ ), axial angle ( $\theta$ ), transverse momentum ( $p_T$ ) etc. The pseudo-rapidity (i.e.,  $\eta = -\ln[\tan(\theta/2)]$ ) and transverse rapidity (i.e.,  $y_T$ ) are also commonly used variables. As a first step, we construct histograms of a variable in each of  $N$  events. In the histogram, contents of any two bins  $a$  and  $b$  are the random variables to measure correlations. Thus, the correlation, in this thesis, refers to an auto-correlation between the contents of two arbitrary bins  $a$  and  $b$  of the histogram averaged over all the  $N$  collision events. The correlation determines if it is more or less likely, relative to random chance, to find a particle in bin  $b$ , given a particle in bin  $a$ . This correlation is studied in detail in M. Daugherty's thesis [1][37][5].

The correlations between the contents of two arbitrary bins  $a$  and  $b$  are given using the definition of Pearson's correlation coefficient.

$$\begin{aligned}
Corr(a, b) &= \frac{Cov(a, b)}{\sqrt{Var(a).Var(b)}} \\
&= \frac{\frac{1}{N} \sum_{i=1}^N (n_i - \bar{n})_a (n_i - \bar{n})_b}{\sqrt{\frac{1}{N} \sum_{i=1}^N (n_i - \bar{n})_a^2 \frac{1}{N} \sum_{i=1}^N (n_i - \bar{n})_b^2}} \\
&= \frac{\overline{(n - \bar{n})_a (n - \bar{n})_b}}{\sqrt{\frac{1}{N} \sum_{i=1}^N (n_i - \bar{n})_a^2 \frac{1}{N} \sum_{i=1}^N (n_i - \bar{n})_b^2}},
\end{aligned} \tag{3.15}$$

where  $N$  represents the number of events and  $\bar{n}$  represents the average bin content over the events for the given bin.

In the context of heavy-ion collision, the contents of a bin are approximately distributed following a Poisson distribution, where mean and variance are equal [i.e.,  $\frac{1}{N} \sum_{i=1}^N (n_i - \bar{n})_a^2 = \bar{n}_a$ ] [54]. Using Poisson's approximation, equation (3.15) can be simplified to:

$$\begin{aligned}
Corr(a, b) &= \frac{\overline{n_a n_b} - \bar{n}_a \bar{n}_b}{\sqrt{\overline{n_a n_b}}} \\
&= \sqrt{\overline{n_a n_b}} \frac{\overline{n_a n_b} - \bar{n}_a \bar{n}_b}{\bar{n}_a \bar{n}_b} \\
&= \sqrt{\overline{n_a n_b}} \frac{\overline{n_a n_b / \epsilon} - \bar{n}_a \bar{n}_b / \epsilon}{\bar{n}_a \bar{n}_b / \epsilon},
\end{aligned} \tag{3.16}$$

where  $\epsilon$  is the size of the bin containing the pair of particles, where  $\overline{n_a n_b}$  is a pair density. Introduction of the  $\epsilon$  removes the dependencies on bin width of a histogram.

Our objective is to extract all correlation signals coming from the particle tracks from an event. We define the sibling density,  $\rho_{sib} = \overline{n_a n_b} / \epsilon$  such that only the tracks from the same event are paired. The density  $\rho_{sib}$  contains a large background coming from the uncorrelated pairs. Similarly, we define the reference density,  $\rho_{ref} = \bar{n}_a \bar{n}_b / \epsilon$  such that the tracks from different events are paired. The track pairs from different events are selected similar to sibling pairs but they are not correlated. The mixed-event reference uses only those track pairs from two events which are both within one of the multiplicity sub-classes in Table 3.5 and if the primary vertices are within 25 cm along the beam axis. Each event is mixed with two other events with comparable multiplicities. Besides the multiplicities ranges given in Table 3.5, each sub-multiplicity range in three most centrality bins (9-18%, 5-9% and 0-5%) were further divided into 10 sub-ranges so that  $\Delta N_{ch} \sim 50$ . This is the same event mixing criteria used and tested in References [1][37][5]. Thus, the difference in densities,  $\Delta\rho = \rho_{sib} - \rho_{ref}$  is expected to be a pure correlation signal. However, experimental artifacts such as detector acceptance and inefficiencies contaminate the measurement, so both the sibling and reference distribution contain some detector related structure. Using the ratio  $\rho_{sib}/\rho_{ref}$ , such structure coming from detector artifacts can be removed. Using Equation (3.16), define the quantity

$$\begin{aligned}
\frac{\Delta\rho}{\sqrt{\rho_{ref}}} &= \frac{Corr(a, b)}{\sqrt{\epsilon}} = \sqrt{\bar{n}_a\bar{n}_b/\epsilon} \frac{\overline{n_a n_b/\epsilon} - \bar{n}_a\bar{n}_b/\epsilon}{\bar{n}_a\bar{n}_b/\epsilon} \\
&= \sqrt{\rho_{ref}} \left( \frac{\rho_{sib} - \rho_{ref}}{\rho_{ref}} \right) \\
&= \sqrt{\rho_{ref}} (r - 1),
\end{aligned} \tag{3.17}$$

where  $r = \frac{\rho_{sib}}{\rho_{ref}}$ . The quantity  $\frac{\Delta\rho}{\sqrt{\rho_{ref}}}$  is interpreted as the number of correlated pairs per final-state particle.

Using the efficiency corrected pre-factor  $\sqrt{\rho'_{ref}}$  the final expression of correlation is written as:

$$\begin{aligned}
Corr(a, b) &= \sqrt{\rho'_{ref}}(r - 1) \\
\implies \frac{\Delta\rho}{\sqrt{\rho_{ref}}} &= \sqrt{\rho'_{ref}}(r - 1),
\end{aligned} \tag{3.18}$$

where the  $(')$  in  $\sqrt{\rho'_{ref}}$  indicates that the density is efficiency corrected. It is dependent on the type of charges taking part in the correlation measure and is discussed in Section 3.8.1.

Angular correlations on difference variables such as  $\eta_\Delta = \eta_1 - \eta_2$  and  $\phi_\Delta = \phi_1 - \phi_2$  are typical in Au-Au collisions at RHIC [5]. Equation 3.18 can be directly applied to construct 1D azimuthal correlations on  $(\phi_\Delta)$  as well. Also, the formulation of auto-correlations can be extended to construct 2D joint auto-correlations on  $(\eta_\Delta, \phi_\Delta)$ , as reported here, as well as on  $(y_{T1}, y_{T2})$  [54].

### 3.8.1 Charge Dependence of Correlations

Because correlations are charge dependent, it is interesting to extend the above formulation for charged pairs of different signs. There are four different possibilities for constructing charged pairs:  $++$ ,  $+-$ ,  $-+$  and  $--$ . Correlations can be defined for each of the ordered pairs: an example for a  $+-$  correlation is given in Equation 3.19.

$$\left(\frac{\Delta\rho}{\sqrt{\rho_{ref}}}\right)^{+-} = \sqrt{\rho'_{ref}} \left(\frac{\rho_{sib}^{+-}}{\rho_{ref}^{+-}} - 1\right) = \sqrt{\rho'_{ref}} \left(\frac{\Delta\rho^{+-}}{\rho_{ref}^{+-}}\right), \quad (3.19)$$

Although the pairs  $+-$  and  $-+$  are identical for unidentified particles, they are different for distinguishable identified particles (e.g.  $\pi^-K^+$  is different from  $\pi^+K^-$ ). However, assuming a small difference in  $+-$  and  $-+$  correlations, the correlation can be divided into four categories: Like-Sign (LS), Unlike-Sign (US), Charge-Dependent (CD) and Charge-Independent (CI). Each of the correlations is defined as:

- $\left(\frac{\Delta\rho}{\sqrt{\rho_{ref}}}\right)^{LS} = \sqrt{\rho'_{ref}} \left(\frac{\rho_{sib}^{LS}}{\rho_{ref}^{LS}} - 1\right) = \sqrt{\rho'_{ref}} \left(\frac{\rho_{sib}^{++} + \rho_{sib}^{--}}{\rho_{ref}^{++} + \rho_{ref}^{--}} - 1\right)$
- $\left(\frac{\Delta\rho}{\sqrt{\rho_{ref}}}\right)^{US} = \sqrt{\rho'_{ref}} \left(\frac{\rho_{sib}^{US}}{\rho_{ref}^{US}} - 1\right) = \sqrt{\rho'_{ref}} \left(\frac{\rho_{sib}^{+-} + \rho_{sib}^{-+}}{\rho_{ref}^{+-} + \rho_{ref}^{-+}} - 1\right)$
- $\left(\frac{\Delta\rho}{\sqrt{\rho_{ref}}}\right)^{CD} = \sqrt{\rho'_{ref}} \left(\frac{\rho_{sib}^{CD}}{\rho_{ref}^{CD}} - 1\right) = \sqrt{\rho'_{ref}} \left(\frac{\rho_{sib}^{LS} - \rho_{sib}^{US}}{\rho_{ref}^{LS} + \rho_{ref}^{US}} - 1\right)$
- $\left(\frac{\Delta\rho}{\sqrt{\rho_{ref}}}\right)^{CI} = \sqrt{\rho'_{ref}} \left(\frac{\rho_{sib}^{CI}}{\rho_{ref}^{CI}} - 1\right) = \sqrt{\rho'_{ref}} \left(\frac{\rho_{sib}^{LS} + \rho_{sib}^{US}}{\rho_{ref}^{LS} + \rho_{ref}^{US}} - 1\right)$

Using approximations  $\rho_{ref}^{++} \approx \rho_{ref}^{--}$  and  $\rho_{ref}^{+-} \approx \rho_{ref}^{-+}$  each of the correlations can be written as follows.

- $\left(\frac{\Delta\rho}{\sqrt{\rho_{ref}}}\right)^{LS} = \sqrt{\rho'_{ref}} \frac{1}{2} \left(\frac{\Delta\rho^{++}}{\rho_{ref}^{++}} + \frac{\Delta\rho^{--}}{\rho_{ref}^{--}}\right)$
- $\left(\frac{\Delta\rho}{\sqrt{\rho_{ref}}}\right)^{US} = \sqrt{\rho'_{ref}} \frac{1}{2} \left(\frac{\Delta\rho^{+-}}{\rho_{ref}^{+-}} + \frac{\Delta\rho^{-+}}{\rho_{ref}^{-+}}\right)$
- $\left(\frac{\Delta\rho}{\sqrt{\rho_{ref}}}\right)^{CD} = \sqrt{\rho'_{ref}} \frac{1}{4} \left(\frac{\Delta\rho^{++}}{\rho_{ref}^{++}} + \frac{\Delta\rho^{--}}{\rho_{ref}^{--}} - 2\frac{\Delta\rho^{+-}}{\rho_{ref}^{+-}}\right)$
- $\left(\frac{\Delta\rho}{\sqrt{\rho_{ref}}}\right)^{CI} = \sqrt{\rho'_{ref}} \frac{1}{4} \left(\frac{\Delta\rho^{++}}{\rho_{ref}^{++}} + \frac{\Delta\rho^{--}}{\rho_{ref}^{--}} + 2\frac{\Delta\rho^{+-}}{\rho_{ref}^{+-}}\right)$

The pre-factor for angular correlation in  $(\eta_\Delta, \phi_\Delta)$  can be approximated [1].

$$\sqrt{\rho'_{ref}} = \lim_{\eta_1, \eta_2 \rightarrow 0} \frac{1}{2\pi} \sqrt{\frac{dN_{ch,1}}{d\eta_1} \frac{dN_{ch,2}}{d\eta_2}}, \quad (3.20)$$

where  $dN_{ch,1}$  and  $dN_{ch,2}$  represents selected charge types in the correlations.

For CI correlations, the pre-factor is  $\sqrt{\rho'_{ref}}^{CI} = \left[\frac{1}{2\pi} \frac{dN_{ch}}{d\eta}\right]$ . One of the common approaches of writing the other pre-factors is to write them in terms of the CI correlation pre-factor (e.g.,  $\sqrt{\rho'_{ref}}^{LS} = \sqrt{\rho'_{ref}}^{US} = \sqrt{\frac{1}{2}\rho'_{ref}}^{CI}$  and  $\sqrt{\rho'_{ref}}^{CD} = \sqrt{\rho'_{ref}}^{CI}$ ) [37][1].

### 3.9 Normalization

The correlation space contains different particle correlations in different defined momentum ranges. We want to find the relative magnitudes of each correlation throughout the entire space. The relative magnitude is obtained by multiplying the correlations by a weighting factor. The weighting factor for each correlation is defined such that the correlations sum up to

the non-identified charge-independent (CI) angular correlations in integrated momentum space for each centrality.

$$\left[ \frac{\Delta\rho}{\sqrt{\rho_{ref}}} \right]_{CI, p_T > 0.15 GeV} = \sum_i \sum_j \omega_{ij} \left[ \frac{\Delta\rho}{\sqrt{\rho_{ref}}} \right]_{ij}, \quad (3.21)$$

where  $i$  indicates the PID combinations such as  $\pi^+\pi^+$ ,  $\pi^+\pi^-$ ,  $\pi^+K^+$  etc. and  $j$  indicates the transverse rapidity ( $y_T$ ) ranges.

The required relationship and the weighting factors can be derived as follows. Using the definition of pair normalized correlations, the CI correlation for integrated  $p_T$  is written as:

$$\left[ \frac{\Delta\rho}{\rho_{ref}} \right]_{CI, p_T > 0.15 GeV} = \frac{\frac{N_{ref}}{N_{sib}} n_{sib} - n_{ref}}{n_{ref}}, \quad (3.22)$$

where  $N$  indicates the total number of respective pairs in the angular ( $\eta_\Delta, \phi_\Delta$ ) space and  $n$  indicates the number of pairs in each bin of the angular space. The total number of non-identified sibling or reference pairs is the sum of the pairs in each identified pair ( $\pi^+\pi^+$ ,  $\pi^+\pi^-$ ,  $\pi^+K^+$  etc.).

$$\begin{aligned} \left[ \frac{\Delta\rho}{\rho_{ref}} \right]_{CI, p_T > 0.15 GeV} &= \frac{\frac{N_{ref}}{N_{sib}} \sum_\alpha n_{sib, \alpha} - \sum_\alpha n_{ref, \alpha}}{n_{ref}} \\ &= \sum_\alpha \frac{n_{ref, \alpha}}{n_{ref}} \left[ \frac{\frac{N_{ref, \alpha}}{N_{sib, \alpha}} n_{sib, \alpha} - n_{ref, \alpha} + \left( \frac{N_{ref}}{N_{sib}} - \frac{N_{ref, \alpha}}{N_{sib, \alpha}} \right) n_{sib, \alpha}}{n_{ref, \alpha}} \right], \end{aligned} \quad (3.23)$$

where  $\alpha$  runs over all PID pairs in all momentum sub-spaces. The factor in parenthesis is negligibly small (see Appendix 8) contributing a small constant offset to  $\left[ \frac{\Delta\rho}{\rho_{ref}} \right]_\alpha$ .

Therefore, the CI correlations with appropriate pre-factor can be approximately written as:

$$\left[ \frac{\Delta\rho}{\sqrt{\rho_{ref}}} \right]_{CI, p_T > 0.15 \text{ GeV}} \approx \left[ \frac{1}{2\pi} \frac{dN_{ch}}{d\eta} \right] \sum_{\alpha} \frac{n_{ref,\alpha}}{n_{ref}} \left[ \frac{\frac{N_{ref,\alpha}}{N_{sib,\alpha}} n_{sib,\alpha} - n_{ref,\alpha}}{n_{ref,\alpha}} \right], \quad (3.24)$$

where the pre-factor,  $\left[ \frac{1}{2\pi} \frac{dN_{ch}}{d\eta} \right]$ , has been reported in Table III in Reference [12]. Similarly, the second term,  $\frac{n_{ref,\alpha}}{n_{ref}}$ , is estimated using efficiency corrected spectra data and the third term,  $\left[ \frac{\frac{N_{ref,\alpha}}{N_{sib,\alpha}} n_{sib,\alpha} - n_{ref,\alpha}}{n_{ref,\alpha}} \right]$ , is the pair-normalized correlations for each PID pair in each  $y_T$  range.

The efficiency corrected identified particle spectra for Au+Au  $\sqrt{s_{NN}} = 200$  GeV are presented in STAR and PHENIX spectra papers [49] and [11], respectively. The factor  $\frac{n_{ref,\alpha}}{n_{ref}}$  in Equation 3.24 is related to the efficiency corrected spectra as in Equation 3.25,

$$\begin{aligned} \frac{n_{ref,\alpha}}{n_{ref}} &= \frac{\frac{dN^i}{d\eta} \frac{dN^j}{d\eta}}{\left[ \frac{dN_{ch}}{d\eta} \right]^2} \\ &= \frac{\int_{y_T^k} 2\pi p_T dp_T \frac{dN^i}{2\pi p_T dp_T d\eta} \int_{y_T^l} 2\pi p_T dp_T \frac{dN^j}{2\pi p_T dp_T d\eta}}{\left[ \frac{dN_{ch}}{d\eta} \right]^2}, \end{aligned} \quad (3.25)$$

where  $i$  and  $j$  are particle species in different  $y_T$  ranges indexed by  $k$  and  $l$ . The denominator,  $\left[ \frac{dN_{ch}}{d\eta} \right]$ , in Equation 3.25 is obtained from unidentified particle spectra in the Reference [12] while the numerator can be calculated using model representation of the efficiency corrected particle spectra.

The STAR spectra paper [49] presents the yield of identified particles per unit rapidity for different centralities. However, the provided momentum

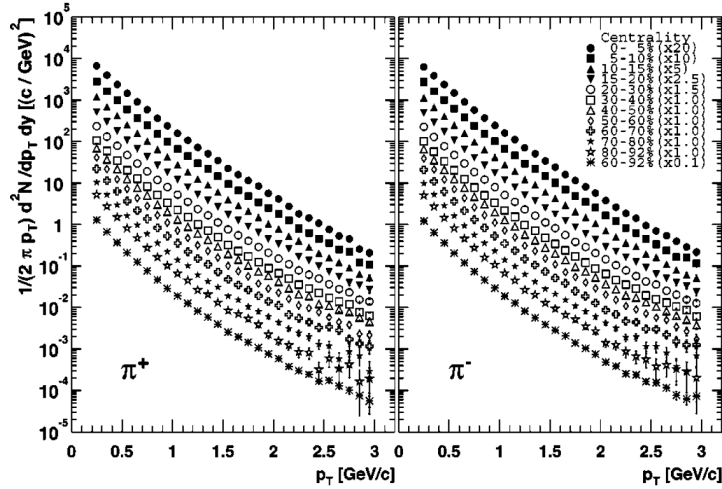


**Figure 3.8** Centrality dependence of the  $p_T$  distribution for  $\pi^+$ (left) and  $\pi^-$  (right) in Au+Au collisions at  $\sqrt{s_{NN}}=200$  GeV. The different symbols are chosen for different centrality bins. The error bars are statistical only. For visual clarity, data points are scaled vertically as quoted in the figure [11].

ranges for identified particle yield are narrow ( $p_T < 1$  GeV/c), while the present analysis considers wider ranges of momenta ( $0.15 < p_T < 3.2$  GeV/c). Therefore, we use the PHENIX spectra paper [11], which provides the yield of identified particles for wider ranges of momenta. The baseline of comparison of the present analysis is in Reference [12], which estimates the yield of all particles (unidentified particles) based on STAR spectra. So, further scaling of the yield is implemented before making the final comparison. The scaling process is discussed in the following steps.

The STAR and PHENIX spectra papers [49] [11] provide identified particle yields per unit rapidity ( $\frac{dN^i}{2\pi p_T dp_T dy}$ ) for each PID (represented by index  $i$ ). The Figure 3.8 shows the  $p_T$  distribution for  $\pi^+$  and  $\pi^-$  as an example. The

Particle type	$\pi^-$	$\pi^+$	$K^-$	$K^+$	$\bar{p}$	$p$
Scale Factor ( $S$ )	1.09	1.05	1.16	1.12	2.15	1.95

**Table 3.14** STAR to PHENIX scale factors for  $\pi^\pm$ ,  $K^\pm$ ,  $\bar{p}$  and  $p$ .

PHENIX spectra for each particle type is normalized to the STAR spectrum and a scale factor ( $S$ ) is obtained where

$$S \equiv \frac{[dN/dy]_{STAR}}{[dN/dy]_{PHENIX}}. \quad (3.26)$$

For each particle spectrum in both STAR and PHENIX,  $\frac{dN}{dy} / \frac{N_{part}}{2}$ <sup>3</sup> versus  $\left(\frac{N_{part}}{2}\right)^{1/3}$  is approximately described with a linear fitting function and integrated to calculate the area between minimum and maximum values of  $\left(\frac{N_{part}}{2}\right)^{1/3}$ . Table 3.14 gives the ratio between those areas for each particle species. Finally, each particle spectra from PHENIX is normalized to the STAR spectra using those scale factors.

The next step is to calculate the charged particle multiplicity per unit pseudorapidity ( $\eta$ ) from the scaled data where

$$\begin{aligned} \frac{dN^i}{2\pi p_T dp_T d\eta} &= \frac{dy}{d\eta} \frac{dN^i}{2\pi p_T dp_T dy} \\ &= \frac{p_T \cosh \eta}{\sqrt{p_T^2 \sinh^2 \eta + m_T^2}} \frac{dN^i}{2\pi p_T dp_T dy}, \end{aligned} \quad (3.27)$$

---

<sup>3</sup> $N_{part}$  is the number of participant nucleons per collision. For the most peripheral collision its value is 2 where as for the most central collisions its value is about 350 (total number of nucleons in two gold nuclei is  $2 \times 197 = 394$ ).

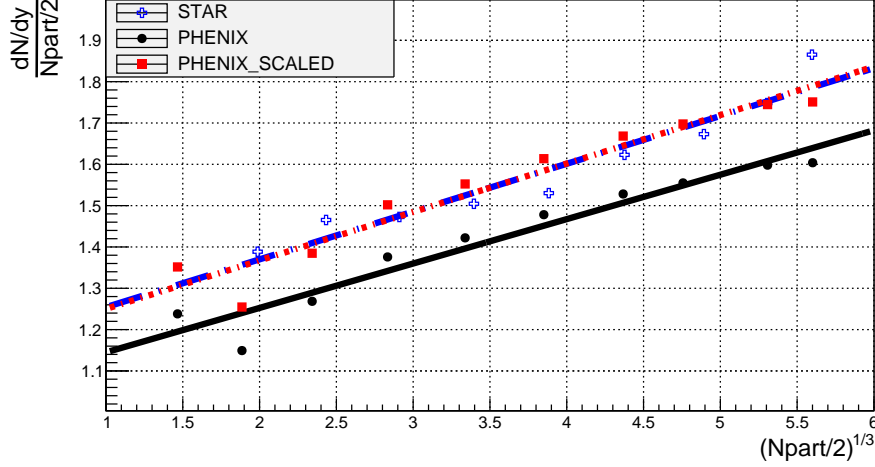


**Figure 3.9** Particle yield for  $\pi^-$  as a function of  $(N_{part})^{1/3}$ . STAR and PHENIX spectra are in dashed blue and bold black lines respectively. The dotted red line is obtained by scaling the PHENIX spectrum to STAR.

where  $i$  indicates the particle species,  $\pi^\pm$ ,  $K^\pm$ ,  $\bar{p}$  and  $p$ . As  $\eta$  approaches 0, Equation 3.27 reduces to:

$$\begin{aligned} \frac{dN^i}{2\pi p_T dp_T d\eta} &= \frac{p_T}{m_T} \frac{dN^i}{2\pi p_T dp_T dy} \\ \implies \frac{dN^i}{d\eta} &= S \int_0^\infty 2\pi p_T dp_T \frac{p_T}{m_T} \frac{dN^i}{2\pi p_T dp_T dy}, \end{aligned} \quad (3.28)$$

where  $S$  is the scale factor listed in Table 3.14. The spectrum is fitted with an appropriate fitting function as described in [12] and the integral in Equation 3.28 is computed to obtain  $\frac{dN^i}{d\eta}$  for each PID. Finally, the contributions from each PID are added together to get  $\frac{dN'}{d\eta}$  where  $'$  indicates that the yield per  $\eta$  doesn't include unidentified particles. The  $\frac{dN'}{d\eta}$  is then compared with similar quantity in Reference [12] that includes all particles. The particle

spectrum,  $\frac{dN'}{d\eta}$ , is compared with the spectrum for all charged particles (see Figure 3.10), and another scale factor  $S' = 1.014$  is obtained using:

$$S' \equiv \frac{[dN/d\eta]_{All\ Particles}}{[dN/d\eta]_{Identified\ Particles}}, \quad (3.29)$$

where the numerator is obtained from [12] and the denominator is obtained from scaled PHENIX spectra.

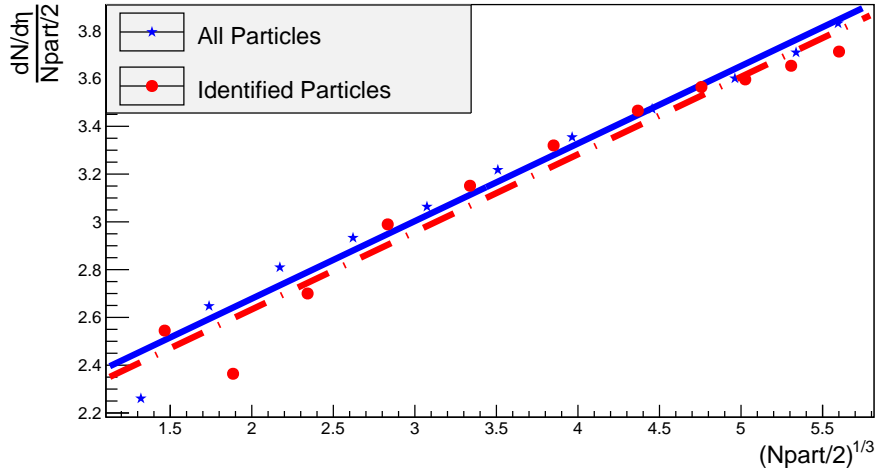


**Figure 3.10** Particle yield per unit  $\eta$  as a function of  $(N_{part})^{1/3}$ . The dashed line represents the sum of particle yields for all PID (obtained from the scaled PHENIX spectrum) while the solid line represents the all-particle yield (obtained from [12]).

With the scale factors  $S$  and  $S'$  defined in 3.26 and 3.29, respectively, the PHENIX identified particle spectrum in [11] can be compared with the all-particle spectrum in [12] where

$$\begin{aligned} \frac{dN^i}{2\pi p_T dp_T d\eta} &= SS' \frac{p_T}{m_T} \left[ \frac{dN^i}{2\pi p_T dp_T dy} \right] \\ \implies \frac{dN^i}{d\eta} &= \int_{y_T=a}^{y_T=b} 2\pi p_T dp_T \frac{dN^i}{2\pi p_T dp_T d\eta}, \end{aligned} \quad (3.30)$$

and  $i$  is the identified particle type, and  $a$  and  $b$  are ranges of  $y_T$  for each PID.

Using Equation 3.30, the yield of each particle species,  $\frac{dN^i}{d\eta}$ , in different ranges of momentum ( $y_T = a$  to  $b$ ) were calculated. To calculate the yield, the distribution,  $\frac{dN^i}{2\pi p_T dp_T d\eta}$ , is plotted as a function of  $p_T$ . The data are fitted with an appropriate fitting function ( e.g., an exponential function) and integrated numerically within the range of momentum. Finally, the yield spectrum for each PID is interpolated to obtain the yield in centralities presented in [12]. With Equation 3.30, the factor  $\frac{n_{ref,\alpha}}{n_{ref}}$  in Equation 3.25 can be computed.

In Tables 3.15-3.20, particle yields,  $\frac{dN}{d\eta}$ , of each particle pair species for different  $y_T$ -bins for different centralities are presented. Using the tables, a weight factor for any combination of particle species in any ranges of momenta within a centrality is constructed. For example, the product of pre-factor times weight factor for the  $\pi^+ K^+$  correlation in the most central collisions (centrality 10) and,  $1.0 \leq y_T^\pi < 1.5$  and  $2.0 \leq y_T^K < 2.5$  is  $[\frac{1}{2\pi}671] \frac{75.2578 \times 2.15172}{671 \times 671}$ .

$\pi^-$ 

$N_{part}$	$\frac{dN}{d\eta}_{total}$	$\frac{dN}{d\eta}_{y_T \in (1.0, 1.5)}$	$\frac{dN}{d\eta}_{y_T \in (1.5, 2.0)}$	$\frac{dN}{d\eta}_{y_T \in (2.0, 2.5)}$	$\frac{dN}{d\eta}_{y_T \in (2.5, 3.0)}$	$\frac{dN}{d\eta}_{y_T \in (3.0, 3.8)}$
4.6	5.2	0.827403	0.768999	0.492963	0.18949	0.0452515
10.5	13.9	1.92333	1.85306	1.24373	0.496861	0.117688
20.5	28.8	3.82544	3.8161	2.66855	1.10053	0.258969
36	52.8	6.84549	7.06098	5.12211	2.16929	0.507734
58.1	89	11.2561	11.9822	8.97757	3.88704	0.905819
86.4	139	17.0357	18.655	14.3645	6.33092	1.47024
124.6	209	25.0163	28.1666	22.2474	9.96176	2.30641
176.8	307	36.182	41.8975	33.9086	15.406	3.55706
244.4	440	50.9972	60.6802	50.2233	23.1152	5.3241
304.1	564	64.3558	78.042	65.5701	30.433	6.99867
350.3	671	74.8465	91.9083	77.9683	36.3794	8.35798

**Table 3.15** Centrality evolution of integrals in  $y_T$  bins for  $\pi^-$  $\pi^+$ 

$N_{part}$	$\frac{dN}{d\eta}_{total}$	$\frac{dN}{d\eta}_{y_T \in (1.0, 1.5)}$	$\frac{dN}{d\eta}_{y_T \in (1.5, 2.0)}$	$\frac{dN}{d\eta}_{y_T \in (2.0, 2.5)}$	$\frac{dN}{d\eta}_{y_T \in (2.5, 3.0)}$	$\frac{dN}{d\eta}_{y_T \in (3.0, 3.8)}$
4.6	5.2	0.840791	0.76772	0.488882	0.182038	0.0436037
10.5	13.9	1.95211	1.84525	1.22697	0.476668	0.113224
20.5	28.8	3.87801	3.79094	2.62075	1.05465	0.248831
36	52.8	6.93124	6.9988	5.0108	2.07701	0.487349
58.1	89	11.3838	11.8525	8.75329	3.71901	0.868707
86.4	139	17.2104	18.4202	13.9673	6.0538	1.40904
124.6	209	25.2451	27.7648	21.5785	9.52096	2.20908
176.8	307	36.4715	41.2308	32.8123	14.7176	3.40509
244.4	440	51.347	59.6203	48.4976	22.0736	5.09417
304.1	564	64.7447	76.5962	63.2296	29.0543	6.69435
350.3	671	75.2578	90.1422	75.1192	34.7258	7.99298

**Table 3.16** Centrality evolution of integrals in  $y_T$  bins for  $\pi^+$

$K^-$

$N_{part}$	$\frac{dN}{d\eta}_{total}$	$\frac{dN}{d\eta}_{y_T \in (0.0, 1.0)}$	$\frac{dN}{d\eta}_{y_T \in (1.0, 1.5)}$	$\frac{dN}{d\eta}_{y_T \in (1.5, 2.0)}$	$\frac{dN}{d\eta}_{y_T \in (2.0, 2.5)}$
4.6	5.2	0.133412	0.0907341	0.0349634	0.0137362
10.5	13.9	0.324568	0.23959	0.0998968	0.0329209
20.5	28.8	0.674324	0.533644	0.23578	0.0674513
36	52.8	1.2579	1.05661	0.487954	0.124214
58.1	89	2.15038	1.90017	0.90806	0.209868
86.4	139	3.36931	3.10368	1.52229	0.325499
124.6	209	5.11809	4.89585	2.45508	0.489666
176.8	307	7.65817	7.58855	3.88048	0.725753
244.4	440	11.1528	11.4083	5.93211	1.04753
304.1	564	14.3979	15.0389	7.90312	1.34412
350.3	671	16.9973	17.9915	9.5169	1.58053

**Table 3.17** Centrality evolution of integrals in  $y_T$  bins for  $K^-$

$K^+$

$N_{part}$	$\frac{dN}{d\eta}_{total}$	$\frac{dN}{d\eta}_{y_T \in (0.0, 1.0)}$	$\frac{dN}{d\eta}_{y_T \in (1.0, 1.5)}$	$\frac{dN}{d\eta}_{y_T \in (1.5, 2.0)}$	$\frac{dN}{d\eta}_{y_T \in (2.0, 2.5)}$
4.6	5.2	0.140855	0.0916056	0.0358883	0.0088953
10.5	13.9	0.345037	0.242952	0.102377	0.0246255
20.5	28.8	0.721344	0.542993	0.241372	0.056842
36	52.8	1.35327	1.07808	0.499133	0.115716
58.1	89	2.32517	1.94305	0.928317	0.212683
86.4	139	3.65902	3.1792	1.55557	0.353258
124.6	209	5.58087	5.02252	2.50786	0.565313
176.8	307	8.38356	7.79541	3.96266	0.887508
244.4	440	12.2539	11.733	6.05616	1.34901
304.1	564	15.8583	15.4786	8.06706	1.7908
350.3	671	18.7512	18.5264	9.71334	2.15172

**Table 3.18** Centrality evolution of integrals in  $y_T$  bins for  $K^+$

$p^-$ 

$N_{part}$	$\frac{dN}{d\eta}_{total}$	$\frac{dN}{d\eta}_{y_T \in (0.0, 1.0)}$	$\frac{dN}{d\eta}_{y_T \in (1.0, 1.5)}$	$\frac{dN}{d\eta}_{y_T \in (1.5, 2.0)}$
4.6	5.2	0.119428	0.0337872	0.00411507
10.5	13.9	0.275676	0.0984696	0.0137204
20.5	28.8	0.544448	0.235544	0.0355639
36	52.8	0.967393	0.492167	0.0783724
58.1	89	1.57968	0.922405	0.152453
86.4	139	2.37539	1.55438	0.263744
124.6	209	3.4653	2.51762	0.436303
176.8	307	4.97768	3.99407	0.704575
244.4	440	6.96766	6.12469	1.09631
304.1	564	8.7494	8.17542	1.47654
350.3	671	10.1417	9.85643	1.78984

**Table 3.19** Centrality evolution of integrals in  $y_T$  bins for  $\bar{p}$  $p^+$ 

$N_{part}$	$\frac{dN}{d\eta}_{total}$	$\frac{dN}{d\eta}_{y_T \in (0.0, 1.0)}$	$\frac{dN}{d\eta}_{y_T \in (1.0, 1.5)}$	$\frac{dN}{d\eta}_{y_T \in (1.5, 2.0)}$
4.6	5.2	0.145649	0.0389596	0.00519628
10.5	13.9	0.337821	0.114685	0.0174097
20.5	28.8	0.670429	0.276146	0.0452439
36	52.8	1.19706	0.579686	0.0998644
58.1	89	1.96409	1.09011	0.194468
86.4	139	2.96666	1.84151	0.336677
124.6	209	4.34763	2.9887	0.557272
176.8	307	6.27494	4.7496	0.900351
244.4	440	8.82573	7.29375	1.40147
304.1	564	11.1209	9.74461	1.88797
350.3	671	12.9207	11.7547	2.2889

**Table 3.20** Centrality evolution of integrals in  $y_T$  bins for  $p$

### 3.10 Statistical Uncertainties

Statistical error associated with the sibling ( $n_{sib}$ ) and reference ( $n_{ref}$ ) pair counts are propagated to the error in the correlation,  $\frac{\Delta\rho}{\sqrt{\rho_{ref}}}$  defined in Equation 3.18. The statistical errors in the sibling and reference pair counts are determined by the number of pairs in each  $(\eta_{\Delta}, \phi_{\Delta})$  bin [55]. However, the final errors are sensitive to how the reference density is defined as shown by Ray and Bhattarai [56]. In this thesis, we have generated the reference density by mixing each event with two similar, but different events. The statistical error in  $\frac{\Delta\rho}{\sqrt{\rho}}$  is given by  $\left[ \frac{1}{N_{sib}(\eta_{\Delta}, \phi_{\Delta})} + \frac{1}{N_{ref}(\eta_{\Delta}, \phi_{\Delta})} \right]^{1/2}$  where  $N_{sib}$  and  $N_{ref}$  are the total number of sibling and mixed-event reference pairs, for all events, in bin  $(\eta_{\Delta}, \phi_{\Delta})$ . Note that the  $error \propto 1/\sqrt{Number\ of\ pairs}$  rather than  $1/\sqrt{Number\ of\ Tracks}$  due to noise cancellation feature of the event mixing method [55][56]. In this thesis, we have used large data sample with more than 50 million events. Therefore, the statistical errors, in most of the cases, are significantly smaller than the correlation signals. However, in some centralities, such as the most-peripheral centrality, the mean multiplicities are smaller and the errors increase. Similarly, for  $K$  and  $p$  the multiplicities are smaller resulting in larger errors. Also, the multiplicities monotonically decrease as we go farther and farther from 0 in relative pseudorapidity. In such cases at large  $|\eta_{\Delta}|$ , the statistical error dominates the correlation structure.

### 3.11 Systematic Uncertainties

Systematic uncertainties in non-identified particle angular correlations have been presented in References [1][37][5]. There multiple sources of systematic uncertainty including secondary particle contaminations, uncorrected residual pileup contamination (see Chapter 4), uncorrected residual two-particle inefficiencies (see Section 3.4.1), collision centrality determination (see Section 3.5.2) and various, minor detector effects discussed in Reference [5].

The 12% particle contamination from non-primary sources [5] such as weak decays of  $K_S^0$ ,  $\Lambda$ ,  $\bar{\Lambda}$  and from secondary particle production from detector material near the collision vertex is the dominant source of systematic uncertainty. It contributes up to  $\pm 3\%$  uncertainty for non-identified correlations [37][5]. As we have discussed in Section 3.4 particles having global DCA < 3 cm were selected in this analysis. Reducing the DCA cut reduces the relative fraction of secondary contamination. It was found that the correlations did not change significantly by lowering the DCA to 1 cm. We therefore assume a  $\pm 3\%$  systematic uncertainty for the present data due to secondary particle contamination.

The effect of pileup contamination on correlation structure was presented and discussed in Chapter 4. Uncertainties due to residual, uncorrected pileup are negligible given the performance of the pileup filter and correction procedure for the Run11 data discussed in Chapter 4. Other systematic error sources are of order a few percent or less, or only affect localized region (one or two bins) near  $(\eta_\Delta, \phi_\Delta) \sim (0, 0)$ .

For the correlations of identified particles a new source of systematic error must be included, that associated with inefficiency and impurities in particle identification (see Chapter 5). In Chapter 5 it is shown that  $\pi$ ,  $K$  and  $p$  identification efficiency drops to below 80% at higher  $p_T$  and each particle type suffers from 5-10% contamination. For  $p_T < 2$  GeV/ $c$  both the efficiency and purity of identified  $\pi$ ,  $K$  and  $p$  is close to 100%. For the higher  $p_T$  bin PID contamination may affect the correlation structure. This source of systematic uncertainty will be considered and its effects estimated for azimuthal, non-jet quadrupole [5] component of the correlations in the next chapter. Uncertainties in the higher  $p_T$  correlation data are about 2% from PID impurities.

# Chapter 4

## Pileup

### 4.1 Introduction

Pileup can produce spurious results in angular correlations [5]. Event pileup produces a characteristic ‘W’ shape (see Figure 4.2) on the  $\eta_{\Delta}$  axis in the correlation structure due to asymmetry in  $\eta$  distributions from out-of-time partial events [5][57].

A small level of pileup contamination is seen in data from STAR and a method for its removal was implemented in run 2001<sup>1</sup> and 2004 data for Au-Au collisions at 62 and 200 GeV. The method was devised by Duncan Prindle from the University of Washington and was successful in removing pileup from these [5]. Note that before looking for this method a *vertex ranking* cut was applied to filter pileup events but it was passing an unacceptable number of pileup events. However, this method of filtering pileup did not work when it was applied to run 2010 data. Also, the method was not as efficient in run 2011 as it was in run 2001/2004 data.

In this chapter, we will briefly discuss Duncan’s method of removing pileup. We will show how the method doesn’t work in run 2010 data. Subse-

---

<sup>1</sup>RHIC run 2 was accomplished 2001

quently, we will discuss 3 other methods that attempt to remove pileup. First, we will change the Distance of Closest Approach (DCA) cut. The global DCA cut of less than 1 cm worked, but only partially. Second, utilizing a trend of global versus primary tracks, a band cut of  $4\sigma$  will be applied. This method is found to work well. Finally, we will impose a TOF matching criterion for each track (i.e., a track is selected only if it has both TPC and TOF hits). This method is also found to be insufficient at removing all pileup. We advocate the use of the  $4\sigma$  cut to remove pileup contamination in the run 2010 Au-Au collision data.

Because of different levels of pileup contamination in run 2011 data, a different set of cuts was required to remove pileup in run 2011. These cuts, based on Duncan's pileup filter and the associated correction procedure worked to remove pileup in run 2011. The set of pileup cuts are discussed below.

## 4.2 Pileup

In the STAR detector the bunch crossing time is 120 *ns*, whereas the time for ions to move from the central membrane of the TPC to the readout planes (drift time) is 40  $\mu s$ . Because of the larger drift time, the probability of mixing the tracks from a triggered event and an untriggered event increases. The mixing of tracks from untriggered events to the tracks in the triggered event is called pileup. The untriggered events are called pileup events. For the

RHIC beam luminosity<sup>2</sup>, the probability of two collisions happening within the TPC drift time window of 40  $\mu s$  is very small, but not completely ignorable. Based on the occurrence time of a pileup event with respect to a triggered event, there are two types of pileup: pre-triggered pileup and post-triggered pileup. In the pre-triggered pileup, tracks from an event that occurs just before the triggered events are mixed, whereas in post-triggered pileup, the tracks from the event that occurs just after the triggered event are mixed with the tracks from the triggered events. The pileup event is removed in different levels using different signatures that the triggered events leave in the detectors.

### 4.3 Pileup Signatures in STAR Run 2010

It has been reported that STAR run 2001 and 2004 data for Au-Au collisions at 62 GeV and 200 GeV have low pileup contamination (0.05% and 0.5%, respectively) [5]. In Figure. 4.1, charge independent angular correlations of the 62 GeV data in centrality 37%-46% are shown. The left and right panel of the figure show pileup uncorrected and corrected correlations respectively. The method of pileup correction is discussed in Section 4.3.1. The correlation studies of Run 2001/2004 can be treated as standard for angular correlation analysis. In Figure 4.2, charge independent angular correlations for Au-Au 200 GeV run 2010 minimum bias data<sup>3</sup> are presented. No pileup event removal

---

<sup>2</sup>Integrated luminosity for run 2010 and 2011 Au+Au collisions at  $\sqrt{s_{NN}}=200$  GeV are respectively 10.3  $nb^{-1}$  and 9.79  $nb^{-1}$  [58]

<sup>3</sup>Run 2010 Minimum-Bias Data: Production-P10ik, Trigger name - vpd-mb, Trigger IDs-260001, 260011, 260021, 260031

techniques are imposed in Figure 4.2. The figures with percentages on the top left corner of each picture reflect the approximate centrality of the collision. It is evident that the characteristic ‘W’ shape is more prominent in Figure 4.2 than the left plot of Figure 4.1, suggesting an increase of pileup contamination.

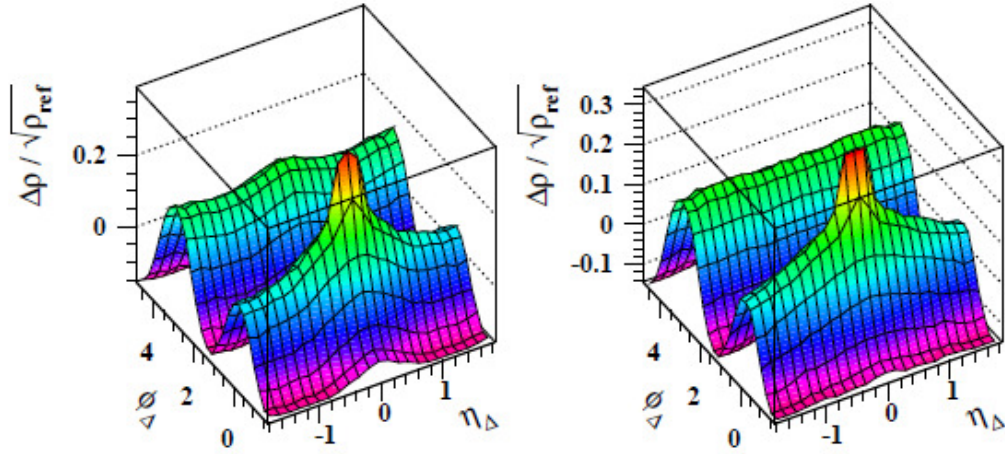


**Figure 4.1** Au-Au 62 GeV Run 2004. Left: Uncorrected angular correlations from 62 GeV 37-46% central Au-Au collisions showing pileup distortions, especially evident as the W-shaped non-uniformity of the away-side ridge on  $\eta_{\Delta}$ . Right: The same data with pileup correction applied [5].

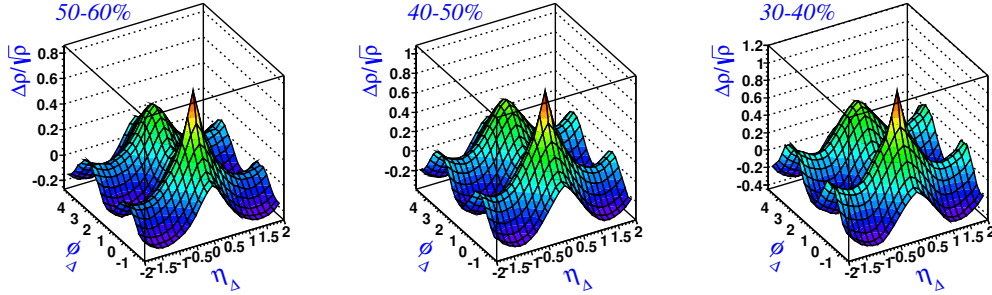


**Figure 4.2** Au-Au 200 GeV Run 2010 charge independent angular correlations showing significant distortion of the angular correlations for different approximate centralities. No vertex ranking cut has been applied.

### 4.3.1 Pileup Removal

#### Vertex Ranking

In order to determine which vertex candidate corresponds to the triggered event, a *rank* is assigned to each candidate. A cut is made based on numerical value of the rank to select events. The vertex ranking cut is defined using:

- average dip angle<sup>4</sup>,
- number of TPC tracks matched with BEMC hits and
- number of TPC tracks that cross the TPC membrane.

A detailed explanation of vertex ranking is found in Anthony Robert Timmins' PhD thesis [59] and in STAR documents [60]. The following correla-

---

<sup>4</sup>Dip angle is the angle between momentum of the particle and the drift direction,  $\theta = \cos^{-1}(p_z/p)$ [8].

tions in Figure 4.3 are based on the optimum value of the vertex ranking cut:  $vertex\ ranking > -2.5$ . Although this cut reduces pileup, it can not remove pileup completely. However, because it is defined using a basic vertex ranking parameters, it is taken as a basic cut. Unless stated otherwise, the vertex ranking cut is implemented in all correlations.

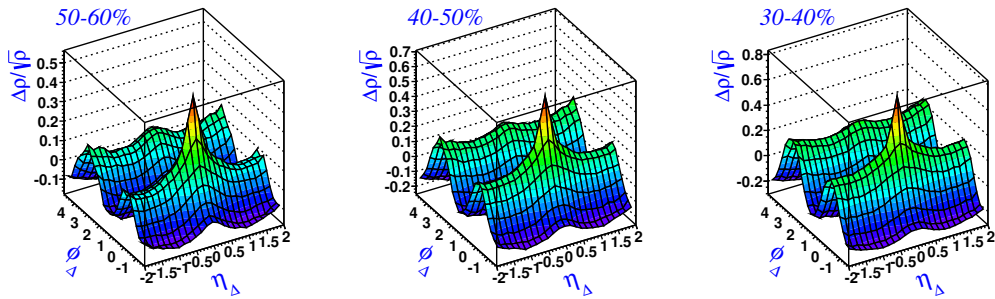


**Figure 4.3** Au-Au 200 GeV Run 2011 charge independent angular correlations for different approximate centralities. Vertex Ranking  $> -2.5$ .

### Duncan's Method

Duncan Prindle devised a method of removing pileup on the basis of tracking artifacts. A signature of pileup is expected to be seen in the distribution of the projection of the first and last space points of a track on the  $z$ -axis (along beam axis), called  $Z_{first}$  and  $Z_{last}$  points, respectively. Suppose we have a pre-triggered pileup event. As the tracks from the event cross the central membrane of TPC, they split into two halves and move toward opposite directions of the TPC. The distribution of the  $Z_{first}$  and  $Z_{last}$  peaks at the space point where the first and last point of tracks from the pileup event contribute. The dynamics of the drifting electrons produced from a pileup event

is such that the first and last points of all tracks have the same  $Z_{first}$  and  $Z_{last}$  values. Similarly, a post pileup event contributes to a peak in  $Z_{last}$ . Duncan's method is based on the distribution of  $Z_{first}$  and  $Z_{last}$  in the TPC. The details are documented in the following websites [61], [62] and [63] and in Elizabeth Oldag's PhD thesis [37].

Duncan's method was implemented in STAR Au-Au data from run 2001 and 2004 and Cu-Cu data from run 2005 . The method was successful in removing pileup in these data sets. The pileup corrected correlations for these data are shown in Figure 4.1. However, this method is not sufficient to remove pileup in run 2010 and 2011 data. The details of run 2011 will be discussed in the next section. In Figure 4.4, the angular correlations of run 2010 after making Duncan's cut (suggested optimum value of cut: pileup cut (-20cm to 20cm)) without including vertex ranking cut are presented.

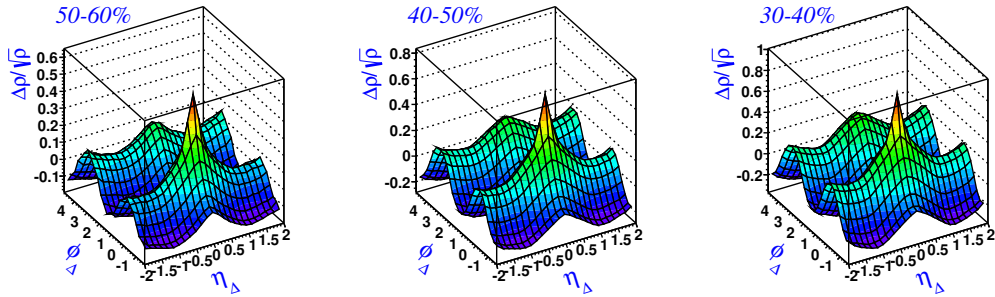


**Figure 4.4** Au-Au 200 GeV Run 2010 charge independent angular correlations. Duncan's pileup filter  $\left[ \frac{\Delta\rho}{\sqrt{\rho_{ref}}} (Cut) \right]$  (-20,20)cm has been implemented. Vertex ranking cut is not included.

It has been estimated that this pileup removal method is 75% effi-

cient [5]. Using the following equations the pileup corrected correlations are obtained,

$$\begin{aligned} \frac{\Delta\rho}{\sqrt{\rho_{ref}}} (NoCut)^a &= \frac{\Delta\rho}{\sqrt{\rho_{ref}}} (NoPileup) + \frac{\Delta\rho}{\sqrt{\rho_{ref}}} (Pileup), \\ \frac{\Delta\rho}{\sqrt{\rho_{ref}}} (Cut)^b &= \frac{\Delta\rho}{\sqrt{\rho_{ref}}} (NoPileup)^c + (1 - f) \frac{\Delta\rho}{\sqrt{\rho_{ref}}} (Pileup)^d. \end{aligned}$$

The following pileup corrected correlations (Figures 4.5 and 4.6 ) are obtained using the efficiency  $f=75\%$ . It is seen that the method has not removed pileup completely. In contrast, the pileup corrected correlations for run 2001 and 2004, shown in the right panel of Figure 4.1, are pileup free (visually).

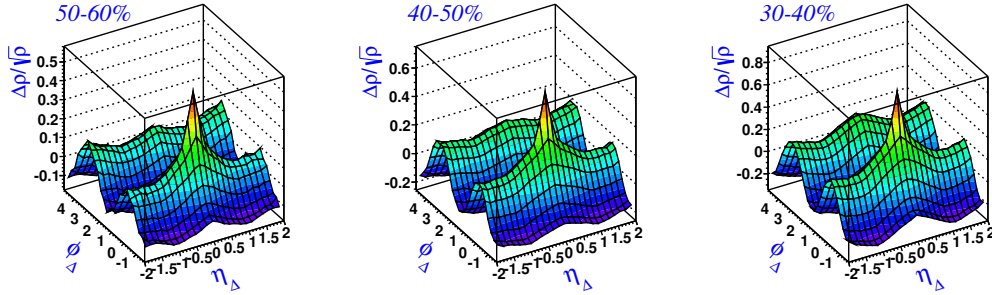


**Figure 4.5** Au-Au 200 GeV Run 2010 charge independent angular correlations. Duncan's pileup corrected  $\left[ \frac{\Delta\rho}{\sqrt{\rho_{ref}}} (NoPileup) \right]$  for efficiency 75%. Vertex ranking cut is not included.

<sup>a</sup>Correlations before Duncan's pileup filter  $\frac{\Delta\rho}{\sqrt{\rho_{ref}}} (NoCut)$

<sup>b</sup>Duncan's pileup filtered correlations refers to  $\frac{\Delta\rho}{\sqrt{\rho_{ref}}} (Cut)$

<sup>c</sup>Duncan's pileup corrected (efficiency corrected) correlations refers to  $\frac{\Delta\rho}{\sqrt{\rho_{ref}}} (NoPileup)$

<sup>d</sup>Duncan's pileup refers to  $\frac{\Delta\rho}{\sqrt{\rho_{ref}}} (Pileup)$

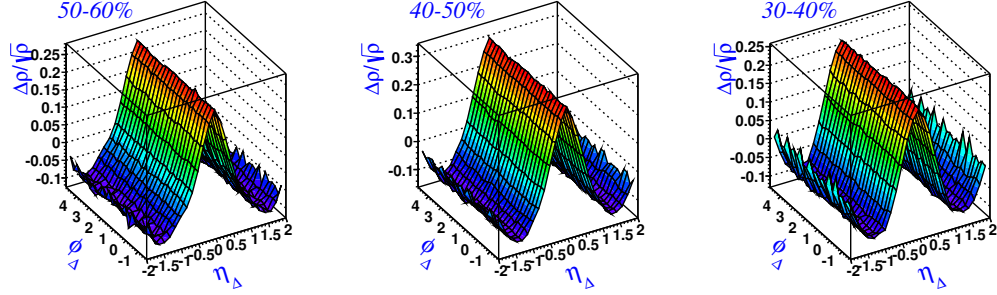


**Figure 4.6** Au-Au 200 GeV Run 2010 charge independent angular analysis. Duncan's pileup  $\left[ \frac{\Delta\rho}{\sqrt{\rho}} (Pileup) \right]$  for efficiency 75%.

Considering the error bars of the pileup correction efficiency to be  $\pm 10\%$ , the pileup corrected correlations were obtained for efficiencies such as 65% and 85% instead of suggested the 75%. No improvement in the correlations was found. This result requires additional methods of pileup removal. However, when the vertex ranking cut (i.e.  $Vertex\ Ranking > -2.5$ ) is included along with Duncan's cut, the pileup filter works better. Figure 4.7 shows correlations after using Duncan's pileup filter along with the vertex ranking cut. The efficiency corrected correlations for an efficiency of 75% are shown in Figure 4.8.

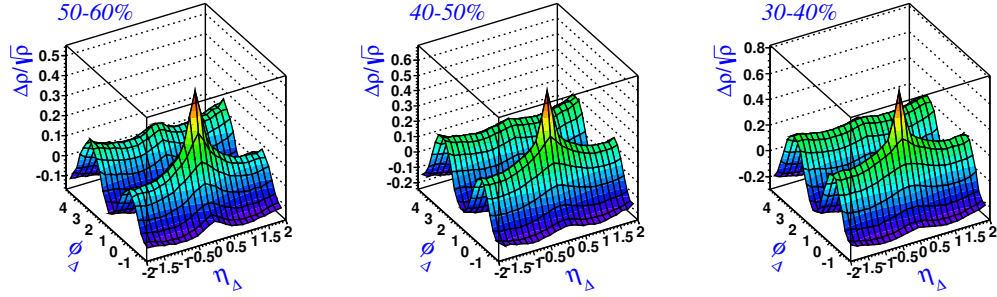


**Figure 4.7** Au-Au 200 GeV Run 2010 charge independent angular correlations. Duncan’s pileup filter  $\left[ \frac{\Delta\rho}{\sqrt{\rho_{ref}}} (Cut) \right]$  as well as vertex ranking cut ( $> -2.5$ ) are included.

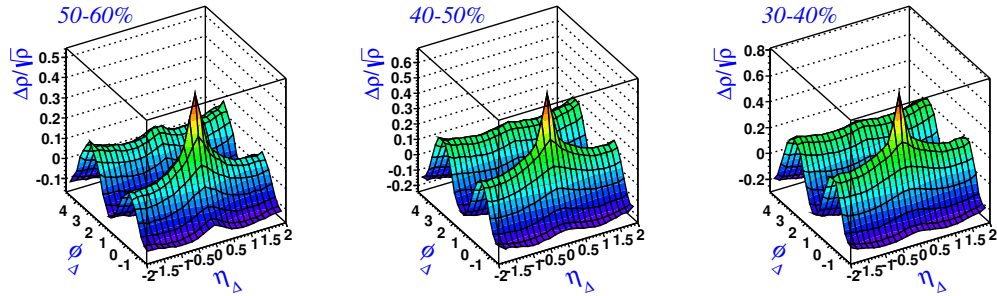


**Figure 4.8** Au-Au 200 GeV Run 2010 charge independent angular correlations. Duncans pileup corrected  $\left[ \frac{\Delta\rho}{\sqrt{\rho_{ref}}} (NoPileup) \right]$  for efficiency 75% along with vertex ranking cut.

## TOF Matching

Time of Flight (TOF) detector information can be used to identify pileup events. A track that has both TPC and TOF hits is highly likely to be from a triggered event because having TOF hits is one of the requirements to trigger a collision event. Thus, rejection of the tracks having TPC hits

only and no TOF tracks allows us to separate pileup free event tracks. In Figure 4.9, correlations of tracks that hit both the TPC and TOF are shown. The correlation structure shows that the TOF matching criteria is significant in removing pileup event tracks. However, large statistics ( $\sim 40\%$ ) are compromised when the TOF matching criterion is imposed in data selection. Therefore, this method of pileup removal is not used here.

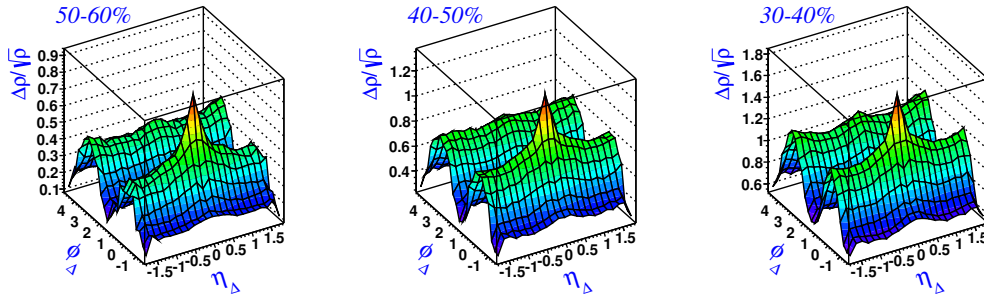


**Figure 4.9** Au-Au 200 GeV Run 2010 charge independent angular correlations for tracks having both TPC and TOF hits. Vertex ranking cut is not included (compare this figure with Figure 4.2). The lower TOF acceptance than TPC acceptance is reflected in lower value of  $|\eta_{\Delta}|$ .

### Global DCA Cut

Global DCA refers to the distance of closest approach between the global track model and the primary vertex. The tracks that are associated with the primary collision vertex are called primary tracks whereas all the tracks reconstructed during the time of event trigger window ( $40\mu s$ ) are called global tracks. The decay of particles during the flight from the collision vertex contribute to global tracks. Also, tracks from pileup events contribute to the

global tracks.

In Figure 4.2, the correlations for a Global DCA from 0-3 cm are presented. If the cut is tightened to 0-1 cm, a significant fraction of pileup is removed. The correlations for a Global DCA cut of 0-1 cm are shown in Figure 4.10.

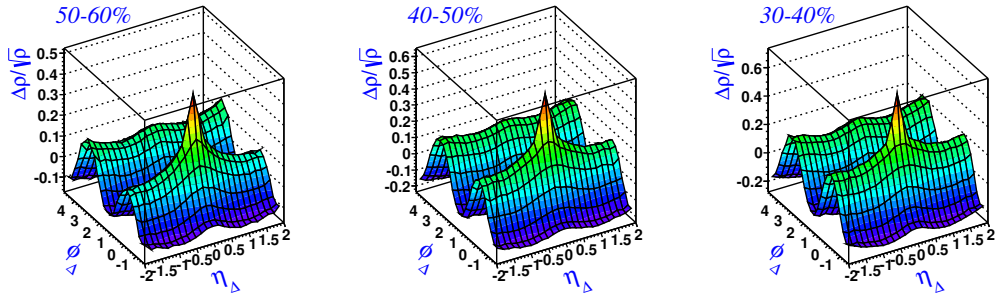


**Figure 4.10** Au-Au 200 GeV Run 2010 charge independent angular correlations. Global DCA cut 0-1 cm. Vertex ranking cut is included.

The comparison shows that the pileup contamination can be reduced by reducing the global DCA cut. However, the cut is not effective enough to remove pileup signatures completely. On the other hand, we have to throw out a lot of tracks while reducing the global DCA. Also,  $DCA \leq 1$  cm removes more low  $p_T$  tracks than high  $p_T$ , which distorts the correlation structures relative to Run 2001/2004. The cost of reducing the global DCA can be seen in the multiplicity distribution in Figure 4.11 and Global the DCA vs  $p_T$  distribution in Figure 4.12.

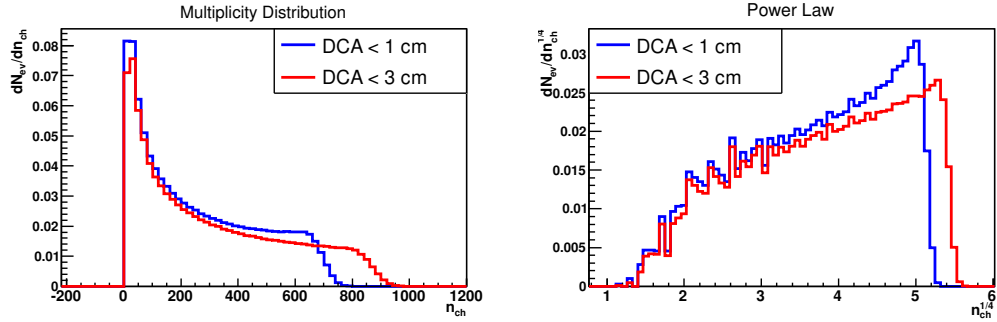


**Figure 4.11** Run 2010 multiplicity distribution. Left: Multiplicity distribution for global DCA 0-1 cm and 0 – 3 cm. Right: Power law based transformation of the distribution in the left panel.

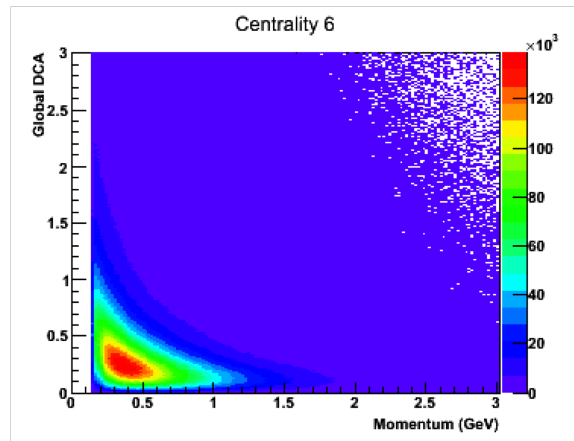
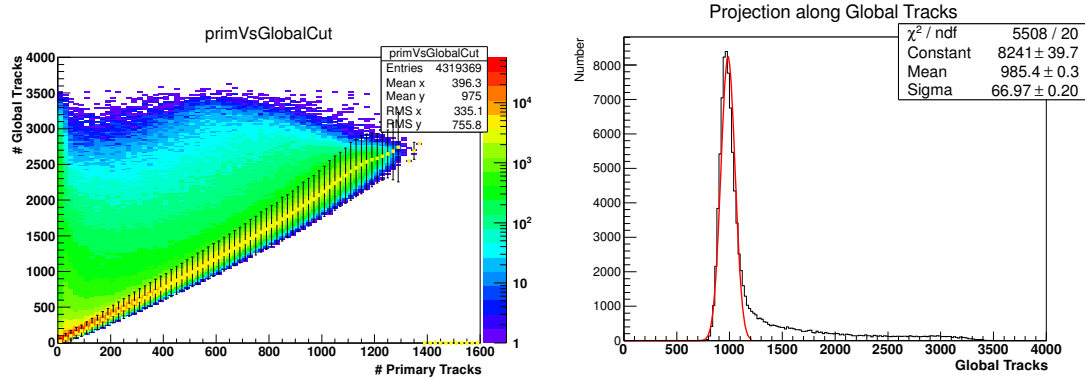


**Figure 4.12** Au-Au 200 GeV Run 2010 momentum versus global DCA distributions for a centrality 30-40%. There is a significant density of low momentum particles between  $1 < DCA < 3$  cm

### Global Vs Primary Track Band Cut

The event-wise global versus primary tracks distribution follows an almost linear trend. Figure 4.13 below shows the global versus primary track distribution in the left panel and a projection along global tracks in a certain

bin of primary tracks in the right panel. In the projection it is seen that the distribution follows a Gaussian trend with a long tail as shown in 4.13b. Each primary track bin is projected along global tracks to obtain the mean and  $\sigma$ . The TPC events with pileup contamination are expected to contain a larger number of global tracks. In a set of multiples of  $\sigma$ , a cut of  $4\sigma$  is found to be the most optimum for removing pileup while minimizing good event loss. Figure 4.14 shows the correlations after removing events having global tracks above  $4\sigma$ . This cut removes pileup more effectively than the previously described methods. The correlations of the rejected events (events that lie outside of the  $4\sigma$  band) are shown in Figure 4.15.



(a) Global versus primary tracks distribution after making basics cuts such as  $\eta \leq 1$ . The vertical bars in the trend line indicate the  $4\sigma$  of the projection distribution in respective primary track bin.

(b) Projection along global tracks for (520-540) primary tracks. A Gaussian fit is drawn in red. The fit parameters are shown in legend

**Figure 4.13** Global versus primary tracks distribution.

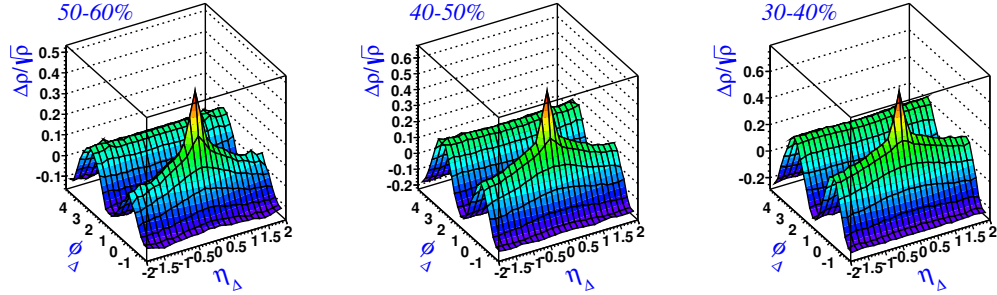


**Figure 4.14** Au-Au 200 GeV Run 2011 charge independent angular correlations. A  $4\sigma$  band cut is applied. The correlations do not show signatures of pileup explicitly.

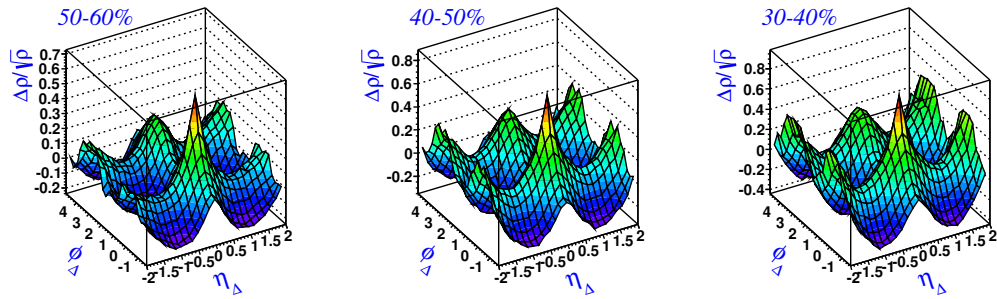


**Figure 4.15** Au-Au 200 GeV Run 2011 charge independent angular correlations of  $4\sigma$  band rejected events. The pileup contributes significantly to the correlations.

The correlations inside the band, shown in Figure 4.14 along with the correlation of rejected events by  $4\sigma$  cut, Figure 4.15, shows circumstantial evidence that the  $4\sigma$  band cut is a reasonable cut to make. However, it is not straight forward to explain why the  $4\sigma$  cut is good at removing pileup.

The decision of the multiple of the  $\sigma$  cut is based on observations of correlation structures. The larger  $\sigma$  cut can't remove the 'W' shaped structure

(i.e. pileup) completely whereas statistics is compromised in the smaller  $\sigma$  cut.

#### 4.4 Pileup Signatures in STAR Run 2011

Effort has been made to remove pileup in run 2011. Pre-pileup and post-pileup possibilities are accounted for and a protection method is implemented in run 2011 triggers. Both of the pre- and post pileup protections are applied in 3 of the 5 minimum-bias triggers <sup>5</sup> in Run 2011 Au-Au collision data at  $\sqrt{s_{NN}} = 200$  GeV. However, the protection implemented is not fully successful at removing all pileup. In Figure 4.16 charge independent angular correlations for trigger IDs 350003 and 350013 of Au-Au 200 GeV run 2011 (called half protected) are presented. No extra pileup filtering techniques are imposed. The percentages on the top left corner of each picture reflects the centrality of the collision. The vertex ranking cut reduces the pileup. The correlations after making the vertex ranking cut is shown in Figure 4.17.

Similarly, Figures 4.18 and 4.19 show the correlations without and with vertex ranking cut respectively for three minimum-bias triggers 350023, 350033 and 350043 (called fully protected). Because of the pre and post-pileup removal algorithm, correlation structures have less ‘W’ shaped structure.

---

<sup>5</sup>Trigger IDs 350003, 350013, 350023, 350033, 350043

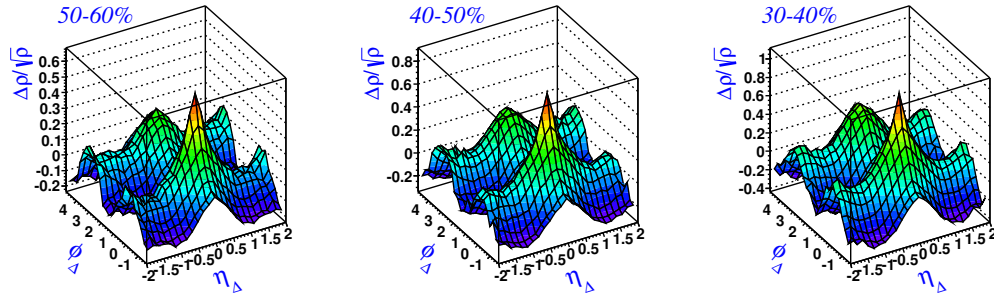


**Figure 4.16** Au-Au 200 GeV Run 2011 (half protected trigger IDs 350003 and 350013) Charge Independent Angular Correlations. Vertex ranking cut is not included.

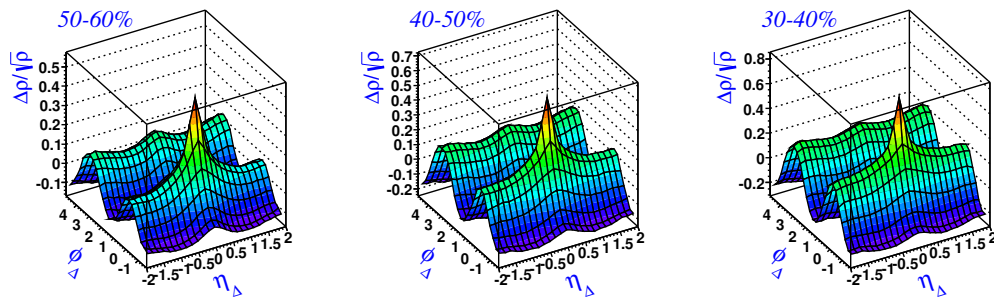


**Figure 4.17** Au-Au 200 GeV Run 2011 (half protected trigger IDs 350023, 350003 and 350013) Charge Independent Angular Correlations. Vertex ranking cut is included.

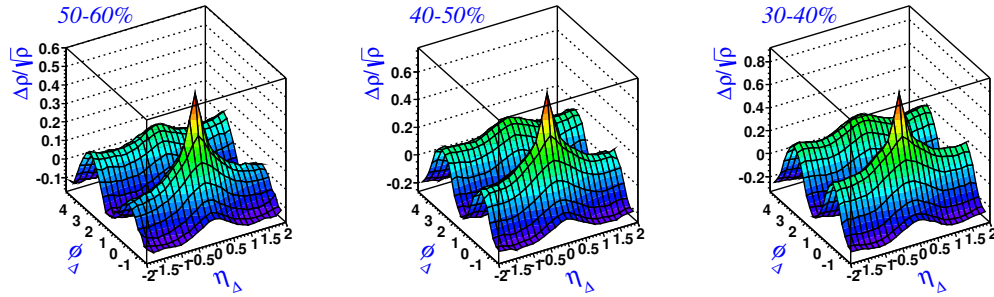


**Figure 4.18** Au-Au 200 GeV Run 2011 (fully protected trigger IDs 350023, 350033 and 350043) Charge Independent Angular Correlations. Vertex ranking cut is not included.

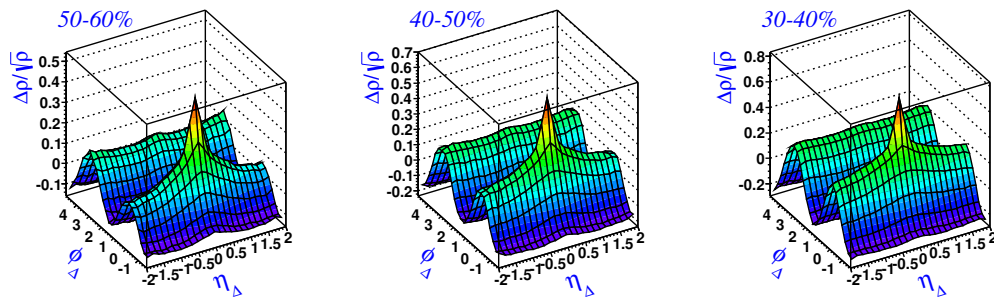


**Figure 4.19** Au-Au 200 GeV Run 2011 (fully protected trigger IDs 350023, 350033 and 350043) Charge Independent Angular Correlations. Vertex ranking cut is included.

#### 4.4.1 Pileup Removal

##### Duncan's Method

For the doubly protected run 2011 data, Duncan's method seems to be more effective than in run 2010. In the following Figure 4.20, the angular correlations of run 2011 after using Duncan's filter  $\left[ \frac{\Delta\rho}{\sqrt{\rho_{ref}}} (Cut) \right]$  are presented.

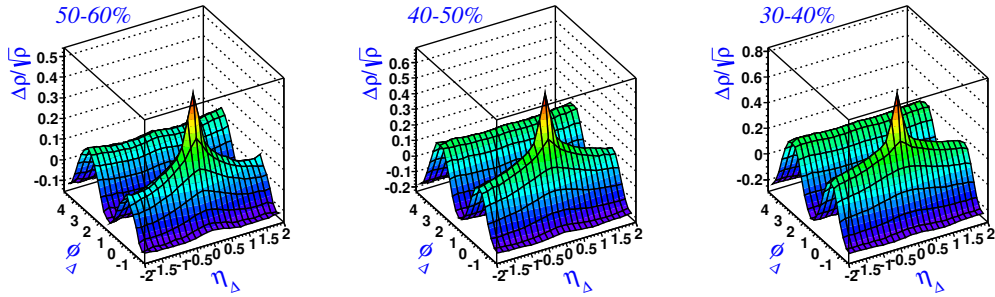


**Figure 4.20** Au-Au 200 GeV Run 2011 (fully protected trigger IDs 350023, 350033 and 350043) charge independent angular correlations. Vertex ranking cut is included. Duncan's pileup filter  $\left[ \frac{\Delta\rho}{\sqrt{\rho_{ref}}} (Cut) \right]$  is applied.

In Figure 4.21, Duncan's pileup corrected  $\left[ \frac{\Delta\rho}{\sqrt{\rho_{ref}}} (NoPileup) \right]$  for efficiency 75%.

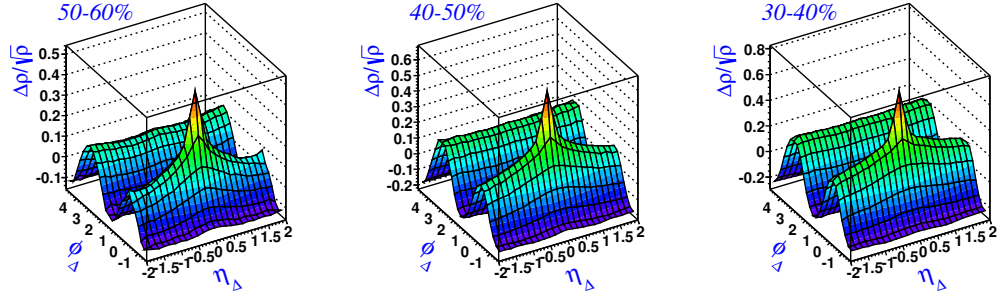


**Figure 4.21** Au-Au 200 GeV Run 2011 (fully protected trigger IDs 350023, 350033 and 350043) Duncan’s pileup corrected  $\left[ \frac{\Delta\rho}{\sqrt{\rho_{ref}}} (NoPileup) \right]$  for efficiency 75%. Vertex ranking cut is included.

## 4.5 Conclusion

To remove the pileup in angular correlations, different methods are implemented. Run 2010 Au-Au collision data needed different techniques to remove pileup compared to run 2001/2004 data. A cut of  $4\sigma$  in global versus primary track distribution was found to be optimal. And for run 2011 with pre and post-pileup trigger protection, the vertex ranking cut and Duncan’s pileup filter along with the filter efficiency correction procedure were found to be optimal.

## Chapter 5

# Particle Identification

### 5.1 Introduction

One of the main goals of this thesis is to measure and analyze two-particle correlations between identified particle species. Thus, identification of particles with optimum efficiency and purity (defined in Section 5.6) is an important step of this study. The mass of the particle is the most fundamental discriminatory measure for particle identification (PID). However, if the uncertainty in the measurement of  $m$  is large, the distributions of  $m$  of two different particle species overlap, making it statistically challenging to discriminate the species from their mass. In such a situation, other measures, such as a particle's mass squared ( $m^2$ ), energy loss per unit length ( $dE/dx$ ), time of flight<sup>1</sup> ( $\beta^{-1}$ ), etc. or their combinations are better choices. In this chapter, the particle identification method using combined independent measures,  $dE/dx$  and  $\beta^{-1}$ , is discussed.

---

<sup>1</sup> $\beta^{-1}$  is related to time of flight as shown in Equation 5.2.

## 5.2 PID using $dE/dx$

As a high energy charged particle passes through the gaseous medium of the TPC, it loses energy. The energy loss per unit length ( $dE/dx$ ) is measured in the anode pads of the TPC as described in Chapter 2. Figure 5.1 shows the energy loss of the charged particles per unit length of gaseous medium at different momenta of the particles.

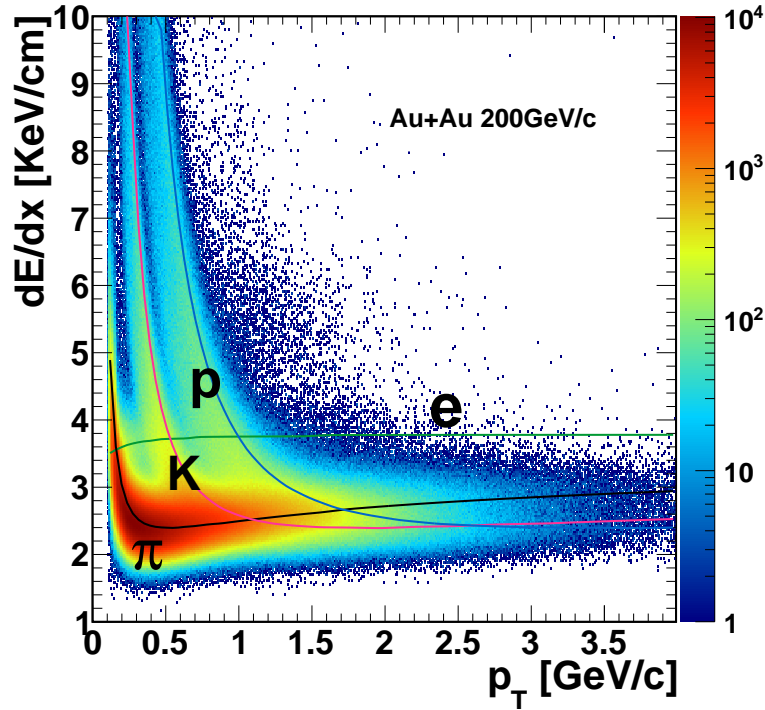


**Figure 5.1** Energy loss by charged particles per unit distance in TPC for the particles of different momenta.

It is seen that the likelihood of energy loss is different for different particle species at lower momentum. The expected value of  $dE/dx$  for  $\pi$ ,  $K$ ,  $p$  and  $e$  are estimated using the Bichsel function [64] and overlaid on the distribution.

From the distribution, it is visually clear that a *proton* track can be discriminated from  $\pi$  and  $K$  up to 1 GeV. Similarly, a  $K$  track can be separated from  $\pi$  up to 0.5 GeV. However, for higher momenta the overlapping distributions make it difficult to achieve high purity in particle identification. It is also seen that identification of electron tracks is not straightforward.

The  $dE/dx$  follows a Landau distribution with a long tail to the right (higher value). The distribution is well approximated with a log-normal distribution. Therefore,  $\log(dE/dx)$  is a better choice of statistic, since the resulting distribution is a Gaussian. A convenient statistic for the purpose of PID would be as follows [65].

$$n\sigma_{dE/dx}^i = \frac{\log(dE/dx) - \log(dE/dx)_{expected}^i}{\sigma_{\log(dE/dx)}}, \quad (5.1)$$

where  $\log(dE/dx)$  is obtained from the data,  $i$  is the particle type ( $\pi, K, p, e$  etc.),  $\log(dE/dx)_{expected}^i$  is the expected value from the Bichsel function for the given mass of particle type  $i$  and  $\sigma_{\log(dE/dx)}$  is the resolution calculated using the spread of the  $(dE/dx)$  distribution and the number of fit points used in the track fit. If the  $dE/dx$  is calibrated ideally, the statistic  $n\sigma_{dE/dx}^i$  would give a Gaussian distribution with a mean and sigma of 0 and 1, respectively. In the data analysis process, the spread (standard deviation) of the  $n\sigma_{dE/dx}^i$  distribution is chosen to discriminate one particle form another. The smaller the sigma, the higher the purity (defined in Section 5.6) of the identified particle sample. However, the higher purity lowers the statistics, giving a very low efficiency (low count of identified particle sample) of particle identification.

We choose a cut in sigma for which the desired purity and efficiency (defined in Section 5.6) of identified particles is obtained. Using the statistic  $n\sigma_{dE/dx}^i$ ;  $\pi$ ,  $K$ , and  $p$  can be identified up to  $p_T \leq 1$  GeV/c with reasonable efficiency and purity. However, because the distributions merge with each other for higher momentum, the statistic doesn't have sufficient particle discriminating power for higher  $p_T$ . We use another independent measure,  $\beta^{-1}$ , from the TOF PID at  $p_T > 1$  GeV.

### 5.3 PID using $\beta^{-1}$

Figure 5.2 shows the  $\beta^{-1}$  distribution of the charged particles. The  $\beta^{-1}$  is calculated using the detector information from TOF.

$$\beta^{-1} = \frac{c}{v} = \frac{ct}{L}, \quad (5.2)$$

where  $c$  is the speed of light,  $t$  is the time of flight of the charged particle from the VPD to TOF, as discussed in Chapter 2, and  $L$  is the spatial distance covered by the particle during flight.

The fits in Figure 5.2 are obtained using the expected inverse velocity of a particle  $i$ , for a given momentum ( $p$ , measured by TPC) and rest mass of the particle ( $m_i$ ) as shown in Equation 5.3.

$$\beta_{i,expected}^{-1} = \frac{c}{v} = \frac{\gamma mc^2}{pc} = \frac{\sqrt{p^2c^2 + m_i^2c^4}}{pc} = \sqrt{1 + \frac{m_i^2c^2}{p^2}}. \quad (5.3)$$

Among several statistics based on  $\beta^{-1}$  (because it has constant resolution at higher momentum and a more Gaussian like distribution [65]) we use

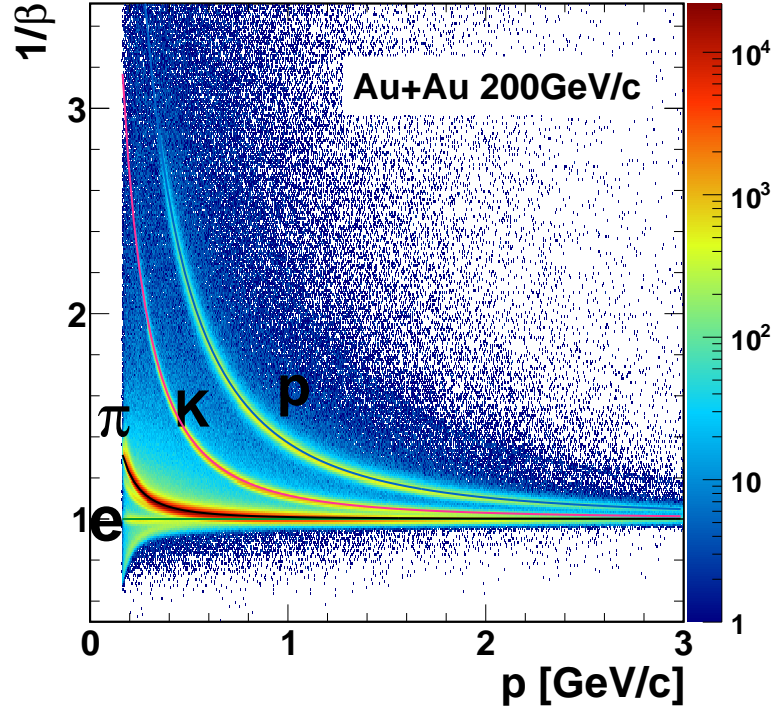


**Figure 5.2** Inverse velocity distribution of the charged particles as a function of momentum.

$\frac{\Delta\beta_i^{-1}}{\beta^{-1}}$  where  $i$  is the type of particle.

$$\frac{\Delta\beta_i^{-1}}{\beta^{-1}} = \frac{\beta^{-1} - \beta_{i,expected}^{-1}}{\beta^{-1}} = 1 - \frac{L}{ct} \sqrt{1 + \frac{m_i^2}{p^2}} \quad (5.4)$$

For a given particle  $i$ , the distribution of the statistic  $\frac{\Delta\beta_i^{-1}}{\beta^{-1}}$  is close to Gaussian with a mean of 0. However, for Au+Au collision data, the tail of the distribution gets longer, making it better described by a Student's T function,

$$p(x; \mu, \lambda, \nu) = \frac{1}{B(\frac{1}{2}, \frac{\nu}{2})} \sqrt{\frac{\lambda}{\nu}} \left( 1 + \frac{\lambda(x - \mu)^2}{\nu} \right)^{-\frac{\nu+1}{2}}, \quad (5.5)$$

where  $\mu$  is mean of the distribution,  $\nu$  is the degree of freedom,  $\lambda$  is the scale parameter and  $B$  is the *Beta* function [65].

Although the PID for  $p_T \leq 2$  GeV using  $\beta^{-1}$  is more efficient than that using  $dE/dx$ , PID above  $p_T > 2$  GeV becomes inefficient because of the overlapping distributions of  $\pi$ ,  $K$  and  $p$ . We use a 2-dimensional approach to improve PID efficiency and purity.

#### 5.4 PID using $dE/dx$ and $\beta^{-1}$

One of the commonly adopted techniques for PID is to use either  $dE/dx$  information from the TPC or to use  $\beta^{-1}$  data from TOF separately and make cuts to identify particles. There are techniques to combine information from the TPC and TOF to achieve better PID [66]. In this thesis, however, a different approach is used to combine TPC and TOF information simultaneously by introducing a 2-dimensional distribution in different ranges of momenta. When TPC and TOF information are used separately, PID cuts are made on the basis of rectangular area whose corners may contain contamination. However, in the simultaneous treatment, the PID cut is based in circular, elliptical or any other, more complicated area that doesn't have as much contamination [65]. This method, hence, gives better PID efficiency and purity (defined in Section 5.6).

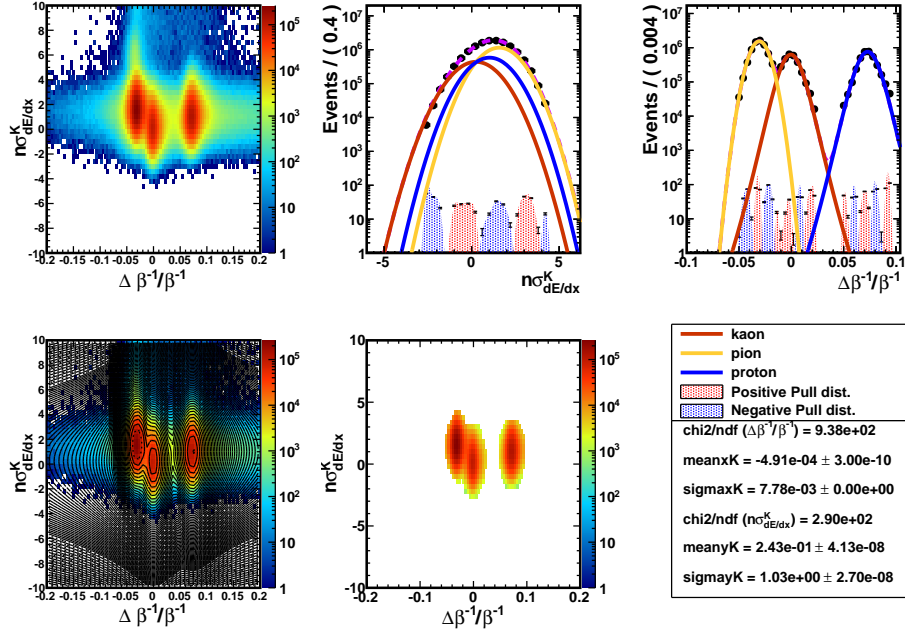


**Figure 5.3** 2-dimensional distribution charged particles in  $\Delta\beta_k^{-1}/\beta^{-1}$  and  $n\sigma_{dE/dx}^k$ . The distribution is fit for *kaons* using both Gaussian ( $y$ -axis) and Student's T ( $x$ -axis) distributions. The pull-distribution is the ratio of difference of data and fitting function to error in each bin.

Figure 5.3 shows an example of a 2-dimensional distribution for  $1.90 \leq p < 1.95$  GeV/c and  $0.6 \leq \eta < 0.8$  with *kaon* mass assumption. On the top left, a raw distribution is shown. On the lower middle, only the statistically significant section cut is shown. The lower middle plot is fitted for 3-particles:  $\pi$ ,  $K$ , and  $p$ ; the fitting results are shown in top middle ( $n\sigma_{dE/dx}^k$  fitted with Gaussian) and right ( $\Delta\beta_k^{-1}/\beta^{-1}$  fitted with Student's T) figures. Figure 5.4 shows same Figure as 5.3 but at higher momentum.

It shows that it is hard to fit such distributions as individual particle distributions overlap and separation power<sup>2</sup> is lost.

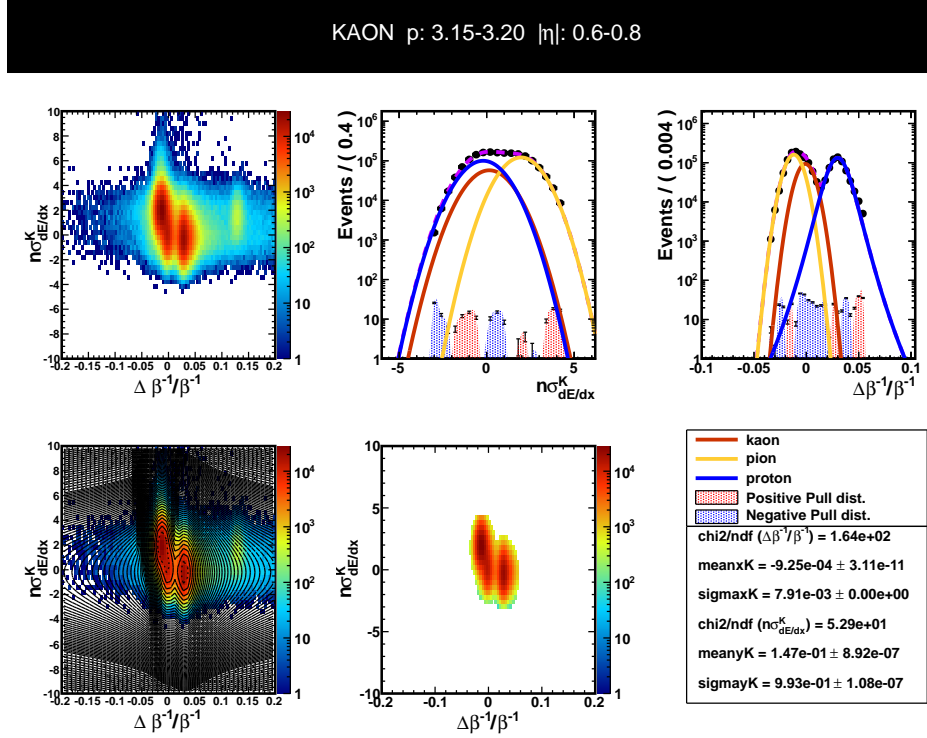


**Figure 5.4** 2-Dimensional distribution charged particles in  $\Delta\beta_k^{-1}/\beta^{-1}$  and  $n\sigma_{dE/dx}^k$ . The distribution is fit for *kaons* using both Gaussian ( $y$ -axis) and Student's T( $x$ -axis) distributions. The pull-distribution is the ratio of difference of data and fitting function to error in each bin.

<sup>2</sup>Separation power =  $\frac{|\mu_i - \mu_j|}{\sqrt{\sigma_i^2 + \sigma_j^2}}$ , where  $i$  and  $j$  are particle types with  $\mu$  mean and  $\sigma$  standard deviations of their distributions.

## 5.5 Probability cut

For identification of a particle from a distribution of particles, a good question to ask would be, “what is the probability of a particle being a particle of a certain type?”. The fitting parameters from the multi-particle fit are utilized to construct a probability measure. The probability is measured for a one-dimensional distribution as follows.

$$p^i(X) = \frac{N^i \times f^i(X; \Theta^i)}{\sum_{j=e,\pi,K,p} [N^j \times f^j(X; \Theta^j)]}, \quad (5.6)$$

where for  $i^{th}$  particle,  $p^i(X)$  is the probability of  $X$  coming from probability density function  $f^i(X; \Theta^i)$  with  $\Theta^i$  as a set of parameters and  $N^i$  is fraction of yield such that  $\sum_i N^i = 1$ . For a Gaussian distribution, the parameter sets  $\Theta^i$  includes mean  $\mu^i$  and standard deviation  $\sigma^i$ . For the Student's T distribution,  $\mu^i$  is mean of the distribution,  $\nu^i$  is the degree of freedom and  $\lambda^i$  is the scale parameter. Because of the complicated shape of the distributions, it is usually hard to find the yield. Therefore, a Monte Carlo method is adopted to calculate the yield fractions.

Similarly, for a 2-dimensional distribution the probability measure is given as follows.

$$p^i(X, Y) = \frac{N^i \times f^i(X; \Theta_X^i) \times f^i(Y; \Theta_Y^i)}{\sum_{j=e,\pi,K,p} [N^j \times f^j(X; \Theta_X^j) \times f^j(Y; \Theta_Y^j)]}, \quad (5.7)$$

where  $X$  and  $Y$  represent types of probability density functions (*PDF*) and  $\Theta^i$  represents the parameter set in the *PDF*. In this thesis, the Gaussian and

Student's T *PDFs* are used.

In Equations 5.6 and 5.7, the value of the probability is  $0 \leq p^i \leq 1$ . We choose a threshold cut and select a type of particle.

Another important cut that is made before making the probability cut is the  $2D$   $n\sigma$  cut. The distance of measured value from the mean ( $\mu$ ) normalized by its standard deviation  $\sigma$  is called  $n\sigma$ . The cut on  $n\sigma$  removes the points in distribution which are far away from its mean by taking points within an elliptical shape. The  $2D$   $n\sigma$  cut is defined as

$$\begin{aligned} \frac{n\sigma_X^2}{a^2} + \frac{n\sigma_Y^2}{b^2} &\leq 1, \quad \text{where} \\ n\sigma_X &= \frac{X - \mu_X}{\sigma_X}, \quad X = \frac{\Delta\beta^{-1}}{\beta^{-1}} \quad \text{and} \\ n\sigma_Y &= \frac{Y - \mu_Y}{\sigma_Y}, \quad Y = n\sigma_{dE/dx}, \end{aligned} \quad (5.8)$$

where  $a$  and  $b$  are either of semi-major or semi-minor axes. In the current thesis data analysis, the values of both  $a$  and  $b$  are chosen to be 3.

## 5.6 Efficiency and Purity

The  $2D$  fitting of the distributions allows us to extract fitting parameters which can be utilized to simulate the distribution using a Monte Carlo. The Monte Carlo sample is refitted to find the selected tracks,  $N_{Sel}$ . Having information from both the number of Monte Carlo tracks,  $N_{MC}$  and  $N_{Sel}$ , the PID efficiency is defined as the proportion of particles of a given species that are identified correctly by the PID selections.

$$\mathcal{E}^i = \frac{N_{Sel}^i}{N_{MC}}, \quad (5.9)$$

where  $\mathcal{E}^i$  is the efficiency of the  $i^{th}$  particle species. The efficiency calculation is made after making pre-cuts such as a cut in  $2D$   $n\sigma$  as discussed in Section 5.4 and probability  $p$  as discussed in Section 5.5.

Similarly, the purity  $\mathcal{P}^i$  of the PID is defined as the ratio between the number of correctly identified particles and the total selected.

$$\mathcal{P}^i = \frac{N_{Sel}^i}{\sum_j N_{Sel}^j}, \quad (5.10)$$

where  $i$  is a particle type where as  $j$  includes all particle types.

Because of the slightly different distributions of particles in different momentum ( $p$ ) and pseudo-rapidity ( $\eta$ ), the efficiency  $\mathcal{E}$  and purity  $\mathcal{P}$  for each particle is a function of  $\eta$  and  $p$ . As discussed earlier in Section 5.2 and 5.3, the distributions of particles for higher  $p$  overlap with each other making it hard to identify them correctly. This results in a reduction in both  $\mathcal{E}$  and  $\mathcal{P}$  of PID. In fact, this is one of the factors used to choose the upper bound of the momentum for PID. In this thesis, the upper bound of momentum is chosen to be  $p_T \leq 3.20$  GeV. Figures 5.5, 5.6 and 5.7 show how the efficiency and purity of PID change with  $p$  and  $\eta$ . It is seen that the efficiency and purity for *pions* and *kaons* drops rapidly for  $p > 2.5$  GeV, whereas it tends to stay high for *protons*. In the right bottom panel of each Figure 5.5, 5.6 and 5.7, the total purity tends to stay high because of larger particle concentration at lower momenta.

PION PID Cut(0.60) Efficiency and Purity

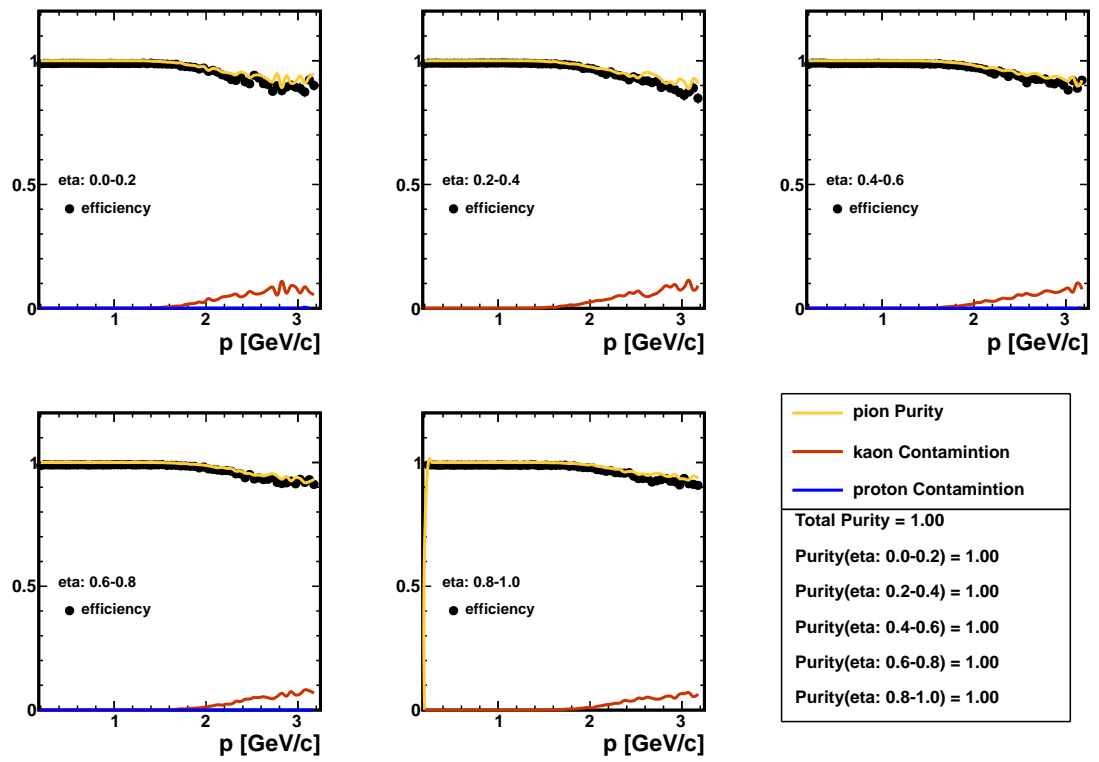


**Figure 5.5** Efficiency and Purity of  $\pi$  as a function of  $p$  and  $\eta$ . Together with the probability cut of 0.6,  $2D n\sigma$  cut,  $a = b = 3$ , was applied.

### KAON PID Cut(0.60) Efficiency and Purity

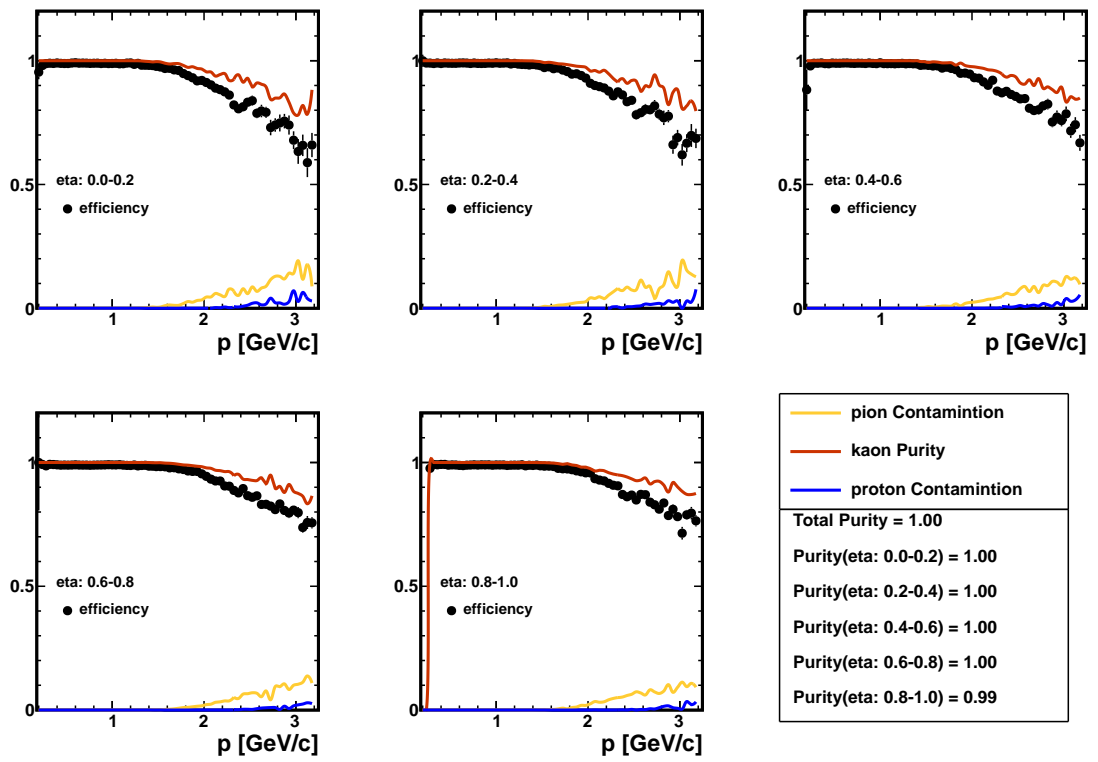


**Figure 5.6** Efficiency and Purity of  $K$  as a function of  $p$  and  $\eta$ . Together with the probability cut of 0.6,  $2D n\sigma$  cut,  $a = b = 3$ , was applied.

PROTON PID Cut(0.60) Efficiency and Purity

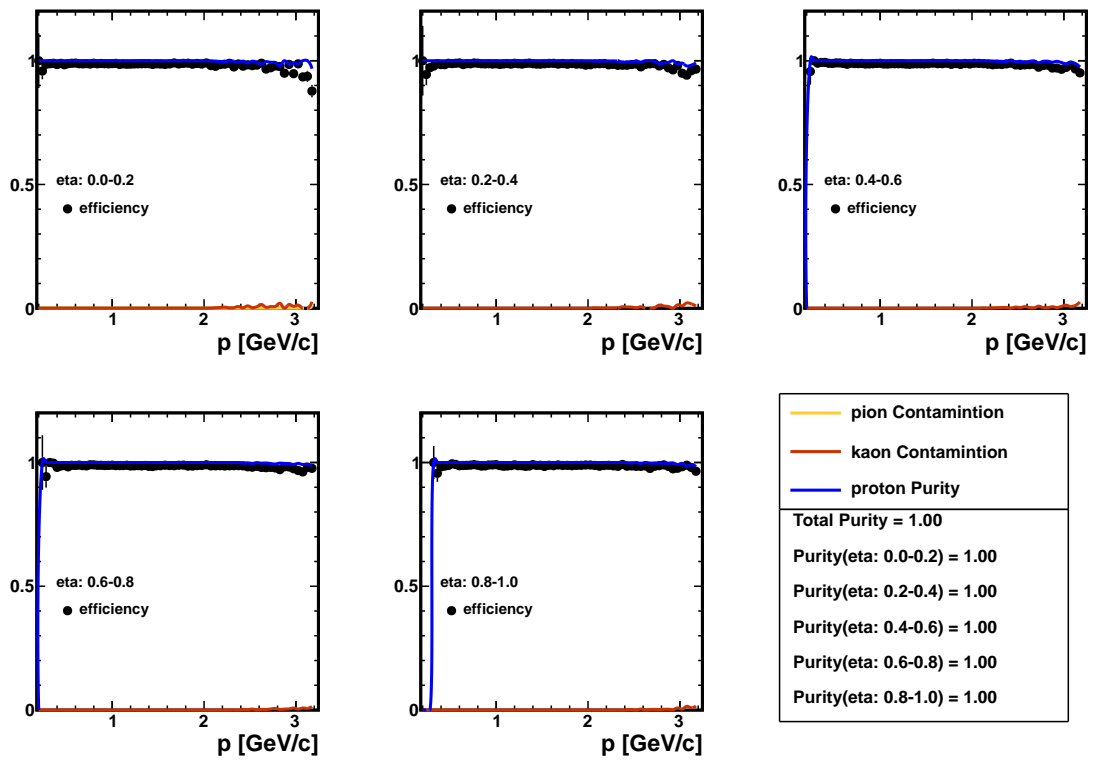


**Figure 5.7** Efficiency and Purity of  $\pi$  as a function of  $p$  and  $\eta$ . Together with the probability cut of 0.6,  $2D n\sigma$  cut,  $a = b = 3$ , was applied.

## Chapter 6

# Identified Particle Correlation

### 6.1 Introduction

In previous chapters a brief formal discussion of correlations was presented. In this chapter the results for identified particle correlations in different momentum sub-spaces are presented. The two-particle correlations are functions of the charge-signs of particles in the pair, the type of particles in the pair, the centrality, and the momentum ranges in which the correlations are measured. There are 11 centralities (numbered 0 through 10), 6 particle pair combinations ( $\pi\pi, \pi K, \pi p, Kp$  and  $pp$ ) where each particle pair type is separated into two categories of charge-sign: Like-Sign ( $LS$ ) and Unlike-Sign ( $US$ ). Each of the correlations is measured in different cut bins of momentum sub-space as defined in Chapter 3.

In this Chapter we will first present unidentified particle correlations for Run 2010 and 2011 data for comparison with previous results from Run2001 and 2004. The main features of unidentified particle correlations such as the centrality evolution of different components in the correlations are discussed. Next, we will present the most general features in identified particle correlations and discuss how the correlation of all particles in  $p_T$ -integrated space

compares to it. For the identified particle correlations, only the results from Run 2011 are presented in this thesis. Finally, the physics results for the quadrupole correlations component are presented and discussed.

## 6.2 Unidentified Particle Correlations

The unidentified particle charge independent (CI) correlations for Au+Au collision data at 200 GeV for Run 2001/2004 have been studied in Reference [5][37]. Except for small variations due to residual pileup effects, the correlations in Run 2010/11 are similar to those in Run 2001/2004. In these correlations the main components include:  $\cos(\phi_\Delta)$  (dipole) and  $\cos(2\phi_\Delta)$  (azimuthal harmonics, quadrupole), a 1D Gaussian on  $\eta_\Delta$ , a 2D same-side Gaussian, and a sharply peaked 2D exponential about  $(\eta_\Delta, \phi_\Delta) \rightarrow (0, 0)$ . The same-side Gaussian peak is hypothesized to be dominated by minijets (minimum-bias jets) and the sharp, exponential peak is understood to be due to quantum correlations called HBT (Hanbury Brown and Twiss effect [67]) and  $e^+e^-$  background pair production. The 1D Gaussian is due to soft physics (hadronization, soft gluon fragmentation and charge-ordering effects [68])[5][69]. The correlation

structure is well described by a 6-component (11-parameter) fit model.

$$\begin{aligned}
F &= A_{Dipole} \cos(\phi_\Delta - \pi) + A_{Quadrupole} \cos(2\phi_\Delta) \\
&+ A_{2DGaus} \exp \left\{ -\frac{1}{2} \left[ \left( \frac{\phi_\Delta}{\sigma_{\phi_\Delta}} \right)^2 + \left( \frac{\eta_\Delta}{\sigma_{\eta_\Delta}} \right)^2 \right] \right\} \\
&+ A_{1DGaus} \exp \left\{ -\frac{1}{2} \left( \frac{\eta_\Delta}{\sigma_0} \right)^2 \right\} \\
&+ A_{2DExpo} \exp \left\{ - \left[ \left( \frac{\phi_\Delta}{w_{\phi_\Delta}} \right)^2 + \left( \frac{\eta_\Delta}{w_{\eta_\Delta}} \right)^2 \right]^{1/2} \right\} + A_{Offset}, \quad (6.1)
\end{aligned}$$

where  $A_{Dipole}$ ,  $A_{Quadrupole}$ ,  $A_{2DGaus}$ ,  $A_{1DGaus}$ ,  $A_{2DExpo}$  and  $A_{Offset}$  are amplitudes of the Dipole, Quadrupole, 2D Gaussian, 1D Gaussian, 2D exponential and offset components, respectively. For illustration, the components are shown in Figure 6.5. The fitting parameters for unidentified particles in  $p_T$ -integrated momentum space have been studied [1][5]. In this thesis, besides making a qualitative discussion of the different components of correlations, I will focus on investigating the quantitative measure of parameter called  $v_2^2[2D]$ , proportional to  $A_{Quadrupole}$ . The event-wise azimuthal anisotropy in the particle distribution is thought to be the cause of  $v_2^2[2D]$  and it is conventionally called *elliptic flow*. It is related to the fitting parameter azimuthal quadrupole amplitude ( $A_{Quadrupole}$ ) discussed in [5][69], where

$$A_{Quadrupole}[2D] = 2 \frac{1}{2\pi} \frac{dN_{ch}}{d\eta} v_2^2[2D], \quad (6.2)$$

where [2D] indicates that the quantities are obtained using 2-dimensional fitting procedure to 2D  $(\eta_\Delta, \phi_\Delta)$  data. If the pre-factor is not applied to the correlations, then  $A_{Quadrupole}[2D] = 2v_2^2[2D]$ .

The model elements in Equation 6.1 were studied in detail for  $p_T$ -integrated non-identified two-particle correlations in References [1][5]. The elements of the model, e.g. dipole, quadrupole, 2D Gaussian etc, were determined from observed structures in the correlation data, and not from any physical model of the reaction. Four of the model elements were obtained directly from correlation observed in  $p+p$  minimum-bias data for LS, US with low  $p_T$  cut and with higher  $p_T$  cut. These plots reveal 4 distinct structures [70][71][72][73]. For the LS-soft, the 2D exponential due to the HBT are seen, and 1D Gaussian due to soft, longitudinal fragmentation. For US-soft the 2D exponential due to conversion  $e^+e^-$  pairs and the 1D Gaussian are seen. Similarly, in LS and US-hard correlations the 2D Gaussian and the away-side dipole are seen. The 2D Gaussian and away-side dipole from the  $p+p$  correlations are well described by PYTHIA jets with no lower  $p_T$  cut-off, i.e., minijets, which are dominated by  $Q \sim 5$  GeV. For the Au+Au collision data, these same model elements, plus the quadrupole, accurately describe the  $p_T$ -integrated, non-identified correlations. The quadrupole is required by the Au+Au data. In Elizabeth Oldag's  $p_T$ -dependent non-identified particle correlation analysis, two new features appear: the 2D Gaussian develops a leptokurtic shape at higher  $p_T$  and in more central collision, and in some  $(y_T, y_T)$  bins there are small dips near  $(\eta_\Delta, \phi_\Delta) \sim (0, 0)$  [37].

Previous experience in fitting correlation data with Equation 6.1 shows that the quadrupole element is the least sensitive to fitting ambiguities and has small systematic uncertainty. For this reason, the present fitting analysis

focuses on the quadrupole for the 2000 correlation plots. It is impractical to obtain high quality determination of all model elements for all 2000 correlation plots produced in this thesis in a reasonable time frame. For example, the sudden increase in the  $\eta$  width of the same-side 2D Gaussian peak near mid-centrality has only been seen in  $p_T$ -integrated non-identified particle correlations. It is important to find out whether or not this same ridge and sudden appearance occurs for  $pi$ ,  $K$  and  $p$ . However, that requires meticulous fitting effort to ensure that all fitting ambiguities are under control. The effort must wait for later, focused study.

### 6.2.1 Run 2010

Figures 6.1 and 6.2 show Like-Sign( $LS$ ) and Unlike-Sign( $US$ ) 2D two-particle correlations on  $(\eta_\Delta, \phi_\Delta)$  of all particles for 200 GeV  $p_T$ -integrated data from Run 2010. These results are obtained from about 140-million minimum-bias events. The correlations are measured in 11 centrality bins. To remove pileup, the vertex ranking cut and Duncan's pileup cut have been applied. As an additional cut, all the tracks are required to have a TOF hit. Therefore, the  $\eta_\Delta$  axis of the correlation is narrower than the standard range of  $(-2, 2)$ . In [5] the features of charge independent (CI) correlations in Au+Au collisions were presented. The sum of the LS and US pair correlations in Figures 6.1 and 6.2 compare well with the CI correlations in [1][5] with respect to the Dipole, Quadrupole, 1D Gaussian, 2D Gaussian and 2D Exponential components.

No pre-factor was applied to the correlations in Figures 6.1 and 6.2.

As discussed in Chapter 3, the pre-factors for LS and US correlation can be related to pre-factor in CI correlations, where

$$\begin{aligned}\sqrt{\rho'_{ref}{}^{LS}} &= \sqrt{\frac{1}{2}\rho'_{ref}{}^{CI}} = \frac{1}{\sqrt{2}} \left[ \frac{1}{2\pi} \frac{dN_{ch}}{d\eta} \right] \\ \sqrt{\rho'_{ref}{}^{US}} &= \sqrt{\frac{1}{2}\rho'_{ref}{}^{CI}} = \frac{1}{\sqrt{2}} \left[ \frac{1}{2\pi} \frac{dN_{ch}}{d\eta} \right],\end{aligned}\tag{6.3}$$

where  $\frac{dN_{ch}}{d\eta}$  can be used from reported values in Table III of [5].

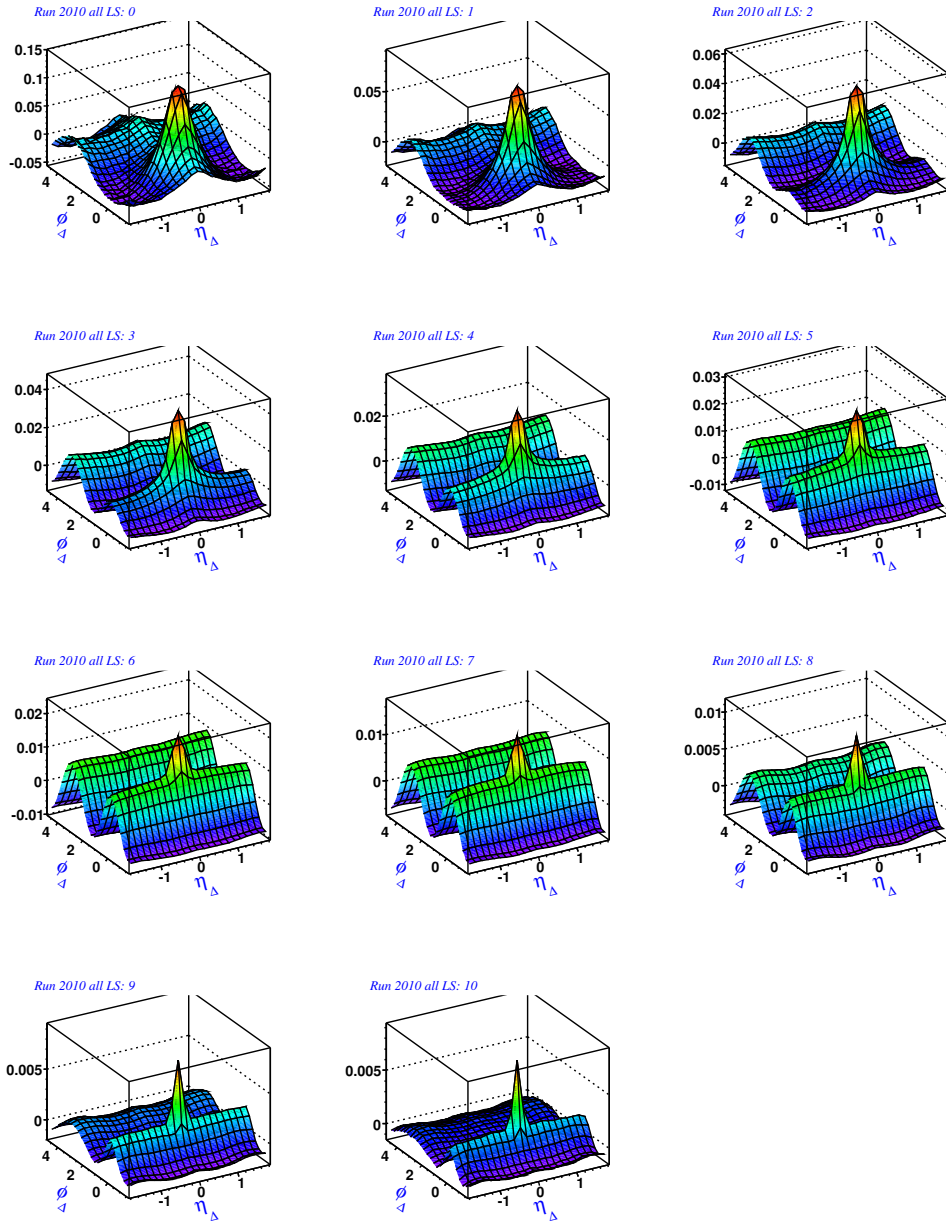


**Figure 6.1** Like-Sign correlations,  $\frac{\Delta\rho}{\rho_{ref}}$ , of all particles for 200 GeV  $p_T$ -integrated data from Run 2010. Correlations are in approximately 10% fractional centrality from centrality IDs 0 through 8 and in 5% fractional centrality in centrality IDs 9 and 10. No pre-factor has been applied.

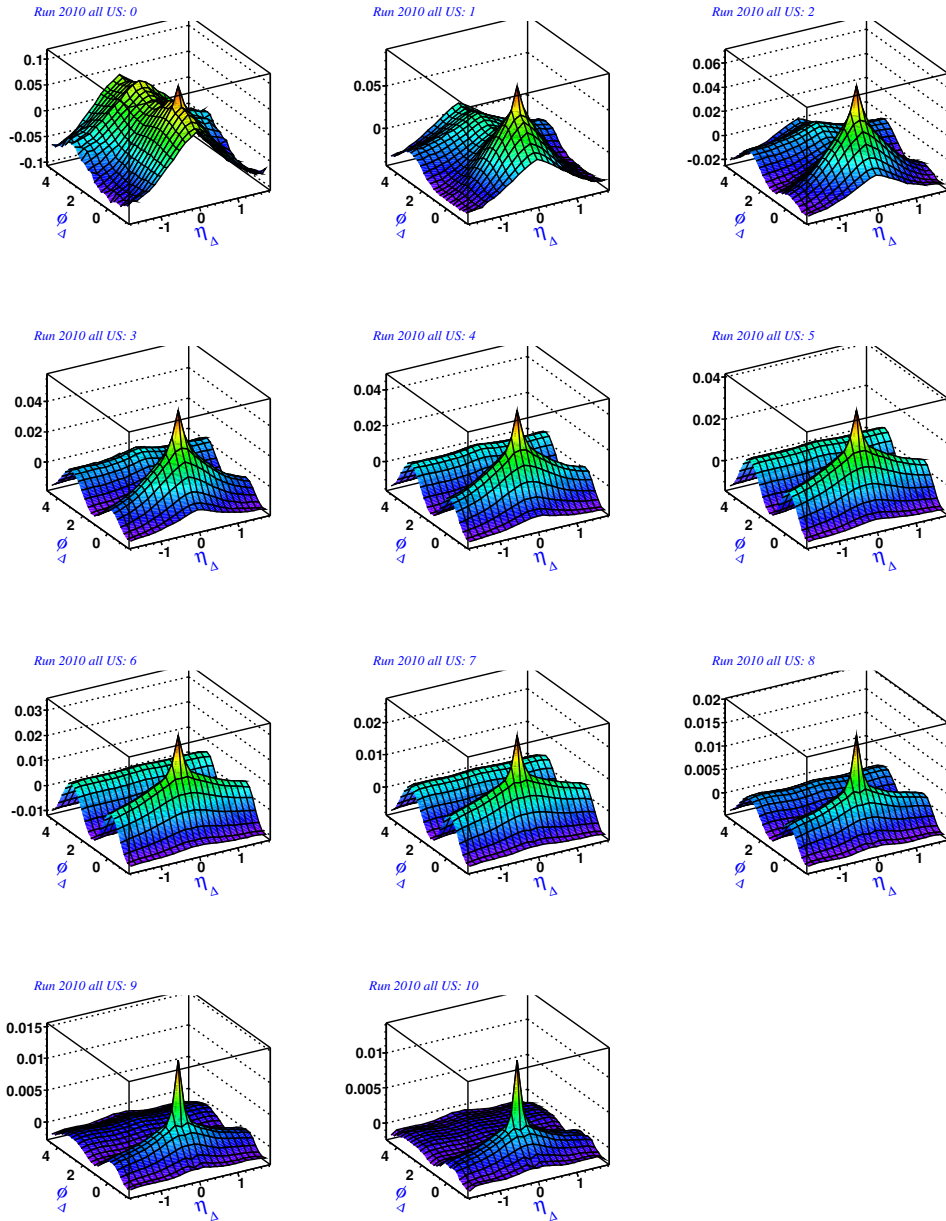


**Figure 6.2** Unlike-Sign correlations,  $\frac{\Delta\rho}{\rho_{ref}}$ , of all particles for 200 GeV  $p_T$ -integrated data from Run 2010. Correlations are in approximately 10% fractional centrality from centrality IDs 0 through 8 and in 5% fractional centrality in centrality IDs 9 and 10. No pre-factor has been applied.

### 6.2.2 Run 2011

Figures 6.3 and 6.4 show LS and US 2D two-particle correlations on  $(\eta_\Delta, \phi_\Delta)$  for all particles for 200 GeV  $p_T$ -integrated data from Run 2011. These correlations have been measured from about 11-million minimum-bias events. The correlations are measured in 11 centrality bins. To remove pileup, the vertex ranking cut and Duncan's pileup cut were applied. The correlations have same features such as dipole, quadrupole, 1D Gaussian, 2D Gaussian and 2D exponential components as seen previously. Figure 6.5 shows the fit decomposition in one centrality bin. Figures 6.6 and 6.7 show the model fit and residual (i.e., data- fit) of US correlations in Figure 6.4 after fitting with the function in Equation 6.1. The negligibly small residue demonstrates that the fitting function is sufficient to represent the structure in the correlations.

As in Run 2010 *LS* and *US* correlations, no pre-factor has been applied to the correlations in Figures 6.3 and 6.4. The pre-factors can be calculated using 6.3.

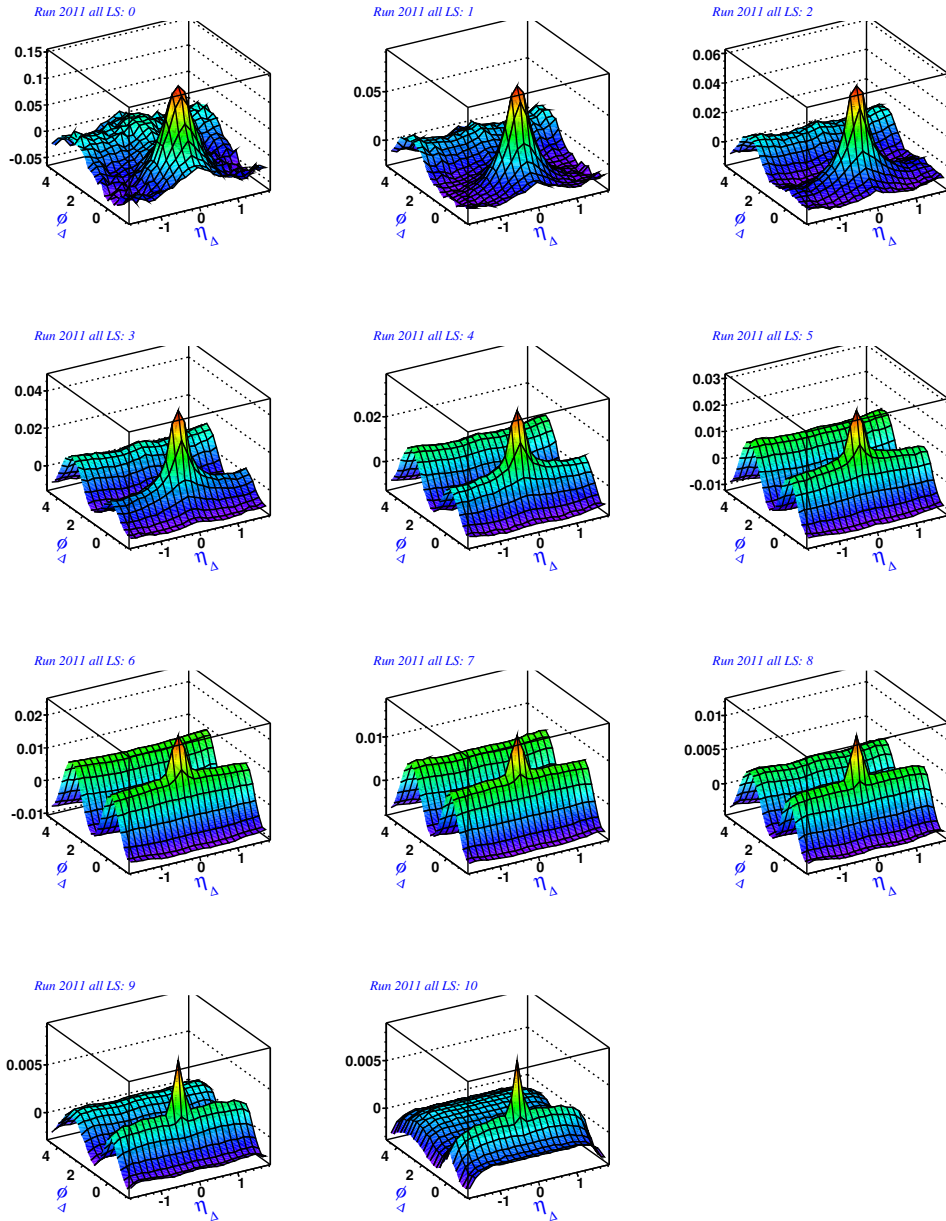


**Figure 6.3** Like-Sign correlations,  $\frac{\Delta\rho}{\rho_{ref}}$ , of all particles for 200 GeV  $p_T$ -integrated data from Run 2011. Correlations are in approximately 10% fractional centrality from centrality IDs 0 through 8 and in 5% fractional centrality in centrality IDs 9 and 10. No pre-factor has been applied.

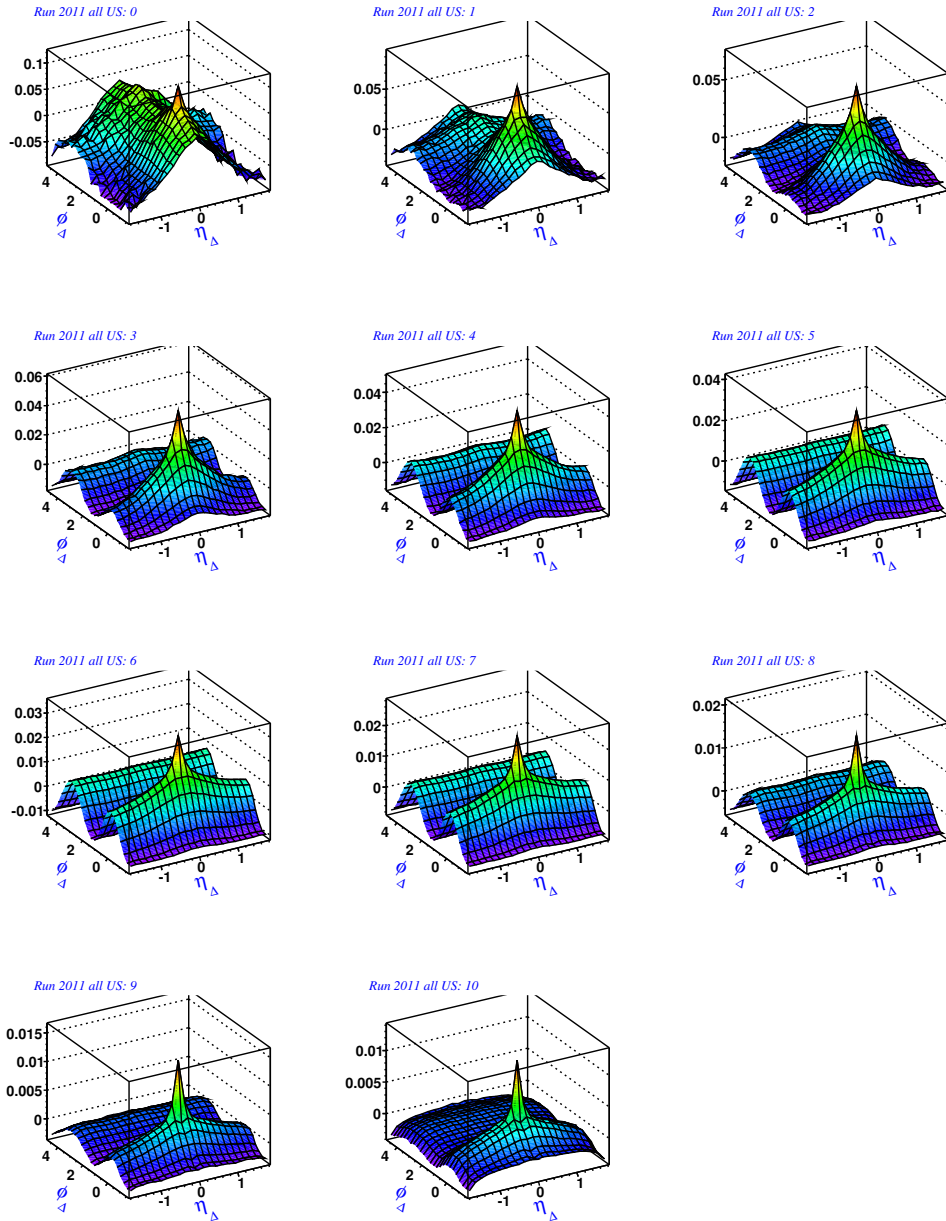


**Figure 6.4** Unlike-Sign correlations,  $\frac{\Delta\rho}{\rho_{ref}}$ , of all particles for 200 GeV  $p_T$ -integrated data from Run 2011. Correlations are in approximately 10% fractional centrality from centrality IDs 0 through 8 and in 5% fractional centrality in centrality IDs 9 and 10. No pre-factor has been applied.

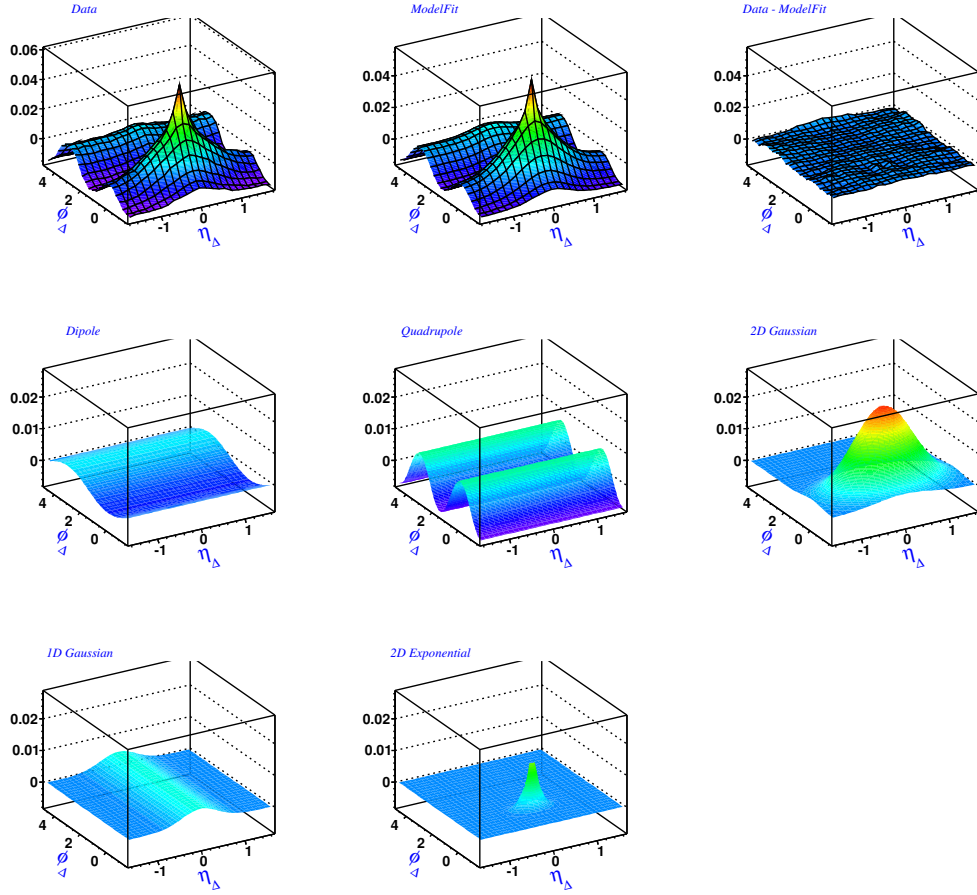


**Figure 6.5** Fit decomposition of the 55-64% centrality Unlike-Sign correlations,  $\frac{\Delta\rho}{\rho_{ref}}$ , of all particles for 200 GeV  $p_T$ -integrated data from Run 2011. The top panels show from left to right the correlations from data, model fit and residuals. The middle panels show the dipole, quadrupole and same-side 2D Gaussian. The bottom panels similarly show the 1D Gaussian on  $\eta_{\Delta}$  and the 2D exponential. For visual clarity the middle and bottom rows are zoomed in by a factor of 2.

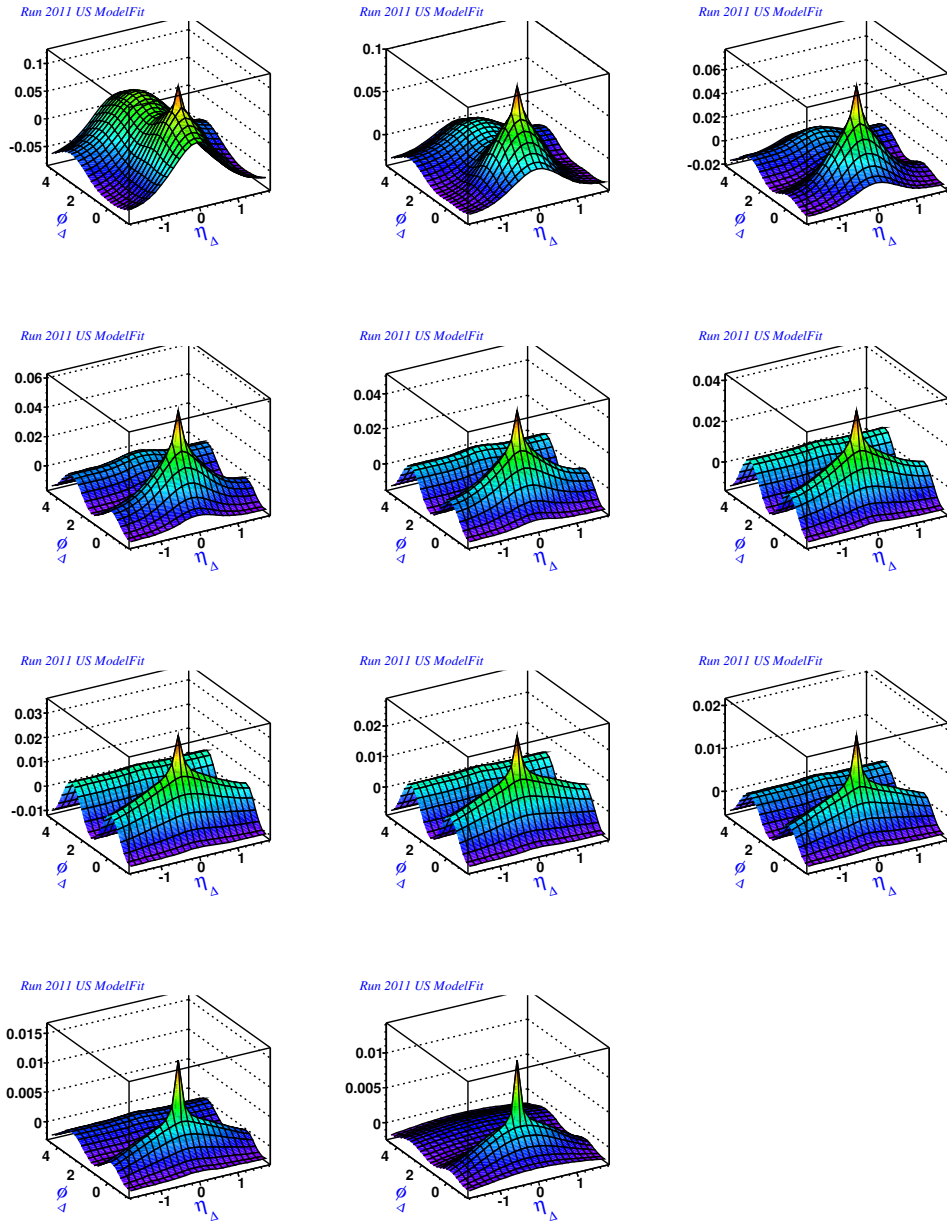


**Figure 6.6** Fits to Unlike-Sign correlations,  $\frac{\Delta\rho}{\rho_{ref}}$ , in Figure 6.4.

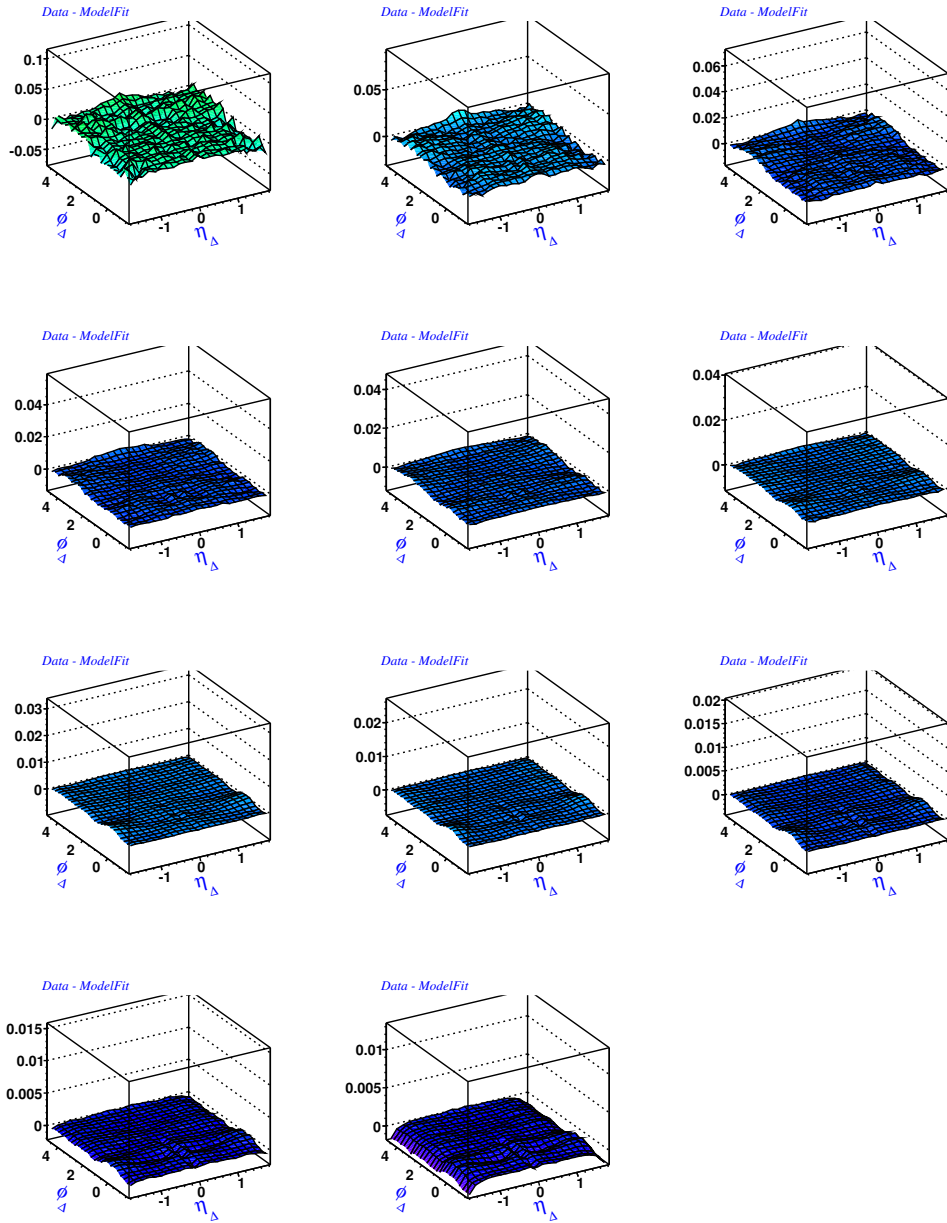
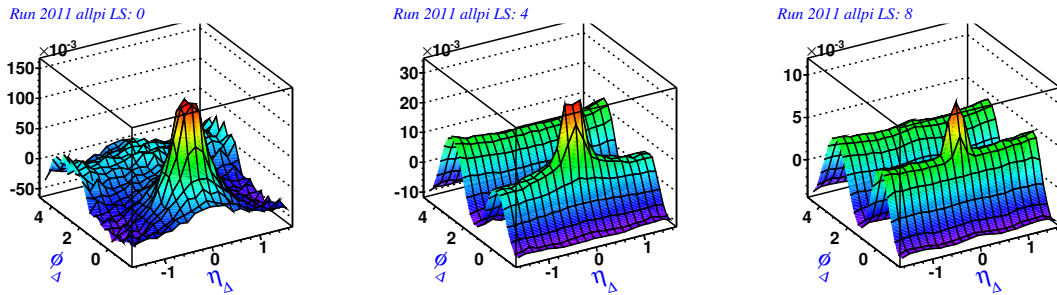


Figure 6.7 Residuals from fits to Unlike-Sign correlations,  $\frac{\Delta\rho}{\rho_{ref}}$ , in Figure 6.4.

The particle identification has provided an opportunity to explore the correlations between the particles of known types. We will present evidence of several new features of identified particle correlations in next sub-sections.

### 6.3 $\pi - \pi$ Correlations

The  $p_T$  integrated  $\pi - \pi$  correlations are similar to the all-particle correlations. This is because *pions* are the dominant particle species produced in the collisions at the lower momentum which dominate the  $p_T$  integrated results. Figures 6.8 and 6.9 show LS and US correlations for 3 centralities. All the features seen in all-particle correlations are seen in *pion-pion* correlations.



**Figure 6.8** Like-Sign correlations,  $\frac{\Delta\rho}{\rho_{ref}}$ , of *pions* for 200 GeV  $p_T$ -integrated data from Run 2011. The correlations are in centrality IDs 0, 4 and 8 (i.e., centrality percentages 84 – 93%, 50 – 60% and 10 – 20% respectively). No pre-factor has been applied.

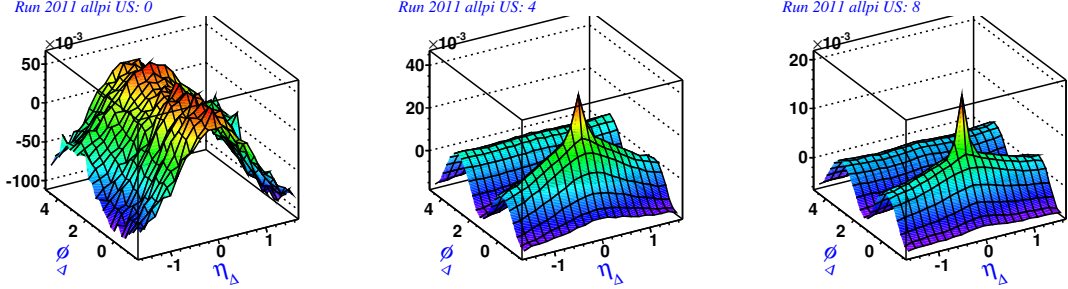


**Figure 6.9** Unlike-Sign correlations,  $\frac{\Delta\rho}{\rho_{ref}}$ , of *pions* for 200 GeV  $p_T$ -integrated data from Run 2011. The correlations are in centrality IDs 0, 4 and 8 (i.e., centrality percentages 84 – 93%, 50 – 60% and 10 – 20% respectively). No pre-factor has been applied.

However, different ranges of momenta contribute different weight to  $p_T$ -integrated correlations. Figure 6.10 shows the LS correlations for different momentum cut bins for a centrality bin 5. From Figure 6.10 it is evident that the sharp peak in LS correlation (quantum correlation) appears almost exclusively in diagonal cut bins (e.g., cut bins 0, 6, 12, 18 and 24). In the diagonal cut bins the vector difference between the pair of momenta can be small, which allows the HBT correlations to dominate at  $(\eta_\Delta, \phi_\Delta) \rightarrow (0, 0)$ . A few cut bins such as 1, 2, 5 and 10 show some new features which were not seen in  $p_T$  integrated correlations. In cut bins 1 and 5, a closer look shows that there is a small volcano shaped enhancement in correlations around  $(\eta_\Delta, \phi_\Delta) \rightarrow (0, 0)$ . However, in cut bins 2 and 10 there is a suppression in correlation. The reason for suppression in the correlation near  $(\eta_\Delta, \phi_\Delta) \rightarrow (0, 0)$  is not well understood. However, Coulomb repulsion might be playing a role to prevent

two particles from being too close to each other resulting a small suppressed correlation in that region.

Similarly, Figure 6.11 shows the US correlations in different momentum cut bins in the same centrality as in Figure 6.8. In the US correlations, the sharp 2D exponential peak dominate the diagonal bins. Besides a Coulomb attraction between the unlike-signed *pions*, the correlation between  $e^+$  and  $e^-$  contamination<sup>1</sup> might have contributed to the correlations. The near side 2D Gaussian amplitude increases as the momentum of the particles increases. For example, in cut bin 24, the 2D Gaussian structure is a dominant component whereas in cut bin 0 the 2D exponential component is dominant.

The correlations in all- $y_T$  cut bins have been studied for all 11 centrality bins. The most common features for the  $\pi - \pi$  correlations can be summarized as follows.

### **Like-Sign Correlations:**

Quadrupole model element is evident in all centralities and all cut bins conforming non-identified particle correlation result. Similarly, a 2D Gaussian on  $(\eta_\Delta, \phi_\Delta)$  and dipole (jets) appear at higher  $y_T$  only, where gluon fragmenting into LS  $\pi + \pi$  is energetically more demanding than into  $\pi^+$  and  $\pi^-$ . However, 1D Gaussian on  $\eta_\Delta$  is seen only in the peripheral collision centralities at lower  $y_T$ . Similarly, the 2D exponential is present only along diagonal cut bins

---

<sup>1</sup>The identified particles are not 100% pure. Contamination of electrons in the pion sample is one of the major causes of lower pion purity at lower momentum.

(e.g., 0, 6, 12, 18 and 24) as expected for HBT correlations. Minijets and elliptic flow correlations are evident throughout the  $y_T$  and centrality ranges. The unknown structures at (0,0) in  $y_T$  bins 1, 5 (low  $y_T$ ) is perhaps due to Coulomb repulsion between low  $p_T$  pions.

### **Unlike-Sign Correlations:**

The dipole, quadrupole and 2D Gaussian are significant in all centralities and all cut bins for the US correlations. The 1D Gaussian on  $\eta_\Delta$  appears only in the lower half of the momentum range (e.g., cut bins: 0, 1, 2, 3, 5, 6, 7, 8, 10, 11, 12, 15 and 16) and for centrality  $< 4$  (peripheral collisions). Similarly, the 2D exponential component appears in a band close to the diagonal bins (e.g. cut bins: 0, 1, 2, 5, 6, 7, 8, 10, 11, 12, 13, 15, 16 and 17) only. The 2D Gaussian and dipole appears much more prominently than in LS correlations and the 2D Gaussian develops the leptokurtic shape at higher  $y_T$  bins as expected for HBT. This is also seen in non-identified particle correlations and may indicate the reduction in the “ridge” correlation relative to the central ( $\eta_\Delta \sim 0$ ) portion of the jet. Evidence of the same-side,  $\eta$ -elongation, or the “ridge” seen in non-identified 2D-exponential seen at lower  $y_T$ , as expected for conversion  $e^+e^-$ .

These results suggest that minijets and elliptic flow correlations are evident in all centralities and  $y_T$  bins, while soft physics related correlations due to hadronization, soft-fragmentation and charge-ordering effects appear only in more peripheral collisions at lower  $p_T$ .

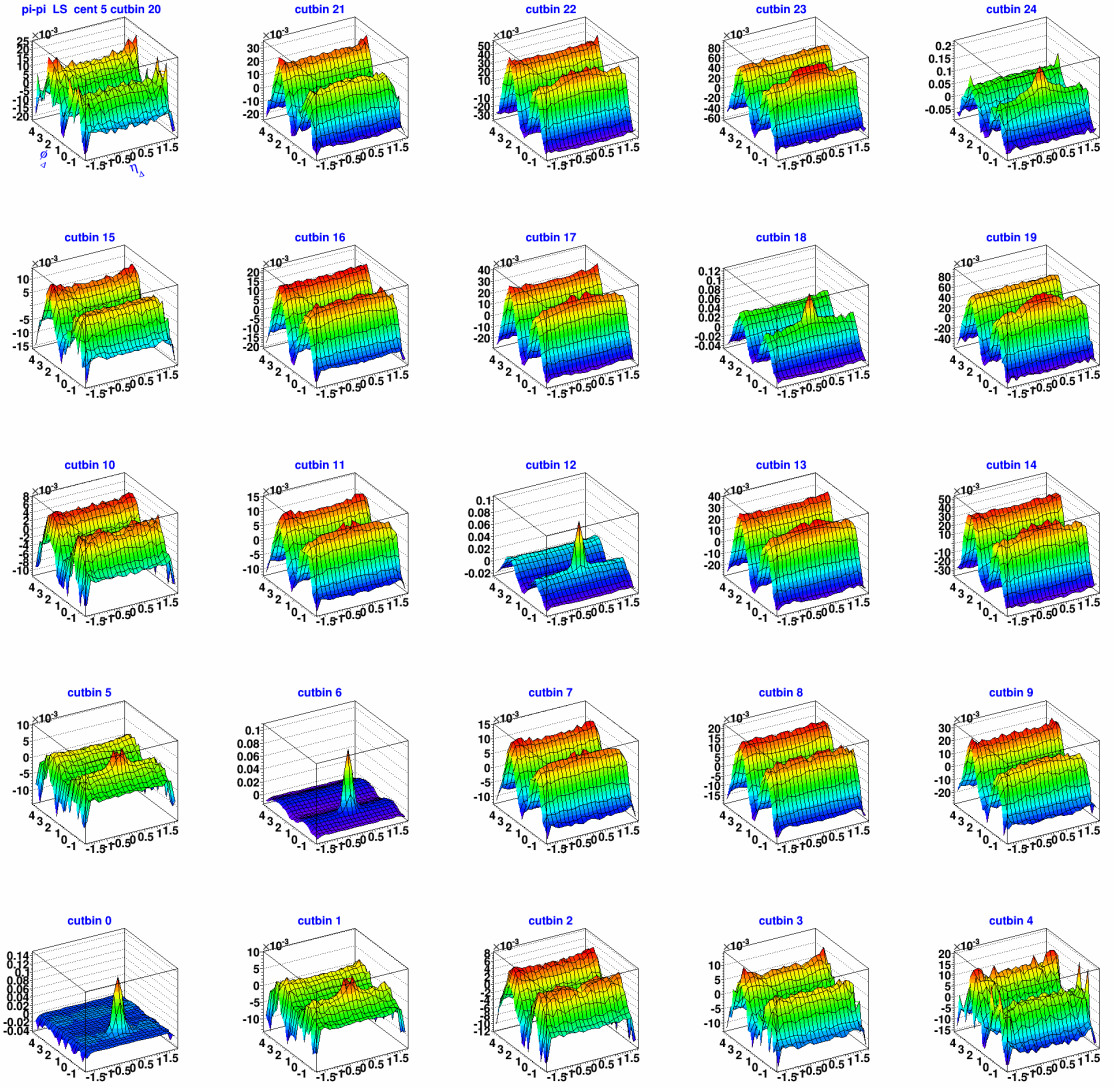


**Figure 6.10** Like-Sign correlations,  $\frac{\Delta\rho}{\rho_{ref}}$ , of *pions* for 200 GeV in different  $y_T$  sub-bins for a centrality 38 – 46%. The  $y_T$  spectrum is sub-divided into  $5 \times 5 = 25$  cut bins for the correlations. The binning scheme is discussed in Chapter 3. Correlations in  $(y_{T1}, y_{T2})$  are statistically equal to those in symmetric bin  $(y_{T2}, y_{T1})$ .

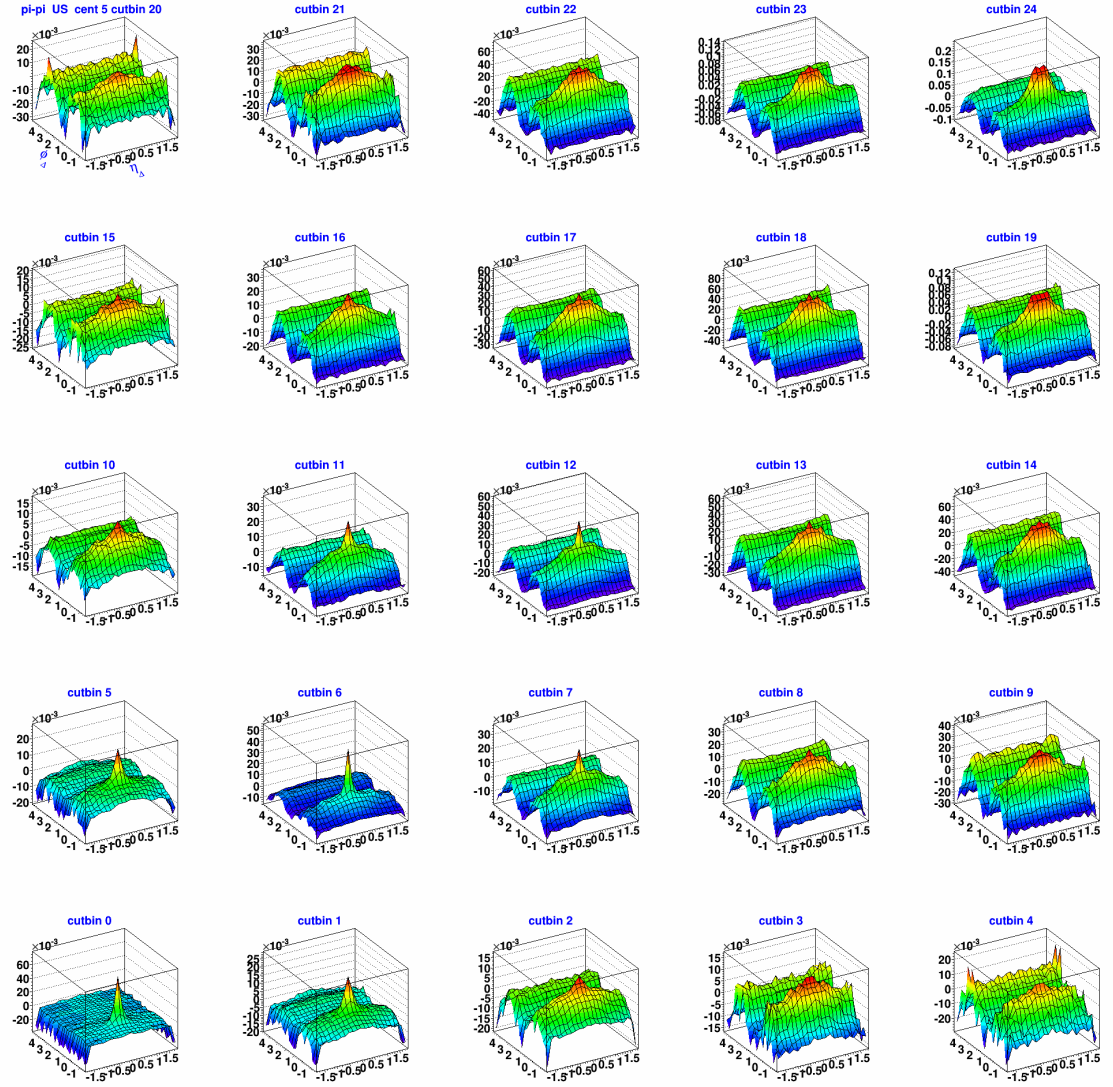


**Figure 6.11** Unlike-Sign correlations,  $\frac{\Delta\rho}{\rho_{ref}}$ , of *pions* for 200 GeV in different  $y_T$  sub-bins for a centrality 38 – 46%. The  $y_T$  spectrum is sub-divided into 5 sub-bins that creates  $5 \times 5 = 25$  cut bins for correlations. The binning scheme is discussed in Chapter 3. Correlations in  $(y_{T1}, y_{T2})$  are statistically equal to those in symmetric bin  $(y_{T2}, y_{T1})$ .

**Fitting Parameter  $v_2^2[2D]$ :**

All the *pion-pion* correlations were fitted using some or all components of the 6-component fitting model in Equation 6.1. The correlation structures strongly evolve with centrality and with the momentum cut bin. There are many sharp transitions in the structures. In some centralities, correlations in a cut bin are completely different than the correlations in another cut bin in its neighborhood. Based on visual observation, in some spaces, the correlation (e.g., cut bin 15 in LS correlations Figure 6.10) structure can be represented with just two components, the dipole and quadrupole. Fitting with more than the required components potentially causes fitting ambiguities. In some spaces, the 6-component model is not sufficient to represent the structure in the data. For example, the “volcano” structure in cut bin 5 of LS correlations in 6.10 cannot be modeled with the 6-components. Therefore, fitting all correlation structures with a single model suffers either from fit ambiguities or from poor overall description of data. Based on visual inspection of correlation structures, only the relevant components of the 6-component model have been used in the present fitting procedure to reduce the effect of fitting ambiguities while obtaining a reasonable description of the correlations. A careful and minute study of each structure is ultimately required to find the best fitting parameters for all model elements. From the pool of 2134 correlations structures (correlations of 2 types (LS and US) and 11 centralities  $\times$  25  $\pi$ - $\pi$ , 16  $K$ - $K$ , 9  $p$ - $p$ , 20  $\pi$ - $K$ , 15  $\pi$ - $p$ , and 12  $K$ - $p$  cut bins) correlations, it is a challenge to come up with a suitable fit function in order to accurately determine the

a trends of all the parameters. The results in this thesis are representative of the general trends of the parameters.

Figure 6.12 shows the cut bin-wise trend of  $v_2^2[2D]$  with centrality. The  $x$ -axis of the figure represents a measure of centrality,  $\nu$  (defined as  $\frac{N_{binary}}{N_{participant}/2}$ )<sup>2</sup>, computed at fixed energy (200GeV) reported in Table III [5]. The trends of  $v_2^2[2D]$  for most of the momentum bins are consistent with previously studied trend.

---

<sup>2</sup>As discussed in Chapter 3:  $N_{binary} \equiv N_{bin}$  and  $N_{participant} \equiv N_{part}$ .

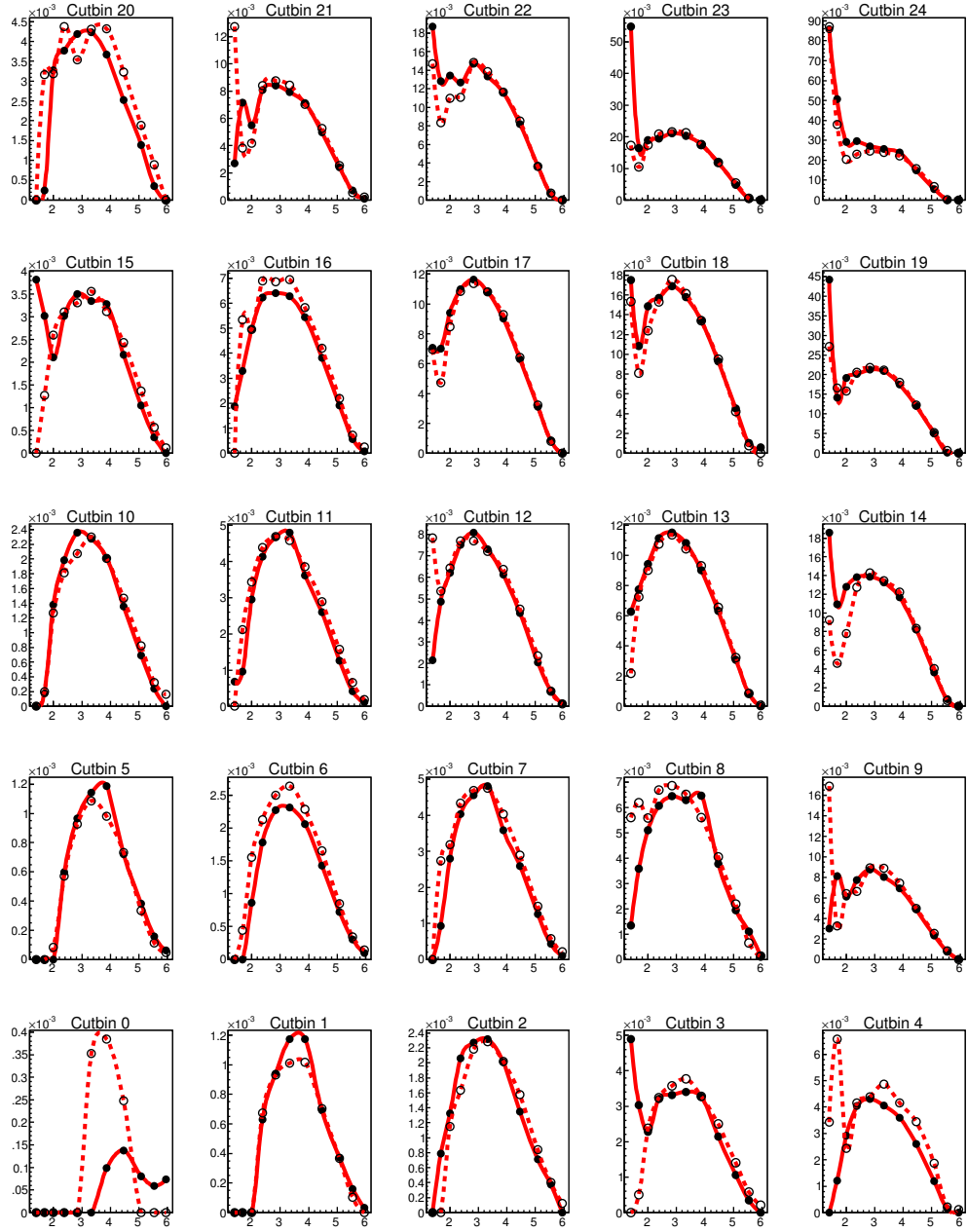


**Figure 6.12**  $\pi$ - $\pi$   $v_2^2[2D]$  as a function of centrality measure  $\nu$  (most peripheral in left to most central in right). LS: bold line with filled circle. US: dotted line with open circle. The 25 cut bins are according to binning scheme for  $\pi - \pi$  correlations as discussed in Chapter 3.

## 6.4 $K - K$ Correlations

Figure 6.13 and 6.14 show  $p_T$ -integrated  $K - K$  correlations. New feature, a “volcano” like shape, appears centered at  $(\eta_\Delta, \phi_\Delta \rightarrow (0, 0))$  in US correlations. Similarly, in LS correlations, 2D Gaussian and 2D exponential component are not seen as a dominant components.

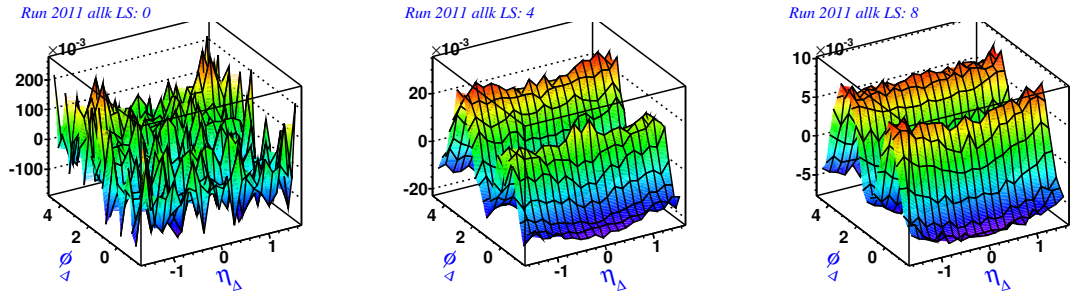


**Figure 6.13** Like-Sign correlations,  $\frac{\Delta\rho}{\rho_{ref}}$ , of *kaons-kaons* for 200 GeV  $p_T$ -integrated data from Run 2011. The correlations are in centrality IDs 0, 4 and 8 (i.e., centrality percentages 84 – 93%, 50 – 60% and 10 – 20% respectively). No pre-factor has been applied.

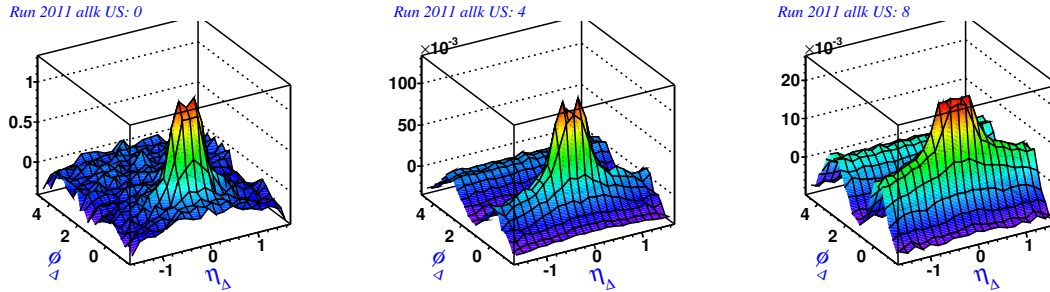


**Figure 6.14** Unlike-Sign correlations,  $\frac{\Delta\rho}{\rho_{ref}}$ , of *kaons-kaons* for 200 GeV  $p_T$ -integrated data from Run 2011. The correlations are in centrality IDs 0, 4 and 8 (i.e., centrality percentages 84 – 93%, 50 – 60% and 10 – 20% respectively). No pre-factor has been applied.

Figures 6.15 and 6.16 show that in centrality 38 – 46% correlations in different momentum ranges show different shapes. The structure of correlations are representative of the general trends of structures in all centralities. In the diagonal bins of  $K$ - $K$  US correlations, the structure due to  $\phi$ -meson decay to  $K^+K^-$  (discussed in next section 6.4) dominates the structure. Although there is a visible 2D Gaussian component in US correlations, it is completely absent in LS correlations. In LS correlations, in diagonal bins (e.g., in cut bins: 0, 5, 10, 15), a 2D exponential is a significant component. This component is possibly due to HBT correlations.

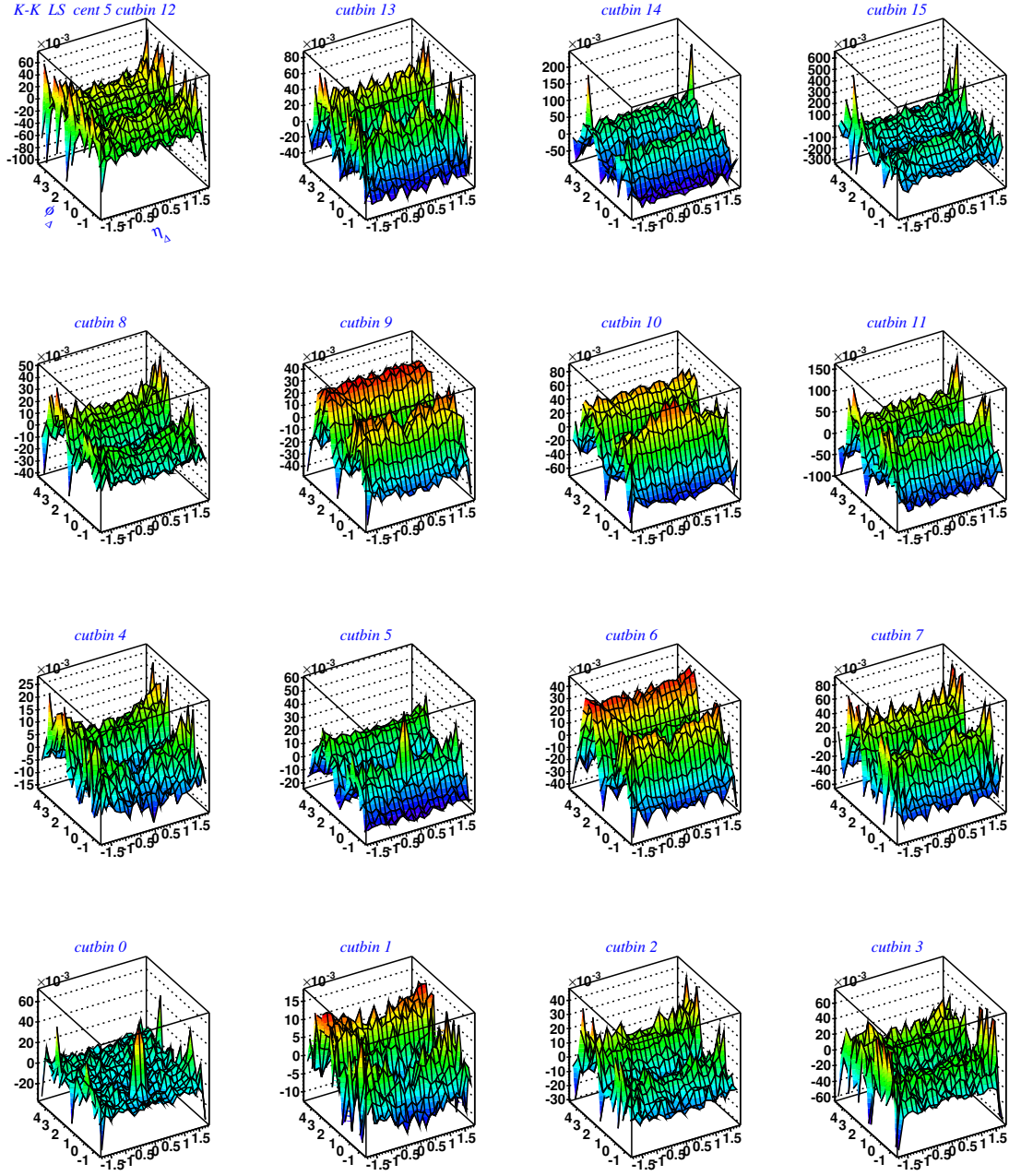


**Figure 6.15** Like-Sign correlations,  $\frac{\Delta\rho}{\rho_{ref}}$ , of kaons for 200 GeV in different  $y_T$  sub-bins for a centrality 38 – 46%. The  $y_T$  spectrum is sub-divided into 4 sub-bins that creates  $4 \times 4 = 16$  cut bins for correlations. The binning scheme is discussed in Chapter 3.

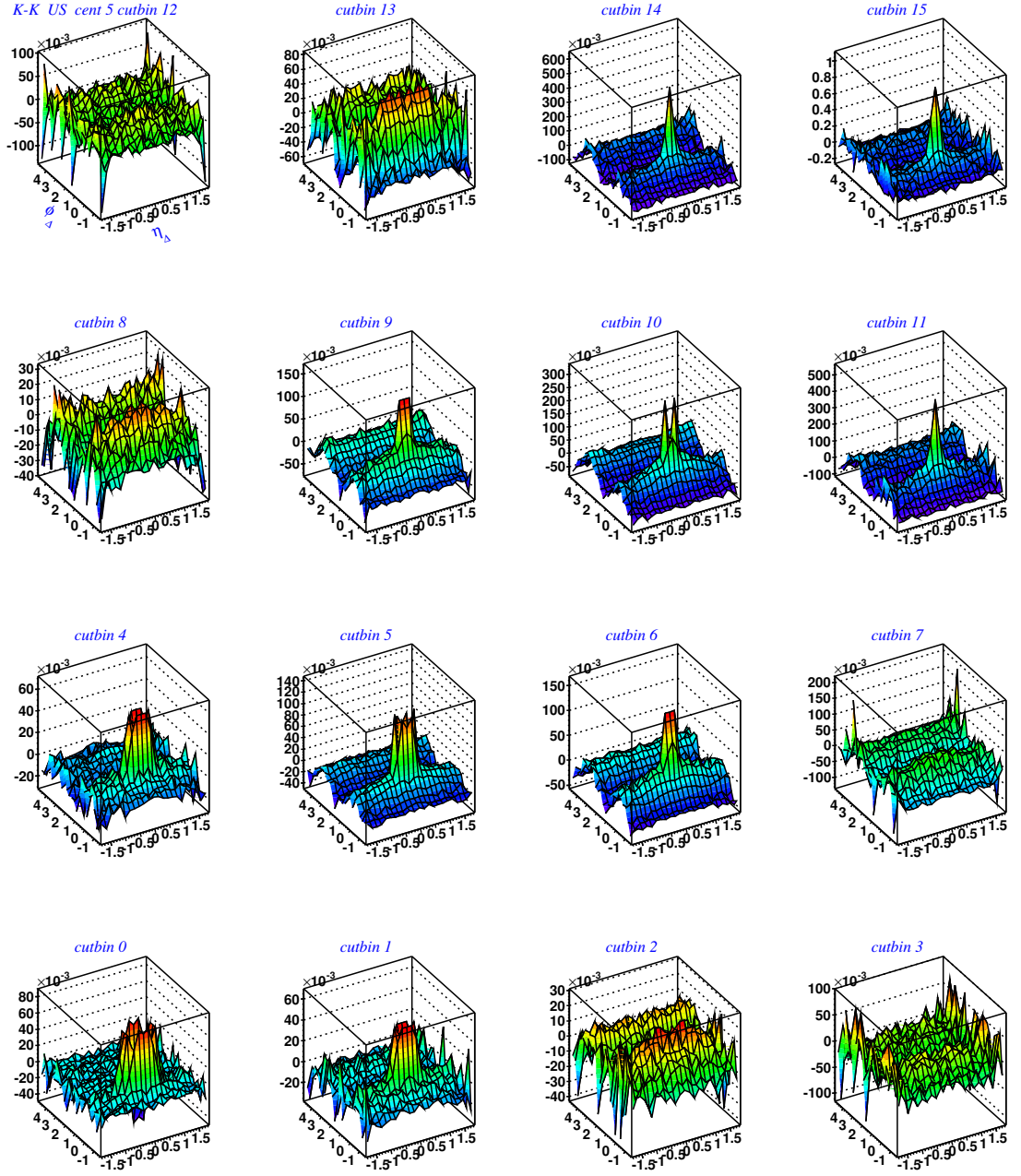


**Figure 6.16** Unlike-Sign correlations,  $\frac{\Delta\rho}{\rho_{ref}}$ , of kaons for 200 GeV in different  $y_T$  sub-bins for a centrality 38 – 46%. The  $y_T$  spectrum is sub-divided into 4 sub-bins that creates  $4 \times 4 = 16$  cut bins for correlations. The binning scheme is discussed in Chapter 3.

### $\phi$ -Meson Decay:

The  $\phi$ -meson is a resonant particle of mass  $1019.4 \text{ MeV}/c^2$  [74]. It is formed by a strange quark and anti-quark pair in the early stage of the collision and decays through different channels. The  $\phi \rightarrow K^+ + K^-$  is one of the dominant channels. In  $K - K$  US correlations a clean signal of  $\phi$  decay is seen. Because of the radial thrust of the system formed after the collision, the decay products of the  $\phi$ -meson hit detector at an opening angle  $< 180^\circ$ . The opening angle is a function of parent  $\phi$ -meson momentum; becoming narrower for higher momentum. Because of the opening angle there is an enhancement in the correlation for  $(\eta_\Delta, \phi_\Delta) \approx \text{opening angle}$ . The opening angle can be derived using definition of invariant mass. When a mass  $M$  decays to two masses  $m_1$  and  $m_2$  near mid-rapidity with respective momenta  $p_1$  and  $p_2$ , the opening angle  $\theta$  between the momenta can be derived using Equation 6.4, given approximately by

$$\begin{aligned} M^2 &= m_1^2 + m_2^2 + 2(E_1 E_2 - \vec{p}_1 \cdot \vec{p}_2) \\ &\approx m_1^2 + m_2^2 + 2\sqrt{m_1^2 + p_{T1}^2} \sqrt{m_2^2 + p_{T2}^2} - 2p_{T1} p_{T2} \cos \theta, \end{aligned} \quad (6.4)$$

where  $m_1 = m_2 = 0.4937 \text{ GeV}/c^2$  (mass of  $K$ ),  $M = 1019.4 \text{ MeV}/c^2$  (mass of  $\phi$ -meson) and  $p_T \gg p_Z$  is assumed for high momentum at mid-rapidity. Value of  $y_T$  corresponding to  $p_T$  is derived from  $y_T = \ln [(m_T + p_T)/m]$  and  $m_T^2 = p_T^2 + m^2$ .

In this thesis, the bin width of histogram along  $\eta_\Delta$  is  $0.16 = 7.93 \text{ deg}$  at  $\eta_\Delta = 0$  and bin width along  $\phi_\Delta$  is  $0.25 = 14.4 \text{ deg}$ . Therefore, the symmet-

$y_{T1}$	$y_{T2}$	$\theta$ deg
0.5	0.5	58.7
1.0	0.5	5.4
1.0	1.0	25.1
1.5	1.5	13.8
2.0	2.0	8.1

**Table 6.1** The opening angle  $\theta$  for different combination of  $y_{T1}$  and  $y_{T2}$ .

rical volcano shape in correlation appears elongated along  $\eta_{\Delta}$ . Table 6.1 lists the opening angles for different combinations of  $y_T$ -pairs. It is seen that the opening angle is larger when  $y_{T1} = y_{T2}$ .

### LS Correlations:

Figure 6.15 shows LS correlations for centrality 5. The LS correlations in *kaons* have dipole and quadrupole as main components in all centralities. The 2D exponential due to HBT is present only in diagonal bins (e.g., 0, 5, 10 and 15). In centrality  $> 2$ , 2D Gaussian appears in higher momentum region (e.g., cut bins 10, 11, 14, 15). There is negative same side 2D Gaussian in centrality  $> 3$  in some of the lower momentum off-diagonal bins (e.g., 1, 2, 3, 4, 6, 7, 8, and 9). This is a new correlation feature, not obviously observed in unidentified particle correlations, and much stronger than  $\pi$ - $\pi$ . For higher  $y_T$ , it may be due to hadronization kinematics where hadron fragmentation into like-signed  $K^{\pm}$ - $K^{\pm}$  pair is energetically disfavored at the momentum range studied in this thesis. Similarly, for off-diagonal cut bins ( $y_{T1} \neq y_{T2}$ ) it may indicate kinematic suppression of soft fragmentation into nearby, LS

kaon pairs.

### US Correlations:

Figure 6.16 shows LS correlations for centrality 5. As a new feature, a same-side ‘volcano’ peak which is shown to be consistent with  $\phi \rightarrow K^+ + K^-$  decays appears (see Section 6.4). The  $\phi$  decay dominates the diagonal cut bins on lower momentum region. There was no attempt to fit the correlation due to resonance decay of  $\phi$ . Therefore, the decay region was excluded from the model fitting. The cut of resonance region in  $\eta_\Delta$  was made on the basis of opening angles as shown in Table 6.1. The US correlation doesn’t show 1D Gaussian and 2D exponential components however, dipole, quadrupole and 2D Gaussian components are found in all centralities.

Attempts were made to make a cut in invariant mass such that all tracks those could potentially be decay of  $\phi$ -meson be removed. The attempts was not successful because the  $\phi$ -meson is spread in wider range of invariant mass spectrum. Therefore, the region contributed by the decay correlations were removed and the remaining structure were fitted to extract important fitting parameters such as  $v_2[2D]$ .

### Fitting Parameter $v_2^2[2D]$ :

Figures 6.17 and 6.18 show some of the examples of effectiveness of fitting function for LS and US correlation and Figure 6.19 shows one of the fitting parameters,  $v_2^2[2D]$ , for cut bin 5. Figure 6.20 shows the cut bin-wise

trend of  $v_2^2[2D]$  with centrality. The  $x$ -axis of the figure represents a measure of centrality,  $\nu$ , computed at fixed energy (200 GeV) and reported in Table III [5]. The trends of  $v_2^2[2D]$  for most of the momentum bins are consistent with previously studied trends.

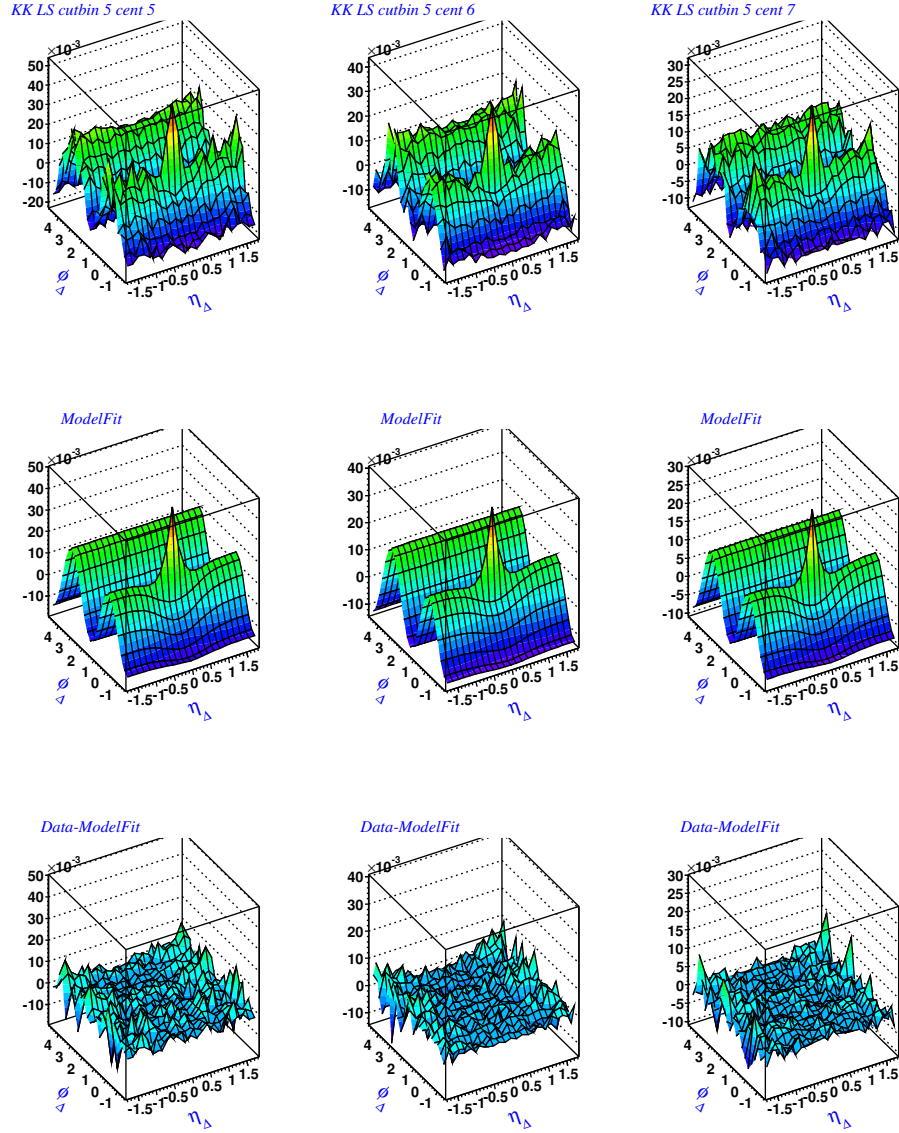


**Figure 6.17** Top row: LS correlations,  $\frac{\Delta\rho}{\rho_{ref}}$ , of *kaons* in cut bin 5 for centralities 38 – 46%, 28 – 38% and 18 – 28%. Middle row: model fit of the correlations on the top row. Bottom row: residual (data from top row - model fit from middle row) showing that the model describes all the statistically significant structures

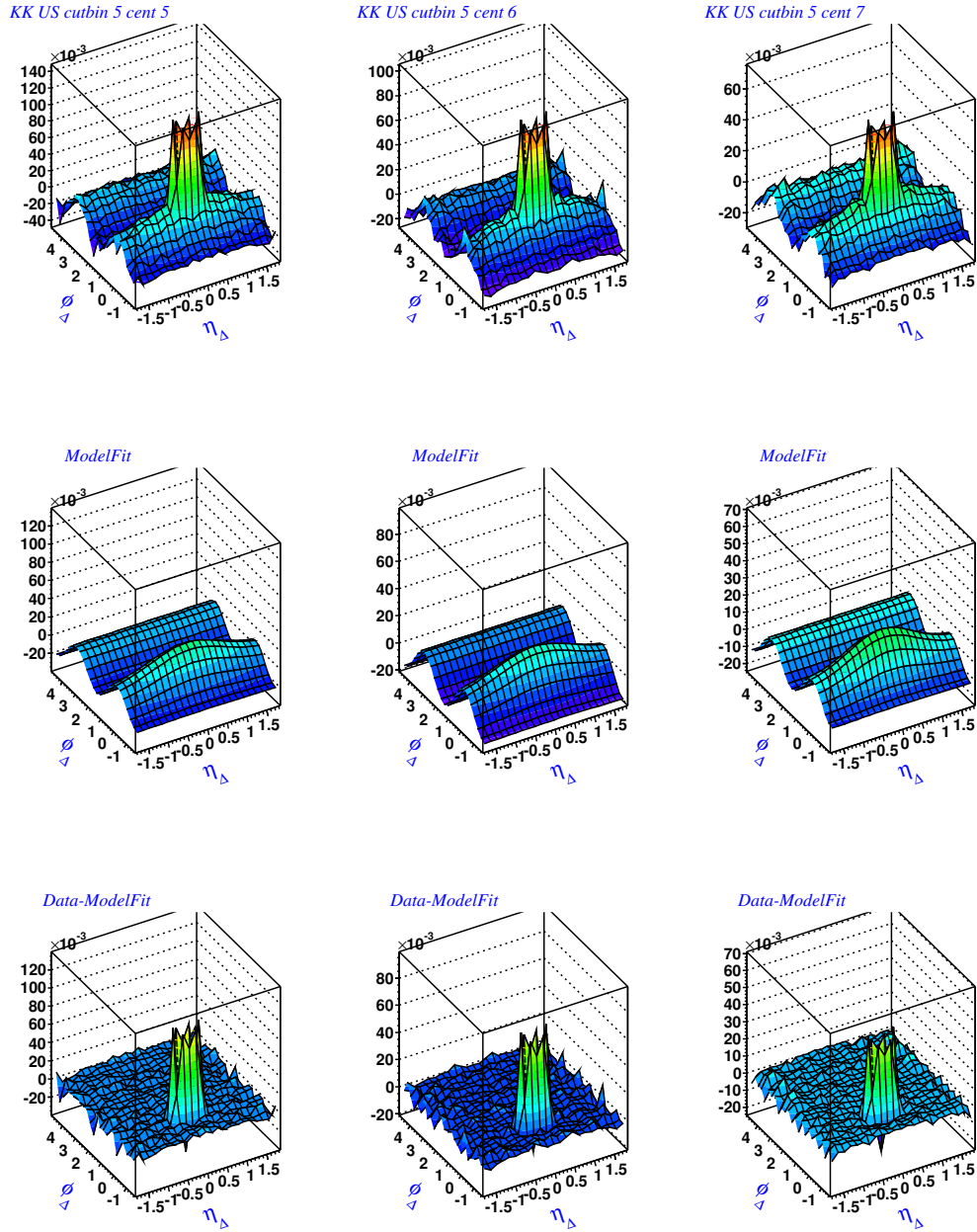


**Figure 6.18** Top row: US correlations,  $\frac{\Delta\rho}{\rho_{ref}}$ , of kaons in cut bin 5 for centralities 38-46%, 28-38% and 18-28%. Middle row: model fit of the correlations. Bottom row: residual (data - model fit). The volcano like region was excluded before fitting the correlations. 146

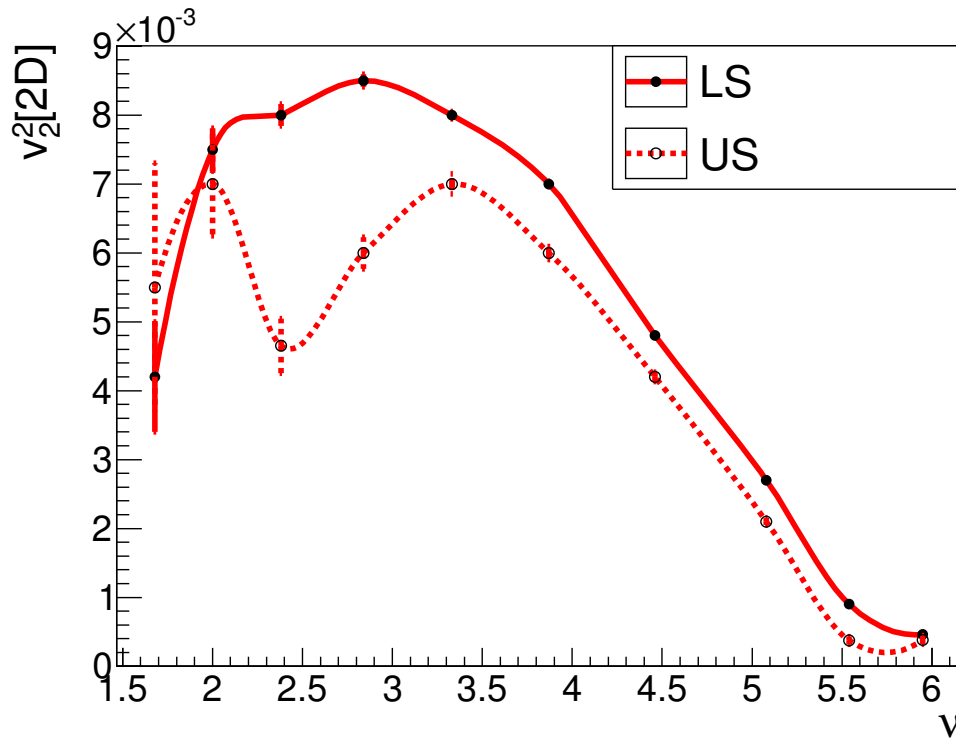


**Figure 6.19** *kaon-kaon*  $v_2^2[2D]$  as a function of centrality measure  $\nu$  for  $(y_T, y_T)$  cut bin 5. The error bars are fitting errors only. Because of low statistics in the most peripheral centrality bin, the correlation was not fitted there.

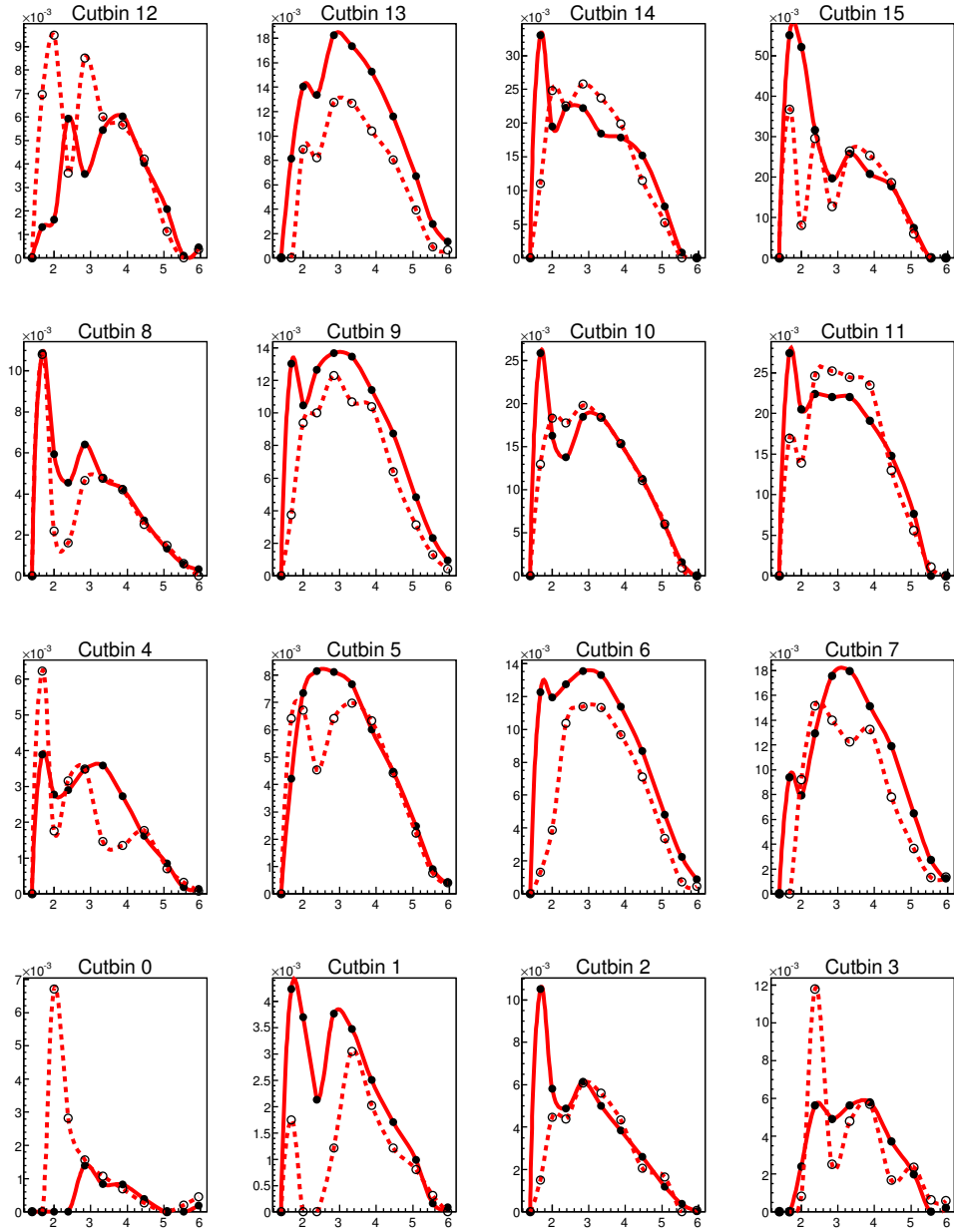


**Figure 6.20** *kaon-kaon*  $v_2^2[2D]$  as a function of centrality measure  $\nu$  (most peripheral in left to most central in right). LS: bold line with filled circle. US: dotted line with open circle. The 16 cut bins are according to binning scheme for  $K - K$  correlations as discussed in Chapter 3. Due to low statistics the fitting parameters for the most peripheral centrality bin were not obtained and were set to 0.

## 6.5 $p - p$ Correlations

Figure 6.21 and 6.22 show  $p_T$ -integrated  $p-p$  correlations. Similarly, in Figures 6.23 and 6.24 evolution of correlation with the momentum ranges for a centrality bin 38-46% are presented. As a new feature, there is huge same-side suppression in the correlation around  $(\eta_\Delta, \phi_\Delta) \rightarrow (0, 0)$  in both LS and US correlations. This suppression increases toward lower  $y_T$ , which suggests kinematic suppression of soft parton fragmentation into  $p-p$  and  $\bar{p}-\bar{p}$  pairs. Baryon number conservation would require fragmentation into  $p, \bar{p}, p, \bar{p}$ , or 4 nucleons. Therefore the determining physics is conservation of baryon number which requires protons to be made in  $p-\bar{p}$  pairs, if these are from fragmenting gluons. The mid-rapidity region in Au+Au system has lower, net baryon number so any sort of fragmentation from that system must produce protons only in  $p-\bar{p}$  pairs. This requirement costs  $2 \times 938$  MeV in energy, which strongly reduces the probability of such processes in the  $p_T$  ranges studies in this thesis. If we looked at  $p_T > 10$ 's of GeV/c then I would expect the suppression to go away. We see a hint of that in data at the higher  $y_T$  compared with the lower.

Because of the magnitude of this same-side suppression it may not be possible to determine the presence or not of a positive 2D Gaussian (jet structure) in LS correlations. Also, 2D exponential component is not seen as a dominant component. The same-side suppression is present in US but not as strong as for LS correlation. This weaker suppression is consistent with the interpretation in terms of soft parton fragmentation into  $p-\bar{p}$  which does not require as much energy. The quadrupole can however be fitter for both LS

and US correlation. Similarly, 2D Gaussian and dipole are evident at higher  $y_T$ .

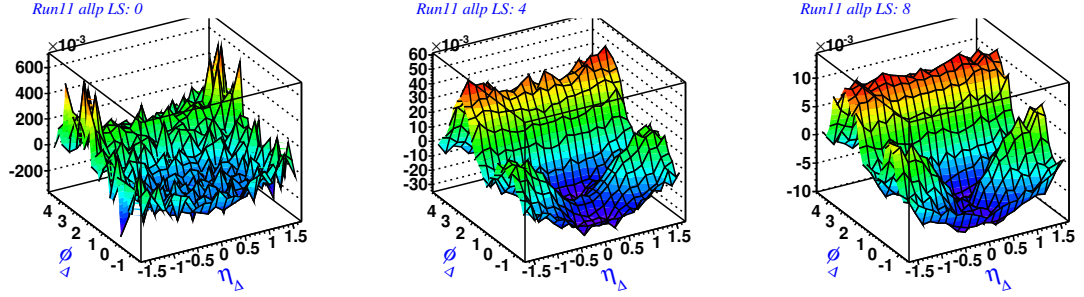


**Figure 6.21** Like-Sign correlations,  $\frac{\Delta\rho}{\rho_{ref}}$ , of *protons* for 200 GeV  $p_T$ -integrated data from Run 2011. The correlations are in centrality IDs 0, 4 and 8 (i.e., centrality percentages 84 – 93%, 50 – 60% and 10 – 20% respectively). No pre-factor has been applied.

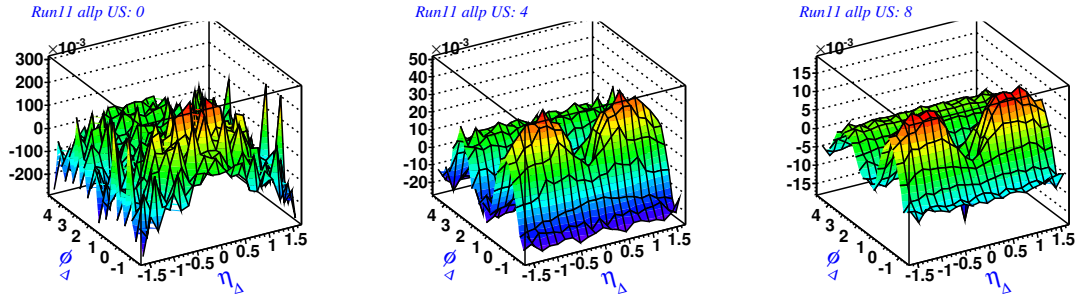
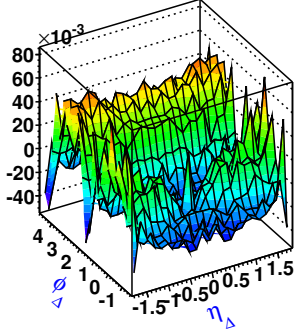
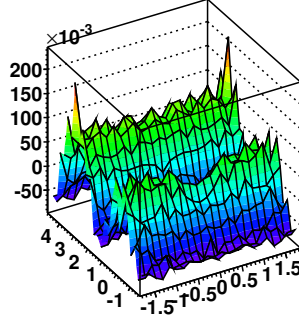


**Figure 6.22** Unlike-Sign correlations,  $\frac{\Delta\rho}{\rho_{ref}}$ , of *protons* for 200 GeV  $p_T$ -integrated data from Run 2011. The correlations are in centrality IDs 0, 4 and 8 (i.e., centrality percentages 84 – 93%, 50 – 60% and 10 – 20% respectively). No pre-factor has been applied.

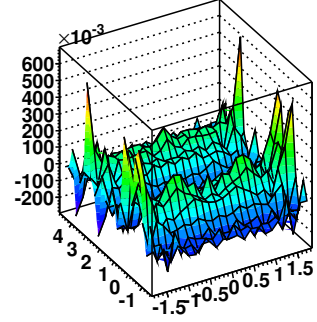
*p-p LS cent 5 cutbin 6*



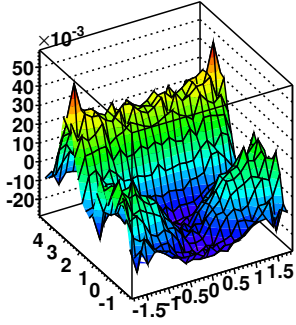
*cutbin 7*



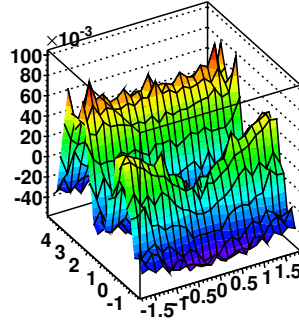
*cutbin 8*



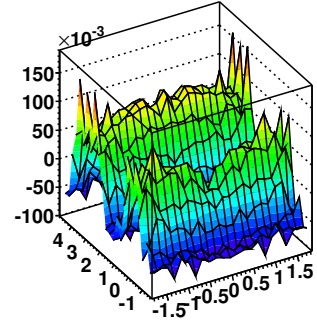
*cutbin 3*



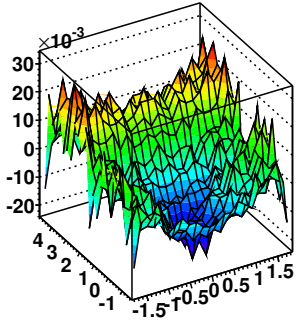
*cutbin 4*



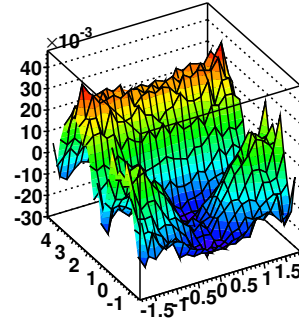
*cutbin 5*



*cutbin 0*



*cutbin 1*



*cutbin 2*

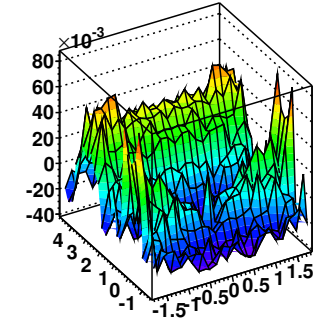


**Figure 6.23** Like-Sign correlations,  $\frac{\Delta\rho}{\rho_{ref}}$ , of *protons* for 200 GeV in different  $y_T$  sub-bins for a centrality 38-46%. The  $y_T$  spectrum is sub-divided into 3 sub-bins that creates  $3 \times 3 = 9$  cut bins for correlations. The binning scheme is discussed in Chapter 3.

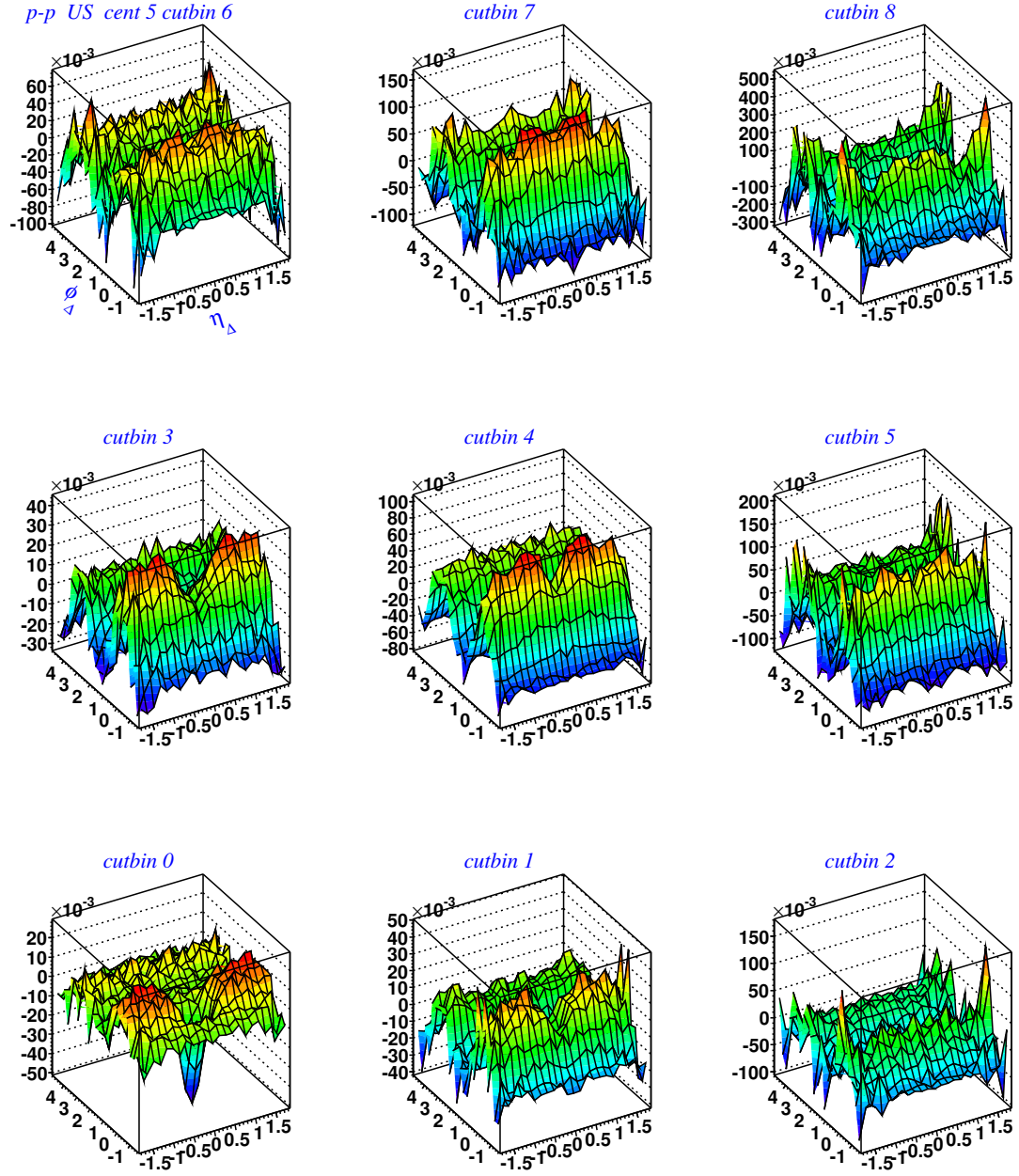


**Figure 6.24** Unlike-Sign correlations,  $\frac{\Delta\rho}{\rho_{ref}}$ , of *protons* for 200 GeV in different  $y_T$  sub-bins for a centrality 38-46%. The  $y_T$  spectrum is sub-divided into 3 sub-bins that creates  $3 \times 3 = 9$  cut bins for correlations. The binning scheme is discussed in Chapter 3.

**Fitting Parameter  $v_2^2[2D]$ :**

Figures 6.25 and 6.26 show examples of the effectiveness of the fitting function for LS and US correlation and Figure 6.27 shows one of the fitting parameters,  $v_2^2[2D]$ , for cut bin 5. Figure 6.28 shows the cut bin-wise trend of  $v_2^2[2D]$  with centrality. The  $x$ -axis of the figure represents a measure of centrality,  $\nu$ , computed at fixed energy (200 GeV) and reported in Table III [5]. The trends of  $v_2^2[2D]$  for most of the momentum bins are consistent with previously studied trends. These are the first, true  $p+p$   $v_2^2[2D]$  measurements.

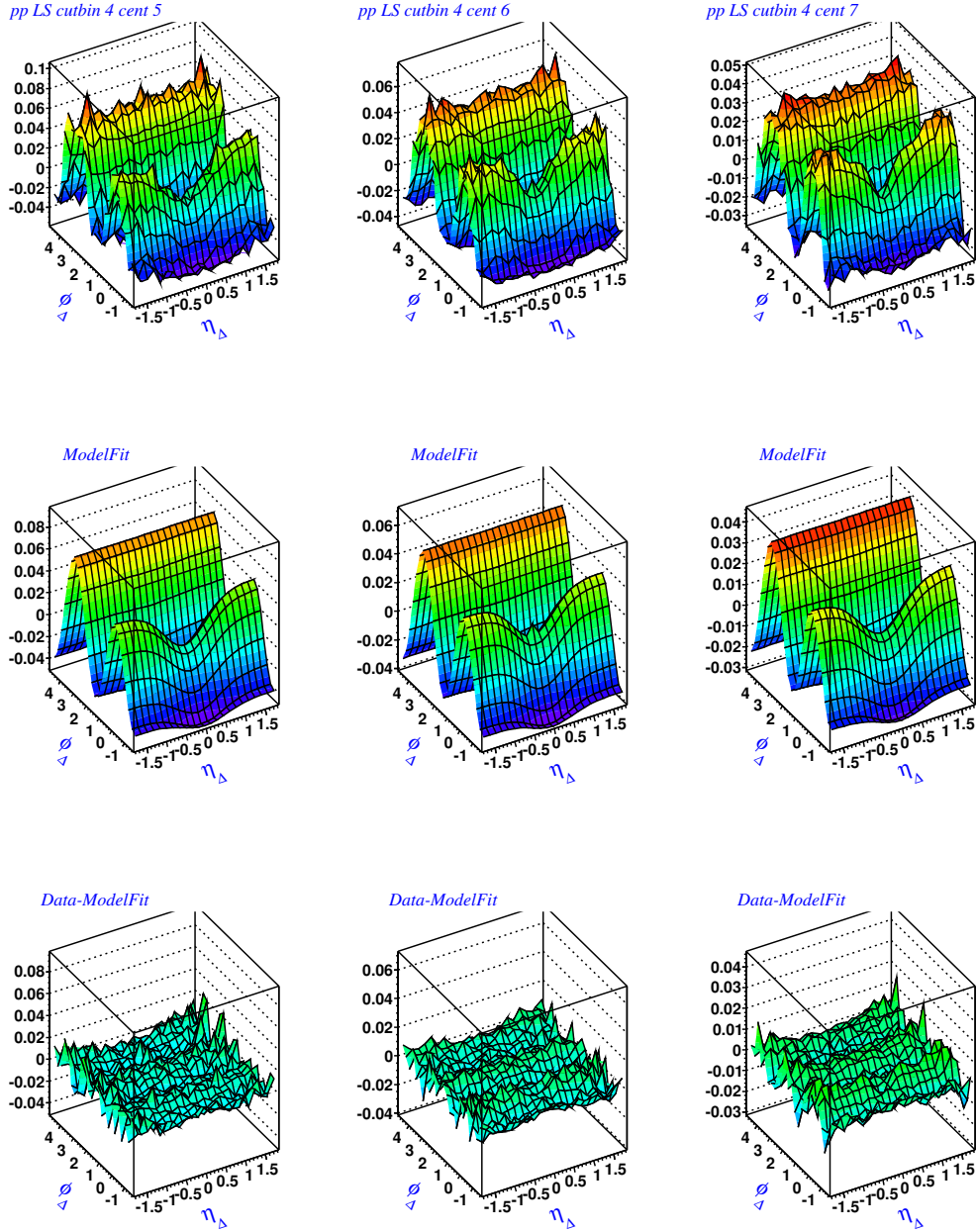


**Figure 6.25** Top row: LS correlations,  $\frac{\Delta\rho}{\rho_{ref}}$ , of *protons* in cut bin 5 for centralities 38 – 46%, 28 – 38% and 18 – 28%. Middle row: model fit of the correlations on top row. Bottom row: residual (data from top row - model fit from middle row).

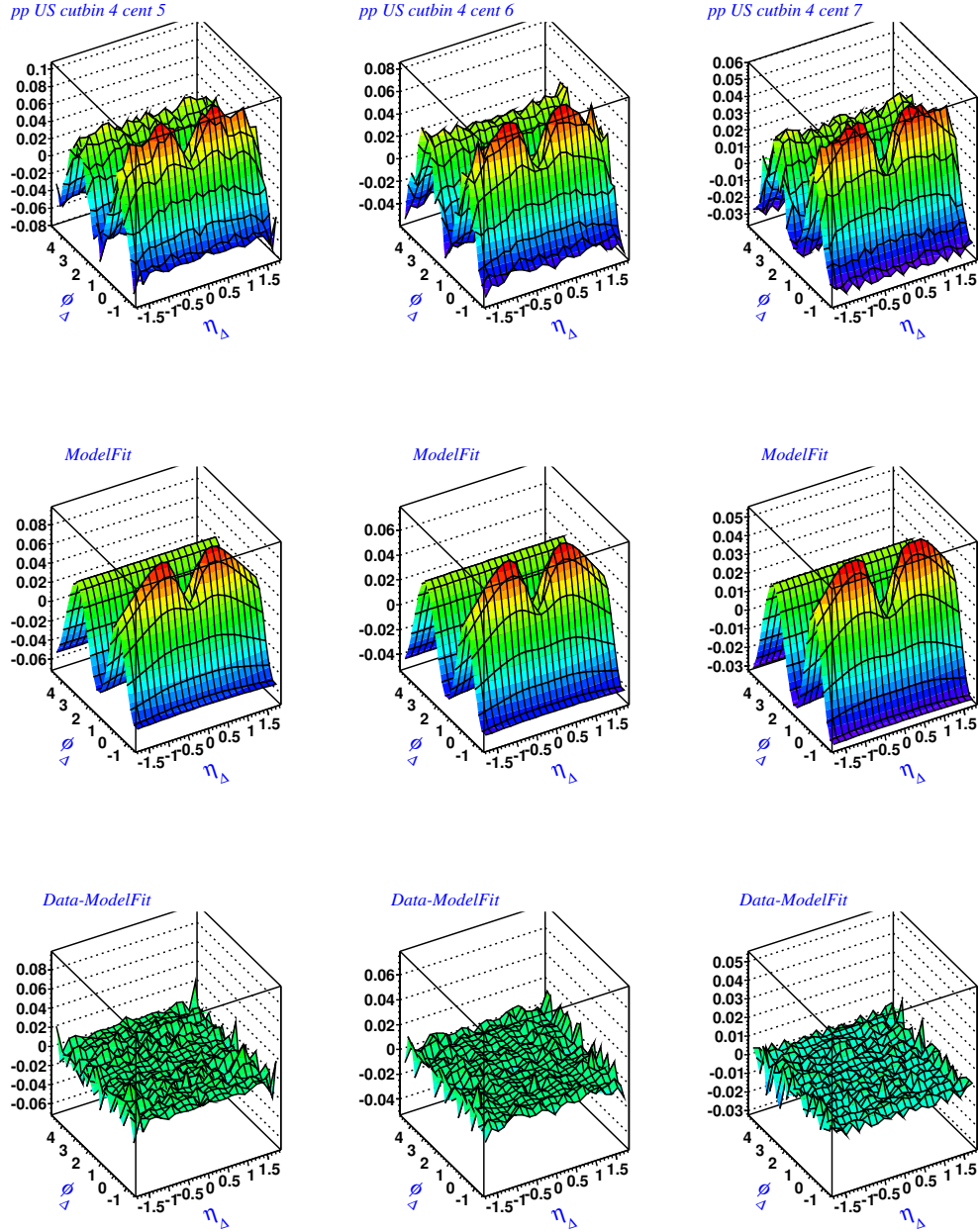


**Figure 6.26** Top row: US correlations,  $\frac{\Delta\rho}{\rho_{ref}}$ , of *protons* in cut bin 4 for centralities 38-46%, 28-38% and 18-28%. Middle row: model fit of the correlations. Bottom row: residual (data - model fit).

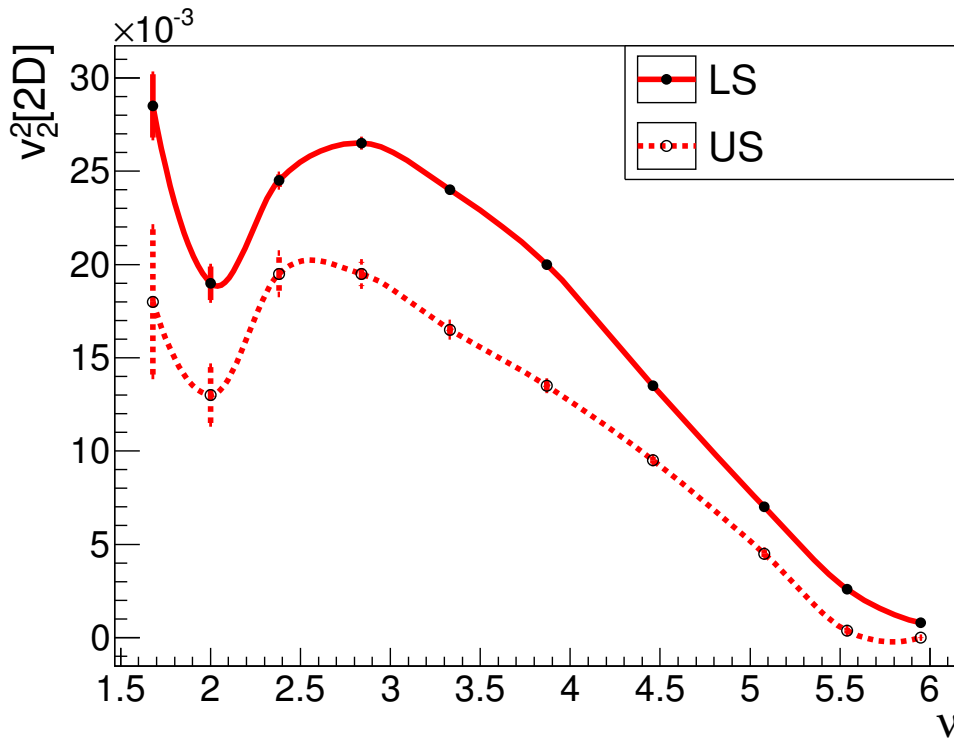


**Figure 6.27** *proton-proton*  $v_2^2[2D]$  as a function of centrality measure  $\nu$  for  $(y_T, y_T)$  cut bin 4. The error bars are fitting errors only. Because of low statistics in the most peripheral centrality bin, the correlation was not fitted there.

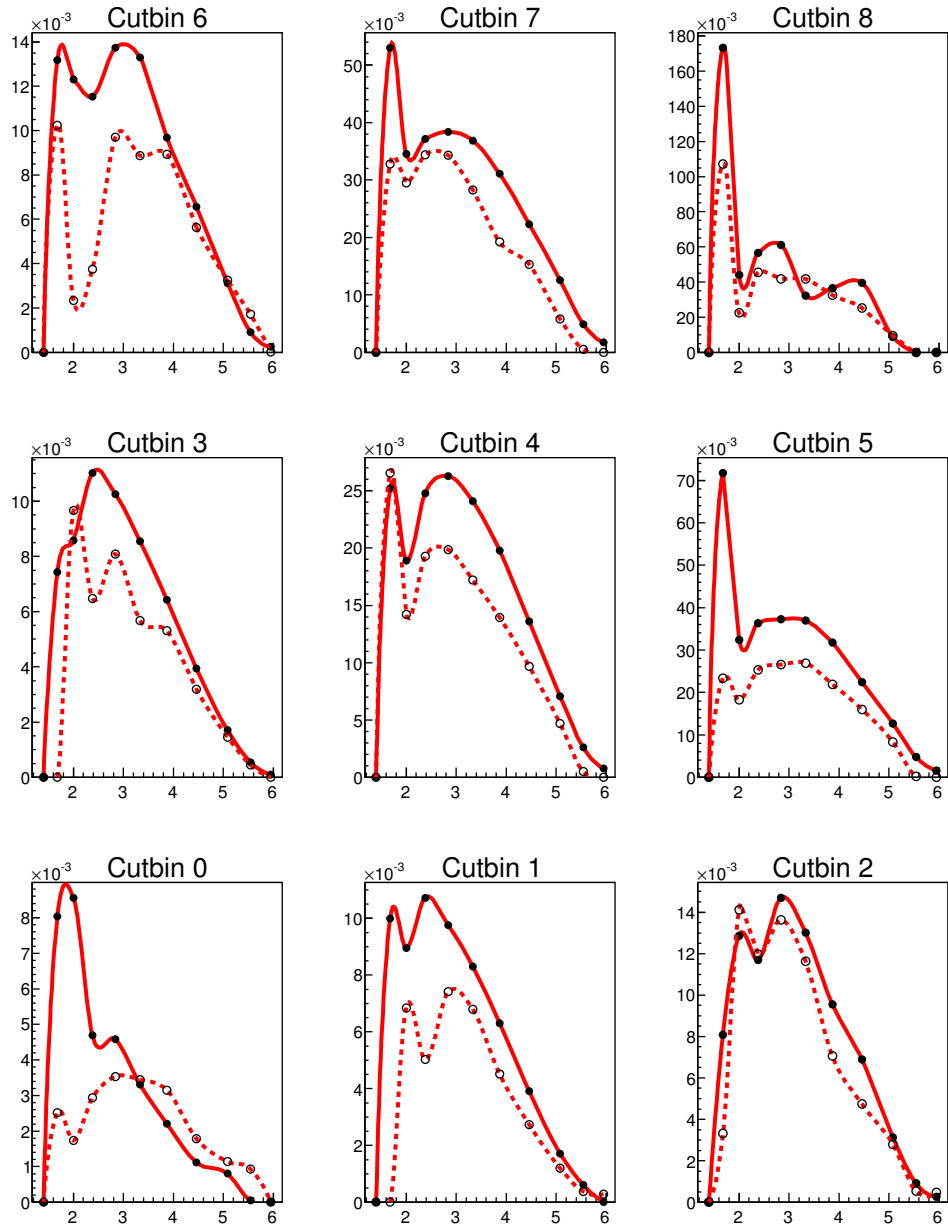


**Figure 6.28** *proton-proton  $v_2^2[2D]$  as a function of centrality measure  $\nu$  (most peripheral in left to most central in right). LS: bold line with filled circle. US: dotted line with open circle. The 9 cut bins are according to binning scheme for  $p - p$  correlations as discussed in Chapter 3. Due to low statistics the fitting parameter for the most peripheral centrality bin, the correlations were not fitted. The results for this bin are plotted at 0.*

## 6.6 $\pi - K$ Correlations

Figures 6.43 and 6.44 show *pion-kaon* correlations for 200 GeV  $p_T$ -integrated data from Run 2011. Compared to *all-particle* correlations or  $\pi$ - $\pi$  correlations, the  $\pi$ - $K$  LS correlation doesn't show a positive peak around  $(\eta_\Delta, \phi_\Delta) \rightarrow (0, 0)$  in most of the centralities. The  $\pi$ - $K$  US correlations, however, are comparable to  $\pi$ - $\pi$  US correlations.

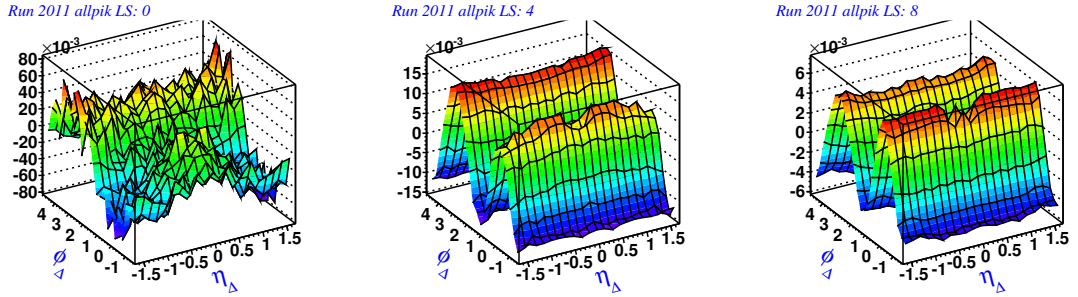


**Figure 6.29** Like-Sign correlations,  $\frac{\Delta\rho}{\rho_{ref}}$ , of *pion-kaon* for 200 GeV  $p_T$ -integrated data from Run 2011. The correlations are in centrality IDs 0, 4 and 8 (i.e., centrality percentages 84 – 93%, 50 – 60% and 10 – 20% respectively). No pre-factor has been applied.

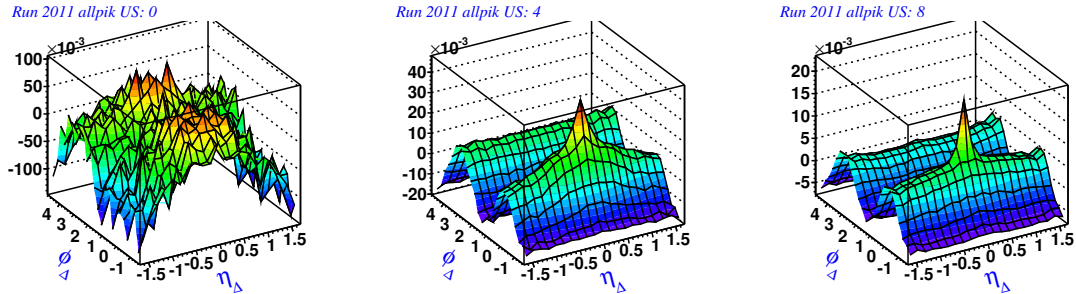


**Figure 6.30** Unlike-Sign correlations,  $\frac{\Delta\rho}{\rho_{ref}}$ , of *pion-kaon* for 200 GeV  $p_T$ -integrated data from Run 2011. The correlations are in centrality IDs 0, 4 and 8 (i.e., centrality percentages 84 – 93%, 50 – 60% and 10 – 20% respectively). No pre-factor has been applied.

In Figures 6.31 and 6.32 the evolution of  $\pi$ - $K$  LS and US correlations as a function of momentum are shown. The correlations presented are for centrality bin 38-46%. In the LS correlations, the 2D positive exponential peak is absent. The same-side 2D Gaussian amplitude changes from negative in the lower momentum region to a small positive amplitude in the higher momentum region. The 2D Gaussian for higher  $y_T$  is expected for parton fragmentation into the heavier kaon. The Quadrupole is common structures in all centralities for both LS and US correlations.

In the US correlations, most of the cut bins show dipole, quadrupole, 2D Gaussian and 2D exponential as major components in correlations. The 2D exponential component is possibly due to Coulomb attraction. However, in some cut bins (e.g., cut bin 16) the structure is possibly due to the resonance

decay of  $K^* \rightarrow K + \pi^3$ .

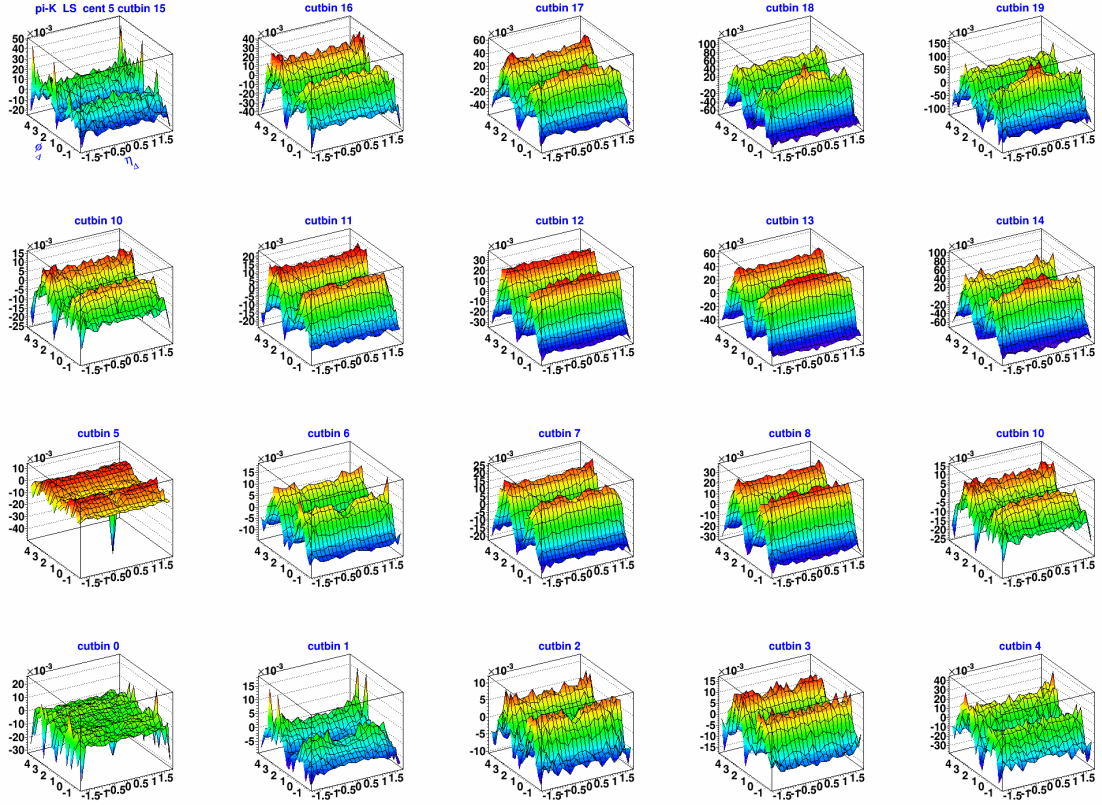


**Figure 6.31** Like-Sign correlations,  $\frac{\Delta\rho}{\rho_{ref}}$ , of *pion-kaon* for 200 GeV in different  $y_T$  sub-bins for a centrality 38-46%. The  $y_T$  spectrum for *pion* is subdivided into 5 sub-bins and *kaon* is subdivided into 4 sub-bins that creates  $5 \times 4 = 20$  cut bins for correlations. The binning scheme is discussed in Chapter 3.

---

<sup>3</sup> $K^*$  is a resonant particle of mass  $891.66 MeV/c^2$ . The dominant decay channel of  $K^*$  to  $K-\pi$  pairs of opposite charge signs [74].

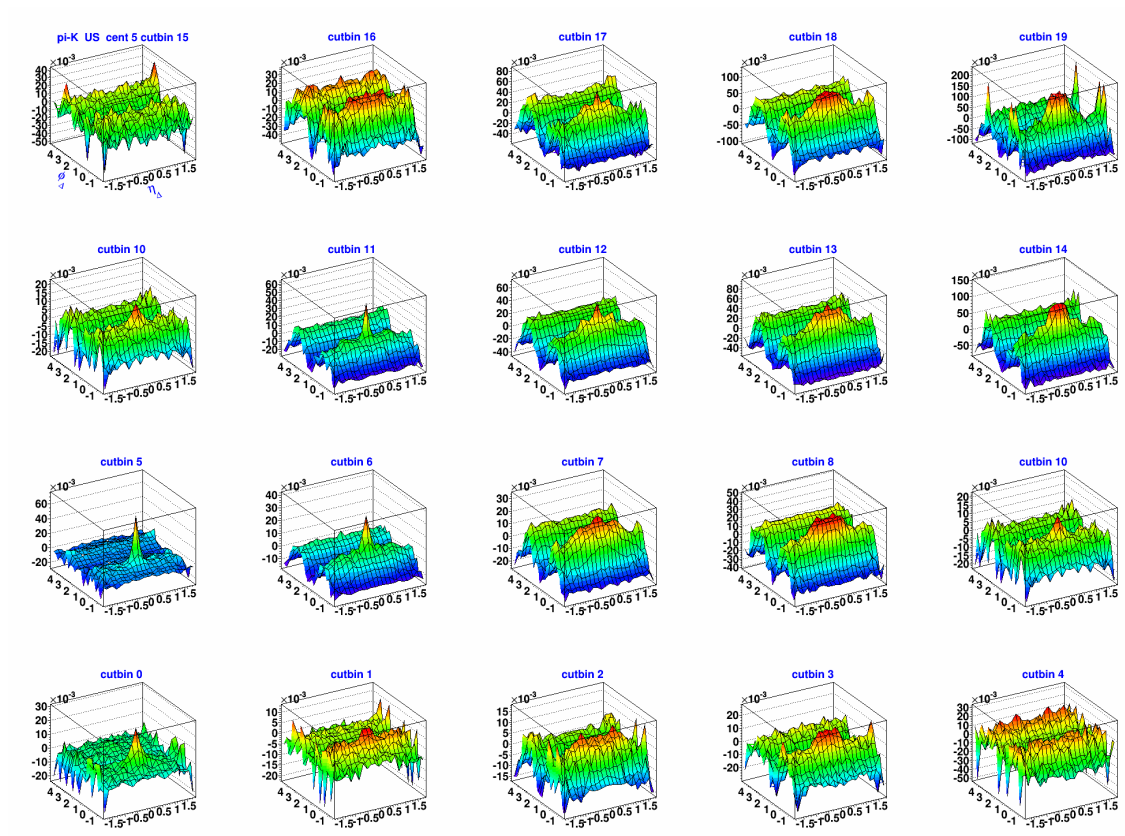


**Figure 6.32** Unlike-Sign correlations,  $\frac{\Delta\rho}{\rho_{ref}}$ , of *pion-kaon* for 200 GeV in different  $y_T$  sub-bins for a centrality 38-46%. The  $y_T$  spectrum for *pion* is subdivided into 5 sub-bins and *kaon* is subdivided into 4 sub-bins that creates  $5 \times 4 = 20$  cut bins for correlations. The binning scheme is discussed in Chapter 3.

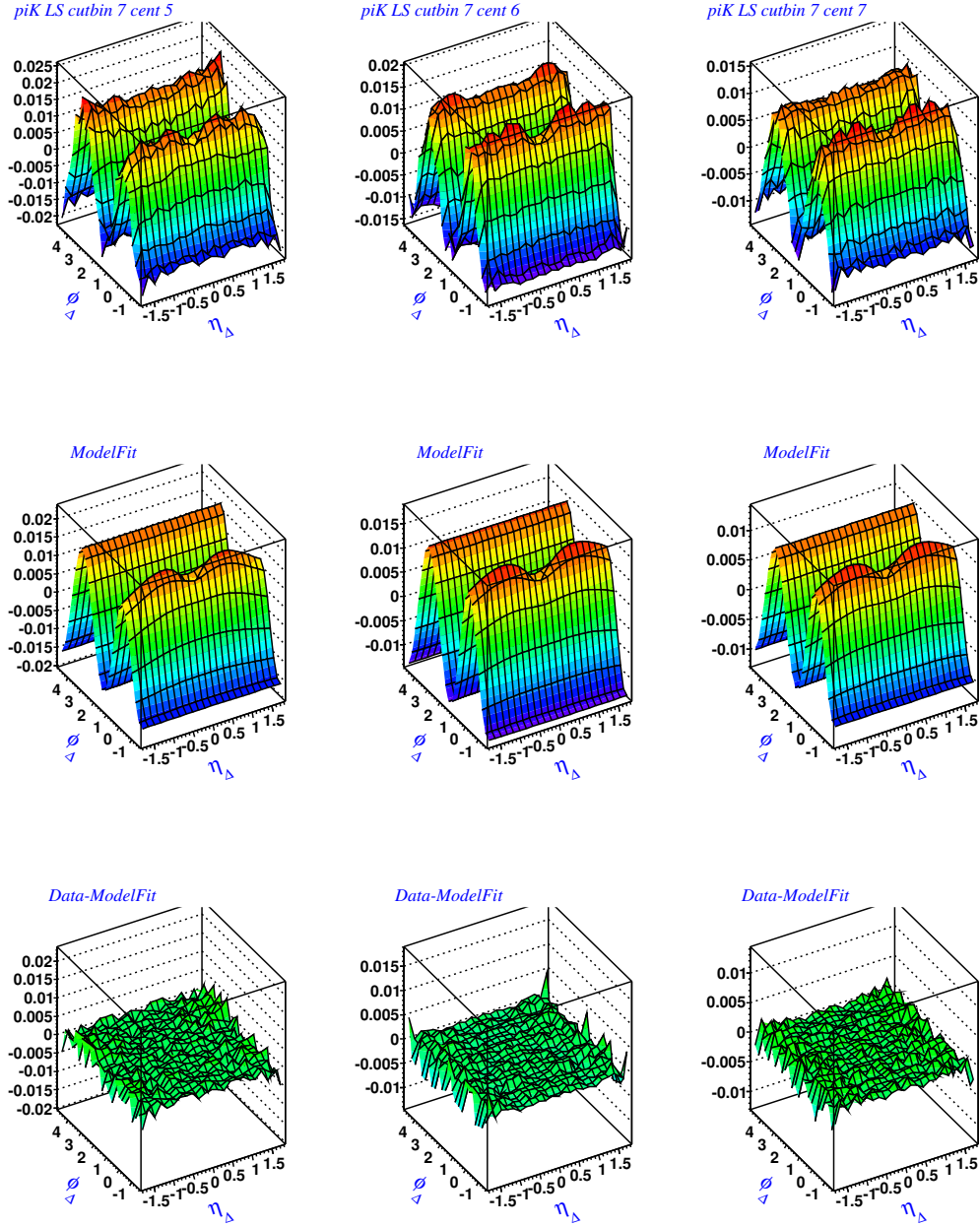


**Figure 6.33** Top row: LS correlations,  $\frac{\Delta\rho}{\rho_{ref}}$ , of *pion-kaon* in cut bin 7 for centralities 38 – 46%, 28 – 38% and 18 – 28%. Middle row: model fit of the correlations on top row. Bottom row: residual (data from top row - model fit from middle row).

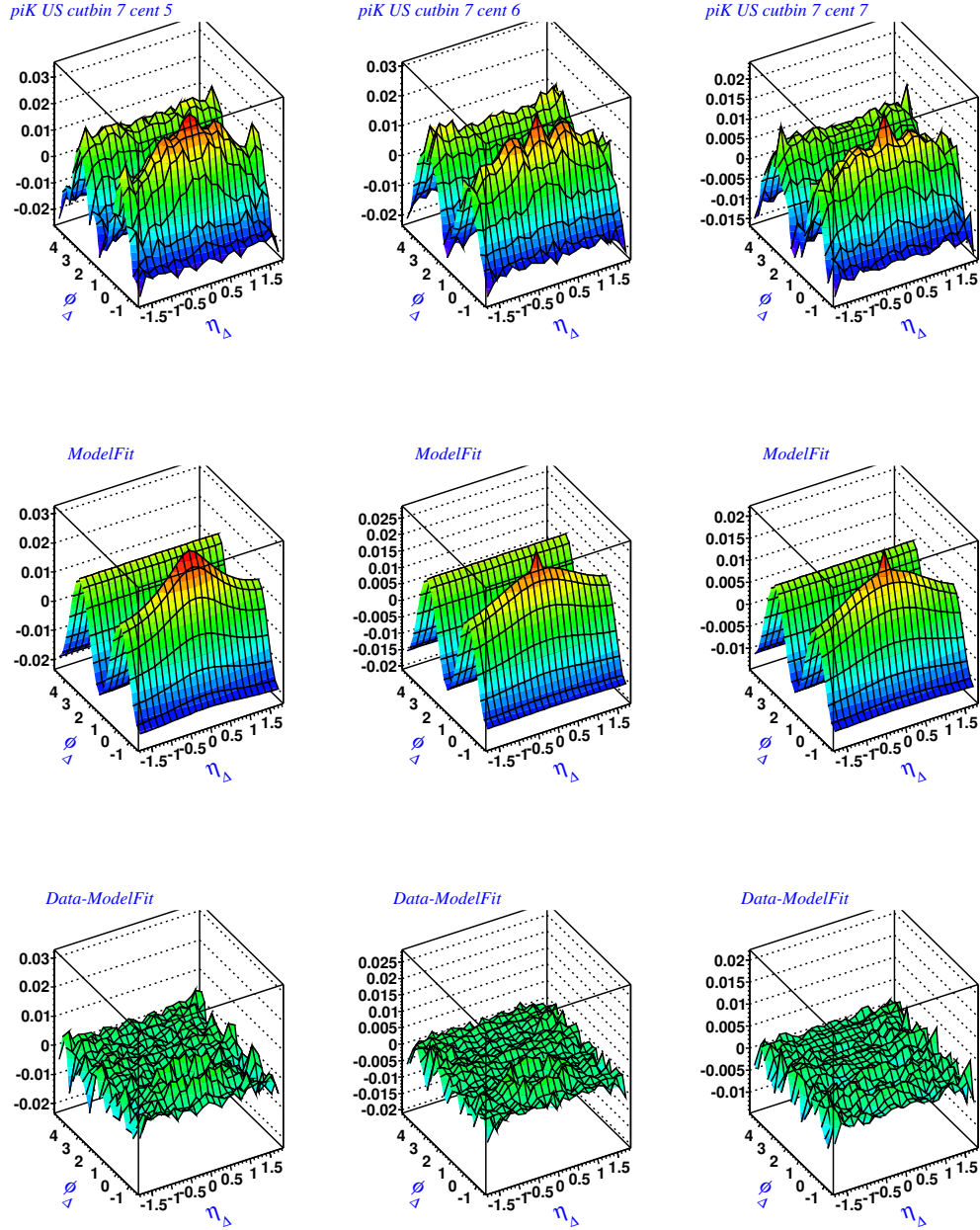


**Figure 6.34** Top row: US correlations,  $\frac{\Delta\rho}{\rho_{ref}}$ , of *pion-kaon* in cut bin 7 for centralities 38 – 46%, 28 – 38% and 18 – 28%. Middle row: model fit of the correlations on top row. Bottom row: residual (data from top row - model fit from middle row).

In Figures 6.33 and 6.34 model fitting of  $\pi$ - $K$  LS and US correlations for a particular cut bin in three centralities are shown. The LS correlation is fitted with dipole, quadrupole and negative 2D Gaussian components. The US correlations, however, are fitted with all 6-components. A volcano shaped structure in the residual of US correlation fitting (bottom row in Figure 6.34) is possibly due to the resonance decay of  $K^*$ . Figure 6.35 shows the evolution of  $v_2^2[2D]$  as a function of the centrality parameter  $\nu$  for  $(y_T, y_T)$  cut bin 7.

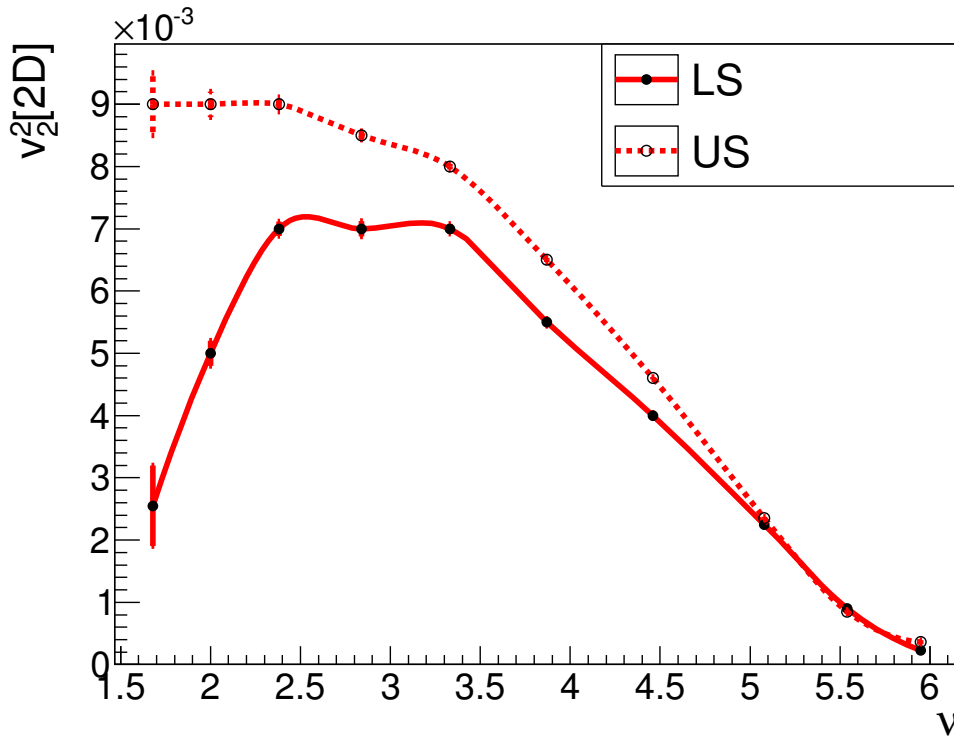


**Figure 6.35** *pion-kaon*  $v_2^2[2D]$  as a function of centrality measure  $\nu$  for  $(y_T, y_T)$  cut bin 7. The error bars are fitting errors only. Because of low statistics in the most peripheral centrality bin, the correlation was not fitted there.

## 6.7 $\pi - p$ Correlations

Figures 6.36 and 6.37 show *pion-proton* correlations for 200 GeV  $p_T$ -integrated data from Run 2011. Compared to *all-particle* correlations or  $\pi-\pi$  correlations, the  $\pi-p$  LS correlation doesn't show a positive peak around  $(\eta_\Delta, \phi_\Delta) \rightarrow (0, 0)$  in most of the centralities. Except for the most peripheral centrality bin, the *pi-p* US correlations are comparable to  $\pi-\pi$  US correlations. In the most peripheral centrality, the 1D Gaussian in  $\eta_\Delta$  doesn't show as a prominent component.

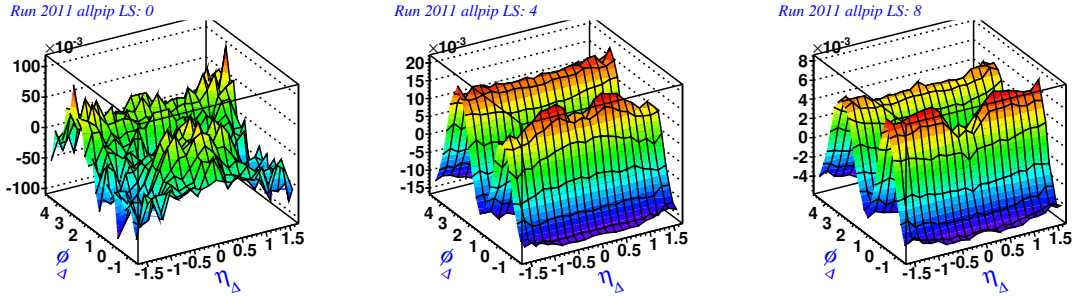


**Figure 6.36** Like-Sign correlations,  $\frac{\Delta\rho}{\rho_{ref}}$ , of *pion-proton* for 200 GeV  $p_T$ -integrated data from Run 2011. The correlations are in centrality IDs 0, 4 and 8 (i.e., centrality percentages 84 – 93%, 50 – 60% and 10 – 20% respectively). No pre-factor has been applied.

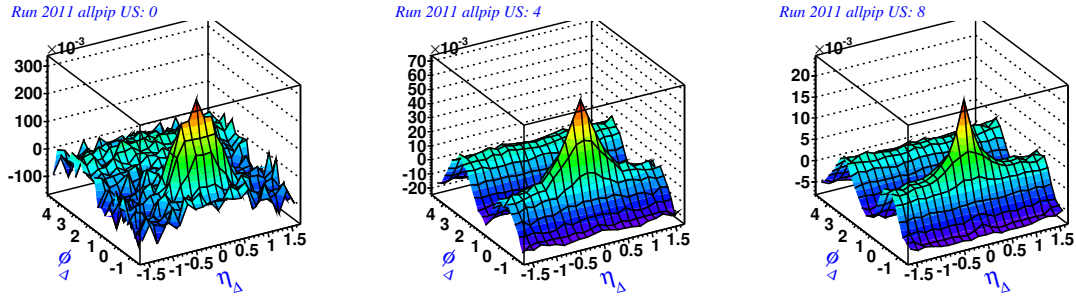


**Figure 6.37** Unlike-Sign correlations,  $\frac{\Delta\rho}{\rho_{ref}}$ , of *pion-proton* for 200 GeV  $p_T$ -integrated data from Run 2011. The correlations are in centrality IDs 0, 4 and 8 (i.e., centrality percentages 84 – 93%, 50 – 60% and 10 – 20% respectively). No pre-factor has been applied.

In Figures 6.38 and 6.39 the evolution of *pi-p* LS and US correlations as a function of momentum are shown. The correlations presented are for a centrality bin 38-46%. In the LS correlations, the 2D positive exponential peak is absent because HBT correlation is absent in different species of particles. The same-side 2D Gaussian amplitude changes from negative in lower momentum region to small positive amplitude in higher momentum region. The near-side suppression in correlation at (0,0) indicates kinematic suppression in fragmenting to proton, which requires  $p\bar{p}$  pair production with its large energy cost. The quadrupole is common structures in all centralities in LS correlation. The dipole becomes stronger at higher  $y_T$

In the US correlations, most of the cut bins show dipole, quadrupole, 2D Gaussian and 2D exponential as major components in correlations. However, in some cut bins (e.g., cut bin 5) a structure (broad in  $\eta_{\Delta}$ , same-side peak

at (0,0)) possibly due to resonance decay of  $\bar{\Lambda} \rightarrow \pi^+ + \bar{p}$ <sup>4</sup>. If the structure is not due to the  $\Lambda$ -decay, it is a new feature in correlations. It is interesting to note that this new feature dominates the correlation structure only in cut bin 5. Also note that  $\Lambda$  decays a few cm from the primary vertex. The decay products ( $\pi, p$ ) may therefore be included in primary particle sample used for the correlation analysis.

---

<sup>4</sup> $\Lambda$  is a particle of mass  $1115.68 MeV/c^2$ . The dominant decay channel of  $\Lambda$  to  $p$ - $\pi$  pairs of opposite signs [74].

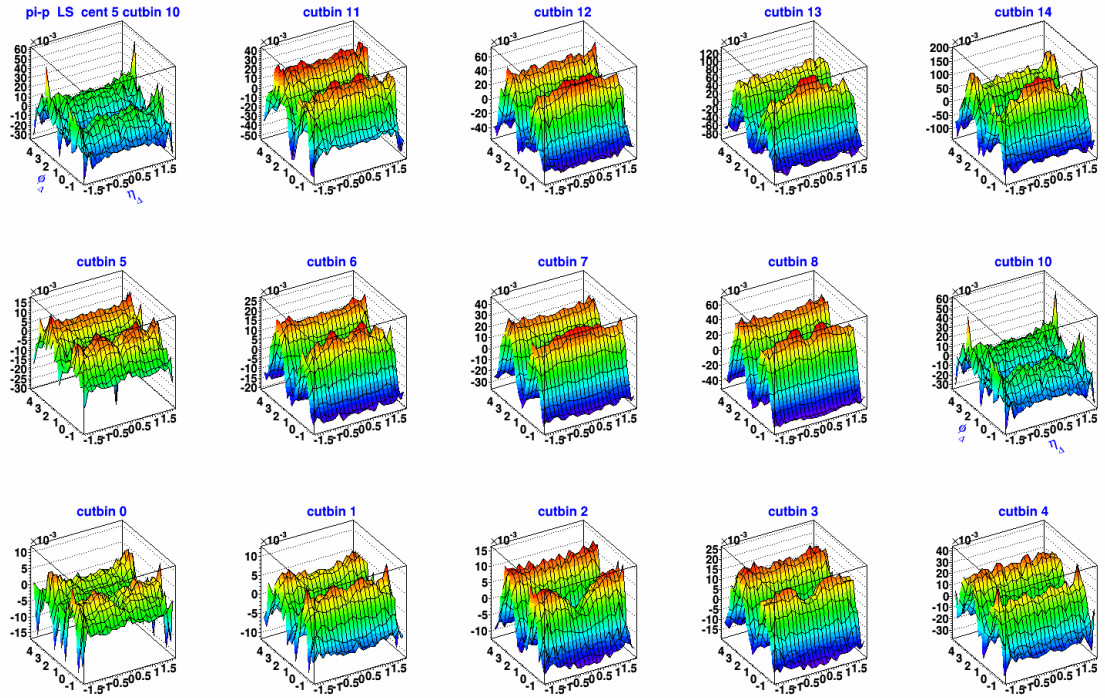


**Figure 6.38** Like-Sign correlations,  $\frac{\Delta\rho}{\rho_{ref}}$ , of *pion-proton* for 200 GeV in different  $y_T$  sub-bins for a centrality 38-46%. The  $y_T$  spectrum for *pion* is subdivided into 5 sub-bins and *proton* is subdivided into 3 sub-bins that creates  $5 \times 3 = 15$  cut bins for correlations. The binning scheme is discussed in Chapter 3.

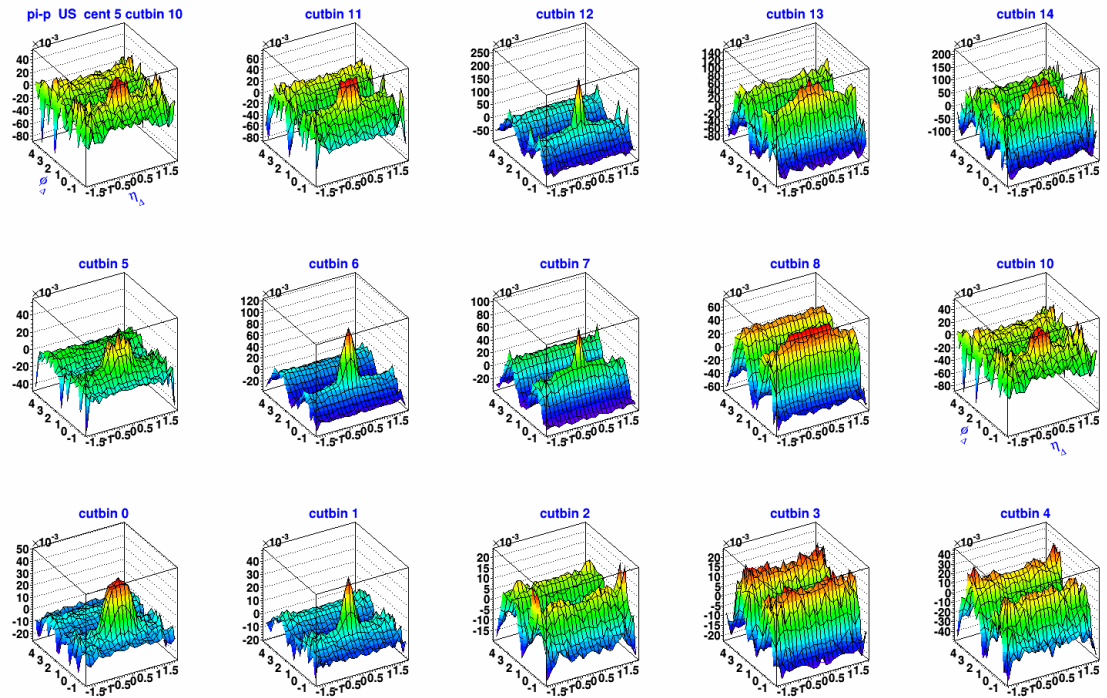


**Figure 6.39** Unlike-Sign correlations,  $\frac{\Delta\rho}{\rho_{ref}}$ , of *pion-proton* for 200 GeV in different  $y_T$  sub-bins for a centrality 38-46%. The  $y_T$  spectrum for *pion* is sub-divided into 5 sub-bins and *proton* is sub-divided into 3 sub-bins that creates  $5 \times 3 = 15$  cut bins for correlations. The binning scheme is discussed in Chapter 3.

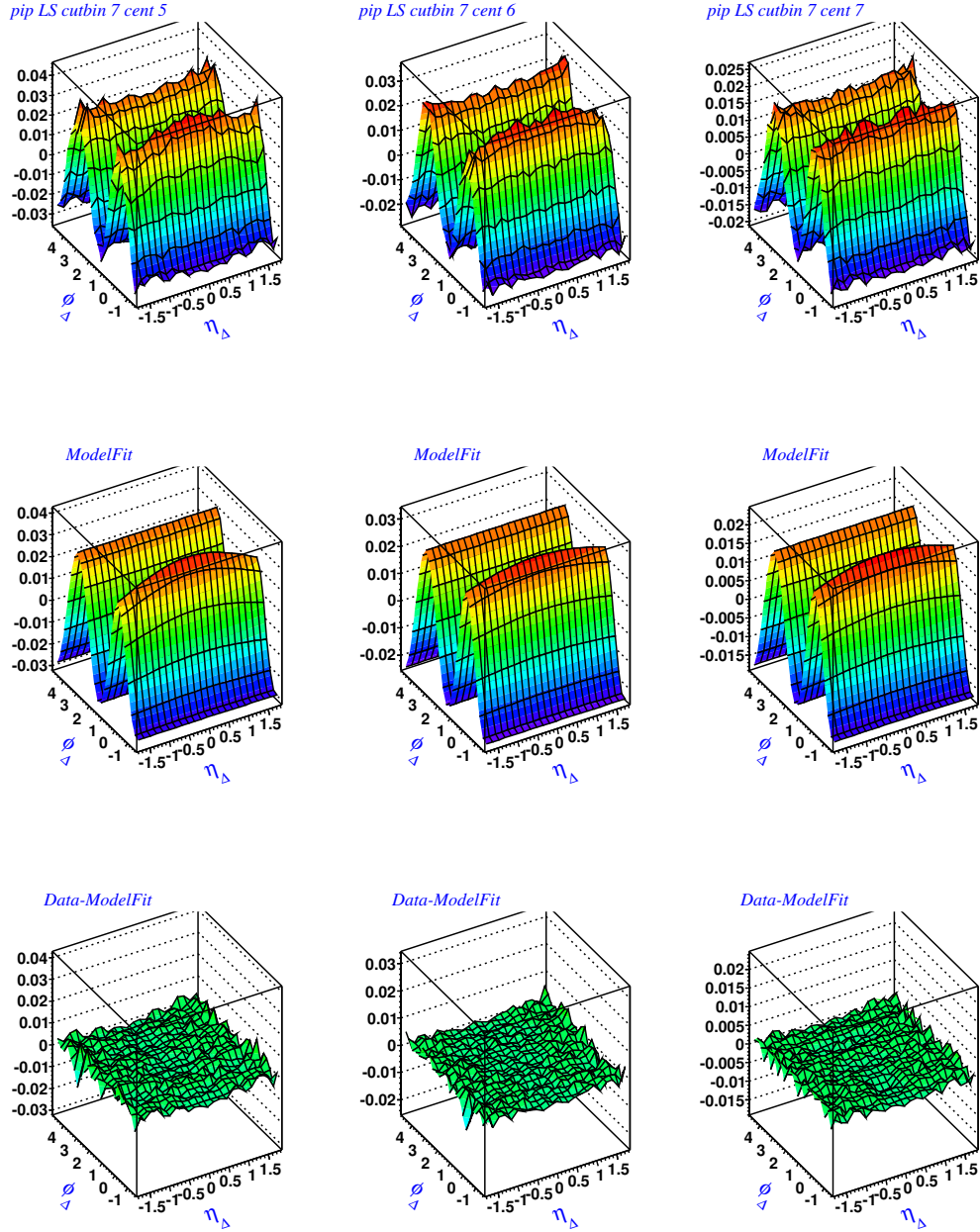


**Figure 6.40** Top row: LS correlations,  $\frac{\Delta\rho}{\rho_{ref}}$ , of *pion-proton* in cut bin 7 for centralities 38-46%, 28-38% and 18-28%. Middle row: model fit of the correlations. Bottom row: residual (data - model fit).

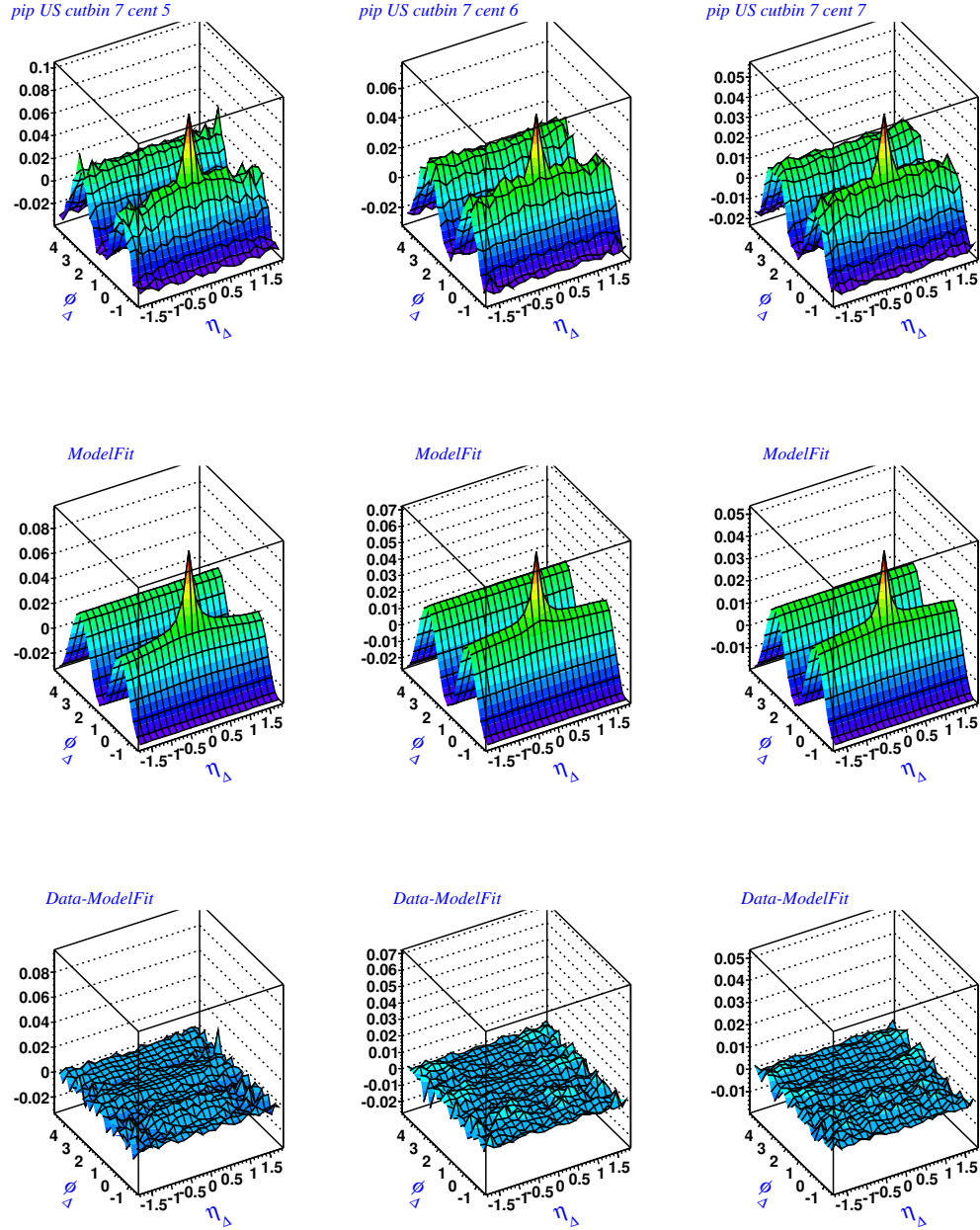


**Figure 6.41** Top row: US correlations,  $\frac{\Delta\rho}{\rho_{ref}}$ , of *pion-proton* in cut bin 7 for centralities 38-46%, 28-38% and 18-28%. Middle row: model fit of the correlations. Bottom row: residual (data - model fit).

In Figures 6.40 and 6.41 model fitting of  $pi$ - $p$  LS and US correlations for a particular cut bin in three centralities are shown. The LS correlation is fitted with dipole, quadrupole and negative 2D Gaussian components. The US correlations, however, are fitted with all 6-components. Figure 6.42 shows the evolution of  $v_2^2[2D]$  as a function of the centrality parameter  $\nu$  for  $(y_T, y_T)$  cut bin 7.

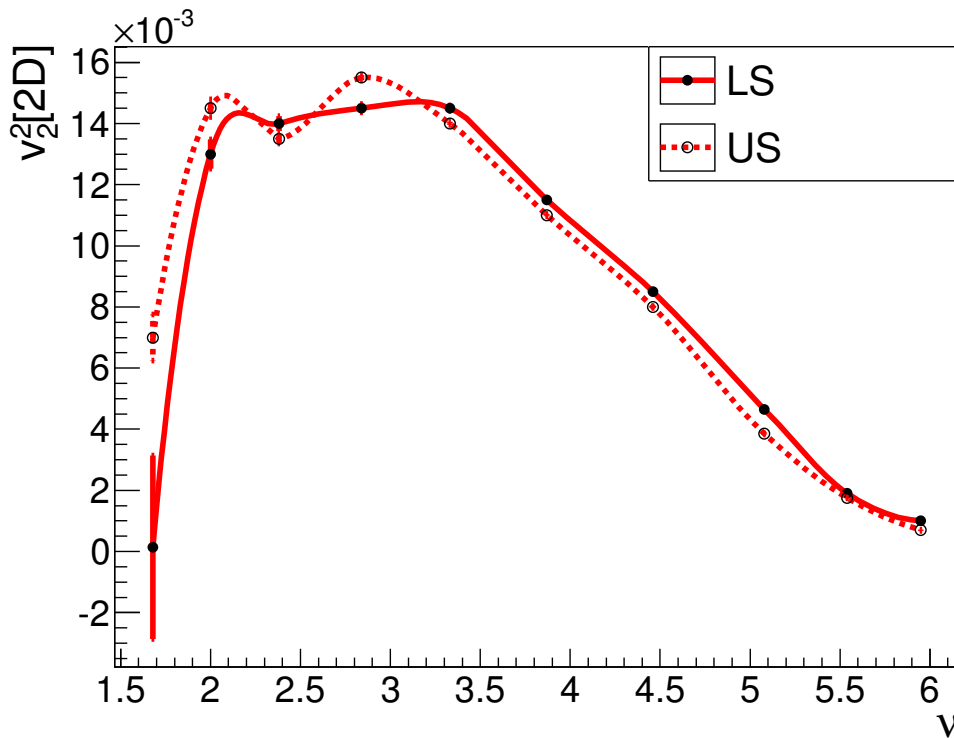


**Figure 6.42**  $\pi$ - $p$   $v_2^2[2D]$  as a function of centrality measure  $\nu$  for  $(y_T, y_T)$  cut bin 7. The error bars are fitting errors only. Because of low statistics in the most peripheral centrality bin, the correlation was not fitted there.

## 6.8 $K - p$ Correlations

Figures 6.43 and 6.44 show *kaon-proton* correlations for 200 GeV  $p_T$ -integrated data from Run 2011. Compared to *all-particle* correlations or  $\pi$ - $\pi$  correlations, the  $K$ - $p$  LS correlation doesn't show a positive peak around  $(\eta_\Delta, \phi_\Delta) \rightarrow (0, 0)$  in most of the centralities. Similarly, US correlations do not show the sharp 2D exponential peak..

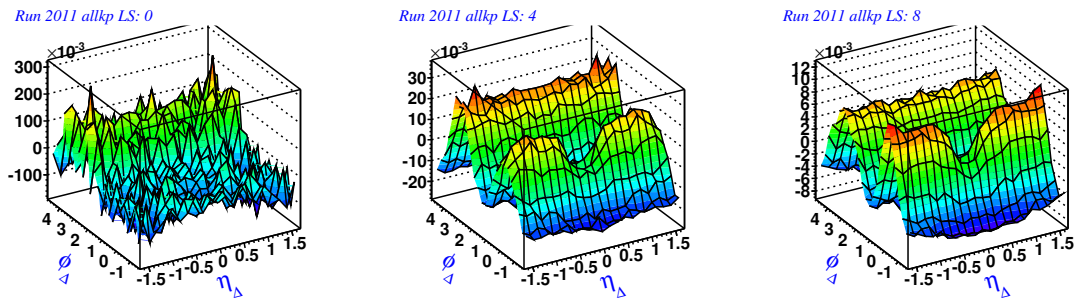


**Figure 6.43** Like-Sign correlations,  $\frac{\Delta\rho}{\rho_{ref}}$ , of *kaon-proton* for 200 GeV  $p_T$ -integrated data from Run 2011. The correlations are in centrality IDs 0, 4 and 8 (i.e., centrality percentages 84 – 93%, 50 – 60% and 10 – 20% respectively). No pre-factor has been applied.

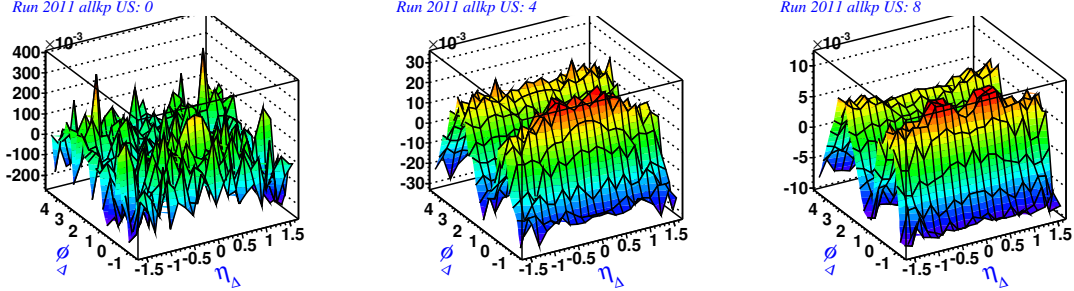


**Figure 6.44** Unlike-Sign correlations,  $\frac{\Delta\rho}{\rho_{ref}}$ , of *kaon-proton* for 200 GeV  $p_T$ -integrated data from Run 2011. The correlations are in centrality IDs 0, 4 and 8 (i.e., centrality percentages 84 – 93%, 50 – 60% and 10 – 20% respectively). No pre-factor has been applied.

In Figures 6.45 and 6.46 the evolution of  $K$ - $p$  LS and US correlations as a function of momentum are shown. The correlations are presented for a centrality bin 38-46%. In the LS correlations, the 2D positive exponential peak is absent. The same-side 2D Gaussian amplitude remains negative in most of the cut bins. The suppression in correlations may be due to reduced probability of nearby  $K$ - $p$  due to baryon number and flavor conservation where to get the LS  $K$ - $p$  pair requires fragmenting into  $K^+, K^-, p, \bar{p}$  costing a bing energy. There is no evidence of jet-structure in LS correlations. The quadrupole is common structures in all centralities for both LS and US correlations. In the US correlations, most of the cut bins show quadrupole and 2D Gaussian as major components in correlations. However, in some cut bins (e.g., cut bin 4) the structure is possibly due to resonance decay of  $\Lambda(\bar{15}20) \rightarrow K^+ + \bar{p}^5$ .

---

<sup>5</sup> $\Lambda(1520)$  is a resonant particle of mass  $1119.5 MeV/c^2$ . The possibility of  $\Lambda(1520)$  decay

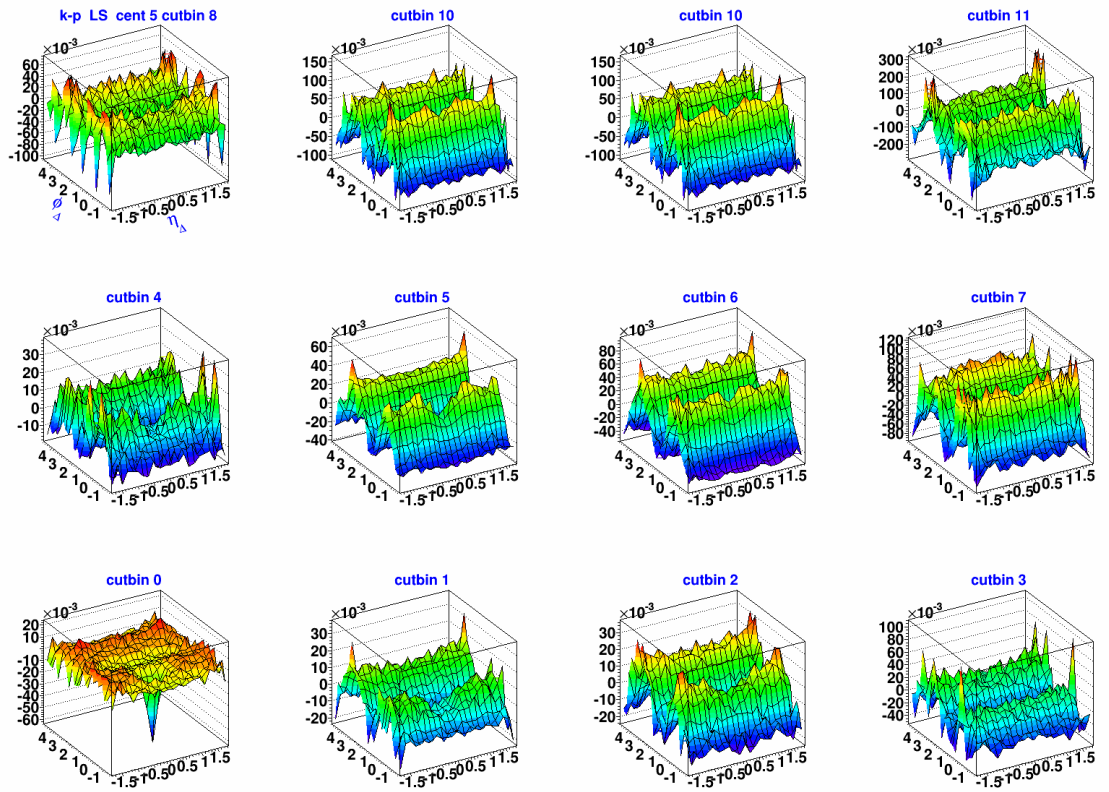


**Figure 6.45** Like-Sign correlations,  $\frac{\Delta\rho}{\rho_{ref}}$ , of *kaon-proton* for 200 GeV in different  $y_T$  sub-bins for a centrality 38-46%. The  $y_T$  spectrum for *kaon* is sub-divided into 4 sub-bins and *proton* is sub-divided into 3 sub-bins that creates  $4 \times 3 = 12$  cut bins for correlations. The binning scheme is discussed in Chapter 3.

---

into  $K^-p$  pairs has been studied in [75].

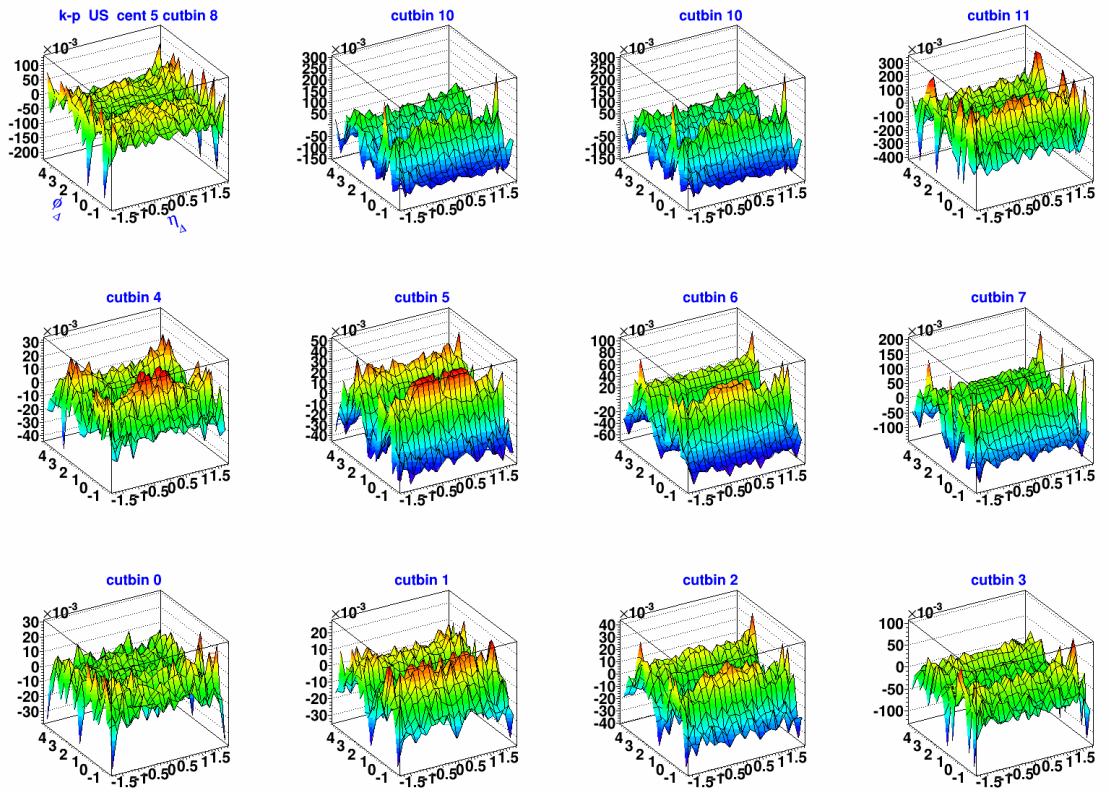


**Figure 6.46** Unlike-Sign correlations,  $\frac{\Delta\rho}{\rho_{ref}}$ , of *kaon-proton* for 200 GeV in different  $y_T$  sub-bins for a centrality 38-46%. The  $y_T$  spectrum for *kaon* is sub-divided into 4 sub-bins and *proton* is sub-divided into 3 sub-bins that creates  $4 \times 3 = 12$  cut bins for correlations. The binning scheme is discussed in Chapter 3.

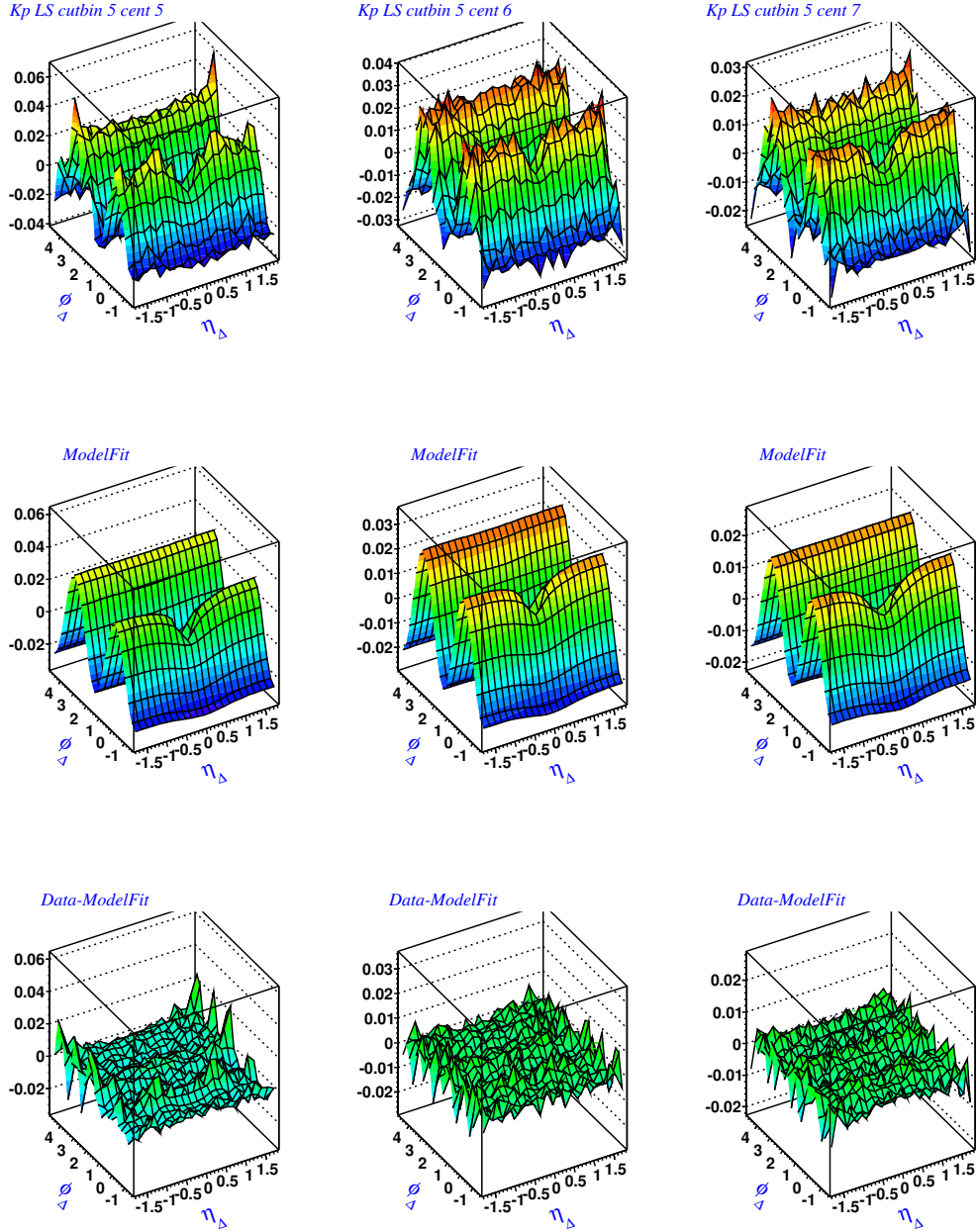


**Figure 6.47** Top row: LS correlations,  $\frac{\Delta\rho}{\rho_{ref}}$ , of *kaon-proton* in cut bin 5 for centralities 38-46%, 28-38% and 18-28%. Middle row: model fit of the correlations. Bottom row: residual (data - model fit).

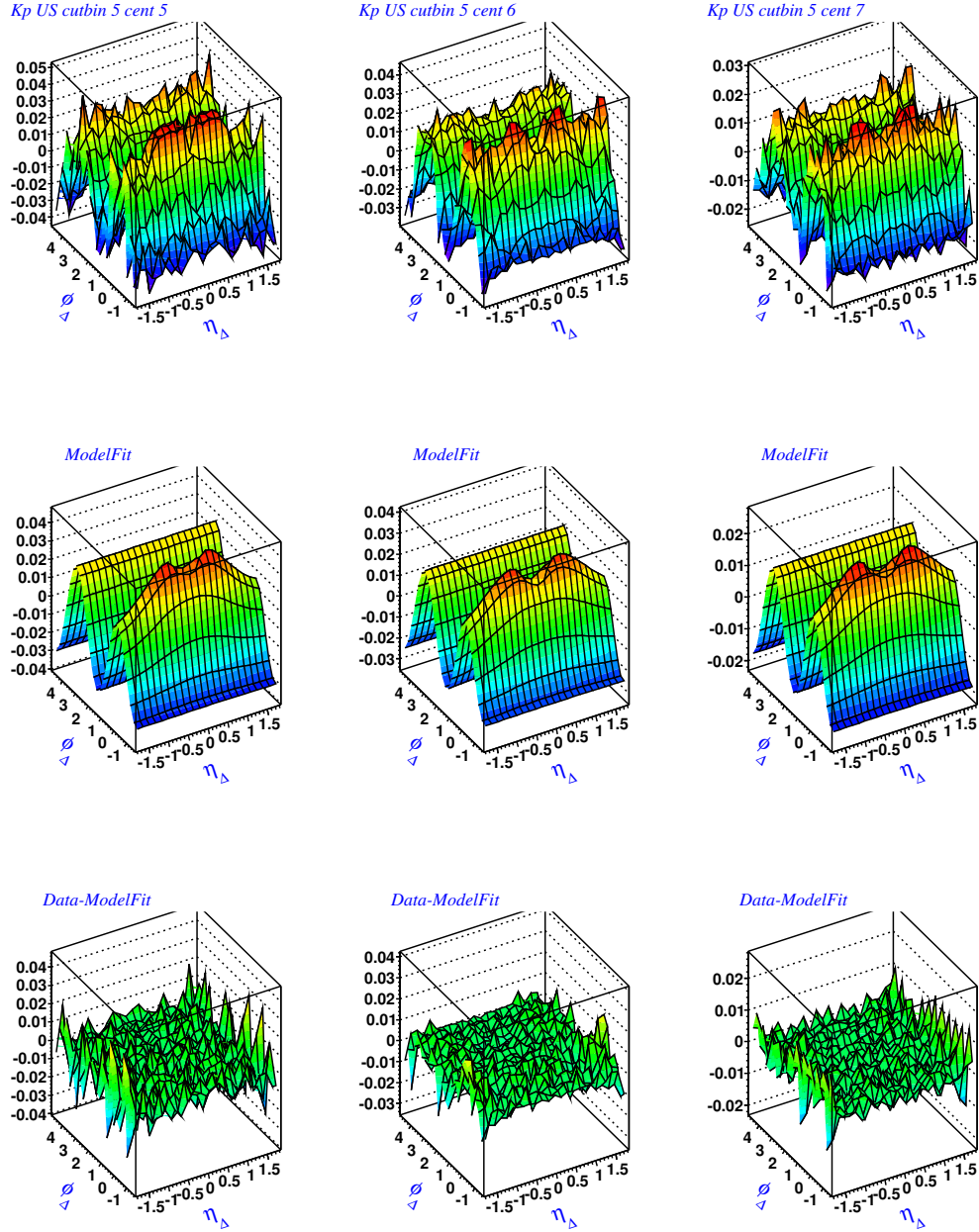


**Figure 6.48** Top row: US correlations,  $\frac{\Delta\rho}{\rho_{ref}}$ , of *kaon-proton* in cut bin 5 for centralities 38-46%, 28-38% and 18-28%. Middle row: model fit of the correlations. Bottom row: residual (data - model fit).

In Figures 6.47 and 6.48 model fitting of  $K$ - $p$  LS and US correlations for a particular cut bin in three centralities are shown. Both of the LS and US correlations are fitted with dipole, quadrupole and negative 2D Gaussian and 2D exponential components. Figure 6.49 shows the evolution of  $v_2^2[2D]$  as a function of the centrality parameter  $\nu$  for  $(y_T, y_T)$  cut bin 5.

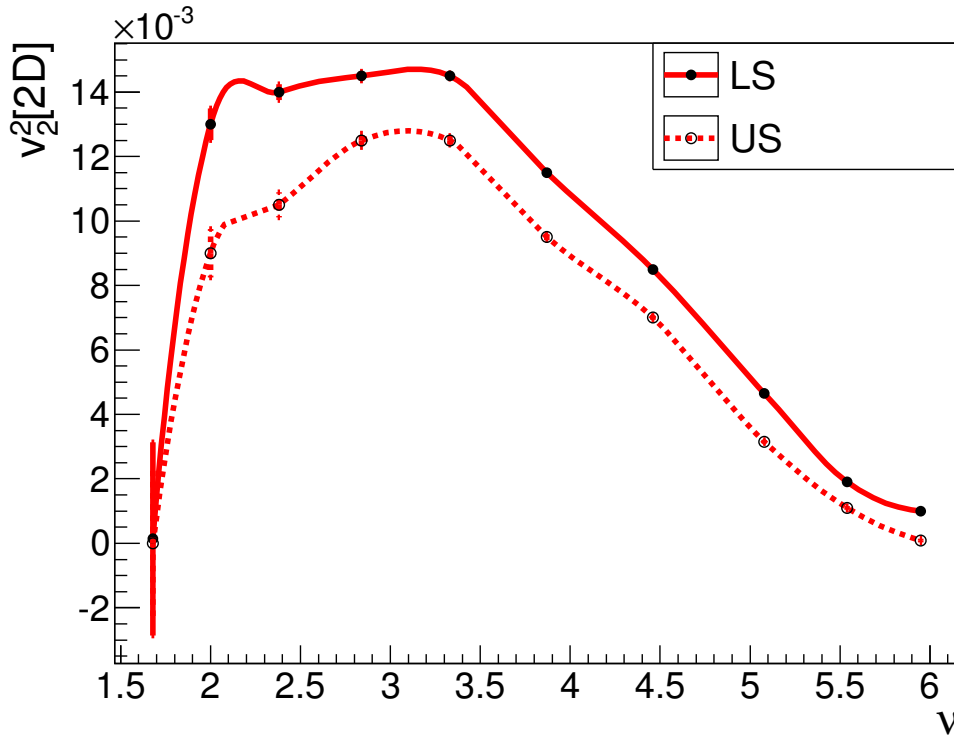


**Figure 6.49** *kaon-proton*  $v_2^2[2D]$  as a function of centrality measure  $\nu$  for  $(y_T, y_T)$  cut bin 5. The error bars are fitting errors only. Because of low statistics in the most peripheral centrality bin, the correlation was not fitted there.

## 6.9 $v_2[2D]$ and measured $v_2[EP]$

$v_2[EP]$  of identified particles have been measured as a function of  $p_T$  in Au+Au collisions at  $\sqrt{s_{NN}} = 200$  GeV by the PHENIX experiment [13][4]. In the paper [13],  $v_2[EP]$  was measured using event-plane method, in which single particle density in azimuth ( $\phi$ ) and estimated reaction-plane angle  $\Psi$  (in paper  $\Phi_{RP}$ ) are used. However, we have used two-particle pair density in  $(\eta_\Delta, \phi_\Delta)$  and no reaction plane angle is required while calculating  $v_2^2[2D]$ . Because  $v_2[EP]$  measured in Reference [13] and  $v_2[2D]$  are essentially identical [76], results are expected to be comparable in selected regions of momentum space (in selected cut bins). However, the identified particle dependent  $v_2[EP]$  measurement of Reference [13] differs from the present measurements in several ways: (1) only one particle of the pair is identified, those used to determine the reaction-plane are non-identified, (2) the central tracking arm and beam counter used for the reaction-plane are separated in  $\eta$  by 3-4 units, (3) the identified particles are binned in  $p_T$  while the reaction-plane particles are not, and (4) it is assumed that the quadrupole amplitude  $A_Q(\eta_\Delta) \propto v_{2,PID}(\eta_1) v_{2,non-PID}(\eta_2)$ <sup>6</sup> where  $|\eta_1| < 0.35$ ,  $|\eta_2| \in [3, 4]$  and such factorization has not been demonstrated. In the present data both particles are identified, both cover the same  $|\eta| \leq 1.8$  range<sup>7</sup>, both are binned in  $p_T(y_T)$  and only  $A_Q = 2v_2^2[2D]$  is reported where the factorization assumption is not needed. Besides these differences, centrality cuts, particle identification efficiencies are also not one-to-one comparable.

---

<sup>6</sup>PID = identified particle

<sup>7</sup>When only TPC is included,  $|\eta| \leq 2$ .

Therefore, we cannot make a quantitative comparisons of the  $\sqrt{v_2^2[2D]}$  to previously studied  $v_2[EP]$ , but instead qualitative comparison of the magnitudes of  $v_2$  are given.

In Figure 6.50,  $v_2[2D]$  measures for identified particle pairs  $\pi$ - $\pi$ ,  $K$ - $K$  and  $p$ - $p$  are shown. The  $v_2[EP]$  results from Reference [13] are overlaid on top of the  $v_2[2D]$  results. The  $v_2[2D]$  are measured from diagonal cut bins (where momenta of both particles in pairs are comparable within the range of the cut bin defined in Section 3.7) for each particle pair. Momentum  $p_T$  is calculated as a mean of the momentum range in each cut bin. Note that the  $p_T$  range is obtained from corresponding  $y_T$  values in the range. The results are of comparable magnitude within errors.

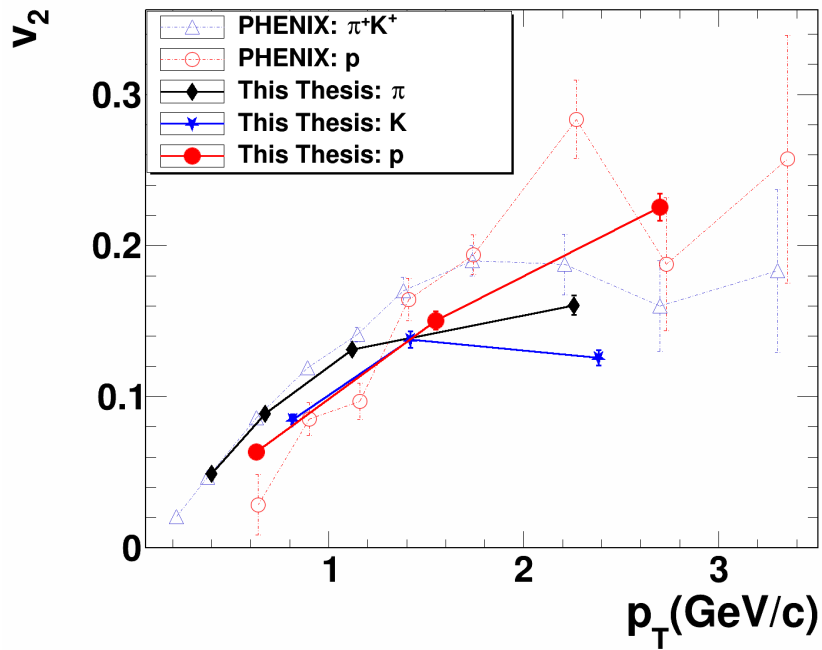


**Figure 6.50** Measurement of azimuthal anisotropy  $v_2[2D]$  of  $\pi$ ,  $K$  and  $p$  as a function of  $p_T$  in Au+Au at 200 GeV. PHENIX results for centrality 40-60% (filled points) have been taken from Reference [13]. Open points are results from current thesis for centrality 46-55%. Error bars in STAR data are systematic errors.

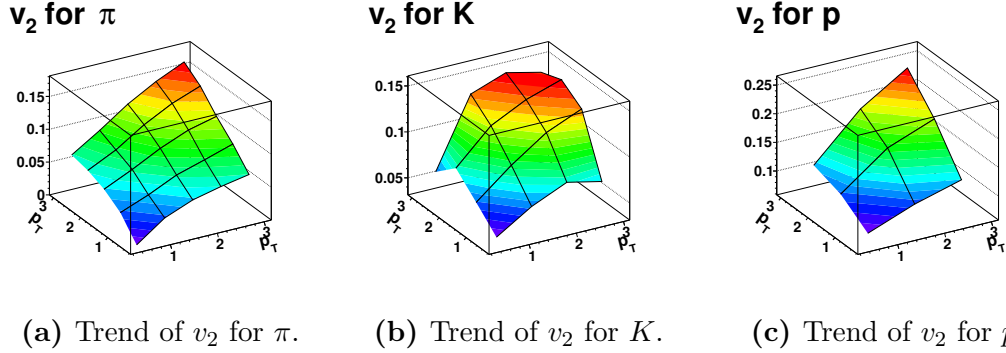


**Figure 6.51** Peak values of  $v_2[2D]$  near mid-central for identified particles as a function  $p_T$  for centrality 46-55%.

## 6.10 Systematic error in $v_2^2$ and $v_2$

PID contamination impurities and inefficiencies associated with the particle identification process causes systematic error (see Section 3.11) for the correlations of identified particles. The systematic error in the correlations propagates to the  $v_2^2$  and  $v_2$  measures. Therefore errors will be discussed in this section.

Measured identified sibling ( $\hat{\rho}_{exp,ij}^{sib}$ ) and reference ( $\hat{\rho}_{exp,ij}^{ref}$ ) pair densities are related to pure sibling ( $\hat{\rho}_{kl}^{sib}$ ) and reference ( $\hat{\rho}_{kl}^{ref}$ ) densities by

$$\begin{aligned}
 \hat{\rho}_{ij,exp}^{sib} &= \sum_{kl} a_{ik} a_{jl} \hat{\rho}_{kl}^{sib} \\
 \hat{\rho}_{ij,exp}^{ref} &= \sum_{kl} a_{ik} a_{jl} \hat{\rho}_{kl}^{ref} \\
 \Delta \hat{\rho}_{ij,exp} &= \hat{\rho}_{ij,exp}^{sib} - \hat{\rho}_{ij,exp}^{ref} \\
 &= \sum_{kl} a_{ik} a_{jl} \Delta \hat{\rho}_{kl},
 \end{aligned} \tag{6.5}$$

where  $i = \pi, K, p$  and  $a_{ik}$  is the probability that assumed particle type  $i$ , is actually particle type  $k$ , and the hat indicates that the densities are unit normal. (see Section 3.8)

From Equation 6.5, the correlation measure is derived using the same procedure discussed in Section 3.8.

$$\begin{aligned}
\frac{\Delta \hat{\rho}_{ij,exp}}{\hat{\rho}_{ij,exp}^{ref}} &= \sum_{kl} a_{ik} a_{kl} \frac{\Delta \hat{\rho}_{kl}}{\hat{\rho}_{ij,exp}^{ref}} \\
&= \sum_{kl} a_{ik} a_{jl} \frac{\hat{\rho}_{kl}^{ref}}{\hat{\rho}_{ij,exp}^{ref}} \frac{\Delta \hat{\rho}_{kl}}{\hat{\rho}_{kl}^{ref}} \\
&\approx \sum_{kl} a_{ik} a_{jl} \frac{\Delta \hat{\rho}_{kl}}{\hat{\rho}_{kl}^{ref}},
\end{aligned} \tag{6.6}$$

where  $\frac{\hat{\rho}_{kl}^{ref}}{\hat{\rho}_{ij,exp}^{ref}} \sim 1$  indicating that the ratio of unit normal densities in  $(\eta_{\Delta}, \phi_{\Delta})$  is approximately independent of PID.

Equation 6.1 can be written as

$$\frac{\Delta \hat{\rho}}{\hat{\rho}^{ref}} = 2v_2^2 \cos(2\phi_{\Delta}) + \dots, \tag{6.7}$$

where  $2v_2^2 = A_{quadrupole}$  and ‘...’ represents all other terms in Equation 6.1. So we may introduce the  $v_{2,ij}^2$  for PID pair  $i, j$ .

$$\begin{aligned}
v_{2,ij,exp}^2 &\approx \sum_{kl} a_{ik}a_{jl}v_{2,kl}^2 \\
&= \sum_{kl} a_{ik}a_{jl}v_{2,kl}^2 + v_{2,ij}^2 - v_{2,ij}^2 \\
&= v_{2,ij}^2 + \sum_{kl} a_{ik}a_{jl}(v_{2,kl}^2 - v_{2,ij}^2),
\end{aligned} \tag{6.8}$$

where  $\sum_{kl} a_{ik}a_{jl}v_{2,ij}^2 = v_{2,ij}^2 \sum_{kl} a_{ik}a_{jl} = v_{2,ij}^2$  because total probability is unity. The systematic error in  $v_{2,ij,exp}^2$  is the difference from the ideal and pure  $v_{2,ij}$ .

$$[v_{2,ij,exp}^2]_{systematic\ error} = \sum_{kl} a_{ik}a_{jl}(v_{2,kl}^2 - v_{2,ij}^2). \tag{6.9}$$

This error is only present for  $p_T > 2$  GeV/c. The average contamination fraction for  $p_T \in [2, 3]$  GeV/c are estimated from Figures 5.5, 5.6 and 5.7. The measured  $v_{2,ij}^2$  at the higher ( $p_T, p_T$ ) and at mid-centralities are also presented in Figures 6.12, 6.20 and 6.28. Using Tables 6.2 and 6.3 and Equation 6.9,  $\Delta v_{2,ij}^2 \equiv [v_{2,ij,exp}^2]_{systematic\ error}$  are calculated for all  $i, j = \pi, K, p$  and fractional error in  $v_2^2$  and  $v_2$  are obtained.

Probability that observed particle is  $\pi, K$  or  $p$  ( $a_{ik}$ )

$\pi$	0.95	0.05	0.00
$K$	0.1	0.88	0.02
$p$	0	0.02	0.98

**Table 6.2** Observed particle probability.

$PID$	$PID$	$v_2^2$	$\Delta(v_2^2)$	$\frac{\Delta(v_2^2)}{v_2^2}$	$\frac{\Delta(v_2)}{v_2}$
$\pi$	$\pi$	0.02000	0.00020	0.0101	0.00505
$\pi$	$K$	0.02200	0.00006	0.00300	0.001499
$\pi$	$p$	0.02800	0.00008	0.00282	0.00141
$K$	$\pi$	0.02200	0.00007	0.00300	0.00149
$K$	$K$	0.02500	-0.00031	-0.01254	-0.006292
$K$	$p$	0.03200	-0.00037	-0.011825	-0.00593
$p$	$\pi$	0.02800	0.00008	0.002821	0.00141
$p$	$K$	0.03200	-0.00037	-0.011825	-0.00593
$p$	$p$	0.04000	-0.00032	-0.00799	-0.00403

**Table 6.4** Particle identification errors and fractional errors in  $v_2$  and  $v_2^2$ .

$v_2^2$  for higher  $p_T$  at mid-centrality

$v_{2,ij}^2$	$\pi$	$K$	$p$
$\pi$	0.02	0.022	0.028
$K$	0.022	0.025	0.032
$p$	0.028	0.032	0.04

**Table 6.3**

$$\begin{aligned}
\text{Fractional error in } v_2^2 &= \frac{\Delta(v_2^2)_{ij}}{v_{2,ij}^2} \\
\text{Fractional error in } v_2 &= \sqrt{\frac{v_{2,ij}^2 + \Delta(v_2)_{ij}}{v_{2,ij}^2}} - 1 = \frac{\Delta(v_2)_{ij}}{v_{2,ij}}
\end{aligned} \tag{6.10}$$

Table 6.4 shows the systematic errors for different combinations of PID. If the contamination probability is independent of centrality, then these fractional errors at mid-centrality approximately apply to all centralities.

Centrality	$\Delta(A_Q)$	$A_Q$	$\frac{\Delta(v_2)}{v_2}$
0	0.00075	0.002	0.17
1	0.00075	0.011	0.034
2	0.00015	0.028	0.026
3	0.00035	0.070	0.025
4	0.00055	0.136	0.020
5	0.00075	0.201	0.018
6	0.009	0.270	0.017
7	0.01	0.268	0.018
8	0.0075	0.179	0.021
9	0.005	0.063	0.039
10	0.0045	0.001	1.35

**Table 6.5** Fractional errors in  $v_2$  for non-identified particles.

The PID error is less than 1% which slightly increases for the larger  $y_T$  values. Table 6.5 shows the error in  $v_2$  for different centralities calculated from error in quadrupole amplitude ( $A_Q$ ). The errors in  $A_Q$  are average values of  $\pm$  errors listed in Table III of Reference [5]. It shows that the systematic errors are about  $\pm 2\%$ - $\pm 4\%$  in  $v_2$  except for the most-peripheral and the most-central bins (bin 0 and 10), where  $v_2 \sim 0$ .

## 6.11 Factorization

The measured  $v_2^2$  is a function of the type of particle-pair and the  $p_T(y_T)$  of each particle in the pair. Factorization assumes that  $v_2^2$  can be decomposed into factors as shown in Equation 6.11

$$v_{2,ij}^2(p_{Ti}, p_{Tj}) = v_{2i}(p_{Ti})v_{2j}(p_{Tj}), \quad (6.11)$$

where  $i, j$  are particle-types and  $p_{Ti}$  and  $p_{Tj}$  are the momenta of the particles. The different combinations of particles and the momentum bins are discussed in Sections 6.8 and 3.7. The factorization is a necessary but not sufficient condition for the quadrupole correlations to be due to independent, event-wise single particle distributions of the form

$$\frac{dN_i}{p_T dp_T d\eta} \Big|_{event\ j} = \frac{dN_i}{p_T dp_T d\eta} [1 + 2v_{2i}(p_T) \cos[2(\phi_i - \Psi_{ij})]], \quad (6.12)$$

where  $\Psi_{ij}$  is reaction plane angle for  $j^{th}$  event.

The correlations measured in particle and momentum spaces allows tests of factorization. If the data agree with factorization, then a single particle event plane source of the quadrupole is consistent with data, but not necessary, as any 2-particle correlation of the form  $k f_i(p_{Ti}) f_j(p_{Tj}) \cos(2\phi_\Delta)$  will agree with factorization results, not just that obtained from a single event plane with angle  $\Psi$ .

The factorization assumption was tested for different type particle correlation types. Figures 6.52, 6.53 and 6.54 show how factorization holds in  $\pi$ - $\pi$ ,  $K$ - $K$  and  $p$ - $p$  LS correlations, respectively. In the figures, the filled dots connected by solid lines are the measured  $v_2^2$  in different momentum bins as a function of centrality. The open triangle symbols are calculated using the factorization principle. For example, in arbitrary  $y_{T1} \times y_{T2}$  bin, a point in each centrality is obtained as  $\sqrt{v_2^2(y_{T1}, y_{T1})} \times \sqrt{v_2^2(y_{T2}, y_{T2})}$ . In diagonal bins it is expected that the product of factors agrees with the  $v_2^2$  values. From the

figures it is evident that for identical particles, the factorization assumption holds within errors. Similarly, Figures 6.55, 6.56 and 6.57 show how factorization holds in  $\pi$ - $K$ ,  $\pi$ - $p$  and  $K$ - $p$ , LS correlations. In the correlations from different species of particles, the factorization assumption holds within errors.

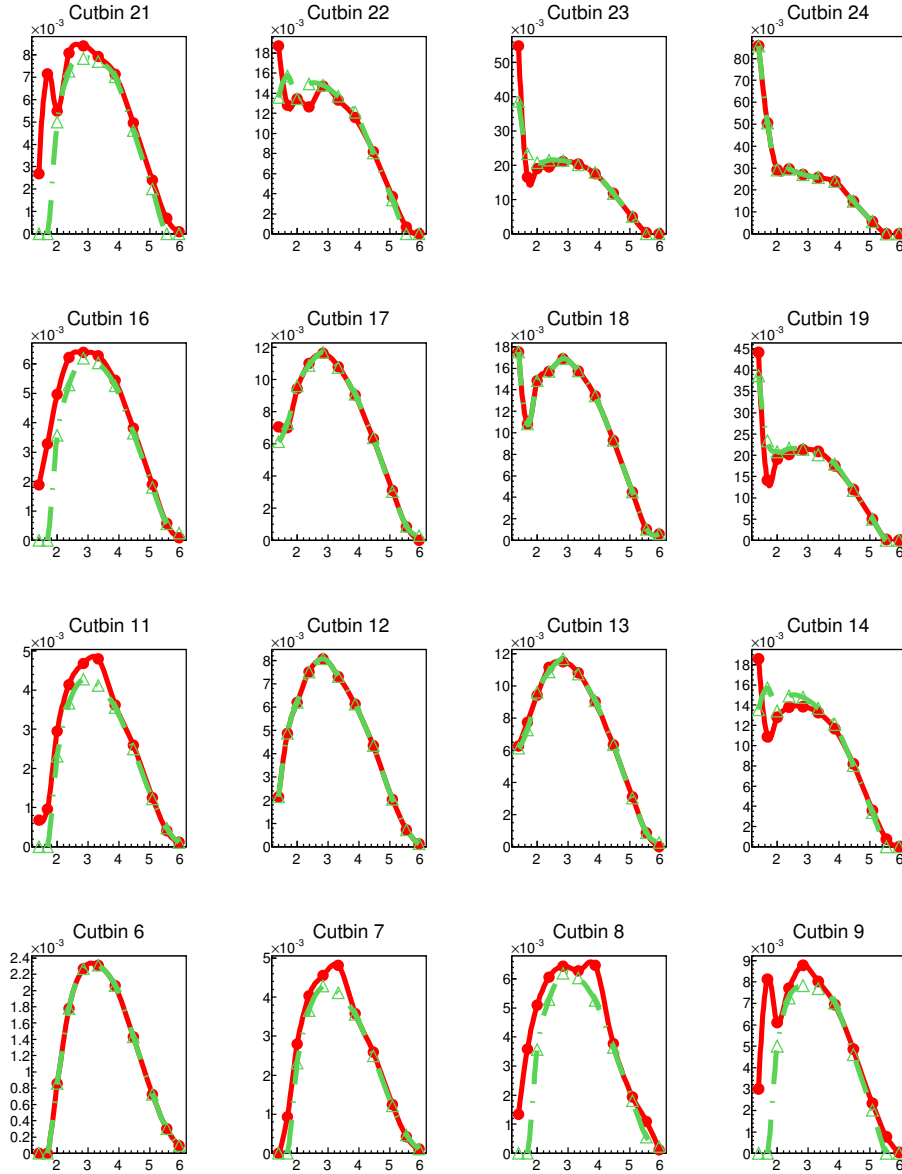


**Figure 6.52** Factorization test.  $x$ -axis in each plot is the centrality measure in previous figures, e.g., Figure 6.49. LS  $v_2^2$  for  $\pi$ - $\pi$  is shown with filled red circle connected by solid red lines and results from factorization for each centrality are shown in green triangles connected with dashed green lines. Results for the lowest  $y_T$  cut bins are excluded due to possible fitting instabilities in cut bin 0. The match between filled lines and dashed line in diagonal bins is by construction.

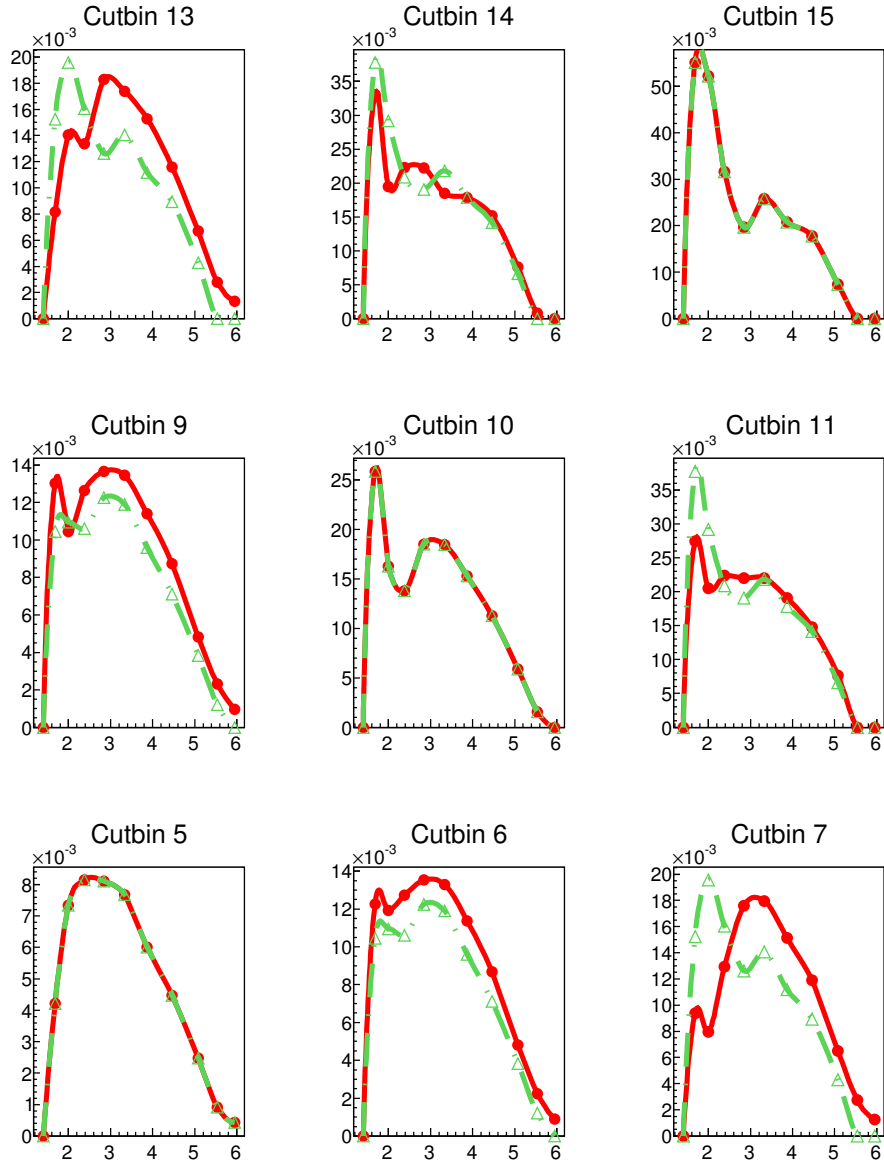


**Figure 6.53** Factorization test.  $x$ -axis in each plot is the centrality measure in previous figures, e.g., Figure 6.49. LS  $v_2^2$  for  $K$ - $K$  is shown with filled red circle connected by solid red lines and results from factorization for each centrality are shown in green triangles connected with dashed green lines. Results for the lowest  $y_T$  cut bins are excluded due to possible fitting instabilities in cut bin 0. The match between filled lines and dashed line in diagonal bins is by construction.

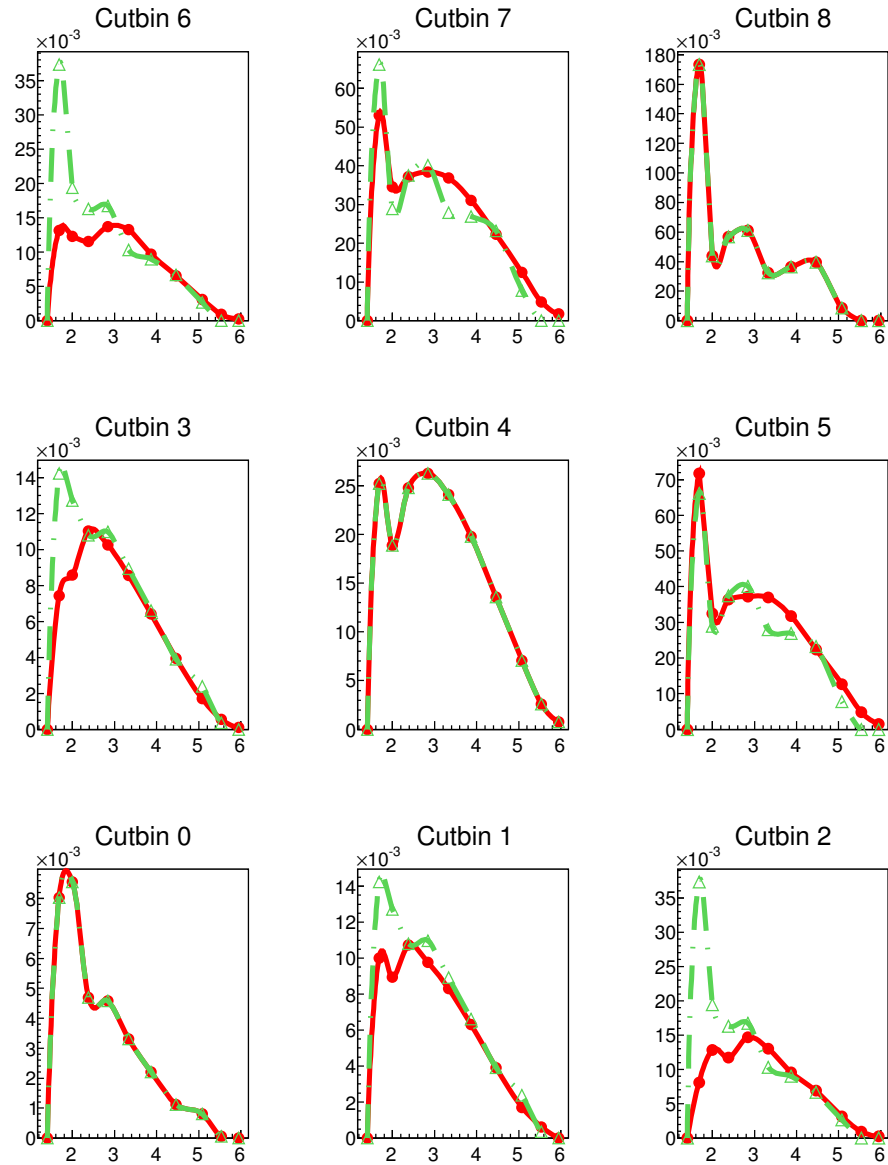


**Figure 6.54** Factorization test.  $x$ -axis in each plot is the centrality measure in previous figures, e.g., Figure 6.49. LS  $v_2^2$  for  $p$ - $p$  is shown with filled red circle connected by solid red lines and results from factorization for each centrality are shown in green triangles connected with dashed green lines. The match between filled lines and dashed line in diagonal bins is by construction.

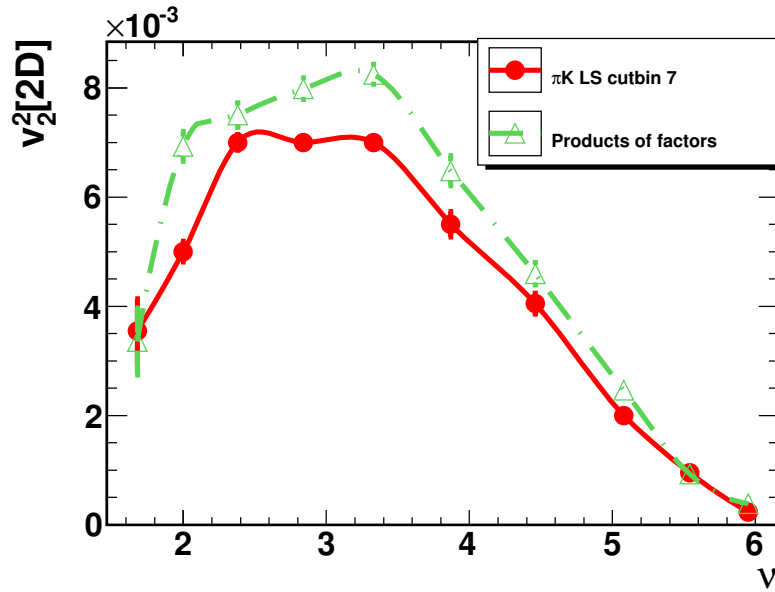


**Figure 6.55** Factorization test.  $x$ -axis in the figure is the centrality measure. LS  $v_2^2$  for  $\pi$ - $K$  for cut bin 7 is shown with filled red circles connected by solid red lines and result from factorization for each centrality are shown in green triangles connected with a dashed green line.

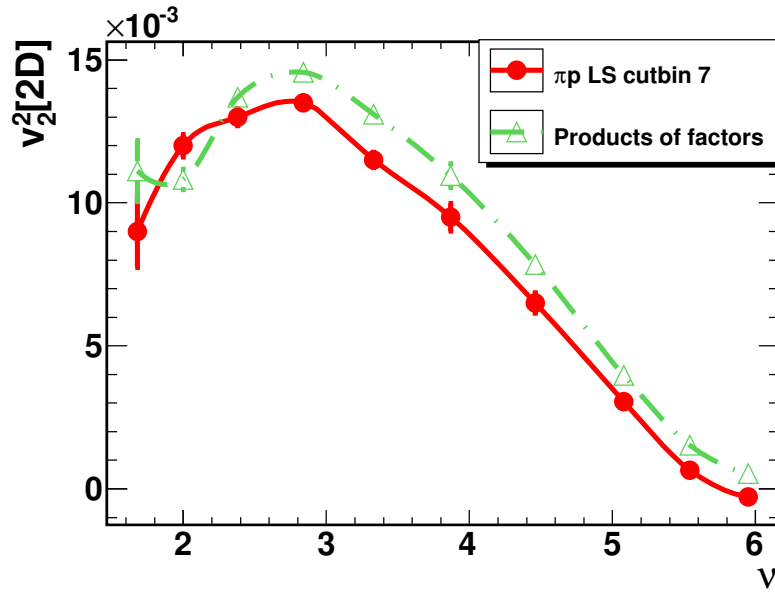


**Figure 6.56** Factorization test.  $x$ -axis in the figure is the centrality measure. LS  $v_2^2$  for  $\pi$ - $p$  for cut bin 7 is shown with filled red circle connected by solid red lines and result from factorization for each centrality are shown in green triangles connected with a dashed green line.

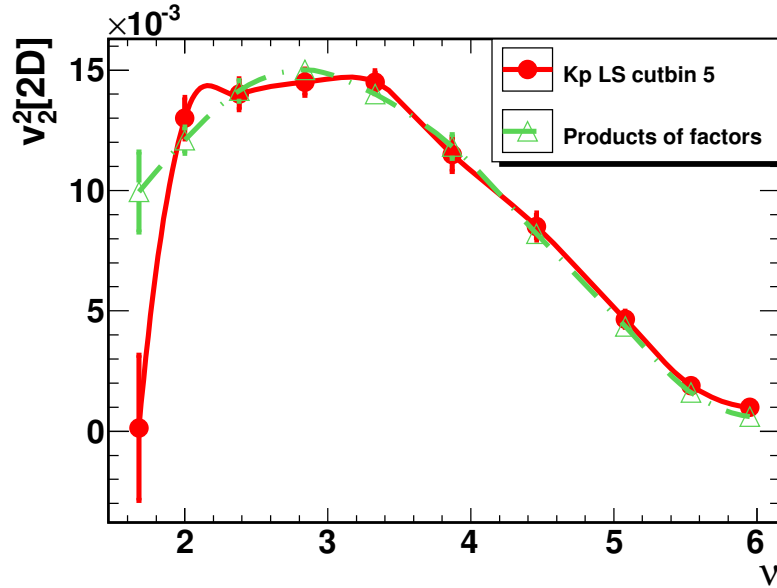


**Figure 6.57** Factorization test.  $x$ -axis in the figure is the centrality measure. LS  $v_2^2$  for  $K$ - $p$  for cut bin 5 is shown with filled red circle connected by solid red line and result from factorization for each centrality are shown in green triangles connected with a dashed green line.

## 6.12 Discussion

The study of two-particle angular correlations of identified particles provides an opportunity to explore the evolution of dynamical processes in the range of momentum and centrality for each combination of particle pair types. The information related in the correlation structures could be useful for advancing more general theoretical models in the future. The CI and CD angular correlations measured in different specific momentum ranges presented in Ref-

erence [1][37] presents useful information on the properties of the hot dense matter formed in the collisions. However, that study did not discriminate the behavior of correlations for particle species such as for *strange mesons* compared to *non-strange mesons* or for *mesons* compared to *baryons*. Also, that study did not provide information on how the particles of different combination of charge pairs (such as ++, --, +-, -+, LS, US)<sup>8</sup> behave in the medium. Therefore, this study provides complete measurements of the light-flavor particles in the two-particle momentum-space, density produced in Au+Au collisions at 200 GeV center of mass per colliding nucleon-nucleon pair.

Despite the dominance of *pions* in the total particle density,  $\pi$ - $\pi$  LS and US correlations do not show all the correlation features seen in the all-particle CI correlations. For example, in LS correlations a 2D exponential is present only when the momentum of both particles in the pair are comparable within a range of cut bins. Such correlations could be used to study correlations with and without HBT. Similarly, the LS correlations do not show a strong 1D Gaussian in  $\eta_\Delta$ . In US correlations the 1D Gaussian appears only in more peripheral centralities. Turning the 1D Gaussian on and off might be informative and facilitate analysis of soft, longitudinal fragmentation.

The *K-K* correlations are interesting because of the presence of *strange* quarks. The LS correlations show a same-side negative 2D Gaussian in more

---

<sup>8</sup>The CI and CD correlations were derived from LS and US correlations. However, the information in LS and US correlations were not studied in detail.

central collisions. This feature is not seen in the all-particle correlations. The negative amplitude may suggest that the formation of  $K^+K^+$  or  $K^-K^-$  at small  $(\eta_\Delta, \phi_\Delta)$  is energetically disfavored. In US correlations, the  $\phi$ -meson decay dominates in the region where the momentum of both particle in the pair are comparable. The correlations from the resonance decay products contain interesting physics [77][78]. However, for the present study, it has been taken as a background.

The  $p$ - $p$  correlations also show significantly different correlations than the all-particle correlations. Possibly, due to lack of energy to form two nearby protons, both LS and US correlations show a near-side negative 2D Gaussian. Many previously unseen structures show up in different momentum ranges. Such correlations may help in understanding baryon production in heavy-ion collisions.

Based on careful observation of correlations structures of identified particles in different collision centralities and in regions of momentum, the following physics results can be inferred.

### **Jets and dijets**

As evidenced primarily by the 2D Gaussian and away-side dipole components of the correlation structures the following can be inferred:

- Jets and dijets are observed in all PID combinations except for  $p$ - $p$  LS and  $K$ - $p$  LS correlations, at least within the  $p_T < 3$  GeV/ $c$  range studied in this thesis.

- The amplitude of the 2D Gaussian increases with  $p_T$  and centrality when measured as the number of correlated pair per final-state particle.
- The same-side,  $\eta$ -elongated “ridge” is observed in  $\pi$ - $\pi$  correlations confirming the essential pion nature of the ridge, but it is not (yet) observed in the non-pion combinations.
- For  $\pi$ - $\pi$  correlations at higher  $(y_T, y_T)$  and centrality the jet-like structure develops a leptokurtic shape, as seen in Reference [37] for non-identified particle correlations on  $y_T$ . This shape evolution from a board Gaussian on  $\eta_\Delta$  to leptokurtic may be due to the reduction in relative strength of the dynamical process(es) causing the ridge, relative to the conventional pQCD jet. A reduction in ridge amplitude at higher  $p_T$  for non-identified particle correlations was reported by Kettler [38] and Oldag [79].
- For production of heavier particle pairs (  $K$  and  $p$ ) the jet correlation’s emergence is pushed to higher  $y_T$ , consistent with the required energy for hadronization into these heavier particles and the energy available from the scattered and fragmenting parton. The energy requirement for LS is much more severe than for US due to the requirement of charge, flavor and baryon number conservation. For example creation of  $\pi^+$ - $\pi^+$  from a neutral source (e.g. gluon) requires production of  $\pi^+, \pi^-, \pi^+, \pi^-$ . Similarly observation of  $K^+$ - $K^+$  requires production of  $K^+, K^-, K^+, K^-$  and  $p$ - $p$  must be from  $p, \bar{p}, p, \bar{p}$ .

- For this reason US jet/dijet production in this  $y_T$  range is larger than LS.

In summary, all of the presented results remain consistent with minimum-bias PYTHIA jets and dijets with trends as expected for the selected kinematic range and with the ridge observations for non-identified particle correlations. The ridge appears to be mainly composed of pions. Observation of a ridge for non-pion correlated pairs remains to be studied.

### $v_2^2[2D]$ - **Quadrupole (elliptic flow)**

As evidenced by the measured quadrupole amplitudes in ranges of momentum following can be inferred:

- The quadrupole is evident in all PID combinations,  $y_T$  and centrality bins with the expected increase with  $p_T$  and characteristic centrality dependence.
- Generally, the present  $v_2(p_T)$  obtained as  $\sqrt{v_2^2(p_{T1}, p_{T2})}$  for  $\pi$ - $\pi$ ,  $K$ - $K$  and  $p$ - $p$  agrees with the event-plane (EP)  $v_2$ .
- The mass scaling reported in EP determined  $v_2(p_T)$  for  $\pi, K, p$  is also observed in the present  $v_2^2[2D]$  along the  $p_{T1} = p_{T2}$  diagonal.
- Off the  $(p_T, p_T)$  diagonal  $v_2^2(p_{T1}, p_{T2})$  for  $\pi$ - $\pi$ ,  $K$ - $K$  and  $p$ - $p$  follows the same mass scaling determined by factorization, i.e.,  $v_{2,ij}^2(p_{T1}, p_{T2}) = v_{2i}(p_{T1}) \times v_{2j}(p_{T2})$  where  $i, j$  are particle types.

- First tests of the factorization hypothesis were done. Factorization is a necessary but not sufficient test of the event-plane (EP) single particle asymmetry source for the quadrupole correlation. Factorization was found to be satisfied for  $\pi$ - $\pi$ ,  $K$ - $K$  and  $p$ - $p$  across centralities and the  $(p_{T1}, p_{T2})$  range studied for mid-rapidity particles ( $\eta < 1.8$ ).
- This means that for these PID combinations the quadrupole correlation is consistent with an EP single particle asymmetry source.
- Similarly, for  $\pi$ - $K$ ,  $\pi$ - $p$  and  $K$ - $p$  factorization is found to be satisfied within errors.

In summary, the  $v_2(p_T)$  for  $\pi$ ,  $K$  and  $p$  follow expectations and factorization seems to be valid for similar as well as dissimilar PID pairs.

### **Soft-longitudinal fragmentation (charge ordering)**

As mainly evidenced by the 1D Gaussian amplitude on  $\eta_\Delta$  the following are inferred

- Soft-longitudinal fragmentation is mainly seen in US  $\pi$ - $\pi$ , to lesser degree in LS  $\pi$ - $\pi$  and even less in  $\pi$ - $K$  US correlations.
- It appears in more peripheral collisions and at lower  $p_T$  consistent with previously seen charge ordering on  $\eta_\Delta$  among the soft hadrons.
- In this thesis I show that this structure is mainly caused by pions.

- Its disappearance in more central collisions provides evidence for final-state interactions which destroy the soft particle fragmentation correlations.

In summary, this analysis shows that the observed charge-ordering effects are dominated by pions, not only because pions dominate the particle multiplicity at low  $p_T$ , but also because the 1D Gaussian is absent in non-pion pairs, even at these low  $p_T$ .

## 2D-exponent

The 2D-exponential components of the correlation are caused by HBT correlations,  $e^+e^-$  conversion contaminations, and final-state Coulomb interaction.

- The 2D-exponent is evident in all the expected PID, LS and US combinations and  $y_T$  ranges.
- For purposes of this analysis these correlations are considered backgrounds.

## New correlation features

In the identified charged particle correlations in ranges of momentum the following new features are observed:

- The same-side “volcano” in  $K^+K^-$  is expected from  $\phi$ -meson decay and is taken to be a background for this analysis. Similarly, for the

other cases where possible evidence of the  $K^* \rightarrow \pi + K$ ,  $\Lambda \rightarrow \pi + p$  and  $\Lambda(1520) \rightarrow K^- + p$  are considered backgrounds.

- The same-side suppression centered at (0,0) is stronger for LS than US, increases for the heavier mass particles and increases at lower  $y_T$ . It is most prominent in  $p$ - $p$  LS and US correlation but very clear in  $K$ - $p$ ,  $K$ - $K$  and  $\pi$ - $p$  LS correlations.

In summary, these unusual anti-correlations and their trends on  $y_T$ , centrality and with respect to particle type provide new kinds of correlations constraints on hadronization models for heavy-ion collisions. The trends in the data suggest that any attempt to describe these correlations must account for energy/momentum conservation (which eliminates AMPT [80] because energy is not conserved in its hadronization model), and charge, flavor and baryon number conservation. LUND string fragmentation [81], PYTHIA [15] type jet formations, AMPT and other coalescence models can now be rigorously tested.

### 6.13 Future Work

This exhaustive survey of identified particle angular correlation as a function of centrality and transverse momentum has brought up potentially very rich information in high energy collisions in RHIC. Because of the complex mechanism of particle formation, the correlations for all identified particle-pairs in all cut bins in all centralities cannot be expected be fitted with the same model. Therefore, finding an appropriate model for each particle type

combination is important. Because of narrower ranges in momentum varying particle production rates, the statistics in all sub-spaces are not equally capable for the correlations fits to measure meaningful physics. Therefore, extending this study with a larger data sample, which reduces statistical fluctuation, would increase the physics impact of this study.

# Chapter 7

## Conclusion

A detailed survey of angular correlations between two identified particles were made as a function of centrality and transverse momentum in Au+Au collisions of  $\sqrt{s_{NN}} = 200$  GeV at STAR. The analysis was done using minimum bias data from Run 2010 and 2011, where the emphasis was to make smallest possible set of cuts in the data.

In this dissertation new two-particle correlations for identified particle pairs were measured. The correlations were measured for 6-types of particle combinations ( $\pi\pi$ ,  $KK$ ,  $pp$ ,  $\pi K$ ,  $\pi p$  and  $Kp$ ) of both like and unlike charged sign particles. These data contain a wealth of new information about the two-particle correlations of identified particles in different projections of 4D space ( $y_{T1}, y_{T2}, \eta_{\Delta}, \phi_{\Delta}$ ).

In  $\pi$ - $\pi$  correlations, the evolution of the same-side peak from a broad Gaussian on  $\eta_{\Delta}$  to a leptokurtic shape suggests a change in the longitudinal broadening mechanism of the jets. The 2D Gaussian and away-side dipole (jets) appear at higher  $y_T$  only, where gluon fragmenting into LS  $\pi^{\pm}$ - $\pi^{\pm}$  is energetically more demanding than into US  $\pi^{\pm}$ - $\pi^{\mp}$  pairs. This analysis shows that the observed charge-ordering effect is dominated by pions, not only be-

cause pions dominate the particle multiplicity at low  $p_T$ , but also because the 1D Gaussian is absent in non-pion pairs, even at these low  $p_T$ .

For all identified particle pair channels where same-side suppression are seen at  $(\eta_\Delta, \phi_\Delta) \sim (0, 0)$ , the trends of the width and depth of suppressions with respect to  $y_T$  and centrality suggest kinematic restriction on fragmentation or hadronization to  $K^\pm K^\pm$  (i.e. strange quark production into  $SS$  or  $\bar{S}\bar{S}$ ) and to 2 baryons ( $pp$  and  $\bar{p}\bar{p}$ ). The same-side suppression centered at  $(0,0)$  is stronger for LS than US, increases for the heavier mass particles and increases at lower  $y_T$ . It is most prominent in  $pp$  LS and  $pp$  US but is also very clear in  $Kp$  LS,  $KK$  LS and  $\pi p$  LS.

Resonance contributions to the correlation structures can be significant. In some cases, a resonance, like the  $\phi$ -meson decay to  $K^+K^-$ , creates a same-side “volcano” peak which dominates the correlation structures. Because resonance decay obscures other important correlation structures, we treated it as an unwanted background in the present analysis.

To extract the quantitative results, a careful and detailed model fitting procedure was adopted so that the identifiable structures and their trends on  $y_T$  and centrality could be quantitatively compared to theories.  $v_2^2[2D]$ , the quadrupole (elliptic flow), is an evident feature in all particle combinations,  $y_T$  and centrality bins with the expected increase with  $p_T$  and characteristic centrality dependence. We measured  $v_2^2[2D]$  for different combinations of particle pairs. Here,  $v_2^2[2D]$  is reported because (1) its fitting is stable (as in non-identified particle correlations) and (2)  $v_2$  is of greatest interest in the

heavy-ion communities. Also, available predictions in the literature are for identified-nonidentified pairs, not for fully identified pairs.

Factorization is a necessary but not sufficient condition for the quadrupole correlation to be due to independent, event-wise single particle distributions. The factorization principle for all  $i, j$  particle types,  $v_{2,ij}^2(p_{Ti}, p_{Tj}) = v_{2i}(p_{Ti}) \times v_{2j}(p_{Tj})$ , was tested for both similar and dissimilar particle pairs. The  $v_2(p_T)$  for  $pi, K, p$  follow expectations and factorization seems to be valid. Similarly, for dissimilar particle pairs as well factorization seems to be valid.

Many characteristic correlations structures for different identified particles are observed and the data provide analysis and theory comparisons opportunities for years to come.

# Chapter 8

## Appendix

### 8.0.1 Approximation

In Equation 3.23, the residual term in parenthesis,  $\left(\frac{N_{ref}}{N_{sib}} - \frac{N_{ref,\alpha}}{N_{sib,\alpha}}\right) = \delta_\alpha$ , is negligibly small because of the similarity in relative sibling to reference pair distributions for each PID and for each  $y_T$  range.

$$\begin{aligned}
 \left(\frac{N_{ref}}{N_{sib}} - \frac{N_{ref,\alpha}}{N_{sib,\alpha}}\right) \frac{n_{sib,\alpha}}{n_{ref,\alpha}} &\equiv \delta_\alpha \frac{n_{sib,\alpha}}{n_{ref,\alpha}} \\
 &= \delta_\alpha \frac{n_{sib,\alpha} - n_{ref,\alpha} + n_{ref,\alpha}}{n_{ref,\alpha}} \\
 &= \delta_\alpha \frac{n_{sib,\alpha} - n_{ref,\alpha}}{n_{ref,\alpha}} + \delta_\alpha \\
 &= \delta_\alpha \frac{\frac{N_{ref,\alpha}}{N_{sib,\alpha}} n_{sib,\alpha} - n_{ref,\alpha} + n_{sib,\alpha} - \frac{N_{ref,\alpha}}{N_{sib,\alpha}} n_{sib,\alpha}}{n_{ref,\alpha}} + \delta_\alpha \\
 &= \delta_\alpha \left[ \frac{\Delta\rho}{\rho_{ref}} \right]_\alpha + \delta_\alpha \left( 1 - \frac{N_{ref,\alpha}}{N_{sib,\alpha}} \right) \frac{n_{sib,\alpha}}{n_{ref,\alpha}} + \delta_\alpha.
 \end{aligned} \tag{8.1}$$

Since  $\delta_\alpha \ll 1$ , all terms in Equation 8.1 are negligible in comparison to the first term of Equation 3.23, i.e.,  $\left[ \frac{\Delta\rho}{\rho_{ref}} \right]_\alpha$ .

## 8.0.2 Fit Parameters

One of the example of pre-factor for  $\pi^- \pi^+$  correlations:

	$y_{T1} \in (1.0, 1.5)$	$y_{T1} \in (1.5, 2.0)$	$y_{T1} \in (2.0, 2.5)$	$y_{T1} \in (2.5, 3.0)$	$y_{T1} \in (3.0, 3.8)$
$y_{T2} \in (1.0, 1.5)$	0.02572	0.02349	0.01495	0.005570	0.001334
$y_{T2} \in (1.5, 2.0)$	0.02391	0.02183	0.01390	0.005177	0.001240
$y_{T2} \in (2.0, 2.5)$	0.01532	0.01399	0.008912	0.003318	0.0007949
$y_{T2} \in (2.5, 3.0)$	0.005892	0.005380	0.003425	0.001275	0.0003055
$y_{T2} \in (3.0, 3.8)$	0.001407	0.001284	0.0008181	0.0003046	7.297e-05

**Table 8.1** Pre-factor for  $\pi^- \pi^+$  for centrality - 0 – 5% .

## Bibliography

- [1] M. S. Daugherty. *Two-Particle Correlations in Ultra Relativistic Heavy Ion Collisions*. PhD thesis, The University of Texas at Austin, 2008.
- [2] Y. Akiba et al. The hot QCD white paper: exploring the phases of QCD at RHIC and the LHC. *arXiv preprint arXiv:1502.02730*, 2015.
- [3] R. Snellings. Elliptic flow: a brief review. *New Journal of Physics*, 13(5):055008, 2011.
- [4] M. Gyulassy. *Structure and Dynamics of Elementary Matter*, chapter The QGP Discovered at RHIC, pages 159–182. Springer Netherlands, Dordrecht, 2004.
- [5] R. L. Ray and M. S. Daugherty. Applicability of Monte Carlo Glauber models to relativistic heavy ion collision data. *J. Phys. G: Nucl. Part. Phys.*, 35, 2008.
- [6] <http://phenix-france.in2p3.fr/liste/lib/RHIC-complex-w.gif>.
- [7] <https://drupal.star.bnl.gov/STAR>.
- [8] M. Anderson et al. The STAR time projection chamber: A Unique tool for studying high multiplicity events at RHIC. *Nucl. Instrum. Meth.*, A499:659–678, 2003.

- [9] [http://www.star.bnl.gov/~ruanlj/MTDreview2010/TOF\\_20040524.pdf](http://www.star.bnl.gov/~ruanlj/MTDreview2010/TOF_20040524.pdf).
- [10] R. Snellings. Elliptic flow: a brief review. *New Journal of Physics*, 13(5):055008, 2011.
- [11] S. S. Adler et al. Identified charged particle spectra and yields in Au + Au collisions at  $\sqrt{s_{NN}} = 200$  GeV. *Phys. Rev. C*, 69:034909, Mar 2004.
- [12] G. Agakishiev et al. Anomalous centrality evolution of two-particle angular correlations from Au-Au collisions at  $\sqrt{s_{NN}} = 62$  and 200 GeV. *Phys. Rev. C*, 86:064902, Dec 2012.
- [13] S. S. Adler et al. Elliptic flow of identified hadrons in Au + Au collisions at  $\sqrt{s_{NN}} = 200$  GeV. *Phys. Rev. Lett.*, 91:182301, Oct 2003.
- [14] F. Wilczek. QCD made simple. *Phys. Today*, 53N8:22–28, 2000.
- [15] T. Sjöstrand et al. PYTHIA 6.4 physics and manual. *Journal of High Energy Physics*, 2006(05):026, 2006.
- [16] M. Gyulassy and X. N. Wang. Hijing 1.0: A monte carlo program for parton and particle production in high energy hadronic and nuclear collisions. *Computer Physics Communications*, 83(2):307 – 331, 1994.
- [17] Frank Wilczek. From notes to chords in QCD. *Nuclear Physics A*, 642(12):c1 – c13, 1998. QCD at Finite Baryon Density.
- [18] U. W. Heinz and M. Jacob. Evidence for a new state of matter: An Assessment of the results from the CERN lead beam program. 2000.

- [19] The STAR Collaboration. Experimental and theoretical challenges in the search for the quark-gluon plasma: The STAR collaboration's critical assessment of the evidence from RHIC collisions. *Nuclear Physics A*, 757(12):102 – 183, 2005. First Three Years of Operation of RHIC.
- [20] The PHENIX Collaboration. Formation of dense partonic matter in relativistic nucleus-nucleus collisions at RHIC: Experimental evaluation by the PHENIX collaboration. *Nuclear Physics A*, 757(12):184 – 283, 2005. First Three Years of Operation of RHIC.
- [21] Reinhard Stock. The physics of dense nuclear matter from supernovae to quark gluon plasma. *Nature*, 337:319–324, 1989.
- [22] E. B. Forsyth and C. Lasky. The Fast Beam Extraction System of the Alternating Gradient Synchrotron. Technical report, Brookhaven National Lab., Upton, NY, 1965.
- [23] E. Malwitz et al. *CERN heavy-ion facility design report*. Number CERN-93-01. CERN, 1993.
- [24] M. Harrison, T. Ludlam, and S. Ozaki. RHIC project overview. *Nuclear Instruments and Methods in Physics Research Section A: Accelerators, Spectrometers, Detectors and Associated Equipment*, 499(23):235 – 244, 2003. The Relativistic Heavy Ion Collider Project: RHIC and its Detectors.

- [25] Arnold P. et al. Transport coefficients in high temperature gauge theories, 2. beyond leading log. *Journal of High Energy Physics*, 2003(05):051, 2003.
- [26] H. Noronha et al. Transport coefficients of hadronic matter near  $T_c$ . *Phys. Rev. Lett.*, 103:172302, Oct 2009.
- [27] A. M. Poskanzer and S. A. Voloshin. Methods for analyzing anisotropic flow in relativistic nuclear collisions. *Physical Review C*, 58(3):8, 1998.
- [28] Matthew Luzum. Collective flow and long-range correlations in relativistic heavy ion collisions. *Physics Letters B*, 696(5):499 – 504, 2011.
- [29] N. Borghini et al. Flow analysis from multiparticle azimuthal correlations. *Phys. Rev. C*, 64:054901, Sep 2001.
- [30] D. Kikoła et al. Nonflow “factorization” and a novel method to disentangle anisotropic flow and nonflow. *Phys. Rev. C*, 86:014901, Jul 2012.
- [31] T. A. Trainor and D. T. Kettler. The azimuth structure of nuclear collisions –I. *International Journal of Modern Physics E*, 17(07):1219–1272, 2008.
- [32] T. A. Trainor. The RHIC azimuth quadrupole: “perfect liquid” or gluonic radiation? *Modern Physics Letters A*, 23(8):20, 2008.

- [33] E. Levin and A. H. Rezaeian. Ridge from the BFKL evolution and beyond. *Phys. Rev. D*, 84:034031, Aug 2011.
- [34] K. Dusling and R. Venugopalan. Evidence for BFKL and saturation dynamics from dihadron spectra at the LHC. *Phys. Rev. D*, 87:051502, Mar 2013.
- [35] B. Z. Kopeliovich, A. H. Rezaeian, and I. Schmidt. Azimuthal asymmetry of pions in pp and pA collisions. *Phys. Rev. D*, 78:114009, Dec 2008.
- [36] A. Ishihara. *Large-Scale Two-Particle Correlation Structures in Au – Au Collisions at  $\sqrt{s_{NN}} = 130$  GeV*. PhD thesis, The University of Texas at Austin, 2004.
- [37] E. W. Oldag. *Two-Particle Correlations in Angular and Momentum Space in Heavy Ion Collisions at STAR*. PhD thesis, The University of Texas at Austin, 2013.
- [38] D. Kettler. *Systematic Azimuth Quadrupole and Minijet Trends from Two-Particle Correlations in Heavy-Ion Collisions*. PhD thesis, The University of Washington, 2013.
- [39] R. L. Ray. Azimuthal quadrupole correlation from gluon interference in 200 GeV and 7 TeV  $p + p$  collisions. *Physical Review D*, 90(054013):10, 2014.
- [40] T. Ludlam M. Harrison and S. Ozaki. RHIC project overview. *Nuclear Instruments and Methods in Physics Research Section A: Acceler-*

- ators, Spectrometers, Detectors and Associated Equipment*, 499(2):235–244, 2003.
- [41] T. Roser and RHIC commissioning team. RHIC status and requirements. *AIP Conference Proceedings*, 572(1):191–195, 2001.
- [42] D. B. Steski and P. Thieberger. Stripping foils at rhic. *Nuclear Instruments and Methods in Physics Research Section A: Accelerators, Spectrometers, Detectors and Associated Equipment*, 613(3):439–441, 2010.
- [43] P. Giubellino. The ALICE detector at LHC. *Nuclear Instruments and Methods in Physics Research Section A: Accelerators, Spectrometers, Detectors and Associated Equipment*, 344(1):27 – 38, 1994.
- [44] CMS Collaboration, R. Adolphi, et al. The CMS experiment at the CERN LHC. *Jinst*, 3(08):S08004, 2008.
- [45] [http://www.star.bnl.gov/protected/common/common2010/trigger2010/200\\_GeV\\_AuAu\\_triggers.pdf](http://www.star.bnl.gov/protected/common/common2010/trigger2010/200_GeV_AuAu_triggers.pdf).
- [46] [https://drupal.star.bnl.gov/STAR/system/files/run11\\_200\\_GeV\\_AuAu\\_triggers.pdf](https://drupal.star.bnl.gov/STAR/system/files/run11_200_GeV_AuAu_triggers.pdf).
- [47] W. J. Llope et al. The TOFp/pVPD time-of-flight system for STAR. *Nuclear Instruments and Methods in Physics Research Section A: Accelerators, Spectrometers, Detectors and Associated Equipment*, 522(3):252 – 273, 2004.

- [48] F. S. Bieser et al. The STAR trigger. *Nucl. Instrum. Meth.*, A499:766–777, 2003.
- [49] B. I. Abelev et al. Systematic measurements of identified particle spectra in  $pp$ ,  $d + Au$ , and  $Au + Au$  collisions at the star detector. *Phys. Rev. C*, 79:034909, Mar 2009.
- [50] Manuel Calderon de la Barca Sanchez. *Charged Hadron Spectra in Au + Au Collisions at  $\sqrt{s_{NN}} = 130$  GeV*. PhD thesis, Yale University, 2001.
- [51] D. Kharzeev and M. Nardi. Hadron production in nuclear collisions at RHIC and high-density QCD. *Phys. Lett. B*, 507(121):8, 2001.
- [52] T. A. Trainor. Understanding RHIC collisions: Modified QCD fragmentation vs quark coalescence from a thermalized flowing medium. *arXiv preprint arXiv:1011.6351*, 2010.
- [53] Karl Pearson. Notes on the History of Correlation. *Biometrika*, 13(1):25–45, October 1920.
- [54] D. J. Prindle and T. A. Trainor. The equivalence of fluctuation scale dependence and autocorrelations. *Journal of Physics: Conference Series*, 27(118):10, 2005.
- [55] J. G. Reid and T. A. Trainor. Statistical fluctuations and pair mixing in two-point correlation analysis. *Nuclear Instruments and Methods in Physics Research Section A: Accelerators, Spectrometers, Detectors and Associated Equipment*, 457(1):378–383, 2001.

- [56] R. L. Ray and P. Bhattarai. Statistical-noise reduction in correlation analysis of high-energy nuclear collisions with event-mixing. *Nuclear Instruments and Methods in Physics Research Section A: Accelerators, Spectrometers, Detectors and Associated Equipment*, 821:142 – 150, 2016.
- [57] R. Reed et al. Vertex finding in pile-up rich events for p+p and d+Au collisions at STAR. *Journal of Physics: Conference Series*, 219(3):032020, 2010.
- [58] <http://www.agsrhichome.bnl.gov/RHIC/Runs>.
- [59] A. R. Timmins. *Neutral Strange Particle Production in Relativistic Cu+Cu Collisions at  $\sqrt{s_{NN}} = 200$  GeV*. PhD thesis, The University of Birmingham, 2008.
- [60] [http://www.star.bnl.gov/webdata/dox/html/StMinuitVertexFinder\\_8cxx\\_source.html](http://www.star.bnl.gov/webdata/dox/html/StMinuitVertexFinder_8cxx_source.html).
- [61] <http://www.star.bnl.gov/protected/jetcorr/prindle/pileup>.
- [62] <http://www.star.bnl.gov/protected/jetcorr/prindle/pileupFinder>.
- [63] <http://www.star.bnl.gov/protected/jetcorr/prindle/pileupCentrality>.
- [64] Hans Bichsel. A method to improve tracking and particle identification in TPCs and silicon detectors. *Nuclear Instruments and Methods in Physics Research Section A: Accelerators, Spectrometers, Detectors and Associated Equipment*, 562(1):154 – 197, 2006.

- [65] Masayuki Wada. *Resonance Particles in Heavy-Ion Collisions*. PhD thesis, The University of Texas at Austin, 2013.
- [66] Shao M. et al. Extensive particle identification with TPC and TOF at the STAR experiment. *Nuclear Instruments and Methods in Physics Research Section A: Accelerators, Spectrometers, Detectors and Associated Equipment*, 558(2):419 – 429, 2006.
- [67] A. Michael et al. Femtoscopy in Relativistic Heavy-Ion Collisions: Two Decades of Progress. *Annual Review of Nuclear and Particle Science*, 55(1):357–402, 2005.
- [68] James Whitmore. Multiparticle production in the fermilab bubble chambers. *Physics Reports*, 27(5):187–273, 1976.
- [69] T. A. Trainor, D. J. Prindle, and R. L. Ray. Challenging claims of nonjet “higher harmonic” components in 2d angular correlations from high-energy heavy-ion collisions. *Phys. Rev. C*, 86:064905, Dec 2012.
- [70] T. A. Trainor, R. J. Porter, and D. J. Prindle. Autocorrelations from fluctuation scale dependence by inversion. *Journal of Physics G: Nuclear and Particle Physics*, 31(7):809, 2005.
- [71] R. J. Porter, T. A. Trainor, STAR Collaboration, et al. Correlations from  $pp$  collisions at  $\sqrt{s} = 200$  GeV. In *Journal of Physics: Conference Series*, volume 27, page 98. IOP Publishing, 2005.

- [72] R. J. Porter and T. A. Trainor. Correlations in pp collisions. *PoS*, page 004, 2006.
- [73] R. J. Porter and T. A. Trainor. Soft and hard components of two-particle distributions on  $(y_t, \eta, \phi)$  from  $pp$  collisions at  $\sqrt{s} = 200$  GeV. *arXiv preprint hep-ph/0406330*, 2004.
- [74] K. A. Olive et al. Review of Particle Physics. *Chin. Phys.*, C38:090001, 2014.
- [75] Abreu P. et al. Inclusive  $\Sigma^-$  and  $\Lambda(1520)$  production in hadronic Z decays. *Physics Letters B*, 475:429 – 447, 2000.
- [76] Kettler D and STAR Collaboration. Azimuth quadrupole systematics in Au-Au collisions. *Journal of Physics: Conference Series*, 270(1):012058, 2011.
- [77] S. Pal, C. M. Ko, and Z. W. Lin. Phi meson production in relativistic heavy ion collisions. *Nuclear Physics A*, 707(34):525 – 539, 2002.
- [78] Chung W. S., G. Q. Li, and C. M. Ko. Phi meson production in heavy-ion collisions at SIS energies. *Nuclear Physics A*, 625(12):347 – 371, 1997.
- [79] D. T. Kettler, D. J. Prindle, and T. A. Trainor. Transverse-rapidity  $y_t$  dependence of the nonjet azimuth quadrupole from 62- and 200-GeV Au-Au collisions. *Phys. Rev. C*, 91:064910, Jun 2015.

- [80] B. Zhang et al. Multiphase transport model for relativistic nuclear collisions. *Physical Review C*, 61(6):067901, 2000.
- [81] Torbjörn Sjostrand. The lund monte carlo for jet fragmentation and  $e^+ - e^-$  physics-jetset version 6.2. *Computer Physics Communications*, 39:347–407, 1986.

## Vita

Prabhat Bhattarai, son of Dharmananda Bhattarai and Sita Devi Bhattarai, was born in Nepal. He graduated from University of Minnesota Duluth with M.S. in Physics in 2010. He entered the University of Texas at Austin in fall 2010 and received doctoral candidacy in Physics in 2013. From 2010-2016 he worked as a graduate teaching assistant and graduate research assistant in the University of Texas at Austin. He was a member of STAR collaboration from 2013-2016. Before 2013 he was a member of MINOS collaboration for neutrino experiment.

Permanent address: Department of Physics, The University of Texas  
at Austin, Austin, TX 78712, USA

This dissertation was typeset with L<sup>A</sup>T<sub>E</sub>X<sup>†</sup> by the author.

---

<sup>†</sup>L<sup>A</sup>T<sub>E</sub>X is a document preparation system developed by Leslie Lamport as a special version of Donald Knuth's T<sub>E</sub>X Program.